



UNIVERSITÀ DEGLI STUDI DI GENOVA
FACOLTÀ DI SCIENZE MATEMATICHE, FISICHE E NATURALI
SCUOLA DI DOTTORATO IN SCIENZE E TECNOLOGIE
PER L'INFORMAZIONE E LA CONOSCENZA
XXXIII CICLO, A.A. 2017 - 2020



A THESIS SUBMITTED FOR THE DEGREE OF
PH.D. IN THEORETICAL PHYSICS

Exploring the Boundary of Perturbative Quantum Chromodynamics

Resummation of Non-Global Logarithms and Soft Superstructure of Jets

by
Chang Wu

AREA 02 - SCIENZE FISICHE
SETTORE SCIENTIFICO-DISCIPLINARE: FIS/02

March 9, 2021

Università degli studi di Genova

The Graduate School

We, the dissertation committee for the above candidate for the
Doctor of Philosophy degree, hereby recommend
acceptance of this dissertation.

Simone Marzani – Dissertation Advisor
Associate Professor, Department of Physics, Genova

Riccardo Ferrando – Chairperson of Defense
Professor, Department of Physics, Genova

Giovanni Ridolfi – Committee Member
Professor, Department of Physics, Genova

Paolo Torrielli – Committee Member
Professor, Università di Torino

Thomas Krajewski – Committee Member
Professor, Aix-Marseille Université

Ferruccio Feruglio – Committee Member
Professor, Università di Padova

Steffen Schumann – External Referees
Professor, Georg-August-Universität Göttingen

Andrea Banfi – External Referees
Reader, University of Sussex

This dissertation is accepted by the Graduate School

©-2020 CHANG WU
ALL RIGHTS RESERVED.
WORD COUNT: 33347

Abstract

This thesis arises in the context of the precision era of Higgs physics from the recent high accuracy data at the Large Hadron Collider (LHC). With the data of an unprecedented level of precision, the theoretical error is now lagging behind. In addition, the accurate theoretical prediction of Standard Model (SM) processes can also lead a path to the discovery of new physics, which thus far has proven so elusive. Indeed, careful analyses of the QCD radiation pattern are crucial to distinguish Standard Model physics from possible new physics signals. In this context, studies of the internal structure of jets, i.e. jet substructure, have proved a valuable addition to LHC phenomenology. Furthermore, in order to obtain the precise predictions, the jet substructure calculations usually involve resummation of the perturbative series, where large logarithms arise from the multi-scale hierarchy.

The aim of this thesis is to explore novel approaches to probe color flow and soft substructure of jets, which is beyond the traditional boundaries of Perturbative Quantum Chromodynamics (pQCD), namely globalness and infrared & collinear (IRC) safety. In this thesis, the impact of non-global logarithms (NGLs) and IRC unsafe observables are studied in detail. In particular, for the non-global case, a novel approach to solving differential equations using artificial neural networks is presented, and we compare the results with the other methods in the literature. In the context of IRC unsafety, the first-principle calculation in resummed perturbation theory for the jet pull angle is performed, along with the resummation formalism is reviewed and improved. As phenomenological applications, each ingredient is studied independently. Moreover, because of the large theoretical uncertainty of IRC unsafe observable, the result is improved by introducing IRC safety projection for the jet pull vector. Additionally, with the purpose of assessing sub-leading color correlations, the novel azimuthal asymmetry distribution is introduced and studied in some detail.

Keywords— Quantum Chromodynamics, All-order Resummation, Evolution Equation, Non-global Logarithms, Infrared and Collinear Unsafety, Jet Substructure, Color Flow

Declaration

The work in this thesis is based on research carried out at the State University of New York at Buffalo, Istituto Nazionale Fisica Nucleare, Genova and Institute for Particle Physics Phenomenology, Durham.

The research described in this thesis was carried out in collaboration with Dr. Simone Marzani, Dr. Andrew Larkoski and Dr. Michael Spannowsky.

The discussion in Chapter 3 contains results will appear in

- S. Marzani, M . Spannowsky and **C. Wu**, “Resummation of Non-Global Logarithms via Neural Network”, in preparation

Chapter 4 includes material discussed in

- A. J. Larkoski, S. Marzani and **C. Wu**, “Theory Predictions for the Pull Angle”, Phys. Rev. D 99, no. 9, 091502 (2019) [arXiv:1903.02275 [hep-ph]].
- A. Larkoski, S. Marzani and **C. Wu**, “Safe Use of Jet Pull,” JHEP 2001 (2020) 104 doi:10.1007/JHEP01(2020)104 [arXiv:1911.05090 [hep-ph]].

Section 5.1 is partially based upon results from the follow ongoing work

- A. J. Larkoski, S. Marzani and **C. Wu**, “Azimutal Asymmetry”, in preparation

Unless explicitly stated in the caption, I have produced all the figures that appear in this work, which will often closely follow those in the corresponding publications.

Contents

Abstract	III
Introduction	1
1 Understanding Infrared Singularities	9
1.1 Perturbative Quantum Chromodynamics	10
1.2 Identification of Infrared Divergences	14
1.3 DGLAP Evolution Equation	24
1.4 Application: NLO Drell-Yan Process	30
1.5 Infrared and Collinear Safety	33
1.6 Resummation of divergent series	34
2 Analytic Resummation Techniques	37
2.1 Perturbation theory to all orders	38
2.2 Transverse momentum distributions	41
2.3 Calculations for jets: the jet mass distribution	48
2.4 Global and non-global logarithms	55
2.5 General resummation formalism	57
3 Resummation of Non-Global Logarithms to All Orders	63
3.1 Structure of non-global logarithms	64
3.2 Evolution equation: Banfi-Marchesini-Smye	70
3.3 Perturbative calculation of NGLs	75
3.4 Solving differential equations with neural networks	79
4 Probing color Flow with Jet Substructure	87
4.1 Seeing in color: jet superstructure	87
4.2 Curiosities: Sudakov safety	92
4.3 Theory predictions for the pull angle	95
4.4 Safe projections of jet pull	105
4.5 Azimuthal asymmetry	118
5 Conclusion and Outlook	121
5.1 Soft Radiation Beyond Leading color	122
5.2 Solver of RG-evolution framework	124

Appendices	127
A Basics of QFT	127
A.1 S-matrix and LSZ reduction formula	127
A.2 Recursion relation for the phase space	128
A.3 Techniques for loop calculations	130
A.4 The large N limit	130
B Basics of QCD	133
B.1 Lagrangian and Feynman rules of QCD	133
B.2 Running coupling	135
B.3 NLO real corrections for the cross-section $e^+e^- \rightarrow$	136
B.4 Quark self-energy diagram	137
B.5 PDF renormalization	137
C Transforms and Special Functions	139
C.1 Laplace and Mellin transforms	139
C.2 Fourier transform	140
C.3 Special functions	140
D Analytical Expressions	143
D.1 One-Loop Feynman Integrals	143
D.2 Multiple soft emission in QED	144
D.3 Extracting the non-cusp anomalous dimension for pull calculation	144
D.4 Soft emissions at wide angle	146
List of Abbreviations	149
List of Figures	151
Acknowledgments	155
Bibliography	157

That's not right. That's not even wrong.
Wolfgang Pauli (1900-1958)

Introduction

One of the central goals of CERN Large Hadron Collider (LHC) is to reach a detailed understanding of the Higgs sector. Besides deepening our understanding of the breaking of the electro-weak symmetry, the determination of the Higgs couplings can also open up the possibility of discovering new physics. Despite the extremely successful prediction of the Higgs boson, which formally completed the Standard Model (SM) of particle physics, the full theory of higher energy scales is still missing. One can view the SM as a low-energy effective field theory (EFT), valid up to some high energy scale. However, intriguing question that cannot be answered within this theory remains. Given the lack of direct evidence for new physics in collider experiments, it becomes important to examine predictions of the SM with an unprecedented precision.

Mathematically, the SM is a quantum field theory (QFT) that exhibits the non-abelian gauge symmetry:

$$SU(3)_C \times SU(2)_L \times U(1)_Y,$$

where the electromagnetic and weak interactions are given by a unified field theory with broken $SU(2)_L \times U(1)_Y$ symmetry, and the strong force, which originates in a quantum number known as color, is described with $SU(3)_C$ gauge theory called as Quantum Chromodynamics (QCD).

In this thesis, we concentrate on the theory of strong interaction, since it constitutes the major contribution of both signal and background processes in any collider experiments. The Lagrangian of QCD is:

$$\mathcal{L} = -\frac{1}{2}Tr(G_{\mu\nu}G^{\mu\nu}) + \sum_{a=1}^{N_f} \bar{\psi}_a (i\gamma_\mu D^\mu - m_a) \psi_a,$$

where D^μ is the covariant derivative, $G_{\mu\nu}$ is the field tensor and g_s is the strong coupling constant.

$$D_\mu = \partial_\mu - ig_s t_a A_\mu^a,$$
$$G_{\mu\nu} = \sum_a t^a G_{\mu\nu}^a, \quad G_{\mu\nu}^a = \partial_\mu A_\nu^a - \partial_\nu A_\mu^a + g_s f_{abc} A_\mu^b A_\nu^c.$$

Calculations in quantum field theory are usually expanded in powers of the coupling constant, where Feynman diagrams are used as a pictorial representation of such perturbation theory. However, such calculations are only reliable, with a small coupling constant $\alpha_s < 1$ that would assure the convergence of the perturbative series. One of the most important properties of QCD is asymptotic freedom, which allows the perturbative prediction of physics above the energy scale that characterizes hadron masses.

Another key fact of QCD, which will be exploited in this thesis, is that physics behaves differently at different energy scales, under renormalization group evolution (RGE). Generally speaking, the method of RGE is a method that describes how the dynamics of some system change when we change the scale. When performing calculations in QFT, two types of singularities will arise from the radiative correction diagrams at the corresponding high energy and low energy limit, which are called ultraviolet (UV) and infrared (IR) singularities.

In particular, in QFT, we must consider arbitrarily short scale, which UV divergent may appear. The theory is called renormalizable if all the information we need from smaller scales can be absorbed with finitely many parameters, such as masses and couplings.

Theorem 1 (Wilson's renormalization procedure). *Let M be the set of scales of momenta, which is a homogeneous space of R_+ . And $\Lambda, \mu \in M$ are the scales of momenta, with $\mu < \Lambda$. For each theory $L \in S$, one finds another theory with $R_{\Lambda\mu}L \in S$, which is the effective theory at the scale μ and the original theory L at the scale Λ . Thus we have a map $R_{\Lambda\mu} : S \rightarrow S$ and $R_{\Lambda_1\Lambda_2} \cdot R_{\Lambda_2\Lambda_3} = R_{\Lambda_1\Lambda_3}$. Therefore an action of the semigroup $R_+^{\leq 1}$ on the space $S \times M$ can be defined by*

$$\lambda \cdot (L, \Lambda) = (R_{\Lambda, \lambda\Lambda}L, \lambda\Lambda).$$

Physicists call this semigroup the renormalization group, which is a slight abuse of mathematical terminology. In other words, the RG is not a group in the traditional mathematical sense; it is only because it maps $S \rightarrow S$, where S is a set of couplings in a theory. The simplest example is the running coupling, but more examples arise from the QCD factorization of hadron scattering. For a general theory, the physical quantities after the renormalization procedure do not depend on the renormalization scale μ . This statement is required for renormalized quantum field theory, by fulfilling the Callan-Symanzik equation

$$\left[\mu^2 \frac{\partial}{\partial \mu^2} + \beta(\alpha_s) \frac{\partial}{\partial \alpha_s} \right] G \left(\frac{A^2}{\mu^2}, \alpha_s \right) = 0,$$

where the beta function describes the running of the coupling constant, defined as

$$\beta(\alpha_s) = \mu^2 \frac{\partial \alpha_s(\mu)}{\partial \mu^2}.$$

With the intention of better describing the renormalization and running of coupling constant in a theory, let's consider the vacuum polarization diagram in

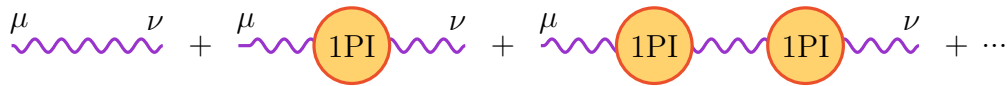


Figure 1. The geometric series for the exact propagator.

QED, also known as the photon self-energy. It can be viewed as a modification to the photon propagator by the virtual electron-positron pair. For the second-order (in e) contribution:

$$\mu \text{ --- } \text{---} \text{---} \nu = i\Pi_2^{\mu\nu}(q).$$

More generally, we can define the sum of all 1-particle-irreducible (1PI) insertions, i.e. $i\Pi^{\mu\nu}(q)$, into the exact photon propagator, which can be interpreted as a geometric series shown in Fig. 1. And the diagram is 1PI if it is still connected after any line is cut. According to the Ward identity $q_\mu \Pi^{\mu\nu}(q) = 0$, which indicate the tensor structure of $\Pi^{\mu\nu}(q)$ in the following form:

$$\Pi^{\mu\nu}(q) = q^2 g^{\mu\nu} - q^\mu q^\nu \Pi(q^2).$$

Ward identity is a diagrammatic expression of the conservation of the electric current (details about the Ward identity will be given in App. A). Moreover, in any S-matrix calculation, the exact propagator will connect to a fermion line, then the terms proportional to q_μ or q_ν vanish. Therefore, geometric series can be expressed as

$$\mu \text{ --- } \text{---} \text{---} \nu = \frac{-ig_{\mu\nu}}{q^2(1 - \Pi(q^2))},$$

where the exact propagator has a pole at $q^2 = 0$, and the amplitude is modified by the residue of the pole, $Z_3 = \frac{1}{1 - \Pi(0)}$, from the tree-level approximation

$$\frac{e^2 g_{\mu\nu}}{q^2} \rightarrow Z_3 \frac{e^2 g_{\mu\nu}}{q^2}.$$

Therefore, we can define an effective charge $e_R = \sqrt{Z_3}e$, this replacement is called charge renormalization. For the leading order correction of the coupling constant α :

$$\alpha \rightarrow \alpha_{eff}(q^2) = \frac{\alpha}{1 - [\Pi(q^2) - \Pi(0)]},$$

we note that the coupling constant becomes q^2 -dependent after the renormalization procedure, and that is why we call it running coupling constant.

On the contrary from the well-controlled UV divergence from the renormalization procedure, IR divergence is known to cancel itself when combining real emission with virtual diagrams for inclusive observables, i.e., total cross-sections.

The cancellation is a consequence of the Kinoshita-Lee-Nauenberg (KLN) theorem [1, 2]. However, for exclusive observables with processes characterized by the presence of two or more widely separated energy scales, the perturbative expansion would contain large logarithms.

Theorem 2 (Kinoshita-Lee-Nauenberg Theorem¹). *In a theory with massless fields, transition rates are free of the infrared divergence (soft and collinear) if the summation over initial and final degenerate states is carried out.*

To improve the accuracy of theoretical predictions, higher-order corrections in the perturbative expansion must be included. In the past years, next-to-leading order (NLO) computations have become standard tools for phenomenological studies, and in some cases, higher-order terms have been calculated up to next-to-next-to-leading order (NNLO) and next-to-next-to-next-to-leading order (N3LO) [3]. However, in regions characterized by large-scale hierarchy, the perturbative expansion is violated due to large logarithmic enhancements. For a generic observable, the cross-section contains terms proportional to logarithms as

$$\begin{aligned}\sigma(v) &= \sigma_0 \left(1 + \alpha_s [c_{12} \log^2 v + c_{11} \log v] + \alpha_s^2 [c_{24} \log^4 v + \dots] \right) \\ &= \sigma_0 \left(1 + \sum_{n=1} \alpha_s^n \sum_{m=1}^{2n} c_{nm} \log^m v \right).\end{aligned}$$

For the singular contribution with either v is close to zero or large, the large logarithm enhanced terms will spoil the convergence of the perturbation theory

$$\alpha_s \log v \sim 1.$$

As a consequence, the perturbative expansion is invalidated, even with a small coupling constant. This situation can be rescued by performing an all-order resummation, thereby the fixed-order treatment is insufficient for accurate theoretical prediction. Therefore, these logarithms need to be resummed to all orders. One can achieve the resummation by restructuring the perturbative series as following:

$$\sigma(v) = g_0(\alpha_s) \exp^{-S(\alpha_s L)},$$

where the function g_0 collects all the constant terms, and the logarithms are located at the exponent, which can be written as

$$S(\alpha_s, L) = Lg_1(\alpha_s L) + g_2(\alpha_s L) + \alpha_s g_3(\alpha_s L) + \dots,$$

the first term is leading logarithm (LL) accuracy and the second one contributes to next-to-leading logarithm (NLL) accuracy. On the other hand, due to the large QCD background, careful studies of QCD radiation that accompanies both signal and background processes can help us discriminate between the two. In this context, studies of the internal structure of jets, i.e., jet substructure, have proved a

¹More details about KLN theorem, along with a brief review of S-matrix can be found in App.A.1

valuable addition to LHC phenomenology. The calculations for jet substructure usually involve resummation of large logarithms, e.g., the jet mass over its transverse momentum. While the above description of resummation is only valid for observables that are sensitive to radiation over the entire final-state phase-space, i.e. global observables, the structure of all-order resummation is known up to next-to-next-to-next-to-leading logarithm (N³LL), for example: Thrust [4] and Angularities [5]. However, global observables are only a subset of observables that are interesting for studying the QCD radiation pattern.

Unfortunately, the procedure described in the previous paragraph can only be performed accurately for a narrow class of observables, that satisfy two basic properties:

- infrared and collinear (IRC) safety: IRC safe observable means it can be calculated as the expansion of the coupling α_s at any order, where the IR singularities cancel themselves between real and virtual corrections.
- globalness: an observable is defined as global, if the radiation is constrained uniformly over the entire phase space.

The first condition ensures the cancellation of soft and collinear singularities, as stated by the KLN theorem. For a general observable $V = V(p_1, \dots, p_n)$, we say the observable is IRC safe if its value does not change in the presence of an arbitrary amount of soft or collinear emissions. From a more physical point of view, the non-perturbative effects like the hadronization process will act as a regulator for the IRC divergences. Therefore, the requirement of IRC safety also indicates that our calculation in perturbative QCD is reliable up to non-perturbative power corrections, which are suppressed by inverse powers of the hard scale.



Figure 2. Cancellation between the real production and virtual loop contribution for gluon 2

While for the second condition, many interesting observables with boundaries in phase space do not obey the second condition, and the non-global logarithms arise from the mis-cancellation of real and virtual emissions of gluons. The lowest order kinematic configurations are shown in Fig. 2, with two large-angle soft gluons, whose energies are ordered $k_1 \gg k_2$. Due to the IRC safety, there is a cancellation between the real emission and virtual loop contribution for gluon 2. However, suppose we only observe the right hemisphere, then the gluon 2 is treated as independent emission and spoils the cancellation with the virtual diagram. The correlated gluon emissions generate a new tower of logarithmic corrections, which are more subtle to treat within the traditional resummation techniques [6, 7].

Furthermore, understanding color flow in hard scattering processes plays a particularly important role in high-energy physics. For instance, it can provide a powerful handle to distinguish the hadronic decay products of color singlets in the final state. However, unlike the mass or electric charge, which are relatively straightforward to measure at the collider experiments, such as LHC. The quantum number related to the particles' strong interactions is color charge, determining the color representation of a jet, however, is highly non-trivial.



Figure 3. QCD color rules for quark–gluon vertices. Black lines denote Feynman-diagram style vertices, colored lines show QCD color connection lines.

Structure of the thesis

This thesis is devoted to the study of two categories of observable beyond the range of traditional Perturbative Quantum Chromodynamics (pQCD), i.e. IRC safety and globalness, with detailed applications about jet soft substructure, in particular the impact of resummation of both ingredients is discussed in detail and some phenomenological results are shown.

The outline starts with the factorization and resummation procedures, which are illustrated as the first part, with color code black, in Fig. 4. The fundamental idea is to explain how a physical quantity can be calculated, despite it may contain IR singularities.

In the second part (color blue), we focus our attention on two intriguing problems of QCD, the resummation of non-global logarithms and IRC unsafe observables. It is worth mentioning that the IRC unsafe observable does not have a valid expansion in coupling constant. However, with the help of the all-order resummation technique, the concept of Sudakov safety would enable perturbation theory beyond the IRC domain. In terms of non-global logarithms (NGLs), some improvements for higher-order calculation and resummation are proposed with artificial neural networks, which can dramatically speed up needed theory calculations.

Finally, combine both ingredients, a phenomenological application for probing color flow with jet substructure, i.e. jet pull, will be shown in Chapter 4. The theoretical understanding of these observables led us to introduce novel azimuthal asymmetry distributions that measure the radiation pattern by looking at the difference between the jet pull vector pointing towards and away from the other jet of interest. In particular, these asymmetries essentially come from soft radiation and introduce a new boundary in phase-space which renders the all-order structure of these observables richer, which will briefly discuss in Sec. 4.5 and Sec. 5.1.

Before discussing all these aspects in detail, in Chapter 1 some features of IR singularities in perturbative QCD are presented, together with a general overview about factorization and conditions that the calculable observables should satisfy

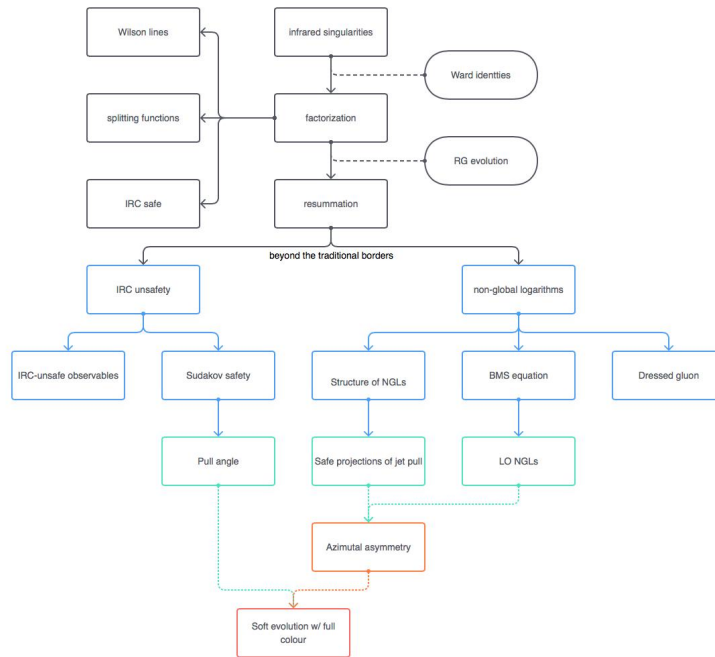


Figure 4. Outline of the thesis: The color denotes the different sections of the thesis. The ovals describe the needed theoretical tools, and the dashed arrowhead lines correspond to the path related to future projects

for the first-principle calculation of pQCD and notations that we are going to use in the rest of the text.

1 Understanding Infrared Singularities

Contents

1.1	Perturbative Quantum Chromodynamics	10
1.1.1	Asymptotic freedom and coupling constant	10
1.1.2	Parton picture of hard scattering	11
1.1.3	Assumptions of perturbative QCD	12
1.1.4	Non-perturbative effects and power corrections	14
1.2	Identification of Infrared Divergences	14
1.2.1	Analytic properties: Landau equations	16
1.2.2	QCD corrections to the electromagnetic vertex	17
1.2.3	Cancellation of infrared divergences in $e^+e^- \rightarrow$ hadrons	18
1.2.4	Strategy of regions	20
1.2.5	Factorization in the soft limit	21
1.3	DGLAP Evolution Equation	24
1.3.1	Splitting Functions	24
1.3.2	Parton Evolution: DGLAP Equations	27
1.3.3	Collinear factorization and Mellin transform	28
1.4	Application: NLO Drell-Yan Process	30
1.5	Infrared and Collinear Safety	33
1.6	Resummation of divergent series	34
1.6.1	Large-order behaviour of perturbation theory	34
1.6.2	Padé approximation	35
1.6.3	Borel-Leroy transform	35

In the previous chapter, we made some general remarks about the formal development of divergences in QFT, as well as some general prescriptions to obtain finite results. In this chapter, we are going to systematically review IR singularities in pQCD and derive many of their properties. Most of the material presented in this chapter does not follow any particular review or book on pQCD, but is organized in a way that is suitable for this thesis, as we intend to introduce useful terminology and fix some notations. For more details, there are many excellent reviews of pQCD, e.g. [8–14].

1.1 Perturbative Quantum Chromodynamics

As mentioned earlier, calculations in QCD are often performed through perturbative expansion in strong coupling. However, in regions characterized by large-scale hierarchy, the perturbative expansion is invalidated even for small coupling. This situation can be rescued by performing an all-order resummation, thereby the fixed-order treatment is insufficient for accurate theoretical prediction.

The structure of IR singularities plays a key role in the all-order structure of perturbation theory. Besides deepening the understanding of perturbative QFT at high orders, it also has many practical applications. For example, IRC safety is the guiding principle for devising new and better jet observables. Jets are collimated sprays of hadrons, which are dominant features of high-energy physics. They originate from accelerated quarks and gluons, thus can provide important clues about the high-energy behavior of parton degrees of freedom. Therefore, they constitute an ideal testing ground to study the fundamental properties of QCD.

In this introduction, we will start with an overview of the basic concepts of pQCD and the key idea about how to factorize the perturbatively-calculable hard scattering functions that describe the hard scattering of point-like partons.

1.1.1 Asymptotic freedom and coupling constant

Here we start from the main feature of QCD, that makes the perturbative treatment possible: asymptotic freedom [15]. We say a theory is asymptotically free if the coupling constant decreases as the energy scale increases.

Furthermore, if the short and long-distance effects are incoherent, we would neglect masses in the calculation within the short-distance region, as masses exhibit the same asymptotic behavior as the running coupling

$$m(\mu^2) = m(\mu_0^2) \exp \left\{ - \int_{\mu_0}^{\mu} \frac{d\lambda}{\lambda} [1 + \gamma_m(g(\lambda))] \right\},$$

$$\lim_{\mu^2 \rightarrow \infty} \frac{m(\mu^2)}{\mu^2} = 0, \quad (1.1.1)$$

where $\gamma_m(g)$ is a perturbative quantity, similar to $\beta_m(g)$ which vanishes as μ increases. The Callan–Symanzik equation, i.e. renormalization-group equation, for massless theory reads:

$$\mu \frac{d}{d\mu} \alpha_s(\mu) = \beta(\alpha_s(\mu)), \quad (1.1.2)$$

where the β function is

$$\beta(\alpha_s) = -2\alpha_s \left(\beta_0 \frac{\alpha_s}{4\pi} + \beta_1 \left(\frac{\alpha_s}{4\pi} \right)^2 + \beta_2 \left(\frac{\alpha_s}{4\pi} \right)^3 + \dots \right). \quad (1.1.3)$$

With the resummation terminology, we can resum the coupling constant at finite orders of accuracy at $N^i\text{LL}$ related to β_i . And the coefficient β_i is known up to 5-loop [16], i.e. $i = 4$. Further details about the explicit result up to $N^3\text{LL}$ will be given in App. B.2. For the leading term

$$\beta_0 = \frac{11}{3}C_A - \frac{4}{3}T_F n_f. \quad (1.1.4)$$

It is positive, as long as there are no more than 16 flavors of quark, thus the sign of β function is negative. Therefore QCD is asymptotically free theory, as α_s decrease while μ increase.

1.1.2 Parton picture of hard scattering

As mentioned earlier, it is well known that the components of hadrons are quarks and gluons, which are generically called partons, as they are part of the hadron. Originally, the parton model was proposed by Richard Feynman in 1969 [17]. Even though QCD has taken over from the old parton model, the field theory extension of the parton model allows us to derive calculable partonic cross-section by separating the long-distance from short-distance effects. Moreover, the parton picture predicted the jet-like structure of the final states of hard interactions. Nowadays the parton model is understood as the lowest order of perturbative QCD calculations.

The fundamental hypothesis of the parton model for deep inelastic scattering (DIS), i.e. the scattering of a lepton on a nucleon (or other hadrons) shown in Fig. 1.1 may be written as

$$\sigma(p, q) = \sum_f \int_0^1 dz \hat{\sigma}_B(zp, q) f_{f/N}(z), \quad (1.1.5)$$

where inelastic means the energy of the collision is such that the nucleon, such as the proton, breaks up into pieces. Given that each parton carries momentum fraction z_i of the proton momentum p , i.e. $p_i = z_i p$, the function $f_{f/N}$ describe the probability of finding a parton of flavor f in the target hadron N , and it is called parton distribution function (PDF), while $\hat{\sigma}_B$ is the Born-level, elastic parton-lepton cross-section.

Note that the basic assumption in the parton model is the absence of interference, either between different flavors or different momentum fractions. Thus it can describe processes separate from the hard scattering. More on this incoherence will be discussed in the next subsection. It is worth mentioning that PDFs are universal objects, which means any proton scattering process can be computed using the same PDFs with an independent perturbative calculation for different parton scattering.

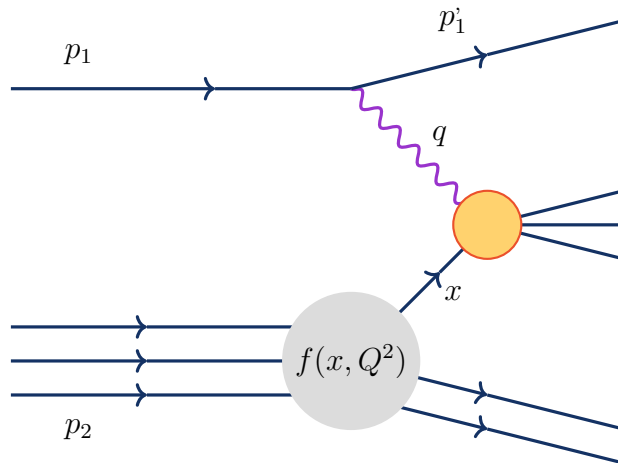


Figure 1.1. Deep inelastic scattering in the parton model.

1.1.3 Assumptions of perturbative QCD

To understand the generalization of parton model to perturbative QCD, it is useful to pinpoint the two main assumptions:

- The pQCD series is asymptotic
- Incoherence of short and long-distance dynamics

Perturbation theory provides a very powerful tool to predict observable quantities from the quantum field theory. It is based on the assumption that every observable can be defined by a power series in the coupling constant of the theory:

$$f(\alpha_s) \sim \sum_{n=0}^{\infty} f_n \alpha_s^n. \quad (1.1.6)$$

If the coupling is small, the first few terms in the series are sufficient to describe the observable. However, in QCD one finds an $n!$ growth of each order at the coefficients f_n [18]. For a small coupling, i.e. $\alpha_s \rightarrow 0$, the series can at best be asymptotic to $f(\alpha_s)$. A series $\sum f_n \alpha_s^n$ is called asymptotic to $f(\alpha_s)$ for $\alpha_s \rightarrow 0$ if, for a given N , the first N terms of the series may as close as desired to $f(\alpha_s)$, i.e. the remainder obeys

$$\left| f(\alpha_s) - \sum_{n=0}^N f_n \alpha_s^n \right| \leq C_{N+1} |\alpha_s|^{N+1}, \quad (1.1.7)$$

where $C_{N+1} |\alpha_s|^{N+1}$ is called as the truncation error. In order to find the N that optimally truncates the asymptotic expansion, we need to find the N that minimizes the truncation error. If C_N follows the same pattern as the coefficients f_N in QCD:

$$C_N \sim N! a^N N^b. \quad (1.1.8)$$

One finds that the error decreases as a function of the order N until N_* by using Stirling's formula for $n!$

$$C_N |\alpha_s|^N = N! a^N |\alpha_s|^N \sim \exp \{N (\log N - 1 - \log X)\}, \quad (1.1.9)$$

where $X = \frac{1}{a|\alpha_s|}$, the last term has a saddle at large N as $N_* = X$. Thus we can get the best approximation to $f(\alpha_s)$ with the maximal resolution of $C_{N_*} |\alpha_s|^{N_*}$. This also suggests two different functions may have the same asymptotic expansion as

$$g(\alpha_s) = f(\alpha_s) + C e^{-\frac{1}{a|\alpha_s|}}. \quad (1.1.10)$$

This ambiguity present in an asymptotic series is called the non-perturbative ambiguity, which will be discussed in the corresponding subsection later. However, if the coupling is small enough, the difference between $g(\alpha_s)$ and $f(\alpha_s)$ may be numerically small and give a well-approximated result, up to power corrections. We will briefly introduce the power corrections in the next subsection and attempt to (re)sum the asymptotic series in Sec. 1.6. (see also Ref. [19] for a pedagogical review.)

The second assumption indicates these properties that hold at each order in the asymptotic series up to power corrections also hold in the full theory, which enables us to separate the perturbative calculable part from the non-perturbative one described by PDF. The factorization theorem can be proved at the level of rigor in theoretical physics [20, 21], such as operator product expansion in Euclidean quantum field theory for inclusive electron-positron annihilation to hadrons.

To be specific, consider inclusive electron-hadron scattering. In the center-of-mass frame, colliding hadrons are Lorentz contracted, and its internal interactions are time dilated. At sufficiently high energies, the hadrons are in virtual states characterized by a definite number of partons that are well separated. Thus the partons do not interact, and each of them carries a fraction z of the hadron's momentum. Therefore, the hard scattering process becomes incoherent, as interactions among partons within a hadron cannot interfere with this hard scattering because they take place at time-dilated scales. For process $e + H \rightarrow X$ with one hadron in the initial state can then schematically be factorized at leading power in the hard scale

$$\sigma_{eH} = \sum_a f_{a/H}(\mu, z) \otimes \hat{\sigma}_B(\mu, z). \quad (1.1.11)$$

As introduced earlier, the function $f_{x/X}(z)$ is called as PDF which describe the distribution of parton x with momentum fraction z in hadron X , and these distribution functions are convolved with the partonic cross-section $\hat{\sigma}_{ab}$, which is denoted by the symbol \otimes .

$$(f_1 \otimes \dots \otimes f_k)(x) = \int_0^1 dx_1 \dots \int_0^1 dx_k \delta(x - x_1 x_2 \dots x_k) f_1(x_1) \dots f_k(x_k). \quad (1.1.12)$$

Hence, the long-distance effect of the distribution functions is separated from the short distance by the factorization scale μ , in such a way that the physical cross-section is independent of this scale. The partonic cross-section $\hat{\sigma}_{ab}$, after the factorization, is calculable if it is IR safe. To be specific, we say a physical quantity τ , e.g., cross-section, is IR safe if τ behave in the large μ limit as

$$\lim_{\mu \rightarrow \infty} \tau \left(\frac{Q}{\mu}, \alpha_s(\mu), \frac{m(\mu)}{\mu} \right) = \hat{\tau} \left(\frac{Q}{\mu}, \alpha_s(\mu) \right) + O \left(\frac{m^n}{\mu^n} \right), \quad n > 0. \quad (1.1.13)$$

This means the IR safe quantities are free of power correction, which we will identify as the non-perturbative effect.

1.1.4 Non-perturbative effects and power corrections

In the first half of Sec. 1.1.3, we have reviewed the properties of the asymptotic series. In the second half, we noted that Eq.(1.1.11) is valid up to power corrections in the hard scale $Q \gg \Lambda_{QCD}$. In addition, due to the properties of non-perturbative ambiguity, Eq.(1.1.10), we have

$$e^{-\frac{1}{a|\alpha_s|}} \sim \left(\frac{\Lambda_{QCD}}{Q} \right)^{\frac{\beta_0}{2\pi a}}, \quad (1.1.14)$$

with the running coupling at LL accuracy, $\alpha_s(Q) \sim \beta_0^{-1} \log^{-1} Q / \Lambda_{QCD}$. And the non-perturbative effects manifest themselves as corrections to the perturbative theory, that is suppressed by the power of $1/Q$. Therefore, Eq.(1.1.11) can be rewritten as

$$\sigma_{AB}(\mu, z) = \sum_{a,b} f_{a/A}(\mu, z) \otimes f_{b/B}(\mu, z) \otimes \hat{\sigma}_{ab}(\mu, z) \left[1 + O \left(\frac{\Lambda_{QCD}^2}{Q^2} \right) \right]. \quad (1.1.15)$$

Moreover, If we ignore the μ dependence, Eq.(1.1.15) can be understood as the lowest order of perturbation theory and gives scaling of the cross-section in $1/Q^2$, reflecting the point-like nature of the constituents. Which is the original parton model of Bjorken and Feynman [17, 22]. In general, Eq.(1.1.15) is valid to any order in perturbation theory, and logarithmic violations of scaling appear through the $f_{x/X}$ and Q/μ dependence. We will discuss more details in Sec. 1.3.

To sum up, these assumptions, described above, statement that the power corrections in the regulated theory should power suppressed in the transition to the full theory.

1.2 Identification of Infrared Divergences

The hard scattering cross-section in hadron collisions can be factorized into the product of non-perturbative contributions, i.e., parton distribution functions that

describe the initial motions of partons, and perturbative hard scattering functions that describe the hard scattering of point-like partons.

The next task is to identify perturbatively-calculable quantities, i.e. IR safe $\hat{\sigma}_{ab}$, after the UV divergences removed by the renormalization procedure. Therefore, much of the discussion in this section will center on identifying and separating the IR safe quantities. More about the properties of IR safety will be discussed at Sec. 1.5.

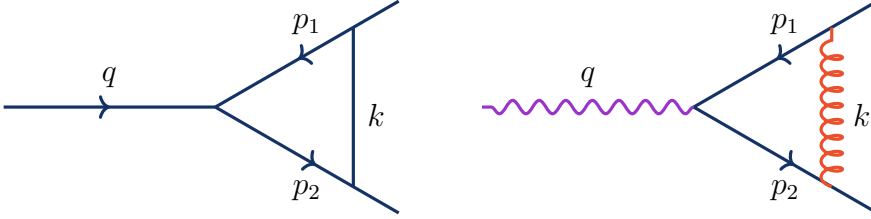


Figure 1.2. One-loop vertex corrections

The IR divergences arise from particle momenta becoming either soft or collinear. In order to illustrate the source of these IR divergences, we start by considering the simple one-loop vertex corrections, i.e. massless three-point function at one loop with two on-shell external legs, shown in Fig. 1.2. This requires the evaluation of Feynman integral for the internal propagators. For simplicity, we first consider the vertex in a scalar theory

$$I = -ig^3\mu^{3\epsilon} \int d^d k \frac{1}{(k^2 + i\epsilon) ((p_1 + k)^2 + i\epsilon) ((p_2 - k)^2 + i\epsilon)}. \quad (1.2.1)$$

We employed dimensional regularization in order to regulate IR singularities when the denominator becomes zero. It is easy to identify the soft singularity with $k \rightarrow 0$, other possible singularity come from either $(p_1 + k)^2$ or $(p_2 - k)^2$ going to zero, which corresponds to the gluon collinear to one of the external legs, hence called as the collinear singularity.

The dimensional regulator ϵ is defined by $d = 4 - 2\epsilon$, where d is the number of dimensions. It is important to remember that the integrals with dimensional regularization are defined for arbitrary ϵ , but only when we choose $\epsilon < 0$, then it can be evaluated as a standard integral. Using the Feynman parametrization and n-dimensional integration, the results can be written in terms of Gamma and beta function, details can be found in App. A.3

$$I = (-ig\mu^\epsilon) \frac{1}{q^2} \frac{g^2}{(4\pi)^2} \left(\frac{4\pi\mu^2}{-q^2} \right)^\epsilon \Gamma(1 + \epsilon) \frac{B(-\epsilon, 1 - \epsilon)}{-\epsilon}. \quad (1.2.2)$$

Evaluating the divergent integrals with the dimensional regulation will give rise to ϵ pole. The above integral is UV-finite, so all the poles in ϵ are entirely infrared. Each of these two types of IR singularities will result in a single ϵ^{-1} pole, and if

the gluon is both soft and collinear the double pole, i.e. ϵ^{-2} , arise. For the detailed calculation, we will elaborate on the latter part of this section.

The physical picture of soft and collinear divergences can be described from parton branching, in Fig.1.3 the example of gluon-gluon branching is shown. For the initial state parton branching, i.e. left side of Fig.1.3, the four-momentum squared of massless parton b is

$$p_b^2 = -2E_a E_c \cos\theta \leq 0, \quad (1.2.3)$$

which $1/p_b^2$ diverges both as $E_c \rightarrow 0$ (soft singularity) and $\theta \rightarrow 0$ (collinear singularity).

Other types of parton branching will be discussed at Sec. 1.3. As a last comment for the parton branching, we can also describe the IRC safe quantities¹ as insensitive to soft or collinear branching. According to KLN theorem, IR divergences in the perturbative theory should cancel between real and virtual contributions. Therefore, such quantities are determined by the short-distance physics and long-distance effects give power corrections, which are power suppressed by the large momentum scale.

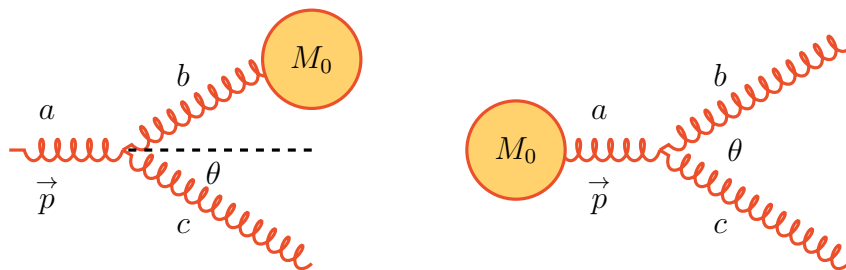


Figure 1.3. Branching of incoming and outgoing gluons

1.2.1 Analytic properties: Landau equations

To see where the soft and collinear singularities may come from, we start from the Feynman integral for the scalar triangle which gives the following expression after Feynman parametrization, introduced in App. A.3

$$I \sim \int_0^1 d\alpha_1 d\alpha_2 d\alpha_3 \delta\left(1 - \sum_{i=1}^3 \alpha_i\right) \int \frac{d^d k}{(2\pi)^d} D^{-3}, \quad (1.2.4)$$

where the D stand for the new denominator

$$D = \alpha_1 k^2 + \alpha_2 (p_1 - k)^2 + \alpha_3 (p_2 + k)^2 + i\epsilon. \quad (1.2.5)$$

Recall Cauchy's theorem, the singularities arise in Eq.(1.2.4) if isolated poles cannot be avoided by contour deformation. The Landau equations summarize the

¹Since we have identified IR divergences contain soft and collinear singularities. From now on, we will call the property of calculable partonic scattering as IRC safety.

conditions for the existence of pinch surfaces, which are surfaces in (k, α) space where D vanishes [23, 24]. Since D is quadratic in momenta, this is equivalent to the condition

$$\frac{\partial}{\partial k^\mu} D(\alpha_i, k^\mu, p_a) = 0. \quad (1.2.6)$$

In summarizing these conditions, we arrive at the Landau equations which state that a pinch surface exists only if the following conditions hold for each point (k_μ, α_i) on the surface:

$$\text{either } l_i^2 = m_i^2, \text{ or } \alpha_i = 0, \quad (1.2.7)$$

$$\text{and } \sum_{i \text{ in loop } s} \alpha_i l_i \epsilon_{is} = 0. \quad (1.2.8)$$

For the three-point vertex function of the scalar theory in Fig.1.2, the Landau equation is simply

$$\alpha_1 k^\mu - \alpha_2 (p_1 - k)^\mu + \alpha_3 (p_2 + k)^\mu = 0. \quad (1.2.9)$$

The solutions to this equation are

$$k^\mu = 0, \alpha_2 = \alpha_3 = 0, \quad (1.2.10)$$

$$k^2 = p_2 \cdot k = 0, \alpha_2 = 0, \quad (1.2.11)$$

$$k^2 = p_1 \cdot k = 0, \alpha_3 = 0. \quad (1.2.12)$$

In the first solution, the loop momentum k is soft, while in the other two solutions it is collinear to either of the two quark legs.

1.2.2 QCD corrections to the electromagnetic vertex

Using this simple but informative example of One-loop vertex correction in scalar theory, we have introduced the soft and collinear divergences. For the QCD loop correction to the electromagnetic vertex, shown on the right side of Fig.1.2. Based on the Feynman rule, the quark-antiquark production vertex can be written in terms of form factor

$$\Gamma_\mu(p_1, p_2, \epsilon) = -ie\bar{u}(p_1) \gamma_\mu v(p_2) (1 + \rho(p_1, p_2, \epsilon)). \quad (1.2.13)$$

For the full calculation, the one-loop QCD vertex correction with dimensional regularization can be read from Feynman rules as

$$\Gamma_\mu(p_1, p_2, \epsilon) = -ieg^2 C_F \mu^{2\epsilon} \int \frac{d^d k}{(2\pi)^d} \frac{\bar{u}(p_1) \gamma^\alpha (\not{p}_1 + \not{k}) \gamma_\mu (\not{k} - \not{p}_2) \gamma_\alpha v(p_2)}{(k^2 + i\epsilon) ((p_1 + k)^2 + i\epsilon) ((p_2 - k)^2 + i\epsilon)}, \quad (1.2.14)$$

where we have applied the color rule $t^a t^a = C_F I$. (see App. B.1)

The Landau equation for the QCD corrections is the same as the scalar theory case, shown in Eq.(1.2.9), where the graphical representation of the solutions are shown in Fig.1.4a.

In the soft region, i.e. small k , we can neglect k^μ in the numerator and k^2 in denominators. This approach is known as eikonal approximation closely related to the Wilson line, which represents a path ordered exponential of gauge fields. Details will be introduced along with factorization in the soft limit later in this section.

$$\rho^{eik}(p_1, p_2, \epsilon) \rightarrow -g^2 C_F \int \frac{d^d k}{(2\pi)^d} \frac{(p_1 \cdot p_2) \bar{u}(p_1) \gamma_\mu v(p_2)}{(k^2 + i\epsilon)(p_1 \cdot k + i\epsilon)(-p_2 \cdot k + i\epsilon)}. \quad (1.2.15)$$

Returning to the full expression, Eq.(1.2.4), as mentioned earlier, it is useful to apply Feynman parametrization, with $n = 3$ in Eq.(A.3.2). Thus the expression becomes

$$\begin{aligned} \Gamma_\mu(p_1, p_2, \epsilon) &= -ieg^2 C_F \mu^{2\epsilon} \int \frac{d^d k}{(2\pi)^d} \int_0^1 d\alpha \int_0^1 d\beta \int_0^1 d\gamma \delta(1 - \alpha - \beta - \gamma) \\ &\quad \times \frac{\bar{u}(p_1) \gamma^\alpha (\not{p}_1 + \not{k}) \gamma_\mu (\not{k} - \not{p}_2) \gamma_\alpha v(p_2)}{[k^2 + 2\alpha k \cdot p_1 - 2\alpha k \cdot p_2 + i\epsilon]^3}. \end{aligned} \quad (1.2.16)$$

Then we can perform the shift $k = k' + \alpha p_1 - \beta p_2$, so that the expression becomes

$$\Gamma_\mu(p_1, p_2, \epsilon) = -2ieg^2 C_F \mu^{2\epsilon} \int \frac{d^d k}{(2\pi)^d} \int_0^1 d\alpha \int_0^1 d\beta \int_0^1 d\gamma \frac{\delta(1 - \alpha - \beta - \gamma) N^\mu}{[k'^2 + \alpha\beta q^2 + i\epsilon]^3}, \quad (1.2.17)$$

where the numerator is

$$N^\mu = \bar{u}(p_1) \gamma^\alpha (\not{k}' + (1 - \beta) \not{p}_1 - \alpha \not{p}_2) \gamma^\mu (\not{k}' + (1 - \alpha) \not{p}_2 - \beta \not{p}_1) \gamma_\alpha v(p_2). \quad (1.2.18)$$

The calculation for the numerator can be simplified with the properties of γ matrix and the equations of motion (see for details in App. D.1). Finally, the one-loop form factor is given by

$$\rho(p_1, p_2, \epsilon) = -\frac{\alpha_s}{2\pi} C_F \left(\frac{4\pi\mu^2}{q^2} \right)^\epsilon \frac{\Gamma(1 + \epsilon) \Gamma^2(1 - \epsilon)}{\Gamma(1 - 2\epsilon)} \left(\frac{1}{\epsilon^2} + \frac{3}{2\epsilon} + 4 + O(\epsilon) \right). \quad (1.2.19)$$

Hence, the soft and collinear singularities are regulated. The double pole is the same as the result, Eq.(1.2.2) in the scalar theory and these double poles are universal in dimensionally regulated massless integrals.

1.2.3 Cancellation of infrared divergences in $e^+e^- \rightarrow \text{hadrons}$

We now discuss more properties of scattering amplitudes in the soft and collinear limits and define the perturbatively calculable quantities. Thus, we consider a

simple example to illustrate the cancellation of infrared divergences, as stated by the KLN theorem. We will come back to a more general definition of IRC safety in Sec. 1.5. As an example, we consider the inclusive production of hadrons in e^+e^- collisions, where the general expression for the cross-section can be written as

$$\sigma_{had} = \sigma_{q\bar{q}}^{(0)} + \frac{\alpha_s}{2\pi} \left(\sigma_{q\bar{q}}^{(1)} + \sigma_{q\bar{q}g}^{(0)} \right) + O(\alpha_s^2), \quad (1.2.20)$$

where the leading order (LO) contribution for the hadronic cross-section in e^+e^- annihilation, can be calculated from the first term of Eq.(1.2.9)

$$\sigma_{q\bar{q}}^{(0)} \equiv \sigma_0 = \frac{4\pi\alpha}{3s} N_c \sum e_q^2, \quad (1.2.21)$$

with the fine structure constant $\alpha = \frac{e^2}{4\pi}$, the quark electric charge e_q , the number of colors N_C and the squared centre-of mass energy $s = q^2$.

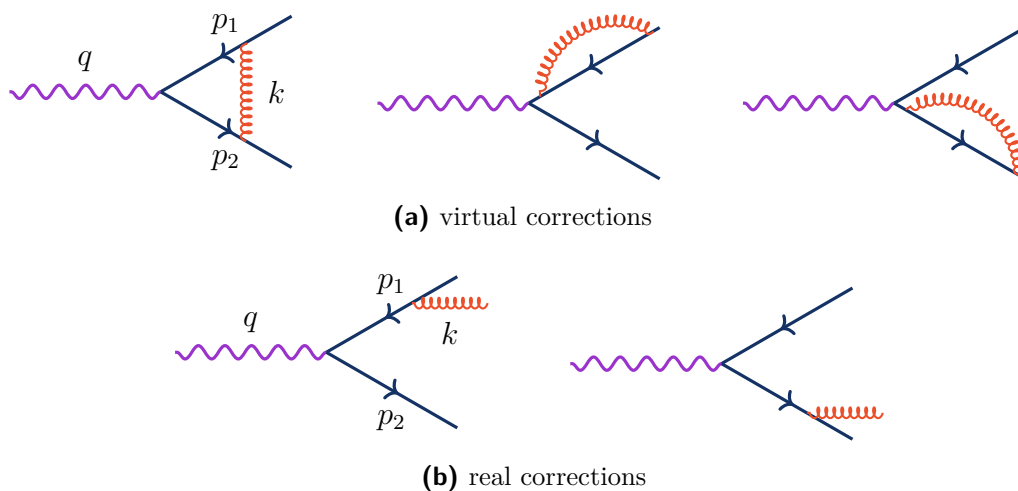


Figure 1.4. Feynman diagrams for the $O(\alpha_s)$ corrections in $e^+e^- \rightarrow \text{hadrons}$

The NLO real and virtual corrections can be calculated from the Feynman diagrams, Fig.1.4², where we have already calculated the virtual correction in the last subsection, more details about the real corrections can be found in App. ???. Thus we obtained the result

$$\sigma_{q\bar{q}}^{(1)} = \sigma_0 \frac{C_F}{\Gamma(1-\epsilon)} \left(\frac{4\pi\mu^2}{s} \right)^\epsilon \left(-\frac{2}{\epsilon^2} - \frac{3}{\epsilon} - 8 + O(\epsilon) \right), \quad (1.2.22)$$

$$\sigma_{q\bar{q}g}^{(0)} = \sigma_0 \frac{C_F}{\Gamma(1-\epsilon)} \left(\frac{4\pi\mu^2}{s} \right)^\epsilon \left(\frac{2}{\epsilon^2} + \frac{3}{\epsilon} + \frac{19}{2} + O(\epsilon) \right). \quad (1.2.23)$$

²Note that the quark self-energy diagram, i.e., the last two diagrams of 1.4a, will vanish due to the LSZ formula guarantees that zeros and infinities cancel with each other, details for the quark self-energy diagram with dimensional regularization can be found in App. B.4

Adding real and virtual contributions, those poles cancel with each other and the result is finite as $\epsilon \rightarrow 0$, and the NLO contribution is

$$\sigma_{qq}^{(1)} + \sigma_{q\bar{q}g}^{(0)} = \sigma_0 \frac{C_F}{\Gamma(1-\epsilon)} \left(\frac{4\pi\mu^2}{s} \right)^\epsilon \left(\frac{3}{2} + O(\epsilon) \right). \quad (1.2.24)$$

For the real emission diagram, Fig.1.4b, the calculation is performed in App. ???. Thus combine both real and virtual contributions, the total hadronic cross section for $e^+e^- \rightarrow \text{hadrons}$ can be obtained as

$$\sigma_{had} = \sigma_0 \left(1 + \frac{\alpha_s}{\pi} + O(\alpha_s^2) \right). \quad (1.2.25)$$

1.2.4 Strategy of regions

The strategy of regions [25] is a technique that allows one to carry out asymptotic expansions of loop integrals in dimensional regularization around various limits. Let's start with the asymptotic expansion of integrals, consider a one-loop self-energy integral with two different particle masses evaluated in $d = 2$, with large-scale hierarchy $m^2 \ll M^2$.

$$I^{asym} = \int_0^\infty dk \frac{k}{(k^2 + m^2)(k^2 + M^2)} = \frac{\log \frac{M}{m}}{M^2 - m^2}. \quad (1.2.26)$$

Since we already know the full solution, we can discuss the expansion of the integrals around the limit of $m \rightarrow 0$. The basic idea for the asymptotic expansion of integrals can be illustrated by the evaluation of the exponential integral, i.e. Euler's integral. For our purpose, clearly, the naive expansion of the integrand leads to trouble, since the series expansion is not valid for the entire range. Therefore, in order to apply this method, we should split the integration into two regions by introducing a cutoff scale Λ . Then one can obtain the expected result by evaluating both integrals with the asymptotic expansion, details can be found in App. D.1.

$$I^{asym} = \int_0^\Lambda dk \frac{k}{(K^2 + m^2)(K^2 + M^2)} + \int_\Lambda^\infty dk \frac{k}{(K^2 + m^2)(K^2 + M^2)}. \quad (1.2.27)$$

Before further discussion for this method, we need to introduce some basic notations. Start with the light-cone basis vectors $n^\mu = (1, 0, 0, 1)$ and $\bar{n}^\mu = (1, 0, 0, -1)$. In this frame, the 4-momentum can be expressed as

$$p^\mu = (n \cdot p) \frac{\bar{n}^\mu}{2} + (\bar{n} \cdot p) \frac{n^\mu}{2} + p_\perp^\mu \equiv (p_+, p_-, p_\perp), \quad (1.2.28)$$

where we have defined the plus and minus components as $p_+ \equiv n \cdot p$ and $p_- \equiv \bar{n} \cdot p$. We now introduce the ‘‘scaling’’ variable λ ,

$$\lambda^2 \sim \frac{p_1^2}{(p_1 - p_2)^2} \sim \frac{p_2^2}{(p_1 - p_2)^2}. \quad (1.2.29)$$

For an example, we can study the integral for the eikonal approximation in $d = 4$:

$$I^{eik} \sim \int \frac{dk^+ dk^- d^2 k_\perp}{(k^+ k^- - k_\perp^2 + i\epsilon)(k^+ + i\epsilon)(-k^- + i\epsilon)}. \quad (1.2.30)$$

With this form, it is easy to identify the regions which lead to IR divergence. In the first case, all components of k^μ vanish at the same time, which is called as the soft region. And in the other two cases, k^μ is finite and parallel to either p_1 or p_2 , which is the collinear region. The components in these regions are at the order of $\sqrt{q^2}$ times powers of scaling variable λ , thus one finds that only the following regions give non-vanishing contributions:

- Hard Region: where k scales as $(1, 1, 1) \sqrt{q^2}$
- Soft Region: where k scales as $k^\mu \sim (\lambda^2, \lambda^2, \lambda^2) \sqrt{q^2}$
- Collinear to p_1 Region: where k scales as $k^\mu \sim (\lambda^2, 1, \lambda) \sqrt{q^2}$
- Collinear to p_2 Region: where k scales as $k^\mu \sim (1, \lambda^2, \lambda) \sqrt{q^2}$

This method is widely used in Soft-Collinear Effective Theory (SCET), details about SCET are beyond the scope of this thesis. Here we only want to point out the power of strategy of regions, as an example, one can also apply the strategy of regions to calculate the QCD corrections to the electromagnetic vertex, the results are collected in App. D.1. (see also in [26] for an overview.)

1.2.5 Factorization in the soft limit

We are now ready to study the factorization properties of real and virtual amplitudes in the soft limit. As we have briefly introduced in Eq.(1.2.15), the radiation of soft gluon can be described by the eikonal approximation. More generally, all the soft radiation can be captured by the Wilson line. A pedagogical introduction to Wilson lines can be found in [26].

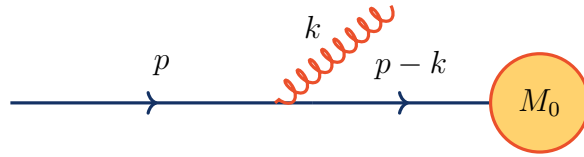


Figure 1.5. Gluon emission from an external fermion line.

Now, we consider the real correction diagram, Fig.1.4b, and we can generalize it to Fig.1.5, where the M_0 represent for a general LO process. According to the QCD Feynman rule, we have

$$M_1(p, k) = u(p) (-ig\gamma^\mu t^a) \epsilon_\mu(k) \frac{i(\not{p} - \not{k})}{(p - k)^2 + i\epsilon} M_0$$

$$\xrightarrow{k \rightarrow 0} t^a g \frac{p^\mu}{p \cdot k} \epsilon_\mu(k) u(p) M_0, \quad (1.2.31)$$

where in the second line, we have applied the soft limit, and $p^\mu/p \cdot k$ is called eikonal factor. We have used the standard notation of Dirac spinor $u(p)$ and the gluon polarization vector $\epsilon_\mu(q)$.

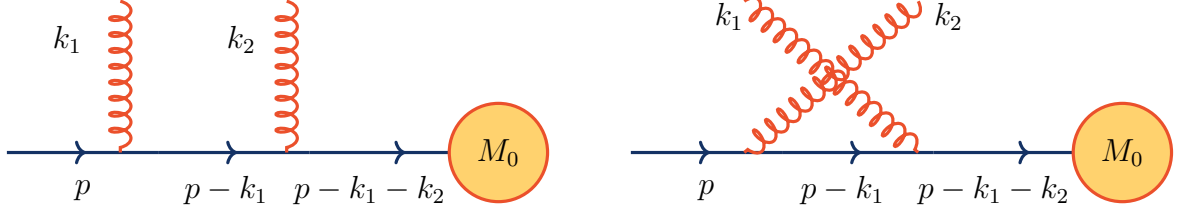


Figure 1.6. Double emission of a gluon from a fermion line

Furthermore, we can define the Feynman rule for the effective coupling of the gluon vertex, i.e. eikonal vertex, based on the result shown on Eq.(1.2.31)

$$\begin{array}{c} p - k \\ \swarrow \\ \text{---} \text{---} \text{---} \\ \searrow \\ p \end{array} \begin{array}{c} \text{---} \text{---} \text{---} \\ \text{---} \text{---} \text{---} \\ \text{---} \text{---} \text{---} \end{array} \begin{array}{c} k \\ \rightarrow \end{array} = gt^a \frac{p^\mu}{p \cdot k}. \quad (1.2.32)$$

The above discussion can be also extended to the emission of two gluons³, and the corresponding diagrams that contribute to this process are shown in Fig.1.6. Then the expression for the amplitude reads

$$\begin{aligned} M_2^{\mu_1 \mu_2}(p, k_1, k_2) &= u(p) M_0 \frac{g^2 t_1^a t_2^a (\not{p} - \not{k}_1 - \not{k}_2)}{(p - k_1 - k_2)^2 + i\epsilon} \left[\frac{\gamma^{\mu_1} (\not{p} - \not{k}_1) \gamma^{\mu_2}}{(p - k_1)^2 + i\epsilon} + \frac{\gamma^{\mu_2} (\not{p} - \not{k}_2) \gamma^{\mu_1}}{(p - k_2)^2 + i\epsilon} \right] \\ &\rightarrow u(p) M_0 \prod_{i=1}^2 gt_i^a \frac{p^{\mu_i}}{p \cdot k_i}. \end{aligned} \quad (1.2.33)$$

The emissions of two soft gluons from a fermion line just becomes the product of two eikonal vertices as shown in Eq.(1.2.32). This can be further extended to multiple soft gluon emission

$$M_n^{\mu_1 \dots \mu_n}(p, k_1, \dots, k_n) = M_0 u(p) \prod_{i=1}^n gt_i^a \frac{p^{\mu_i}}{p \cdot k_i}. \quad (1.2.34)$$

Coming back to the real correction for e^+e^- annihilation to hadrons, we find the full amplitude is

$$M_1(p, k) \rightarrow J^\mu(k) \epsilon_\mu(k) M_0(p), \quad (1.2.35)$$

³The correlated gluon emission doesn't contribute since it is $O(k^2)$, which should be considered at NLL accuracy

where we have introduced the eikonal current, by summing the two terms of the effective coupling shown in Fig.1.4b

$$J^\mu(k) = \sum_{n=1}^2 g t_n^a \frac{p_n^\mu}{p_n \cdot k}, \quad (1.2.36)$$

the t_n^a is the color operators, which satisfy color conservation

$$\sum_n t_n^a = 0, \quad (1.2.37)$$

and the square of an operator t_n^a gives the Casimir of the $SU(N_C)$ representation

$$t_n^{a2} = \begin{cases} C_F & \text{for quark} \\ C_A & \text{for gluon} \end{cases} \quad (1.2.38)$$

Note that the eikonal approximation is insensitive to the spin of the emitting particles [27]. From a physical point of view, this indicates that the soft radiation cannot resolve the details of the short distance interactions. Thus, we can obtain the factorization properties of the soft gluon emission

$$\begin{aligned} |M_1|^2 &= |M_0|^2 J^\mu(k) J^\nu(k) (-g_{\mu\nu}) \\ &= |M_0|^2 g^2 \frac{2C_F (p_1 \cdot p_2)}{(k \cdot p_1)(k \cdot p_2)}. \end{aligned} \quad (1.2.39)$$

Now we can return to the QCD vertex correction, Eq.(1.2.15). The integral can be evaluated in $d = 4$ centre-of-mass system

$$p_1^\mu = E_1 (1, 0, 0, 1), \quad p_2^\mu = E_1 (1, 0, 0, 1) \quad \text{and} \quad k^\mu = (k_0, \vec{k}_\perp, k_z), \quad (1.2.40)$$

where \vec{k}_\perp is the transverse loop momentum, and we define the norm $k_\perp \equiv |\vec{k}_\perp|$. Therefore, the integral becomes

$$\begin{aligned} I^{eik}(p_1, p_2, \epsilon) &= -g^2 C_F \int \frac{d^3k}{(2\pi)^4} \frac{2dk_0 [\bar{u}(p_1) \gamma_\mu v(p_2)]}{(k_0 - k_z + i\epsilon) (-k_0 - k_z + i\epsilon) (k_0^2 - k_z^2 - k_\perp^2 + i\epsilon)} \\ &= g^2 C_F [\bar{u}(p_1) \gamma_\mu v(p_2)] \int \frac{d^3k}{(2\pi)^3} \left[\frac{-(p_1 \cdot p_2)}{2|\vec{k}| (p_1 \cdot k) (p_2 \cdot k)} - \frac{1}{k_\perp^2 (k_z - i\epsilon)} \right]. \end{aligned} \quad (1.2.41)$$

In the second line of the above equation, we have closed the contour integral with 4 poles. As expected, the first term will cancel the real gluon emission, Eq.(1.2.39), while the second integral is a pure phase, called Coulomb phase

$$\int \frac{dk_z d^2k_\perp}{(2\pi)^3} \frac{1}{k_\perp^2 (k_z - i\epsilon)} = - \int dk_z \frac{k_z + i\epsilon}{k_z^2 + \epsilon^2} \int \frac{dk_\perp}{(2\pi)^2} \frac{1}{k_\perp} = \frac{-i}{4\pi} \int \frac{dk_\perp}{k_\perp}. \quad (1.2.42)$$

1.3 DGLAP Evolution Equation

Now that we have examined the factorization properties in the soft limit, we should investigate collinear singularities, which are associated with collinear emission processes and appear in the limit of zero mass. From the example of e^+e^- annihilation to hadrons, we saw that soft and collinear singularities cancel in the expression for the total cross-section. However, for the process where quarks or gluons appear in the initial state, i.e. hadron collision, the corrections to the process will have collinear singularities that do not cancel.

In this section, we will demonstrate the properties of collinear gluon emission. These singular terms will lead to a set of differential equations that govern the momentum dependence of the parton distributions. In the end, we will also briefly discuss the physical interpretation of the aforementioned initial state collinear singularities.

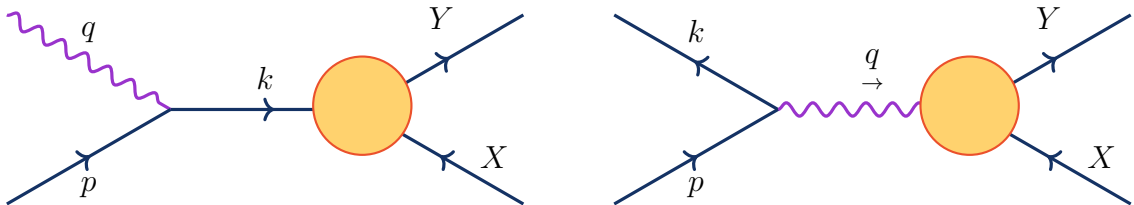


Figure 1.7. General form of diagrams with collinear singularities in QED

1.3.1 Splitting Functions

The basic phenomena associated with collinear singularities in QCD are essentially present in the physics of collinear photon emission in Quantum Electrodynamics (QED). Therefore it is most straightforward to begin by studying the QED case. In this subsection, we will present how a collinear photon emission leads to an analog of a "parton" distribution function.

In QED, diagrams for singularities associated with collinear emission are shown the Fig.1.7, where the collinear singularity appears when the denominator of the intermediate propagator vanishes, i.e. it becomes on-shell. Thus, in both cases, it is natural to consider the diagrams as the transition of a real electron to an almost-real intermediate-state particle and a real photon/electron. In order to derive the matrix element for electron splitting, we first set the kinematics configuration as

$$\begin{aligned}
 p^\mu &= (p, 0, 0, p), \\
 q^\mu &= (zp, p_\perp, 0, zp - \frac{p_\perp^2}{2zp}), \\
 k^\mu &= ((1-z)p, -p_\perp, 0, (1-z)p + \frac{p_\perp^2}{2zp}),
 \end{aligned} \tag{1.3.1}$$

where z is the energy fraction of the photon $E_q = zp$, with the condition $p^2 = q^2 = k^2 = 0$ up to the terms of order p_\perp^2 .

For the matrix element with either left- or right-handed photon polarization, one finds the result as

$$iM_R(e_L^- \rightarrow e_L^- \gamma_R) = -ie \frac{\sqrt{2(1-z)}}{z} p_\perp, \quad (1.3.2)$$

$$iM_L(e_L^- \rightarrow e_L^- \gamma_L) = -ie \frac{\sqrt{2(1-z)}}{z(1-z)} p_\perp. \quad (1.3.3)$$

The squared matrix element averaged over the initial helicities is

$$\begin{aligned} \frac{1}{2} \sum_{pol} |M|^2 &= \frac{1}{2} [|M_L|^2 + |M_R|^2] \\ &= \frac{e^2 p_\perp^2}{z(1-z)} \left[\frac{(1-z)^2 + 1}{z} \right]. \end{aligned} \quad (1.3.4)$$

We have introduced all the pieces needed for the calculation, if we consider the process with a virtual photon, where $M_{\gamma X}$ represent the matrix element for the scattering of a photon from particle X. Then the cross-section reads as

$$\begin{aligned} \sigma(e^- X \rightarrow e^- Y) &= \frac{1}{F} \int d\Pi_k \int d\Pi_Y \left[\frac{1}{2} \sum |M|^2 \left(\frac{1}{q^2} \right)^2 |M_{\gamma X}|^2 \right] \\ &= \int_0^1 dz \int \frac{dp_\perp^2}{p_\perp^2} \frac{\alpha}{4\pi} \left[\frac{(1-z)^2 + 1}{z} \right] \cdot \sigma(\gamma X \rightarrow Y). \end{aligned} \quad (1.3.5)$$

Comparing the above formula to the parton model expression, we can define the transverse momentum integral as a distribution function

$$f_\gamma(z) \equiv \frac{\alpha}{4\pi} \log \frac{s}{m^2} \left[\frac{(1-z)^2 + 1}{z} \right], \quad (1.3.6)$$

where the $\log \frac{s}{m^2}$ represents the collinear singularity, and Eq.(1.3.5) is called the Weizsäcker-Williams equivalent photon approximation [28, 29].

The first diagram in Fig.1.7, i.e. electron transition to real photon and virtual electron, can be treated in the same way, and we find the electron distribution

$$f_e(z) \equiv \delta(1-x) + \frac{\alpha}{2\pi} \log \frac{s}{m^2} \left[\frac{1+x^2}{(1-x)_+} + \frac{3}{2} \delta(1-x) \right], \quad (1.3.7)$$

where the plus distribution $1/(1-x)_+$ is defined in App. C.3. The above discussion has only considered single-photon emission. For higher-order corrections to the photon or electron distribution functions, we must treat the emission of multiple collinear photons. For the process of real photon emission with additional

photon emission, which photon 1 and photon 2 are radiated with transverse momentum $p_{1\perp}$ and $p_{2\perp}$, with $p_{1\perp} \gg p_{2\perp}$. Thus, to order of α^2 , the double photon emission gives the contribution

$$\left(\frac{\alpha}{2\pi}\right)^2 \int_{m^2}^s \frac{dp_{1\perp}^2}{p_{1\perp}^2} \int_{m^2}^{p_{1\perp}^2} \frac{dp_{2\perp}^2}{p_{2\perp}^2} = \frac{1}{2} \left(\frac{\alpha}{2\pi}\right)^2 \log^2 \frac{s}{m^2}. \quad (1.3.8)$$

We can further extend the above analysis to arbitrarily many collinear photons, with integration over the photon phase space corresponding to the ordering.

$$p_{1\perp} \gg p_{2\perp} \gg \cdots \gg p_{n\perp}, \quad (1.3.9)$$

which will give the contribution proportional to

$$\frac{1}{n!} \left(\frac{\alpha}{2\pi}\right)^n \log^n \frac{s}{m^2}. \quad (1.3.10)$$

If photon transverse momenta are ordered in any other way, the above contribution would at least one less power of the logarithm at the same order in α . Thus, the electron momenta are said to be strongly ordered, if the condition of Eq.(1.3.9) holds. This conclusion has an interesting physical interpretation, for the case of the virtual intermediate electron, as intermediate electrons are increasingly virtual towards the hard collision. It is natural to interpret them as components of the physical electron.

In this picture, the electron can be resolved at a finer scale into a more virtual electron and a number of photons. Therefore, it is useful to describe the splitting to be a continuous evolution as a function of the constituent transverse momentum, and the function is determined by the integro-differential equation

$$\frac{d}{d\log Q} f_\gamma(x, Q) = \int_x^1 \frac{dz}{z} \left[\frac{\alpha}{\pi} \frac{1 + (1-z)^2}{z} \right] f_e\left(\frac{x}{z}, Q\right), \quad (1.3.11)$$

$$\frac{d}{d\log Q} f_e(x, Q) = \int_x^1 \frac{dz}{z} \left[\frac{\alpha}{\pi} \left(\frac{1+z^2}{(1-z)_+} + \frac{3}{2} \delta(1-z) \right) \right] f_e\left(\frac{x}{z}, Q\right). \quad (1.3.12)$$

The resulting distribution functions can be used to compute the electron hard scattering, and Eq.(1.3.5) should be replaced by

$$\sigma(e^- X \rightarrow e^- Y + n\gamma) = \int_0^1 dx f_\gamma(x, Q) \sigma(\gamma X \rightarrow Y). \quad (1.3.13)$$

So far we have introduced the evolution equations for $f_\gamma(x, Q)$ and $f_e(x, Q)$, these equations account for the radiation of photons from electrons to all-order. However, there is one more process at the same α order: photon splitting to electron-positron pair. This process must be included, because the process shown in Fig.1.8, has the same logarithmic enhancement.

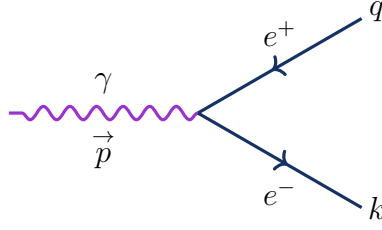


Figure 1.8. Vertex for photon splitting into electron-positron pair

We will skip the calculation for the photon splitting and the positron distribution function $f_{\bar{e}}(x, Q)$, more information can be found in Chapter 17 of [30]. Including the effects of photon splitting, we find the complete evolution equations for electron, positron, and photon distributions in QED

$$\frac{d}{d\log Q} f_{\gamma}(x, Q) = \frac{\alpha}{\pi} \int_x^1 \frac{dz}{z} \left\{ P_{\gamma \leftarrow e}(z) \left[f_e\left(\frac{x}{z}, Q\right) + f_{\bar{e}}(x, Q) \right] + P_{\gamma \leftarrow \gamma}(z) f_{\gamma}(x, Q) \right\}, \quad (1.3.14)$$

$$\frac{d}{d\log Q} f_e(x, Q) = \frac{\alpha}{\pi} \int_x^1 \frac{dz}{z} \left\{ P_{e \leftarrow e}(z) f_e\left(\frac{x}{z}, Q\right) + P_{e \leftarrow \gamma}(z) f_{\gamma}\left(\frac{x}{z}, Q\right) \right\}, \quad (1.3.15)$$

$$\frac{d}{d\log Q} f_{\bar{e}}(x, Q) = \frac{\alpha}{\pi} \int_x^1 \frac{dz}{z} \left\{ P_{\bar{e} \leftarrow e}(z) f_{\bar{e}}\left(\frac{x}{z}, Q\right) + P_{\bar{e} \leftarrow \gamma}(z) f_{\gamma}\left(\frac{x}{z}, Q\right) \right\}, \quad (1.3.16)$$

where the splitting functions $P_{i \leftarrow j}(z)$ are giving by

$$P_{e \leftarrow e}(z) = \frac{1+z^2}{(1-z)_+} + \frac{3}{2} \delta(1-z), \quad (1.3.17)$$

$$P_{\gamma \leftarrow e}(z) = \frac{1+(1-z)^2}{z}, \quad (1.3.18)$$

$$P_{\bar{e} \leftarrow \gamma}(z) = z^2 + (1-z)^2, \quad (1.3.19)$$

$$P_{\gamma \leftarrow \gamma}(z) = -\frac{2}{3} \delta(2-z). \quad (1.3.20)$$

1.3.2 Parton Evolution: DGLAP Equations

For the collinear singularities in QCD associated with collinear gluon and quark emission, similar to the above discussions we can calculate the α_s order corrections to the LO parton cross-section with massless quarks and gluons. Where in QED, we found it natural to include the large logarithm enhancement from the collinear singularity in the parton distributions rather than in the hard-scattering cross-sections, where the singular terms arise in the parton distributions as a function of the logarithm of the momentum scale. When the electron wavefunction is resolved in high energy, as hard scattering momentum transfer Q probes the electron at a distance of order Q^{-1} , it appears as a constituent electron.

To derive the evolution equations for the parton distribution functions in QCD, we can use the same logic as stated above, where the kinematics of collinear gluon

emission is exactly the same as in QED. Thus we can find the evolution equations of the same form as in QED, modified only by the replacement of coupling constant α_s , the insertion of color factor, and including the non-Abelian vertex.

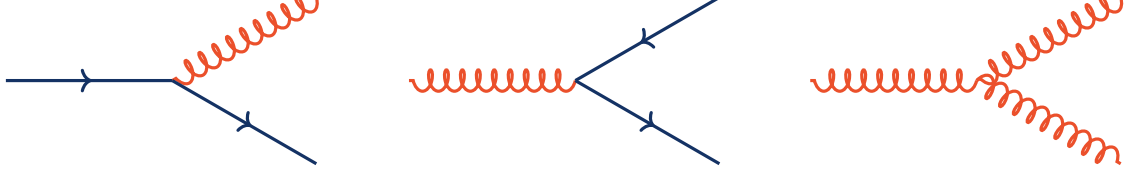


Figure 1.9. Vertices contribute to parton evolution in QCD.

Collinear emission processes in QCD are shown in Fig.1.9, where the first two terms have the same Lorentz structure as those shown in Fig.1.7. Therefore, we find that the first three splitting functions in QCD can be taken from Eq.(1.3.17)-(1.3.19) multiply with the color factors

$$P_{q \leftarrow q}(z) = C_F \left[\frac{1+z^2}{(1-z)_+} + \frac{3}{2} \delta(1-z) \right], \quad (1.3.21)$$

$$P_{g \leftarrow q}(z) = C_F \left[\frac{1+(1-z)^2}{z} \right], \quad (1.3.22)$$

$$P_{q \leftarrow g}(z) = N_f [z^2 + (1-z)^2], \quad (1.3.23)$$

$$P_{g \leftarrow g}(z) = 2C_A \left[\frac{1-z}{z} + \frac{z}{(1-z)_+} + z(1-z) \right] + \beta_0 \delta(1-z). \quad (1.3.24)$$

Therefore, we can modify the QED evolution equations into the evolution equations for parton distributions in QCD, by inserting the color factor and including the new non-Abelian case. These are known as the Dokshitzer-Gribov-Lipatov-Altarelli - Parisi (DGLAP) evolution equations [31–34]:

$$\mu \frac{\partial}{\partial \mu} \begin{pmatrix} f_{q_i}(x, \mu) \\ f_g(x, \mu) \end{pmatrix} = \int_x^1 \frac{dz}{z} \begin{pmatrix} P_{q_i \leftarrow q_j} \left(\frac{x}{z}, \mu \right) & P_{q_i \leftarrow g} \left(\frac{x}{z}, \mu \right) \\ P_{g \leftarrow q_j} \left(\frac{x}{z}, \mu \right) & P_{g \leftarrow g} \left(\frac{x}{z}, \mu \right) \end{pmatrix} \begin{pmatrix} f_{q_j}(z, \mu) \\ f_g(z, \mu) \end{pmatrix}, \quad (1.3.25)$$

where the parton distribution function depends on the UV renormalization scale μ , and the running coupling was absorbed in the splitting function, whose expansion in power of coupling α_s read as

$$P_{i \leftarrow j}(x, \mu_f^2) = \frac{\alpha_s(\mu_f^2)}{\pi} [P^{(0)}(x) + \alpha_s(\mu_f^2) P^{(1)}(x) + O(\alpha_s^2)], \quad (1.3.26)$$

Recently, the state-of-art calculations in QCD splitting functions have achieved N^3LO (4-loop) accuracy, i.e. $P^{(3)}(x)$.

1.3.3 Collinear factorization and Mellin transform

For the production of a system of large mass M , for example, the Drell-Yan process from the scattering of two hadrons, which consists of lepton pair production

together with the hadronic final state. Recall Eq.(1.1.11) that can factorize the cross-section as

$$\begin{aligned} \frac{d\sigma}{dM^2} &= \sum_{a,b} \int dx_a dx_b f_a(x_a, \mu_f) f_b(x_b, \mu_f) \sigma_{ab \rightarrow M}(M^2/\mu_f, \hat{s}, \alpha_s(\mu_f)) \\ &= \sum_{a,b} \sigma_0 \int \frac{dx_a}{x_a} \frac{dx_b}{x_b} f_a(x_a, \mu_f) f_b(x_b, \mu_f) \\ &\quad \times C_{ab \rightarrow M}(z, \alpha_s(\mu_f)). \end{aligned} \quad (1.3.27)$$

In the above equation, we have factored out the LO, i.e. Born-level, partonic cross-section σ_0 , defined as

$$\frac{d\sigma}{dM^2} = \sigma_0(M^2, \alpha_s(M^2)) \delta\left(1 - \frac{M^2}{\hat{s}}\right), \quad (1.3.28)$$

where M^2 is the invariant mass of the lepton pair, and $\hat{s} = x_1 x_2 s$ is the centre-of-mass energy of the parton-parton scattering. The dimensionless hard-scattering functions $C_{ab \rightarrow M}$, in Eq.(1.3.27) depend on

$$z = \frac{M^2}{\hat{s}} = \frac{\tau}{x_1 x_2}. \quad (1.3.29)$$

The generic partonic coefficient function $C(z, \alpha_s(\mu_f))$ is enhanced because of the soft gluon emissions, i.e. $z \rightarrow 1$, similar to the discussion for multiple photon splittings, consider the case of a quark parton line which emits n gluons, shown in Fig.1.10. When a gluon is emitted, it carries an energy fraction of the quark, and the energy of the quark gradually decreases to the fraction $z = z_1 z_2 \cdots z_n$.

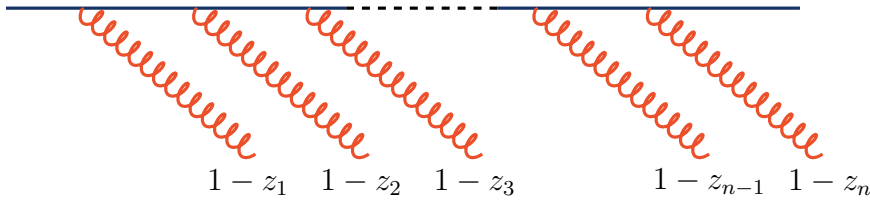


Figure 1.10. Emission of n gluons from a quark line, strongly ordered

When integrating over the emitted gluon phase spaces, as we have done for the emission of multiple photons in Eq.(1.3.8), these enhancements convert into a series of terms

$$\alpha_s^n \frac{\log^k(1-z)}{1-z}, \quad 0 \leq k \leq 2n-1. \quad (1.3.30)$$

Before proceeding to the next step, it is useful to introduce a mathematical tool, as we notice the convolution of Eq.(1.3.27) can be diagonalized with the Mellin transform

$$\mathcal{M}[f \otimes g] = \mathcal{M}[f] \times \mathcal{M}[g]. \quad (1.3.31)$$

The Mellin transform is closely related to the Laplace transform by the change of variable, i.e., Laplace transforms w.r.t $-\log x$. General properties of transformations and inversions can be found in App. C

$$\begin{aligned} \mathcal{M}[f] \equiv \tilde{f}(N) &= \int_0^\infty d(-\log x) e^{-N(-\log x)} f(x) \\ &= \int_0^1 dz z^{N-1} f(z). \end{aligned} \quad (1.3.32)$$

Thus, instead of convolution, Eq.(1.3.27) can be expressed as a product in conjugated space, i.e. Mellin momentum space.

$$\begin{aligned} \mathcal{M}\left[\frac{d\sigma}{dM^2}\right] &= \sigma_0 \sum_{a,b} \tilde{f}_{a/A}(N, \mu_f) \tilde{f}_{b/B}(N, \mu_f) \\ &\quad \times C_{ab \rightarrow M}(N, M^2/\mu_f^2, \alpha_s(\mu_f)). \end{aligned} \quad (1.3.33)$$

So far, we have reviewed the collinear factorization by introducing the factorization scale μ_f , where the momentum scale separates the definition of collinear and hard momenta. The essential property of the hard-scattering function is a re-factorization of soft gluon's singular behavior for $z \rightarrow 1$, which makes re-organize the large logarithms from the IR divergences, i.e. resummation techniques, possible.

1.4 Application: NLO Drell-Yan Process

In this section, we will combine the techniques introduced in this chapter to a detailed calculation of the NLO Drell-Yan process, and the renormalization of PDF will be discussed with the $O(\alpha_s)$ corrections.

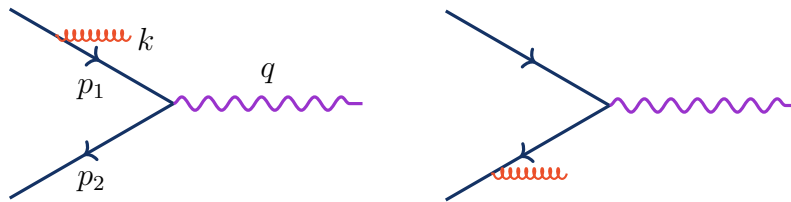


Figure 1.11. Real corrections for the Drell-Yan process

For the NLO QCD correction for the Drell-Yan Process, the real and virtual corrections arise from the real gluon emission and the vertex correction in the initial state. In this section, we will focus on the $q\bar{q} \rightarrow l\bar{l}g$ channel, where the virtual correction is already discussed in Sec. 1.2, and the real correction is illustrated in Fig.1.11.

We now calculate the cross-section for the emission of a real gluon and the same notation as in subsection 1.2.3 is chosen. In addition, we can split the matrix

element into a leptonic and a hadronic part by

$$\int d\Pi_3 \frac{1}{4} \sum |M|^2 = L_{\mu\nu} \int d\Pi_3 H^{\mu\nu}. \quad (1.4.1)$$

Where the 3-body phase space can also be split into two 2-body phase spaces with the recursion relation shown in Fig.1.12 which yields

$$d\Pi_3 = \frac{dM^2}{2\pi} d\Pi_2^H d\Pi_2^L. \quad (1.4.2)$$

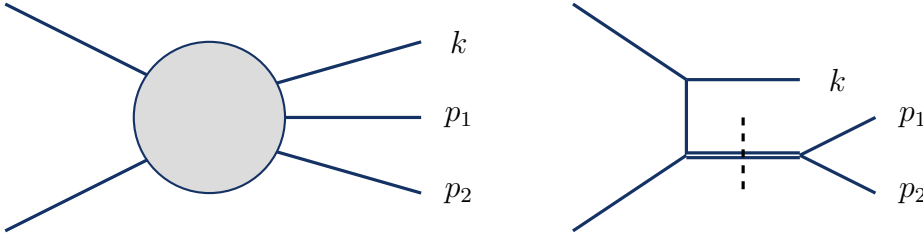


Figure 1.12. Recursion relation for 3-body phase space

The leptonic phase space $d\Pi_2^L$ is the same as in the LO calculation. The details of the phase space integral are given in App. A.2, from Eq.(A.2.1) it follows that

$$d\Pi_2^H = \frac{1}{8\pi} \frac{(4\pi)^\epsilon}{\Gamma(1-\epsilon)} \frac{(s-M^2)^{1-2\epsilon}}{s^{1-\epsilon}} \int_0^1 dy [y(1-y)]^{-\epsilon}. \quad (1.4.3)$$

With the Mandelstam variables, the partonic cross-section for real gluon emission can be written as

$$\frac{\alpha_s}{\pi} \frac{d\sigma^R}{dM^2} = 4\sigma_0 \alpha_s C_F \int d\Pi_2^H \left[\left(\frac{2sQ^2}{tu} + 1 - \epsilon \right) \left(\frac{u}{t} + \frac{t}{u} \right) - 2\epsilon \right]. \quad (1.4.4)$$

Finally, by using the properties of the Γ function and integrating out the hadronic phase space, we obtain the result

$$\frac{d\sigma^R}{dM^2} = \sigma_0 C_F H(\epsilon) \left[\frac{2}{\epsilon^2} \delta(1-z) - \frac{2}{\epsilon} \frac{1+z^2}{(1-z)_+} + 4[1+z^2] \left(\frac{\log(1-z)}{1-z} \right)_+ - 2 \log z \frac{1+z^2}{(1-z)} \right], \quad (1.4.5)$$

$$\frac{d\sigma^V}{dM^2} = \sigma_0 C_F H(\epsilon) \delta(1-z) \left[-\frac{2}{\epsilon^2} - \frac{3}{\epsilon} - 8 + O(\epsilon) \right]. \quad (1.4.6)$$

Adding the real and virtual corrections cancels the double pole, and the leftover ϵ^{-1} pole. Therefore, while in Sec. 1.2.3, the final state radiation has the total cancellation of IR divergences, a residual collinear divergence remains when we deal with the hadron collision with initial state radiation. This is because the difference between these two cases is related to the Born cross-section. For the initial state

case, shown in the left side of Fig. 1.3, the Born cross-section appears as $\sigma_0(zp)$, but the final state radiation Born cross-section is $\sigma_0(p)$. And as we pointed out for the one-loop virtual corrections, both cases share the same kinematics of the Born level, hence proportional to $\sigma_0(p)$.

Therefore, in the initial state a residual divergence $\sigma_0(zp) - \sigma_0(p)$ remains, and this is totally due to collinear behavior as in the soft limit, we will recover the cancellation. In order to cancel this extra divergence, we need to absorb this collinear divergence in PDF, this procedure is called PDF renormalization. The unrenormalized, i.e. bare partonic cross-section to order $O(\alpha_s)$ is found to be

$$\begin{aligned} \frac{d\sigma^{NLO}}{dM^2} &= \frac{d\sigma^R}{dM^2} + \frac{d\sigma^V}{dM^2} \\ &= \sigma_0 H(\epsilon) \left(-\frac{2}{\epsilon} P_{qq}(z) + R(z) \right), \end{aligned} \quad (1.4.7)$$

recall the splitting function from Sec. 1.3

$$P_{qq}(z) = C_F \left[\frac{1+z^2}{(1-z)_+} + \frac{3}{2} \delta(1-z) \right], \quad (1.4.8)$$

and the finite part is

$$R(z) = C_F \left[-8\delta(1-z) + 4 \left[1+z^2 \right] \left(\frac{\log(1-z)}{1-z} \right)_+ - 2 \log z \frac{1+z^2}{(1-z)} \right]. \quad (1.4.9)$$

More details about the PDF renormalization can be found in App. B.5. and the renormalized cross section reads as

$$\begin{aligned} \frac{d\bar{\sigma}^{(1)}(z)}{dM^2} &= \frac{d\sigma^{(1)}(z)}{dM^2} - \int dz_1 \Gamma^{(1)}(z_1) \frac{d\sigma^{(0)}(z_1)}{dM^2} - \int dz_2 \Gamma^{(1)}(z_2) \frac{d\sigma^{(0)}(z_2)}{dM^2} \\ &= \frac{d\sigma^{(1)}(z)}{dQ^2} - 2\Gamma^{(1)}(z)\sigma_0(s), \end{aligned} \quad (1.4.10)$$

where $z = Q^2/s$ and the Born cross section is

$$\frac{d\sigma^{(0)}(\hat{s})}{dM^2} = \sigma_0(\hat{s}) \delta\left(1 - \frac{M^2}{\hat{s}}\right). \quad (1.4.11)$$

In order to cancel the ϵ^{-1} pole multiplying P_{qq} in Eq.(1.4.7), The transition function is defined as

$$\Gamma^{(1)}(z) = -\frac{1}{\epsilon} H(\epsilon) P_{qq}(z). \quad (1.4.12)$$

Therefore, the final finite partonic cross-section is

$$\frac{d\bar{\sigma}^{(1)}(z)}{dM^2} = \sigma_0 R(z). \quad (1.4.13)$$

As a final comment of this section, the definition of Eq.(1.4.12) is not unique. Since $\Gamma(z)$ is not directly observable any kind of renormalization scheme can be adopted, which means that finite part can be moved into $\Gamma(z)$. The convention used here is called the Minimal Subtraction ($\overline{\text{MS}}$) renormalization scheme.

1.5 Infrared and Collinear Safety

Identifying quantities in QCD that are dominated by short-distance behavior lead us to the concept of IRC safety, which has long been a guiding principle for determining if an observable is calculable in perturbative QCD [9, 35]. IRC safe observables are insensitive to arbitrarily soft emissions and collinear splittings. This ensures that the singularities cancel between real and virtual emissions at each fixed-order in perturbative QCD.

To put the concept of perturbative calculability in general context, the basic ideas can be summarized below: For a general observable v , collecting real and virtual contributions together, we can compute the NLO distribution with an appropriate observable-function $U_i(\{k_i\})$ [36], the expression in the soft limit can be written as

$$\begin{aligned} \sigma(v) &= \frac{1}{2s} \int d\Pi_2 |M_0|^2 U_2(p_1, p_2) \\ &+ \frac{1}{2s} \int d\Pi_2 |M_0|^2 \int \frac{d^3k}{(2\pi)^3 2|k|} 2g^2 C_F \frac{(p_1 \cdot p_2)}{(p_1 \cdot k)(p_2 \cdot k)} \\ &\times [U_3(p_1, p_2, k) - U_2(p_1, p_2)]. \end{aligned} \quad (1.5.1)$$

From the second line of the above equation, we can derive the following important properties: Firstly, the complete cancellation of infrared and collinear singularity requires the IRC safe observable as

$$\lim_{p_i \rightarrow 0} U_n(p_1, \dots, p_i, \dots, p_n) = U_{n-1}(p_1, \dots, p_{i-1}, p_{i+1}, \dots, p_n), \quad (1.5.2)$$

$$U_n(p_1, \dots, p_i, p_j, \dots, p_n) = U_{n-1}(p_1, \dots, p_i + p_j, \dots, p_n). \quad (1.5.3)$$

We note here that there exists a wealth of observables that are of great phenomenological interest despite them being IRC unsafe, more about unsafe observables will be introduced in Sec. 4.2.1. As a consequence, arbitrary collinear emissions change the value of the momentum fraction that enters the hard scattering resulting in uncancelled collinear singularities. However, these can sometimes be calculable in perturbative QCD using all-orders resummation, such observables are known as "Sudakov safe" [37] since the perturbative Sudakov factor effectively regulates the singular region of phase space.

Note that for inclusive observables, i.e $U_m(p_1, \dots, p_m) = 1$, the cancellation is complete. Therefore the total cross-section remains unchanged by the emission of soft particles, as we have discussed in Sec. 1.2. Note that for inclusive observables, i.e $U_m(p_1, \dots, p_m) = 1$, the cancellation is complete. Therefore the total cross-section remains unchanged due to the emission of soft particles, as we have discussed in Sec. 1.2. On the other hand, the exclusive distributions, although the singularities cancel, would depend on several scales of energy. Thus manifests itself with the appearance of large logarithmic enhancements to any order in

perturbation theory. In these regions, the reliable theoretical predictions must be resummed to all orders, details about all-order resummation will be discussed in Chapter 2.

1.6 Resummation of divergent series

One of the key assumptions of perturbative QCD, as mentioned above, is that the pQCD series is asymptotic. Despite being divergent in the mathematical sense, the physical quantity of the perturbation theory can be computed as a power series in terms of the small coupling. In this section, we want to give a brief overview of resummation techniques for divergent power series.

1.6.1 Large-order behaviour of perturbation theory

In QFT, the coefficients of the power series often exhibit factorial growth. A common technique, if the large order asymptotic of the series coefficients are known, is Borel resummation [38], For a general function $f(g) = \sum_k f_k g^k$ with the coefficient $f_k \sim (-\alpha)^k k!$, the Borel sum is defined by

$$B(g) = \sum_{n=0}^{\infty} B_n g^n, \text{ with } B_n = \frac{f_n}{n!}. \quad (1.6.1)$$

Recall the perturbation series in QCD, Eq.(1.1.6), $f_n \propto a^n n!$ for large n . Therefore, the expansion coefficients B_n behave like

$$B_n \propto a^n, \quad (1.6.2)$$

so that the Borel sum converges for $|g| < 1/a$, with the expansion

$$\sum_{n=0}^{\infty} B_n g^n = \frac{\gamma}{1 - ag} [1 + O(g)], \quad (1.6.3)$$

where γ is constant. The factorials can be restored using an integral representation of the Γ function:

$$k! = \Gamma(k + 1) = \int_0^{\infty} dt e^{-t} t^k. \quad (1.6.4)$$

If an asymptotic series is Borel summable, then the inverse transform

$$\tilde{f}(t) = \int_0^{\infty} dg e^{-g} B(gt), \quad (1.6.5)$$

uniquely determines the function $\tilde{f}(t) = f(t)$ to which the series is asymptotic, and $\tilde{f}(t)$ is a Laplace transform. Thus the theory of Borel summability is essentially the theory of Laplace transforms.

1.6.2 Padé approximation

However, in practice, the large order asymptotic of the coefficients might not be known analytically. One of the most widely used methods to approximate a function $f(t)$, whose first few expansion coefficients are known, is Padé approximation. It tries to approximate $f(t)$ by two polynomials, $P_M(t)$ and $Q_N(t)$ of degree M and N . The Padé approximant $Z_{[M/N]}(t)$ of order $[M/N]$ is defined by the condition:

$$P_M(t) - Q_N(t) Z_{[M/N]}(t) = O(t^{M+N+1}). \quad (1.6.6)$$

Typically, the symmetric $[N/N]$ Padé approximant features the fastest approximation for increasing N although this depends on the function, for an example, $f(z) = \frac{1}{1+z}$, is shown in Fig.1.13. Therefore, instead of explicitly computing the Borel sum $B(g)$, we simply approximate it using Padé approximation

$$f(t) = \int_0^\infty dg e^{-g} B^{[m/n]}(gt). \quad (1.6.7)$$

This combination of Padé approximation and Borel resummation is called as Borel-Padé approximation.

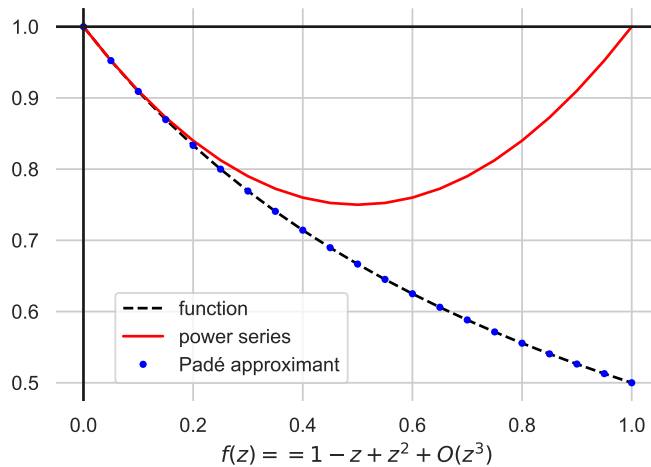


Figure 1.13. Plot of truncated power series expansion and its Padé approximants $[1/1]$

1.6.3 Borel-Leroy transform

Instead of a Borel transform with a leading cut at $1/a$, we may also define a generalized Borel transform, where the leading cut becomes a leading pole, called as Borel-Leroy transform [39], which is defined from the power expansion

$$\begin{aligned} B(g) &= \frac{\gamma}{(1-ag)^{\beta+1}} = \gamma \sum_n \frac{\Gamma(\beta+n+1)}{\Gamma(\beta+1)\Gamma(n+1)} a^n g^n \\ &\propto \sum_n a^n n^\beta g^n, \text{ for large } n. \end{aligned} \quad (1.6.8)$$

Thus, we can divide each coefficient f_n by $\Gamma(n + \beta + 1)$ rather than by $n!$. The inverse Borel-Leroy transformation is

$$f(t) = \int_0^\infty dg g^\beta e^{-g} B_\beta(gt), \quad (1.6.9)$$

and in order to recover $f(t)$, we reinsert the growth factor

$$\Gamma(n + \beta + 1) = \int_0^\infty dt e^{-t} t^{n+\beta}. \quad (1.6.10)$$

2 Analytic Resummation Techniques

Contents

2.1	Perturbation theory to all orders	38
2.1.1	Prologue: different approaches in resummation	38
2.1.2	A first example: threshold resummation	39
2.1.3	Lund diagram	40
2.2	Transverse momentum distributions	41
2.2.1	Impact parameter space	42
2.2.2	Aside: Sudakov form factor and its interpretation	42
2.2.3	NLL resummation formula	43
2.2.4	a_T distribution	45
2.3	Calculations for jets: the jet mass distribution	48
2.3.1	The concept of jets	48
2.3.2	Jet algorithms	49
2.3.3	Leading logarithmic approximation	49
2.3.4	To all-orders	51
2.3.5	Beyond leading logarithms	53
2.4	Global and non-global logarithms	55
2.5	General resummation formalism	57
2.5.1	Coherent branching	57
2.5.2	Renormalization group approach	60

The main topic of this thesis is resummation, and in particular, we focus on first-principle precision calculation for two important types of observables for which resummation techniques are needed, in order to obtain accurate theoretical predictions, namely IRC-unsafe and non-global observables. Before further extension to these aforementioned two types of observables, in this chapter, the basic ideas underlying resummation techniques and analytic calculations for the global part are discussed. After introducing some technology and terminology using threshold resummation as an example, the findings will be extended to two examples: small jet mass and transverse momentum, which are related to some novel methods that we will derive in the remainder of this thesis.

2.1 Perturbation theory to all orders

On Sec. 1.3.3, we have presented the collinear factorization formula for Drell-Yan processes, i.e. $pp \rightarrow \gamma/Z \rightarrow l^+l^-$, with large invariant mass, in this context, the factorization theorem states that it is possible to write the hadronic cross-section as a convolution between a partonic hard scattering coefficient function and parton distributions, with corrections that are power-suppressed by the hard scale Q .

Here, we focus on the region of phase space where the center-of-mass energy \hat{s} is close to the invariant mass, i.e. $\hat{s} \sim M^2$. In this region, additional radiation is forced to be soft, leading to large logarithm enhancements. These logarithms are usually referred to as threshold logarithms. In this section, we will further expand the perturbative formalism developed at Sec. 1.3.3 to all perturbative orders.

2.1.1 Prologue: different approaches in resummation

To obtain reliable predictions, computations of radiative corrections are necessary. According to KLN theorem, we need to be rather "inclusive" in our evaluation to cancel all the IR divergences. The evaluation of the perturbative QCD series is in many cases very cumbersome since we have to deal with an enormous amount of diagrams. As we have briefly introduced earlier, the large logarithm in the partonic cross-section needs to be resummed to all-order, for many interesting observables, one can find the following structure

$$\begin{aligned} \frac{1}{\sigma} \frac{d\sigma}{d\mathcal{O}} &\sim \underbrace{O(1)}_{\text{LO}} + \underbrace{O(\alpha_S)}_{\text{NLO}} + \underbrace{O(\alpha_S^2)}_{\text{NNLO}} + \dots \\ &\sim \exp\left(\underbrace{Lg_1(\alpha_S L)}_{\text{LL}} + \underbrace{g_2(\alpha_S L)}_{\text{NLL}} + \underbrace{\alpha_S g_3(\alpha_S L)}_{\text{NNLL}} + \dots\right), \end{aligned}$$

where we have reorganized the order by order result to logarithmic expansion after the resummation procedure.

Usually, the logarithmic contributions arise from the ratios of different scales. In the previous chapter, we have already observed their behavior, by introducing the renormalization and factorization scales.

The resummation procedure follows from re-factorization, that is, we distinguish between collinear (including soft/collinear radiation) and soft configurations in the hard scattering function. There are different approaches to derive the re-factorization, mainly including:

- Traditional approach
- Effective Theory approach
- Monte Carlo parton shower approach

In this thesis we will mainly concentrate on the traditional approach, details about EFT and Monte-Carlo (MC) approach are beyond the scope of this thesis. However, the starting point for constructing the aforementioned two approaches will be briefly discussed in Sec. 2.5.

2.1.2 A first example: threshold resummation

Recall that the cross-section of Drell-Yan process can be written in factorized form, Eq.(1.3.27) and the conjugated Mellin space, Eq.(1.3.33). The essential property of the hard-scattering functions $C_{ab}(z)$, that makes resummation possible is the re-factorization of the singular behavior at $z \rightarrow 1$

$$C_{ab \rightarrow M}(z, M^2, \mu) = H(M^2, \mu) S\left(1 - z, \frac{M^2}{\mu^2}, \alpha_s(\mu)\right), \quad (2.1.1)$$

as discussed in Sec. 1.3.3, the singular behavior comes from the power of $\log(1-z)$, therefore the quantity S is called soft function, and it can be described either in traditional approach from eikonal approximation or Wilson lines in soft-collinear effective theory (SCET)

For the traditional approach, recall the scattering amplitude in the soft limit which we have derived in Eq.(1.2.34). Thus it is straightforward to prove the factorization at the matrix element level as

$$M_n(p, z_1, \dots, z_n) = \frac{1}{n!} \prod_{i=1}^n M_1(p, z_i), \quad (2.1.2)$$

where the M_1 is the single gluon emission matrix element, and the phase space integral is proportional to

$$dz_1 \cdots dz_n \delta(z - z_1 \cdots z_n). \quad (2.1.3)$$

In order to factorize the Dirac delta function, one can apply the Mellin transform

$$\int_0^1 dx x^{N-1} \delta(z - z_1 \cdots z_n) = z_1^{N-1} \cdots z_n^{N-1}, \quad (2.1.4)$$

and the tower of logarithms in Eq.(1.3.30) converts into the tower in Mellin space

$$\alpha_s^n \log^k \frac{1}{N}, \quad 0 \leq k \leq 2n. \quad (2.1.5)$$

In the soft limit, the corresponding n-gluon contribution to the hard-scattering function at order α_s^n reads

$$C_{ab}^{(n)}(N) \simeq \frac{1}{n!} \left[C_{ab}^{(1)}(N) \right]^n. \quad (2.1.6)$$

The leading logarithmic (LL) approximation is obtained by considering the LLs only, i.e. $k = 2n$. This implies that we could sum over all possible amounts of emissions as

$$\begin{aligned} C_{ab}^{res}(N, \mu_f) &= \sum_n \alpha_s^n(\mu_f) C_{ab}^{(n)}(N) \\ &= \exp \left[\alpha_s C_{ab}^{(1)}(N) \right]. \end{aligned} \quad (2.1.7)$$

2.1.3 Lund diagram

Lund diagram [40] is a graphic tool that represents the emission kinematics in the soft and collinear limit, and each point indicates a given emission with a fraction z of the transverse momentum of the parton and emission angle θ .

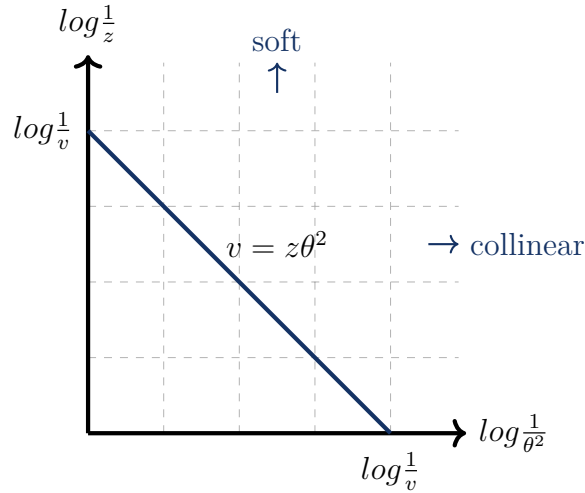


Figure 2.1. Lund diagram: emissions of soft/collinear gluons are uniformly distributed

Firstly, let's rewrite the probability in soft and collinear limit

$$P(z, \theta) dz d\cos\theta = \frac{\alpha_s C_i}{\pi} \frac{dz}{z} \frac{d\theta^2}{\theta^2}, \quad (2.1.8)$$

where C_i is the color factor that depends on the original parton for the emission ($C_i = C_F$ for a quark, and $C_i = C_A$ for a gluon).

Therefore, the emissions of soft and collinear gluons are uniformly distributed in the plane, shown in Fig. 2.1. Moving vertically in the plane we approach the soft limit and horizontally the collinear limit. For a more detailed example, let's consider the ratio of the invariant mass of the quark-gluon system to its total energy:

$$v = \frac{m^2}{E^2} = \sum_i z_i \theta_i^2, \quad (2.1.9)$$

Now we can calculate the cumulative probability distribution $P(x < v)$, which measures the value of this observable less than the value v . In order to simplify this

task, it is worth to point out the emissions in real space (z, θ^2) are exponentially far apart, as they are uniformly distributed in the Lund diagram. Hence there should exist a single dominant emission, corresponds to a line in Fig. 2.1 and no emissions below this line. Therefore, we could find the probability by directly calculating the area of the forbidden triangle, i.e. $\frac{1}{2} \log^2 \frac{1}{v}$. Then, the probabilities of no emissions read as

$$P(x < v) = \left(1 - \frac{\alpha_s C_i \log^2 v}{2\pi N}\right)^N = \exp\left[-\frac{\alpha_s C_i}{2\pi} \log^2 v\right], \quad (2.1.10)$$

where all terms that would contribute to constant or single logarithm have been ignored, this is called as double leading logarithmic approximation (DLLA)

This exponential function is called the Sudakov form factor [41], and this form factor is related to the sum over all degenerate states for soft/collinear emissions, which tamed all the large logarithm divergence. More details about the Sudakov form factor will be discussed at Sec. 2.2

As the last commit in this section, one can find the probability distribution by differentiating the above result

$$p(v) = \frac{d}{dv} P(x < v) = -\frac{\alpha_s C_i \log v}{\pi v} \exp\left[-\frac{\alpha_s C_i}{2\pi} \log^2 v\right]. \quad (2.1.11)$$

2.2 Transverse momentum distributions

In this section, we present the basic ideas for resummation techniques with a focus on the transverse momentum distributions for the Drell-Yan process, which are amongst the most-studied variables in high energy physics. The definition of transverse momentum q_\perp is given by

$$\vec{q}_\perp = \sum_{i=0}^n \vec{k}_{\perp,i}, \quad (2.2.1)$$

where the sum is over the particles that recoil against the lepton pair. In the small- q_\perp limit, we obtain the LO, i.e. Z boson plus one parton, behavior as

$$\frac{1}{\sigma_0} \frac{d\sigma}{dq_\perp^2} = \frac{\alpha_s}{2\pi} \left(\frac{A}{q_\perp^2} \log \frac{M^2}{q_\perp^2} + \frac{B}{q_\perp^2} + C(q_\perp^2) \right) + O(\alpha_s^2), \quad (2.2.2)$$

where this distribution exhibits a double logarithmic divergence when $q_\perp \rightarrow 0$. The small value of $q_\perp = \sqrt{|\vec{q}_\perp|^2}$ comes from two mechanisms: either emission of gluons with small transverse momentum or kinematical cancellation between the transverse momenta of emitted gluons. The former gives the DLLA contribution.

Following similar steps to those discussed earlier in this Chapter, the series can be resummed at LL accuracy, where all sub-leading contributions are ignored

$$\frac{1}{\sigma_0} \frac{d\sigma}{dq_\perp^2} = \sum_{n=1}^{\infty} \left(\frac{\alpha_s}{2\pi}\right)^n A_n \log^{2n-1} \frac{M^2}{q_\perp^2} = \frac{d}{dq_\perp^2} e^{-\frac{\alpha_s C_F}{2\pi} \log^2 \frac{M^2}{q_\perp^2}}, \quad (2.2.3)$$

which exhibits the Sudakov form factor that suppresses the logarithm enhancements from the emission of soft gluons. Thus, the distribution is well-behaved and vanishes in the limit of $q_\perp \rightarrow 0$.

2.2.1 Impact parameter space

Up to now, we have treated multiple soft gluon emissions as independent, uncorrelated processes, which have been simplified since the definition of transverse momentum sum over all individual emissions, i.e., Eq.(2.2.1). This constraint can be cast as a Dirac delta function, which can be expressed through integral representation as a Fourier transforms in impact parameter space. The impact parameter b is conjugated to the transverse momentum q_\perp

$$\delta^{(2)}\left(\vec{q}_\perp - \sum_{i=0}^n \vec{k}_{\perp,i}\right) = \frac{1}{2\pi} \int d^2b_\perp \exp\left[i\vec{b}_\perp \cdot \left(\vec{q}_\perp - \sum_{i=0}^n \vec{k}_{\perp,i}\right)\right]. \quad (2.2.4)$$

For the convenience of discussion, we define the individual emission factors as

$$\nu(k_{\perp,i}) \equiv \frac{\alpha_s C_F}{\pi} \frac{1}{k_{\perp,i}} \log \frac{M^2}{k_{\perp,i}^2}, \quad (2.2.5)$$

which the expression in the impact parameter space yields

$$\nu(b_i) = \frac{1}{2\pi} \int d^2k_{\perp,i} e^{-i\vec{b} \cdot \vec{k}_{\perp,i}} \nu(k_{\perp,i}). \quad (2.2.6)$$

Therefore, the contribution of n gluons which has an overall transverse momentum of q_\perp of the lepton pair thus reads

$$\begin{aligned} \frac{1}{\sigma_0} \frac{d\sigma}{dq_\perp} &= \sum_{n=0}^{\infty} \frac{1}{2\pi n!} \int d^2b e^{i\vec{b} \cdot \vec{q}_\perp} \nu^n(b) \\ &= \frac{1}{2\pi} \int b db J_0(bq_\perp) \exp[\nu(b)], \end{aligned} \quad (2.2.7)$$

in the second line we have summed over all gluon emissions and the Bessel function J_0 arise from the angular integral.

2.2.2 Aside: Sudakov form factor and its interpretation

So far, we have derived the Sudakov form factor, which encodes the resummation of multiple gluon emissions. To see how this works, let's consider gluon emission off a quark where the gluon is collinear with the quark. Then the matrix element is approximated by the splitting function, and the corresponding emission radiator with DLLA becomes

$$R(k_\perp) = \frac{\alpha_s C_F}{\pi} \frac{1}{k_\perp} \log \frac{Q^2}{k_\perp^2} \Rightarrow R_{q \rightarrow qg}(k_\perp, z) = \frac{\alpha_s C_F}{\pi} \frac{1}{k_\perp} P_{qq}(z), \quad (2.2.8)$$

with

$$P_{qq}(z) = C_F \frac{1+z^2}{1-z}. \quad (2.2.9)$$

Therefore, the integration over k_\perp must also be supplemented with one over z . And because the splitting function is divergent at the limit $z \rightarrow 1$, which must be regularized, this is usually achieved through the “+”-function. For a more physical way to ensure finite integrals, to describe the jet production, the emitted gluons must be resolved, i.e. $k_\perp > Q_0$. Thus, due to the momentum conservation, the residual momentum fraction z must be smaller than 1 by a small value of $\epsilon = \frac{k_\perp^2}{Q^2}$, and the Sudakov form factor can be rewritten as

$$S(Q, Q_0) = \exp \left[- \int_{Q_0^2}^{Q^2} \frac{dk_\perp^2}{k_\perp^2} \left(\frac{\alpha_s(k_\perp^2)}{2\pi} \int_0^{1-\epsilon} dz P_{qq}(z) \right) \right], \quad (2.2.10)$$

the z -integral can be approximated by

$$\begin{aligned} \int_0^{1-\epsilon} dz P_{qq}(z) &\approx C_F \left[\int_0^{1-\epsilon} dz \frac{2}{1-z} - \int_0^1 dz (1+z) \right] \\ &= 2C_F \left[\log \frac{Q^2}{k_\perp^2} - \frac{3}{4} \right] \equiv \Gamma_q(Q^2, k_\perp^2), \end{aligned} \quad (2.2.11)$$

where the integrated splitting function Γ is introduced, and clearly, they are identical to the coefficients A and B from Eq.(2.2.3).

Now we can write the Sudakov form factor in a more general form

$$S(Q, Q_0) = \exp \left[- \int_{Q_0^2}^{Q^2} \frac{dk_\perp^2}{k_\perp^2} \frac{\alpha_s(k_\perp^2)}{\pi} \Gamma(Q^2, k_\perp^2) \right], \quad (2.2.12)$$

where the integrated splitting kernels are given by the usual coefficients

$$\Gamma(Q^2, q^2) = A^{(1)} \log \frac{Q^2}{q^2} + B^{(1)}. \quad (2.2.13)$$

We will further interpret the Sudakov form factor in Sec. 2.5.1, and describe it as the probability for a given particle not to radiate a secondary particle between two scales Q and Q_0 .

2.2.3 NLL resummation formula

In order to achieve higher accuracy, the sub-leading terms must be included. Therefore, we would like to extend the resummation formalism for the transverse momentum spectrum beyond LL accuracy. Considering n emissions in the collinear limit, we have

$$\frac{1}{\tilde{\sigma}_0} \frac{d\tilde{\sigma}}{dq_\perp^2} = \sum_{n=0}^{\infty} \frac{1}{n!} \prod_{i=1}^n \int z_i^N dz_i \frac{dk_{\perp i}}{k_{\perp i}} \frac{d\phi_i}{2\pi} \frac{\alpha_s(k_{\perp i})}{2\pi} 2P_{qq}(z_i) \delta^{(2)} \left(\vec{q}_\perp - \sum_{i=0}^n \vec{k}_{\perp, i} \right), \quad (2.2.14)$$

where $\tilde{\sigma}_0$ is the Mellin transform of the hadronic Born cross-section

$$\tilde{\sigma}_0 = \sigma_0 \sum_q f_{q/A}(N, \mu) f_{\bar{q}/B}(N, \mu). \quad (2.2.15)$$

We note that the δ function for the momentum conservation spoils the factorization properties. In order to solve this problem, we can make use of the Fourier representation of the delta-function shown in Eq.(2.2.4), which will give us the desired factorized form. Now we can perform the sum in Eq.(2.2.14), and obtain the exponential form:

$$\begin{aligned} \frac{1}{\tilde{\sigma}_0} \frac{d\tilde{\sigma}}{dq_\perp^2} &= \frac{1}{4\pi^2} \int d^2b e^{i\vec{b}\cdot\vec{q}_\perp} \exp \left[\int dz \frac{dk_T}{k_T} \frac{d\phi}{2\pi} \frac{\alpha_s(k_T)}{\pi} P_{qq}(z) \left(z^N e^{i\vec{b}\cdot\vec{k}_T} - 1 \right) \right] \\ &\equiv \frac{1}{4\pi^2} \int d^2b e^{i\vec{b}\cdot\vec{q}_\perp} e^{-R(b, N)}, \end{aligned} \quad (2.2.16)$$

where the (-1) term has been included in order to account for virtual corrections, We can further integrate over the angle between \vec{b} and \vec{q}_\perp , obtaining a Bessel function

$$\frac{1}{\tilde{\sigma}_0} \frac{d\tilde{\sigma}}{dq_\perp^2} = \frac{1}{2\pi} \int_0^\infty db b J_0(bq_\perp) e^{-R(b, N)}, \quad (2.2.17)$$

and evaluate the radiator of the resummed exponent to NLL accuracy, we find the following result

$$R_N(b, N) = \int_{1/\bar{b}^2}^{M^2} \frac{dk_\perp^2}{k_\perp^2} \frac{\alpha_s(k_\perp^2)}{\pi} \left[\left(A^{(1)} + \frac{\alpha_s(k_\perp^2)}{\pi} A^{(2)} \right) \log \frac{M^2}{k_\perp^2} + B^{(1)} + 2\gamma_{qq}(N) \right], \quad (2.2.18)$$

where $\bar{b} = b \frac{e^{\gamma_E}}{2}$ and the lower bound of the integration from the approximation $1 - J_0(\rho'/b) \approx \Theta(\rho' - 1/\bar{b})$ follow from Ref. [42], details about this approximation are collected in the App. C.2. We have also introduced the coefficients

$$A^{(1)} = C_F, \quad A^{(2)} = \frac{C_F}{2} \left[C_A \left(\frac{67}{18} - \frac{\pi^2}{6} \right) - \frac{5}{9} n_f \right], \quad (2.2.19)$$

$$B^{(1)} = -\frac{3}{2} C_F, \quad (2.2.20)$$

and γ_{qq} is the LO splitting function after the Mellin transform. We note that the N-dependent part can be absorbed into the PDFs using DGLAP evolution equation, leading to PDFs evaluated at the scale $\mu = 1/\bar{b}$.

To achieve the NLL accuracy, the integration over k_\perp at Eq.(2.2.18) must be performed with the two-loop running coupling, more details are collected in App. B.2. Then the resummed exponent can be expressed as the sum of two contributions:

$$R(b) = L f^{(1)}(\lambda) + f^{(2)}(\lambda), \quad (2.2.21)$$

with

$$f^{(1)}(\lambda) = \frac{A^{(1)}}{\pi\beta_0\lambda} [-\lambda - \log(1-\lambda)], \quad (2.2.22)$$

$$f^{(2)}(\lambda) = -\frac{B^{(1)}}{\pi\beta_0} \log(1-\lambda) - \frac{A^{(1)}\beta_1}{\pi\beta_0} \left[\frac{\lambda + \log(1-\lambda)}{1-\lambda} + \frac{1}{2} \log^2(1-\lambda) \right] + \frac{A^{(2)} [\lambda + (1-\lambda) \log(1-\lambda)]}{\pi^2\beta_0^2(1-\lambda)}, \quad (2.2.23)$$

where $\lambda = \alpha_s(M)\beta_0 L$, $L = \log(\bar{b}^2 M^2)$.

As the last step to obtain the resummed expression, the integral over the impact parameter b in Eq.(2.2.17) must be performed. This integration is problematic both at small- and large- b , because the resummed exponent diverges in both limits.

For the small- b corresponds to large q_T which is beyond the control of our resummation formula, and different prescriptions that preserve the logarithmic accuracy can be found in the literature. For example, in Ref. [43] the modification of the logarithms is suggested: $\log(\bar{b}^2 M^2) \rightarrow \log(1 + \bar{b}^2 M^2)$. Alternatively, one could also freeze the radiator below some small values, i.e. $\bar{b}_{min} M < 1$ [44, 45]

The large- b divergence, i.e. $\alpha_s\beta_0 L = 1$ is due to the Landau pole in the running coupling, which is associated to non-perturbative (NP) behavior. In this case, one could introduce an upper limit to the b integration [44, 45], another approach includes deforming the contour integration to avoid the Landau singularity [43].

2.2.4 a_T distribution

In this section, we will concentrate on the resummation of a_T distribution. Recall the production of Z bosons via the Drell-Yan, which subsequently decay to a lepton pair. The a_T is component of the lepton pair (or Z boson) q_T transverse to the thrust axis [46, 47]

$$\hat{n} = \frac{\vec{p}_{t1} - \vec{p}_{t2}}{|\vec{p}_{t1} - \vec{p}_{t2}|}, \quad (2.2.24)$$

where \vec{p}_{t1} and \vec{p}_{t2} are the transverse momenta of the two leptons. For multiple emissions from the incoming partons, with the conservation of transverse momentum, i.e. $\vec{p}_{t1} + \vec{p}_{t2} = -\sum_i \vec{k}_{ti}$. Thus, one can rewrite the axis defined in Eq.(2.2.24) as

$$\hat{n} \approx \frac{\vec{p}_{t1}}{|\vec{p}_{t1}|}, \quad (2.2.25)$$

where we have neglected the multi-emission dependence, as we are projecting the vector sum of the k_{ti} along the axis, therefore the higher-order corrections of $O(k_{ti})$ would only contribute at the level of bilinear or quadratic in small k_{ti}

Now we can parametrize the kinematics in the plane transverse to the beam as

$$\vec{p}_{t1} = p_t (1, 0), \quad (2.2.26)$$

$$\vec{k}_{ti} = k_{ti} (\cos\phi, \sin\phi), \quad (2.2.27)$$

where ϕ_i is the angle of i^{th} emission with respect to the direction of lepton 1 in the plane. Therefore, with all the information discussed above, one can find that the transverse component of the Z boson p_T is

$$a_T = \left| \sum_i k_{ti} \sin\phi_i \right|, \quad (2.2.28)$$

where ϕ_i denotes the angle separation between the i^{th} emission and the axis. In the small q_T region, the azimuthal angle $\Delta\phi$ between final state leptons is in the back-to-back region, i.e. $\Delta\phi \approx \pi$. Hence, the uncertainty for a_T variable is approximately the uncertainty of q_T multiplied by the Sine of a small angle.

We start by considering the integrated cross-section, which is related to the number of events below a fixed value of a_T

$$\Sigma(a_T) = \int_0^{a_T} \frac{d^2\sigma}{da'_T dM^2} da'_T = \Sigma^{(0)} + \alpha_s \Sigma^{(1)} + O(\alpha_s^2). \quad (2.2.29)$$

At the LO, one finds the result similar to q_\perp as

$$\begin{aligned} \Sigma^{(1)}(a_T) &= C_F \int_0^{2\pi} \frac{d\phi}{2\pi} \left(\log^2 \frac{M |\sin\phi|}{a_T} - \frac{3}{2} \log \frac{M |\sin\phi|}{a_T} \right) \\ &= C_F \left(\log^2 \frac{M}{2a_T} - \frac{3}{2} \log \frac{M}{2a_T} + \frac{\pi^2}{12} \right). \end{aligned} \quad (2.2.30)$$

Moreover, one could also derive the NLL resummation formula in Mellin moments space, which enables us to write for the collinear (and optionally soft) gluon emissions

$$\tilde{\Sigma}(N, a_T) = \tilde{\Sigma}^{(0)}(N) W_N(a_T). \quad (2.2.31)$$

Then, the effects of multiple collinear emissions at NLL accuracy can be expressed as

$$\begin{aligned} W_N^{real}(a_T) &= \sum_{n=0}^{\infty} \frac{1}{n!} \prod_{i=1}^n \int dz_i \frac{dk_{\perp i}^2}{k_{\perp i}^2} \frac{d\phi_i}{2\pi} \\ &\times z_i^N 2C_F \frac{\alpha_s(k_{\perp i}^2)}{2\pi} \left(\frac{1+z_i^2}{1-z_i^2} \right) \Theta \left(a_T - \left| \sum_i k_{\perp i} \sin\phi_i \right| \right), \end{aligned} \quad (2.2.32)$$

where $1 - z_i$ denotes the momentum fraction carried away by the emission of i^{th} collinear gluon.

In order to further simplify the above equation, we need to factorize the phase space constraint by using the Fourier representation of the Heaviside step function.

$$\Theta \left(a_T - \left| \sum_i v(k_i) \right| \right) = \frac{1}{\pi} \int_{-\infty}^{\infty} \frac{db}{b} \sin(ba_T) \prod_i e^{ibv(k_i)}. \quad (2.2.33)$$

With both the multiple emission probability and phase space factorizations, one could find the formula similar to Eq.(2.2.17) in q_{\perp} distribution, where the presence of Sine function is the consequence of addressing the one-dimensional sum.

$$W_N^{real}(a_T) = \frac{1}{\pi} \int_{-\infty}^{\infty} \frac{db}{b} \sin(ba_T) e^{R^{real}(b)}, \quad (2.2.34)$$

with the resummed exponent for real gluon emission contribution as

$$R^{real}(b) = \int dz \frac{dk_{\perp}^2}{k_{\perp}^2} \frac{d\phi}{2\pi} z^N 2C_F \frac{\alpha_s(k_{\perp}^2)}{2\pi} e^{ibv(k)} \left(\frac{1+z^2}{1-z^2} \right) \Theta \left(1 - z - \frac{k_{\perp}}{M} \right). \quad (2.2.35)$$

As for the explicit formula for the resummation of the a_T distribution, we also need to include all-order virtual corrections that straightforwardly exponentiate, which yields

$$W_N(a_T) = \frac{1}{\pi} \int_{-\infty}^{\infty} \frac{db}{b} \sin(ba_T) e^{-R(b)}, \quad (2.2.36)$$

where the resummed exponent is

$$\begin{aligned} -R(b) &= R^{real}(b) + R^{virtual}(b) \\ &= \int dz \frac{dk_{\perp}^2}{k_{\perp}^2} \frac{d\phi}{2\pi} 2C_F \frac{\alpha_s(k_{\perp}^2)}{2\pi} \left(\frac{1+z^2}{1-z^2} \right) \\ &\quad \times (z^N e^{ibv(k)} - 1) \Theta \left(1 - z - \frac{k_{\perp}}{M} \right). \end{aligned} \quad (2.2.37)$$

All of the above arguments are very similar to the discussion for q_{\perp} in Sec. 2.2.3. The difference a_T and q_{\perp} arises purely due to the restricting multiple real emission at the step function, where the phase space constraint for the q_{\perp} involves a two-dimensional vector sum $\Theta \left(q_{\perp} - \left| \sum_i \vec{k}_{\perp i} \right| \right)$, while in the present case we have a one-dimensional sum. Therefore, the resummation formula for the a_T variable involves the Sine function, as opposed to the Bessel function J_1 in the resummation for q_{\perp} . And the resummed exponent $R(b)$ is the same for a_T and q_{\perp} .

2.3 Calculations for jets: the jet mass distribution

Let us now apply the traditional approach to jet-shape observable, in this section, we present the calculation of jet invariant mass:

$$m^2 = \left(\sum_{i \in \text{jet}} k_i \right)^2, \quad (2.3.1)$$

where the invariant mass is defined by sum over all partons within the jet cluster.

In our discussion, we focus on QCD jets, i.e. jets which are initiated by a hard parton and subsequently evolve, shown in Fig. 2.2. Our perturbative calculation will be performed at parton level, and mostly focus on the quark-originated jet, but the extension to gluon jet should be pretty straightforward.

2.3.1 The concept of jets

Jets are collimated sprays of hadrons, which are dominant features of interactions in high-energy physics. They originate from accelerated quarks and gluons, thus can provide important clues about the high-energy behavior of quarks and gluons. Therefore, it is an ideal testing ground to study the fundamental properties of QCD.

A jet is measured at the detector with fixed radius R . This region is identified by the transverse momentum p_\perp of collimated particles from individual parton scattering, where the angular size θ is approximately the ratio between the jet mass m and p_\perp .

$$\theta \sim \frac{m}{p_\perp}. \quad (2.3.2)$$

The above description of the jet is captured in the cone region at Fig. 2.2. As we have already briefly discussed the distribution of jet mass in Sec. 2.1.3, which only depends on the dimensionless quantities m/p_\perp and the jet radius dependence will appear at higher orders, with the basic picture of the jet as a collection of the final state, collimated emissions.

However, at the hadron collider, this simple picture is not complete. As protons are composite particles, where multiple parton interactions (MPI) can occur in each proton collision. Furthermore, because the LHC doesn't collide individual pairs of protons, multiple proton-proton interactions can collide in each bunch crossing, which is referred to as pile-up. Both MPI and pileup will contribute additional non-perturbative contributions.

There's another kind of radiation outside of the cone that can affect the jet, as the emissions can land in the jet that arise from re-radiation from outside the jet. The contribution from these re-emissions is called non-global logarithms, or NGLs, which introduce a correlation between physics in and out of the jet.

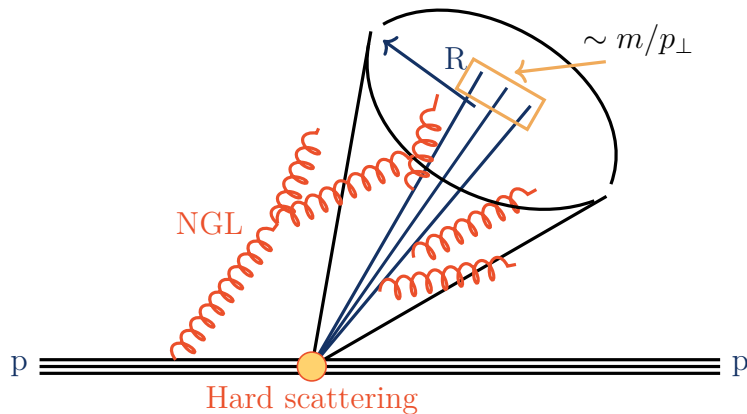


Figure 2.2. Illustration of jets in Hadron-Hadron Collisions

2.3.2 Jet algorithms

Jets can be defined by an algorithm. From a perturbative QCD viewpoint, jets are the product of successive parton branchings. Therefore, these algorithms are trying to invert the branching process by successively recombining two particles into one.

Nowadays, the most popular recombination algorithm is the family of generalized k_t algorithm [48], with the metric is defined by

$$d_{ij} = \min(p_{ti}^{2p}, p_{tj}^{2p}) \Delta R_{ij}^2, \quad d_{iB} = p_{ti}^{2p} R^2, \quad (2.3.3)$$

where p is a free parameter and ΔR_{ij}^2 is the geometric distance in the azimuth-rapidity plane. For instance, $p = 1$ corresponds to the k_t algorithm [49, 50], which clustering the soft particles first. For $p = 0$ we have the Cambridge-Aachen (C/A) algorithm [51, 52], with a purely geometrical distance. Finally, with the choice of $p = -1$ we obtain the anti- k_t algorithm [53], which will cluster hard particles first.

In the context of LHC physics, jets are almost always reconstructed with the anti- k_t algorithm, where the hard jet will grow by successively aggregating soft particles around it until it has reached the geometrical distance R away from the jet axis. Therefore, the hard jets will be insensitive to soft radiation and have a circular shape in the azimuth-rapidity plane.

2.3.3 Leading logarithmic approximation

Similar to the discussion in Sec. 2.2.4, we perform the calculation for the cumulative distribution, which is defined as the normalized cross-section

$$\Sigma(m^2) = \frac{1}{\sigma_0} \int_0^{m^2} dM^2 \frac{d\sigma}{dM^2} = 1 + \alpha_s \Sigma^{(1)} + O(\alpha_s^2). \quad (2.3.4)$$

As a first step, we calculate Eq.(2.3.4) to $O(\alpha_s)$ in soft limit. Recall the eikonal factor for the quark-antiquark dipole, introduced in Eq.(1.2.39)

$$W_{12} = \frac{\alpha_s}{2\pi} (2C_F) \frac{p_1 \cdot p_2}{(p_1 \cdot k)(p_2 \cdot k)}, \quad (2.3.5)$$

where p_1 , p_2 and k are the momenta of the quark, antiquark and soft gluon, respectively. For the calculation, we choose the kinematic as

$$\begin{aligned} p_1 &= \frac{Q}{2} (1, 0, 0, 1) \\ p_2 &= \frac{Q}{2} (1, 0, 0, -1) \\ k &= \omega (1, \sin \theta \cos \phi, \sin \theta \sin \phi, \cos \theta). \end{aligned} \quad (2.3.6)$$

Therefore, the phase space integral with the above configuration reads as

$$\int d\Pi_2 \equiv \int_0^\infty \omega d\omega \int_{-1}^1 d\cos\theta \int_0^{2\pi} \frac{d\phi}{2\pi}. \quad (2.3.7)$$

At the one-loop level, the cumulative distribution is then obtained by adding real and virtual corrections, which uses all the information above we find

$$\begin{aligned} \alpha_s \Sigma^{(1)}(m^2) &= \int d\Pi_2 W_{12} \left[\Theta_{in} \Theta \left(\frac{Qw}{2} (1 - \cos\theta) - m^2 \right) + \Theta_{out} - 1 \right] \\ &= -\frac{2\alpha_s C_F}{\pi} \int_{\cos R}^{1-2\frac{m^2}{Q^2}} \frac{d\cos\theta}{(1 - \cos\theta)(1 + \cos\theta)} \log \frac{Q^2 (1 - \cos\theta)}{2m^2}. \end{aligned} \quad (2.3.8)$$

We can further integrate over θ , and because the transverse momentum p_t of a boosted jet is much larger than its mass m , therefore we have $\rho \ll 1$. For LL accuracy we obtain the result

$$\alpha_s \Sigma^{(1)}(m^2) = -\frac{\alpha_s C_F}{2\pi} \log^2 \frac{1}{\rho} + O(R^2), \quad (2.3.9)$$

where we have expanded the result for small jet radius R and we introduced the dimensionless variable ρ

$$\rho = \frac{4m^2}{Q^2 R^2}. \quad (2.3.10)$$

Furthermore, the above result only contains LL and we also want to include higher accuracy contribution, i.e. collinear behavior. This can be done by compute the modified leading logarithmic [54], by include the residue of the splitting function $P_{qq}(z) = C_F \left(\frac{2}{z} - \frac{3}{2} \right)$ with $z = \frac{2w}{Q}$, and we obtain the result

$$\alpha_s \Sigma^{(1)}(\rho) = -\frac{\alpha_s C_F}{\pi} \left(\frac{1}{2} \log^2 \frac{1}{\rho} + B_q \log \frac{1}{\rho} \right), \quad (2.3.11)$$

with hard-collinear emission coefficient

$$B_q = \int_0^1 dz \left(\frac{P_{qq}(z)}{2C_F} - \frac{1}{z} \right) = -\frac{3}{4}. \quad (2.3.12)$$

The collinear behavior is related to the boosted-objects, which are typically collimated along the jet axis. Moreover, from the computational viewpoint, it is usually easier to perform the factorization in the collinear limit, as already briefly discussed in Sec. 2.2.2, while we also need to take into account the wide-angle soft emission for sub-leading color correlations. Therefore, from now on, we will perform all the calculations in collinear limit first, then extend to the wide-angle soft emission.

As a last comment before going to all-orders, the above discussion can also apply to gluon jet, in which we would have the same expression with different color factor $C_F \rightarrow C_A$ and coefficient $B_q \rightarrow B_g$

$$B_g = \int dz \left(\frac{P_{gg}(z)}{2C_A} - \frac{1}{z} \right) = -\frac{11}{12} + \frac{1}{6} \frac{N_f}{C_A}. \quad (2.3.13)$$

2.3.4 To all-orders

To obtain accurate theoretical predictions in the regime $\rho \ll 1$, we extend the results obtained in the previous section to all-orders. For the jet mass with n gluons in the final state:

$$m^2 = 2 \sum_{i < j} k_i \cdot k_j = \sum_i E_J \omega_i \theta_i^2, \quad (2.3.14)$$

where $E_J = \sum_i w_i = \frac{Q}{2}$ is the jet energy. Again we consider all possible gluon emissions, similar to the discussion in Sec. 2.2 and the cumulative distribution reads

$$\begin{aligned} \Sigma(\rho) &= \sum_{n=0}^{\infty} \frac{1}{n!} \prod_{i=1}^n \int \frac{d\theta_i^2}{\theta_i^2} \int dz_i P_{qq}(z_i) \frac{\alpha_s(z_i \theta_i \frac{Q}{2})}{2\pi} \Theta_{in} \Theta \left(\sum_{i=1}^n z_i \frac{\theta_i^2}{R^2} - \rho \right) \\ &+ \sum_{n=0}^{\infty} \frac{1}{n!} \prod_{i=1}^n \int \frac{d\theta_i^2}{\theta_i^2} \int dz_i P_{qq}(z_i) \frac{\alpha_s(z_i \theta_i \frac{Q}{2})}{2\pi} [\Theta_{out} - 1], \end{aligned} \quad (2.3.15)$$

where the Θ function constrains in the first line spoils the factorization, which can be avoided by the integral representation, i.e. compute the Mellin moments of the cumulative distribution. We note that the argument of the splitting function is energy fraction z_i , which is true if the fractional energy is computed with respect to the parent parton. On the other hand, the energy fraction is calculated regarding the jet energy, $E_J = \frac{Q}{2}$. In the collinear limit, these two fractions are related by rescaling factor x_i , which takes into account the energy carried away by previous emissions

$$x_i = \prod_{j=1}^{i-1} (1 - z_j), \quad (2.3.16)$$

However, the rescaling only gives rise to next-to-next-to-leading logarithm (NNLL) accuracy, hence can therefore be dropped in Eq.(2.3.15). Furthermore, we have used the jet clustering condition in a factorized form, i.e. $\Theta_{in} = \Theta(\theta_i < R)$. For a jet clustered with only two particles, this condition is exact for all members of the generalized k_t algorithm. But with the presence of an arbitrary number of particles, the factorized form might not exist. However, as we introduced in Sec. 2.3.2, the widely used anti- k_t algorithm behaves as a perfect cone in the soft limit, which leads to factorized expression.

At LL accuracy, we only count the maximally logarithm enhanced term, one can further assume that the emissions are strongly ordering, i.e. $z_i \theta_i^2$ themselves are strongly ordered. Therefore, a single emission strongly dominates

$$\Theta\left(\sum_{i=1}^n \rho_i < \rho\right) \approx \Theta(\rho_{i,max} < \rho) = \prod_{i=1}^n \Theta(z_i \rho_i < \rho), \quad (2.3.17)$$

where we have defined $\rho_i = z_i \frac{\theta_i^2}{R^2}$. With the above assumption, we finally have the expression after summing over all emissions

$$\begin{aligned} \Sigma^{LL}(\rho) &= \sum_{n=0}^{\infty} \frac{1}{n!} \prod_{i=1}^n \int \frac{d\rho_i}{\rho_i} \int dz_i P_{qq}(z_i) \frac{\alpha_s(\sqrt{z_i \rho_i} E_J R)}{2\pi} \Theta(\theta < R) \Theta(\rho_i > \rho) \\ &= \exp\left[-\int_{\rho}^1 \frac{d\rho'}{\rho'} \int dz P_{qq}(z) \frac{\alpha_s(\sqrt{z \rho'} E_J R)}{2\pi} \Theta(\theta < R) \Theta(\rho' > \rho)\right] \\ &\equiv e^{-R(\rho)}. \end{aligned} \quad (2.3.18)$$

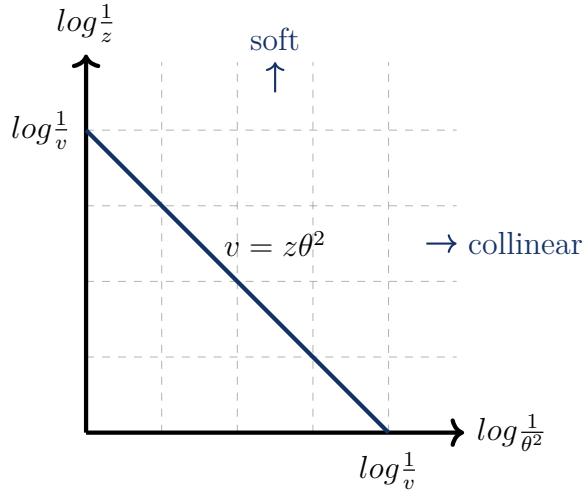


Figure 2.3. Lund diagram for the jet mass distribution

In order to achieve the resummed expressions, we need to evaluate the integrals of the resummed exponent in Eq.(2.3.18) with two-loop running coupling, one-loop splitting function $P_{qq}(z)$ and the soft wide-angle contribution at two-loop, which

corresponds to the two-loop cusp anomalous dimension $K = C_A \left(\frac{67}{18} - \frac{\pi^2}{6} \right) - \frac{5}{9}n_f$. This correction can be absorbed into the running coupling, which is called as Catani-Marchesini-Webber (CMW) scheme [55]

$$\frac{\alpha_s^{CMW}(\mu)}{2\pi} = \frac{\alpha_s(\mu)}{2\pi} + K \left(\frac{\alpha_s(\mu)}{2\pi} \right)^2. \quad (2.3.19)$$

Similar to the q_T resummation formula at NLL accuracy, we can write the resummed exponent as

$$R(\rho) = Lf_1(\lambda) + f_2(\lambda), \quad (2.3.20)$$

where

$$f_1(\lambda) = \frac{C_F}{\pi\beta_0\lambda} \left[(1-\lambda) \log(1-\lambda) - 2 \left(1 - \frac{\lambda}{2} \right) \log \left(1 - \frac{\lambda}{2} \right) \right], \quad (2.3.21)$$

$$\begin{aligned} f_2(\lambda) = & -\frac{C_F B_q}{\pi\beta_0} \log \left(1 - \frac{\lambda}{2} \right) - \frac{C_F K}{4\pi^2\beta_0^2} \left[\log(1-\lambda) - 2 \left(1 - \frac{\lambda}{2} \right) \log \left(1 - \frac{\lambda}{2} \right) \right] \\ & + \frac{C_F \beta_1}{2\pi\beta_0^3} \left[\log(1-\lambda) - 2 \log \left(1 - \frac{\lambda}{2} \right) + \frac{1}{2} \log^2(1-\lambda) - \log^2 \left(1 - \frac{\lambda}{2} \right) \right]. \end{aligned} \quad (2.3.22)$$

For the complete NLL resummation formula, we need to consider two additional contributions: multiple emissions and non-global logarithms [6]. For the multiple emission correction, we can no longer apply the strong-ordering approximation to Eq.(2.3.15). Therefore, similar to the discussion in the previous section, the resummed calculation must be done in the conjugate, i.e. Mellin, space in order to factorize the observable. In the end, we obtain the correction as

$$\mathcal{M} = \frac{e^{-\gamma_E R'(\rho)}}{\Gamma(1 + R'(\rho))}, \quad (2.3.23)$$

where $R'(\rho)$ is the derivative of $R(\rho)$ w.r.t $\log \frac{1}{\rho}$

The all-order structure of NGLs is much richer but can be in general resummed into a factor of $\mathcal{S}(\rho)$, We will discuss it in some detail in the next section and chapter 3. Putting all things together the NLL result reads

$$\Sigma^{NLL}(\rho) = \mathcal{M} e^{-R} \mathcal{S}. \quad (2.3.24)$$

2.3.5 Beyond leading logarithms

As a simple double-check for the all-order results we have obtained in the previous section. We can explicitly calculate the LL contribution at two-loop order, which is similar to the calculation we have done to derive the multi-soft gluon emission effective vertex. Thus the squared matrix element for two soft gluon emissions can be written as the sum of two terms

$$W = C_F^2 W^{(ind)} + C_F C_A W^{(corr)}, \quad (2.3.25)$$

where independent emissions have been discussed in Sec. 1.2.5 and the correlated emission contribute to NLO is shown in Fig. 2.4.

$$W^{(ind)} = \frac{2p_1 \cdot p_2}{(k_1 \cdot p_1)(k_1 \cdot p_2)} \frac{2p_1 \cdot p_2}{(k_2 \cdot p_1)(k_2 \cdot p_2)}, \quad (2.3.26)$$

$$W^{(corr)} = \frac{2p_1 \cdot p_2}{(k_1 \cdot p_1)(k_1 \cdot p_2)} \left[\frac{p_1 \cdot k_1}{(k_2 \cdot p_1)(k_1 \cdot k_2)} + \frac{p_2 \cdot k_1}{(k_2 \cdot p_2)(k_1 \cdot k_2)} - \frac{p_1 \cdot p_2}{(k_2 \cdot p_1)(k_2 \cdot p_2)} \right]. \quad (2.3.27)$$

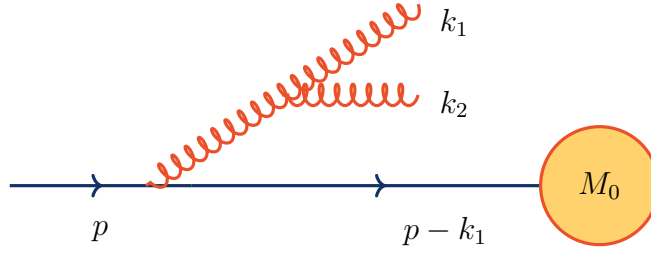


Figure 2.4. Correlated emission of two soft gluons

And since we only want to check the most singular term, i.e. $\alpha_s^2 L^4$ contribution to the cumulative distribution, which should originate from the independent emission of gluons in both soft and collinear limits. Therefore, we have to take into account both virtual gluons emissions, i.e. double real (RR), double virtual (VV) and real-virtual (RV) emission. For the independent emission contribution, the result for RR and VV is

$$W^{(ind)} = \frac{256}{Q^4} \frac{1}{z_3^2 z_4^2} \frac{1}{\theta_3^2 \theta_4^2} \quad (2.3.28)$$

For the RV similar result holds, with a relative minus sign, and we need to count RV term twice since the real emission could be either k_3 (RV) or k_4 (VR). With all the above information, we are now ready to calculate the jet mass distribution at NLO as

$$\frac{d\tilde{\sigma}}{d\rho} \equiv \frac{1}{\sigma_0} \frac{d\sigma}{d\rho} = \alpha_s \frac{d\tilde{\sigma}^{(1)}}{d\rho} + \alpha_s^2 \frac{d\tilde{\sigma}^{(2)}}{d\rho} + O(\alpha_s^3). \quad (2.3.29)$$

The phase space integration region can be divided into four regions according to whether the real gluons k_3 and k_4 are inside or outside the jet of interest, where the condition for a given gluon to end up inside or outside the jet depends on the jet definition. However, for both k_3 and k_4 are outside the jet vanishes since it will result as a massless jet.

The sum of the RR, RV, and VR contributions can be written as

$$\alpha_s^2 \frac{d\tilde{\sigma}^{(2)}}{d\rho} = \int d\Pi W [\delta(\rho - z_3\theta_3^2 - z_4\theta_4^2) - \delta(\rho - z_3\theta_3^2) - \delta(\rho - z_4\theta_4^2)]. \quad (2.3.30)$$

for simplicity purposes, here we rescaled the angular variables as $\theta_i \rightarrow \theta_i/R$, so that $\theta_i < 1$. We note that the emissions in LL approximation are also strongly

ordered in $z\theta^2$, i.e. $z_3\theta_3^2 > z_4\theta_4^2$, or $z_4\theta_4^2 > z_3\theta_3^2$, which means only the largest one will contribute to $\delta(\rho - z_3\theta_3^2 - z_4\theta_4^2)$. Since we are only interested in the LL term, we can consider the approximation of strongly ordered emission of gluons

$$\delta(\rho - z_3\theta_3^2 - z_4\theta_4^2) \rightarrow \delta(\rho - z_3\theta_3^2) \Theta(\rho > z_4\theta_4^2) + 3 \leftrightarrow 4. \quad (2.3.31)$$

Using the explicit forms of square matrix element W and the phase space $d\Pi$ in the collinear limit, we obtain

$$\begin{aligned} \alpha_s^2 \frac{d\tilde{\sigma}^{(2)}}{d\rho} &= - \left(\frac{\alpha_s C_F}{\pi} \right)^2 \int \frac{dz_3}{z_3} \frac{d\theta_3^2}{\theta_3^2} \frac{dz_4}{z_4} \frac{d\theta_4^2}{\theta_4^2} \frac{d\phi}{2\pi} \\ &\quad \times \Theta(z_3 > z_4) [\delta(\rho - z_3\theta_3^2) \Theta(\rho > z_4\theta_4^2) + 3 \leftrightarrow 4], \end{aligned} \quad (2.3.32)$$

and finally we can obtain the result

$$\alpha_s^2 \frac{d\tilde{\sigma}^{(2)}}{d\rho} = -\frac{1}{2} \left(\frac{\alpha_s C_F}{\pi} \right)^2 \frac{1}{\rho} \log^3 \left(\frac{1}{\rho} \right), \quad (2.3.33)$$

which is precisely the same as the double logarithm from the expansion of the resummed exponent.

For sub-leading contributions, since we have used the soft-gluon approximation, therefore the contribution from hard-collinear splittings is missing, which would give $\frac{3}{2} \left(\frac{\alpha_s C_F}{\pi} \right)^2 \frac{1}{\rho} \log^2 \frac{1}{\rho} B_q$. Moreover, for the NLL soft contribution, the approximation in Eq.(2.3.31) is no longer valid. Thus the correction can be obtained by calculating the difference between the left- and right- side of Eq.(2.3.31)

$$\begin{aligned} &\frac{1}{2} \left(\frac{\alpha_s C_F}{\pi} \right)^2 \int \frac{dz_3}{z_3} \frac{d\theta_3^2}{\theta_3^2} \frac{dz_4}{z_4} \frac{d\theta_4^2}{\theta_4^2} [\delta(\rho - z_3\theta_3^2 - z_4\theta_4^2) - \delta(\rho - z_3\theta_3^2) \Theta(z_4\theta_4^2 > \rho) \\ &\quad - 3 \leftrightarrow 4] \\ &= \left(\frac{\alpha_s C_F}{\pi} \right)^2 \int_0^\rho \frac{d\rho_3}{\rho_3} \frac{d\rho_4}{\rho_4} \log \frac{1}{\rho_3} \log \frac{1}{\rho_4} [\delta(\rho - \rho_3 - \rho_4) - \delta(\rho - \rho_3)] \Theta(\rho_3 > \rho_4) \\ &= \left(\frac{\alpha_s C_F}{\pi} \right)^2 \frac{\pi^2}{6} \frac{1}{\rho} \log \frac{1}{\rho} + O(\text{NNLL terms}). \end{aligned} \quad (2.3.34)$$

2.4 Global and non-global logarithms

In the last section, we have discussed the all-order calculation that aims to resum large logarithms of the ratio of the jet mass to the hard scale of the process up to NLL accuracy. And we have verified the LL behavior of the resummed result by performing a two-loop calculation in the soft and collinear limit, which we only considered the independent emission contribution to the eikonal current, i.e. Eq.(2.3.25).

The observables that we have considered so far have the property of exponentiation, which implies the following all-order structure:

$$\Sigma(v) = \left(1 + \sum_n C_n \bar{\alpha}_s^n\right) e^{Lg_1(\alpha_s L) + g_2(\alpha_s L)} + D(v), \quad (2.4.1)$$

where $L = \log 1/v$ and $\bar{\alpha}_s = \alpha_s/2\pi$ and $D(v)$ is called as remainder function that goes to zero for $v \rightarrow 0$. And C_n are not logarithmically enhanced terms, which will contribute to higher accuracy by cross-talk with the LL terms arising from the Sudakov form factors.

Moreover, a common property for the observables that we have discussed so far is that they are sensitive to emissions uniformly over the entire phase space, which is called global observable. At NLL accuracy [6], the all-order structure of the jet mass distribution will be:

$$\begin{aligned} \Sigma(v) &= (1 + \alpha_s C_1^{(q)}) \mathcal{S}(\alpha_s L) e^{-R_q(\alpha_s C_F, L)} + \alpha_s C_1^{(g)} e^{-R_g(\alpha_s C_A, L)} \\ &+ D(\rho), \end{aligned} \quad (2.4.2)$$

where R_q and R_g are the resummed exponents for quark and gluon jets, and the constant term C_1 can be expressed as

$$\begin{aligned} \alpha_s C_1 &= \lim_{v=0} [\Sigma_{NLO}(v) - \Sigma_{NLL, \alpha_s}(v)] = \lim_{v=0} \left[\int_0^v \frac{d\sigma}{dv} dv - \Sigma_{NLL, \alpha_s}(v) \right] \\ &= \lim_{v=0} \left[\sigma_{NLO} - \int_v^{v_{max}} \frac{d\sigma}{dv} dv - \Sigma_{NLL, \alpha_s}(v) \right] \\ &= \sigma_{NLO} + \lim_{v=0} \left[\int_{v_{max}}^v \frac{d\sigma}{dv} dv - \Sigma_{NLL, \alpha_s}(v) \right], \end{aligned} \quad (2.4.3)$$

the numerical estimate for the constant term C_1 will included later.

The new non-global effect is embodied by the function \mathcal{S} , where its fixed-order expansion reads

$$\mathcal{S}(\alpha_s L) = 1 + \sum_{n=2} S_n(\alpha_s L). \quad (2.4.4)$$

As a first step, let's focus our discussion on the fixed-order calculation which illustrates how the leading non-global logarithms arise. And since we are dealing with observable, that is only sensitive to a restricted region of phase-space. We could use the configuration that a gluon emitted outside the region, i.e. outside the jet, and then re-emits a softer gluon inside the jet. Thus, we need to consider the correlated emission to the matrix element of two soft gluons, where the harder gluon k_3 is outside the jet, while the softer gluon k_4 is recombined with the jet.

$$\begin{aligned} S_2 &= -4C_F C_A \left(\frac{\alpha_s}{2\pi}\right)^2 \int \frac{d\omega_3}{\omega_3} \int \frac{d\omega_4}{\omega_4} \Theta(\omega_3 > \omega_4) \int d\cos\theta_3 \int d\cos\theta_4 \Omega(\theta_3, \theta_4) \\ &\times \Theta(\cos\theta_3 < \cos R) \Theta(\cos\theta_3 > \cos R) \Theta(\omega_4 Q(1 - \cos\theta_4) > m^2), \end{aligned} \quad (2.4.5)$$

where the angular function $\Omega(\theta_3, \theta_4)$ is

$$\Omega(\theta_3, \theta_4) = \frac{2}{(\cos\theta_4 - \cos\theta_3)(1 - \cos\theta_3)(1 + \cos\theta_4)}. \quad (2.4.6)$$

The integrals over the energies are straightforward. For the leading NGLs, we only keep the term proportional to $\log^2 \frac{1}{\rho}$

$$\begin{aligned} S_2 &\simeq -2C_F C_A \left(\frac{\alpha_s}{2\pi}\right)^2 \log^2 \frac{1}{\rho} \int_0^1 d\cos\theta_3 \int_0^1 d\cos\theta_4 \Omega(\theta_3, \theta_4) \\ &= -C_F C_A \left(\frac{\alpha_s}{2\pi}\right)^2 \frac{\pi^2}{3} \log^2 \frac{1}{\rho}. \end{aligned} \quad (2.4.7)$$

More details about NGLs and its resummation will be discussed in chapter 3.

2.5 General resummation formalism

In this section, we present the basic ideas that are used to construct the EFT and MC approach in resummation. We start with the coherent branching for multiple emissions in QED, intending to get a better interpretation of the Sudakov form factor, then we will extend this method to QCD. The second goal of this section is to discuss the RGE approach, where we will derive the solution of the RG evolution equation, and the factorization formula and scale separation will be discussed. In the end, a general automated NLL resummation tool will be briefly introduced.

2.5.1 Coherent branching

In this section, we want to extend our discussion for the Sudakov form factor in Sec. 2.2.2 to a more general case with the coherent branching, based on generating functionals [8, 36], the coherent branching is the basic building block for constructing Monte Carlo parton shower algorithms.

Start with the Abelian case and recall the factorization properties of soft emission in Sec. 1.2.5, we can also obtain the expression for the factorization at the cross-section level [36]

$$d\sigma_{m+1}(\{k_i\}, q) = d\sigma_m(\{k_i\}) \times dW_1(q), \quad (2.5.1)$$

where dW_1 is the single emission probability, for a single photon emission, it can be written as

$$dW_1(q) = \frac{\alpha}{\pi} \sum_i e_i^2 \frac{d\omega}{\omega} \frac{d\theta_{iq}^2}{\theta_{iq}^2} \Theta(\theta_{max} - \theta_{iq}), \quad (2.5.2)$$

and we can approximate single emission probability by considering a sum over radiation emitted by independent sources, where the interference, which cancels the radiation at large angles, is approximated by the angular ordering.

Now we want to generalize the single soft photon case to multiple emissions from the same fermionic line. Since we only consider soft photons, which do not carry electric charge, which means both the charge and the momentum of the emitting particle are unchanged. Therefore, the multiple emission probability can be written as

$$dW_n \simeq \frac{1}{n!} \prod_{i=1}^n dW_1(q_i). \quad (2.5.3)$$

To all orders, the multiple emissions can be described by introducing a generating functional:

$$\Phi^{real}[u(q)] = 1 + \sum_{n=1}^{\infty} \int dW_n(q_1, \dots, q_n) u(q_1) \cdots u(q_n), \quad (2.5.4)$$

where we have introduced the measurement function $u(q_i)$ acts as phase-space constraint, similar to the observable function introduced in the first chapter. And one can easily recover the emission probability by successive differentiation

$$dW_n = \frac{\delta \Phi}{\delta u(q_1) \cdots \delta u(q_n)} \Big|_{u=0}. \quad (2.5.5)$$

Moreover, we could also rewrite the Eq.(2.5.4) by using Eq.(2.5.3)

$$\begin{aligned} \Phi^{real}[u(q)] &= 1 + \sum_{n=1}^{\infty} \left[\int dW_1(q_i) u(q_i) \right]^n \\ &= \exp \left[\int dW_1(q) u(q) \right], \end{aligned} \quad (2.5.6)$$

in the second line, we find that the results are simply given by exponentiating the lowest order contribution, which was derived in 1960s in Ref. [56]. For the full results, we also need to include the virtual contribution. According to the IRC safety, the total soft emission has a vanishing effect, which is equivalent to

$$\Phi[u(q)] \Big|_{u=1} = 1, \quad (2.5.7)$$

this is often referred to as the unitarity condition, which will correctly normalize Φ . Therefore, the full result can be written as

$$\begin{aligned} \Phi[u(q)] &= \frac{\Phi^{real}[u(q)]}{\Phi^{real}[u(q)=1]} \\ &= \exp \left[\int dW_1(q) [u(q) - 1] \Theta(Q - \omega) \Theta(\omega\theta - Q_0) \right], \end{aligned} \quad (2.5.8)$$

where in the last line, we have also introduced two constraints. The first one gives an upper limit in the energy for the soft approximation, which is of the order of the hard scale Q . And the second condition introduces an arbitrary lower cut-off

Q_0 for the photon transverse momentum. Moreover, by requiring no real radiation is emitted, i.e. $u(q) = 0$, we could obtain the Sudakov form factor

$$\Phi[u = 0] \equiv S(Q, Q_0) = \exp \left[- \int dW_1(q) \Theta(Q - \omega) \Theta(\omega\theta - Q_0) \right], \quad (2.5.9)$$

which describes the probability that no emission takes place as we have briefly introduced at Sec. 2.2.2. Furthermore, for the vanishing lower cut-off Q_0 , the Sudakov form factor vanished as well. This means there must be some arbitrarily soft radiation in any scattering process, as the probability of no radiation is zero.

For multiple emissions from different fermions, we have to include the effect of interference, which can be approximated by the constraint on the angular ordering. Then, the generating functional can be written as

$$\Phi_{\{k_1, \dots, k_n\}}[u(q)] = \prod_i \Phi_{k_i}[Q, \theta_{max}; u(q)], \quad (2.5.10)$$

where for each fermion external line, we have

$$\Phi_{k_i}[E_{k_i}, \theta_{max}^2; u(q)] = \exp \left[\frac{\alpha}{\pi} \int_0^Q \frac{d\omega}{\omega} \int_0^{\theta_{max}^2} \frac{d\theta^2}{\theta^2} (u(q) - 1) \Theta(\omega\theta - Q_0) \right]. \quad (2.5.11)$$

The above discussion can also be extended to the QCD case, but as consequence of the non-Abelian structure, the factorization is more complicated due to the presence of color matrices and non-Abelian interactions. Applying the eikonal approximation, the $m + 1$ parton matrix element in the soft limit can be written as

$$|M_{m+1}|^2 \rightarrow -g_s^2 \sum_{i,j} \frac{(k_i \cdot k_j)}{(k_i \cdot q)(q \cdot k_j)} \langle M_m | t_i \cdot t_j | M_m \rangle, \quad (2.5.12)$$

where t_i is an abstract color operator, which satisfies color conservation

$$\sum_i t_i | M_m(\{k\}) \rangle = 0, \quad (2.5.13)$$

and the square of the operator t_i gives the Casimir of the $SU(N_c)$ representation

$$t_i^2 = \begin{cases} C_F & \text{for } i \text{ is quark} \\ C_A & \text{for } i \text{ is gluon} \end{cases}, \quad (2.5.14)$$

as a comment, we note that in the large N_c limit, i.e., the MC parton showers, the off-diagonal entries of the color product $t_i \cdot t_j$ will vanish.

Moreover, the soft gluon radiation can also come from the hard gluons, which will carry away color charge. Therefore, the radiation pattern of the soft gluon is more intricate and subtle than in QED. Details about the results and discussions about the QCD case can be found in Ref. [36].

2.5.2 Renormalization group approach

In this section, we will discuss the NLL resummation formula using the renormalization group (RG) evolution approach, which is widely used in effective theories such as SCET, which typically describes resummation by introducing non-local correlation operators, i.e. Wilson lines, and exploits their renormalization group evolution [57, 58].

The renormalization group evolution for a general function $F(\mu)$, i.e., hard, soft and jet function, is

$$\mu \frac{d}{d\mu} F = \gamma_F F = \left(C_F \Gamma_{cusp}(\alpha_s) \log \frac{Q^2}{\mu^2} + \gamma \right) F, \quad (2.5.15)$$

where γ_F is the anomalous dimension. This equation follows from demanding that the final physical result is independent of μ . In real space, the cross-section can be expressed as a convolution of jet and soft functions that depend on the observable v (and other things that are independent of v), and so in the Fourier transformed conjugate b space, the cross-section is a simple product of jet and soft functions.

The solution of the RG equation in Eq.(2.5.15) sums the logarithmic terms to all orders, where the result reads as

$$F(\mu) = \exp \left\{ \int_{\mu_F}^{\mu} \left[C_F \Gamma_{cusp}(\alpha_s) \log \frac{Q^2}{\mu'^2} + \gamma \right] d \log \mu' \right\} F(\mu_F), \quad (2.5.16)$$

where the logarithm appears in an exponential, and the exponential function acts as an evolution matrix $U(\mu_F, \mu)$, which runs down the scale from μ_F to μ .

In order to use this solution in practice, we re-write the integration over the coupling by using the relation

$$\frac{d}{d \log \mu} \alpha_s(\mu) = \beta(\alpha_s(\mu)). \quad (2.5.17)$$

Similarly, we can also re-write the logarithm in the exponent with the relation

$$\log \frac{\nu}{\mu} = \int_{\alpha_s(\mu)}^{\alpha_s(\nu)} \frac{d\alpha}{\beta(\alpha)}. \quad (2.5.18)$$

Therefore, the evolution matrix can be written in the form

$$U(\mu_F, \mu) = \exp [2C_F S(\mu_F, \mu) - A_\gamma(\mu_F, \mu)] \left(\frac{Q^2}{\mu_F^2} \right)^{-C_F A_{\Gamma_{cusp}}(\mu_F, \mu)}, \quad (2.5.19)$$

where we have introduced the quantities S and A_{γ_i} by

$$S(\nu, \mu) = - \int_{\alpha_s(\nu)}^{\alpha_s(\mu)} d\alpha \frac{\Gamma_{cusp}(\alpha)}{\beta(\alpha)} \int_{\alpha_s(\nu)}^{\alpha_s(\mu)} \frac{d\alpha'}{\beta(\alpha')}, \quad (2.5.20)$$

$$A_{\gamma_i}(\nu, \mu) = - \int_{\alpha_s(\nu)}^{\alpha_s(\mu)} d\alpha \frac{\gamma_i(\alpha)}{\beta(\alpha)}. \quad (2.5.21)$$

Recall the change integration of variable in Eq.(2.5.17), therefore it is easy to identify that A_{γ_i} are responsible for the resummation of the single logarithms and the function S for the resummation of the double logarithms by observing that

$$\mu \frac{d}{d\mu} S(\nu, \mu) = -\Gamma_{cusp}(\alpha_s(\mu)) \int_{\alpha_s(\nu)}^{\alpha_s(\mu)} \frac{d\alpha'}{\beta(\alpha')}, \quad (2.5.22)$$

$$\mu \frac{d}{d\mu} A_{\gamma_i}(\nu, \mu) = -\gamma_i(\alpha_s(\mu)). \quad (2.5.23)$$

The explicit expressions for these functions can be obtained by inserting the perturbative expansion of the beta function and the anomalous dimension

$$\beta = -2\alpha_s \left[\frac{\alpha_s}{4\pi} + \beta_1 \left(\frac{\alpha_s}{4\pi} \right)^2 + O(\alpha_s^3) \right], \quad (2.5.24)$$

$$\Gamma_{cusp} = \Gamma_0 \left(\frac{\alpha_s}{4\pi} \right) + \Gamma_1 \left(\frac{\alpha_s}{4\pi} \right)^2 + O(\alpha_s^3), \quad (2.5.25)$$

$$\gamma = \gamma^{(0)} \left(\frac{\alpha_s}{4\pi} \right) + \gamma^{(1)} \left(\frac{\alpha_s}{4\pi} \right)^2 + O(\alpha_s^3). \quad (2.5.26)$$

By inserting these expansions into the integrands of Eq.(2.5.20), one obtains the result at NLL accuracy in \vec{b} space

$$A_\gamma(\nu, \mu) = \frac{\gamma^{(0)}}{2\beta_0} \log r + O(\alpha_s), \quad (2.5.27)$$

$$A_{\Gamma_{cusp}}(\nu, \mu) = \frac{\Gamma_0}{2\beta_0} \log r + O(\alpha_s), \quad (2.5.28)$$

$$S(\nu, \mu) = \frac{\Gamma_0}{4\beta_0} \left[\frac{4\pi}{\alpha_s(\nu)} \left(\frac{r-1}{r} - \log r \right) + \left(\frac{\Gamma_1}{\Gamma_0} - \frac{\beta_1}{\beta_0} \right) \log(1-r+\log r) + \frac{\beta_1}{2\beta_0} \log^2 r \right] + O(\alpha_s), \quad (2.5.29)$$

here, r is the ratio

$$r = \frac{\alpha_s(\mu)}{\alpha_s(\mu_F)}. \quad (2.5.30)$$

Therefore, the general solution of this renormalization group equation is

$$F(\mu) = F(\mu_F) \exp \left[C_F \frac{\Gamma_F}{2\beta_0^2} \left\{ \frac{4\pi}{\alpha_s(\mu_F)} \left(\log r + \frac{1}{r} - 1 \right) + \left(\frac{\Gamma_1}{\Gamma_0} - \frac{\beta_1}{\beta_0} \right) (r-1-\log r) - \frac{\beta_1}{2\beta_0} \log^2 r \right\} - \frac{\gamma^{(0)}}{2\beta_0} \log r \right], \quad (2.5.31)$$

where the first two coefficients of the cusp anomalous dimension Γ and the β -function are

$$\Gamma_0 = 4, \quad (2.5.32)$$

$$\Gamma_1 = 4C_A \left(\frac{67}{9} - \frac{\pi^2}{3} \right) - \frac{80}{9} T_R n_f,$$

and

$$\begin{aligned}\beta_0 &= \frac{11}{3}C_A - \frac{4}{3}T_R n_f, \\ \beta_1 &= \frac{34}{3}C_A^2 - 4T_R n_f \left(C_F + \frac{5}{3}C_A \right).\end{aligned}\tag{2.5.33}$$

To achieve the resummation, one solves the renormalisation-group (RG) evolution equation for each term of the factorization formula for hard, collinear, and soft function, that satisfies the RG invariance as the final result must be independent of the 't Hooft scale μ , which is an artifact from the dimensional regularization. The procedure is summarized in Fig. 2.5

$$\frac{d}{d\log\mu} [H(\mu_h, \mu) J(\mu_j, \mu) S(\mu_s, \mu)] = 0.\tag{2.5.34}$$

Therefore, one can also find the result

$$0 = \frac{1}{H(\mu_h, \mu)} \frac{dH(\mu_h, \mu)}{d\log\mu} + \frac{1}{J(\mu_j, \mu)} \frac{dJ(\mu_j, \mu)}{d\log\mu} + \frac{1}{S(\mu_s, \mu)} \frac{dS(\mu_s, \mu)}{d\log\mu},\tag{2.5.35}$$

where each term in the above equation has nothing but the anomalous dimensions of the different functions, therefore the RG invariance also implies that the sum of the anomalous dimensions vanishes.

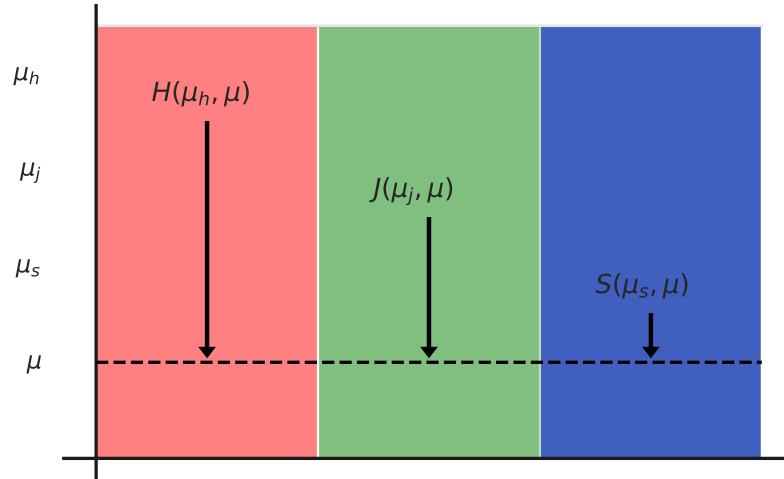


Figure 2.5. Scale separation and of the calculational procedure in renormalization group improved perturbation theory

3 Resummation of Non-Global Logarithms to All Orders

Contents

3.1	Structure of non-global logarithms	64
3.1.1	Strong energy ordering	65
3.1.2	Non-global hemisphere mass integral	68
3.2	Evolution equation: Banfi-Marchesini-Smye	70
3.2.1	Perturbative expansion of the BMS equation	71
3.2.2	Calculation of U_{abj}	72
3.2.3	Symmetries of the BMS equation	73
3.3	Perturbative calculation of NGLs	75
3.3.1	Partial resummed result	77
3.3.2	Dressed gluon approximation	78
3.4	Solving differential equations with neural networks	79
3.4.1	A brief introduction to neural networks	80
3.4.2	Ordinary differential equation examples	81
3.4.3	Structure of BFKL equation	81
3.4.4	Numerical results for NGLs	83
3.4.5	Plan for next steps	85

Up to now in this thesis, the all-order resummation has only been performed for the global part, which accounts for radiation over the entire final state phase-space. This category excludes all observables with hard phase-space cuts. The presence of hard boundaries introduces a new, more intricate, class of large logarithms, which are usually referred to as non-global logarithms (NGLs). In recent years, NGLs have been studied using different methods and approximations, including work on the structure of higher logarithms at fixed order, studies of sub-leading logarithms as well as beyond large N_c limit. In this chapter, we are mainly interested in the hemisphere mass distribution, and more details related to the resummation of the leading NGLs through the evolution equation will be deepened.

3.1 Structure of non-global logarithms

Non-global logarithms were first characterized and understood by Dasgupta and Salam exploiting the MC simulation for leading NGLs at large N_c limit in Ref. [6]. Unlike global logarithms, non-global logarithms arise from the relevant scales within the jet as well as the scale outside the jet. Indeed, while the out-of-jet region is not directly measured, emissions that originate from the outside can still affect the in-jet region of phase space. Thus, in order to achieve an accurate description of a given logarithmic accuracy, the non-global logarithms must be resummed.

The resummation for NGLs at NLL accuracy was achieved by evolution of dipoles in the large N_c limit, numerically solved with a Monte Carlo approach. As an alternative to the MC approach, an evolution equation was derived by Banfi, Marchesini and Smye (BMS) [59]. In recent years, NGLs have been studied using different methods and approximations, for example: leading NGLs up to 5 loops by solving BMS equation were computed in [60], an approximate resummation with n soft subjects was developed [61] and the implementation in a parton-shower framework was done in [62].

There are two facts that make the resummation of the leading non-global logarithm possible. Firstly, these logarithms can only come from the phase space where the gluons are strongly ordered in energy [6]. Second, the strong-energy-ordering approximation leads to simplified cross-sections, particularly at large N_c limit, more details about large N_c can be find in A.4.

In this chapter, we are mainly interested in the hemisphere mass cross section, for example, the doubly differential distribution $\frac{d^2\sigma}{dm_L dm_R}$ in e^+e^- collision [63], where in the limit $m_L \gg m_R$ or vice versa, the NGLs with the form $L = |\log \frac{m_L}{m_R}|$ will give large contributions. The joint differential distribution of the two hemisphere masses can be factorized in the limit that both masses are small [63–65]

$$\frac{d^2\sigma}{dm_L dm_R} = H(Q, \mu) \int dk_L dk_R J(m_L^2 - k_L Q, \mu) J(m_R^2 - k_R Q, \mu) S(k_L, k_R, \mu), \quad (3.1.1)$$

where the μ dependence of all these functions is known up to 3 loops and has been resummed to the N³LL accuracy for global logarithms. Moreover, the soft function has multiple scale dependence, thus one cannot resum all the large logarithms so simply. In practice, we can write the soft function as

$$S(k_L, k_R, \mu) = S_\mu\left(\log \frac{k_L}{\mu}\right) S_\mu\left(\log \frac{k_R}{\mu}\right) S_f\left(\log \frac{k_L}{k_R}\right). \quad (3.1.2)$$

For $S_\mu(L)$ with the μ dependence, its logarithms can be resummed by using the RGE approach, which we have introduced in Sec. 2.5.2, while the resummation of $S_f(L)$ is more subtle. The non-global logarithms are those contained in $S_f(L)$, as we have briefly discussed in Sec. 2.4, there are no double logarithms in $S_f(L)$,

instead it has single logarithms of the form $(\alpha_s L)^n$ and sub-leading logarithms, $\alpha_s^m L^n$ with $m > n$.

3.1.1 Strong energy ordering

In this section, we start with the strong energy ordering (SEO) approximation and the simplifications within the large N_c limit, then we will derive the fixed-order formula up to 3-loop level for the hemisphere mass distribution using strong-energy-ordering [60]. However, the process has become quite involved already in 3 loops.

To begin with, let's consider the squared matrix element for the emission of m gluons off quark line in the a^μ and b^μ directions in the limit of the energy of the gluons being strongly ordered, at large N_c , i.e. $C_F \rightarrow N_c/2$, it can be written as [66]

$$|\mathcal{M}_{ab}^{1\dots m}|^2 = N_c^m g^{2m} \sum_{\text{perms of } 1\dots m} \frac{(p_a \cdot p_b)}{(p_a \cdot p_1)(p_1 \cdot p_2)\cdots(p_m \cdot p_b)}. \quad (3.1.3)$$

In order to simplify the formula, it is useful to pull out the energies from the dot products by

$$(ab) \equiv \frac{a \cdot b}{\omega_a \omega_b} = 1 - \cos\theta_{ab}, \quad (3.1.4)$$

where θ_{ij} is the angle between the directions \vec{p}_i and \vec{p}_j . We then introduced the radiator function as

$$W_{ab}^{1\dots m} = \frac{(ab)}{(a1)(12)\cdots(mb)}, \quad (3.1.5)$$

and

$$P_{ab}^{1\dots m} = \sum_{\text{perms of } 1\dots m} W_{ab}^{1\dots m}. \quad (3.1.6)$$

Then Eq.(3.1.3) can be re-written as

$$|\mathcal{M}_{ab}^{1\dots m}|^2 = N_c^m g^{2m} \frac{1}{\omega_1^2 \cdots \omega_m^2} \mathcal{P}_{ab}^{1\dots m}. \quad (3.1.7)$$

With the above simplification, the differential cross-section for real emission is

$$\frac{1}{\sigma_0} d\sigma_m^R = \sum_m \frac{1}{m!} \bar{\alpha}_s \prod_{i=1}^m \frac{d\omega_i}{\omega_i} \frac{d\Omega_i}{4\pi} \mathcal{P}_{ab}^{1\dots m}, \quad (3.1.8)$$

where we have defined

$$\bar{\alpha}_s \equiv N_c \frac{\alpha_s}{\pi}. \quad (3.1.9)$$

It is easy to check that Eq.(3.1.3) with just one gluon emission is nothing but the eikonal vertex summed over polarizations, as we have discussed in Sec. 1.2.5.

$$\begin{aligned} |\mathcal{M}_{ab}^1|^2 &= 2C_F g^2 \frac{(p_a \cdot p_b)}{(p_a \cdot p_1)(p_1 \cdot p_b)} \\ &\simeq N_c g^2 \frac{1}{\omega_1^2} \mathcal{P}_{ab}^1, \end{aligned} \quad (3.1.10)$$

where we have used the large N_c limit as $C_F = (N_C^2 - 1)/(2N_C) \simeq N_C/2$. For two gluons with $\omega_1 \gg \omega_2$, the quark (Wilson) line emitting gluon 1 first with the rate proportional to \mathcal{P}_{ab}^1 , then the second gluon views gluon 1 as a source, since gluon 2 is much softer. Thus this new line is equivalent to a fundamental Wilson line, which forms a dipole with both antiquark and quark. These two dipoles are then proportional to \mathcal{P}_{a1}^2 and \mathcal{P}_{1b}^2 respectively.

$$\mathcal{P}_{ab}^{12} = \mathcal{P}_{ab}^1 (\mathcal{P}_{a1}^2 + \mathcal{P}_{1b}^2). \quad (3.1.11)$$

For more emissions, one could continue this recursion process. This SEO dipole picture is also well-known as the foundation of Monte-Carlo event generators [67]. Similarly, one could also obtain a useful set of identities for the radiator function

$$W_{ab}^{1\dots m} = W_{ar}^{1\dots(r-1)} W_{ab}^r W_{rb}^{(r+1)\dots m}, \quad (3.1.12)$$

where the above relation can be checked with two and three emission as

$$W_{ab}^{12} = W_{ab}^1 W_{1b}^2 = W_{a2}^1 W_{ab}^2, \quad (3.1.13)$$

$$W_{ab}^{123} = W_{ab}^1 W_{ab}^{23} = W_{a2}^1 W_{ab}^2 W_{2b}^3 = W_{a3}^{12} W_{ab}^3. \quad (3.1.14)$$

Now we also need to consider virtual contributions. Due to the IRC safety of inclusive cross-section, the large logarithm that arises from real emission must be exactly cancelled by virtual corrections. Thus, we should be able to represent virtual contributions as integrals over momenta of exactly the same form as the real emissions. For one-loop level

$$d\sigma^V = -d\sigma^R \propto -N_c g^2 \frac{1}{\omega_1^2} \mathcal{P}_{ab}^1, \quad (3.1.15)$$

which is equivalent to say

$$W_R = P_{ab}^1, \quad W_V = -W_R, \quad (3.1.16)$$

and for an observable that is less inclusive, like the hemisphere mass, there would have an incomplete cancellation between the real and virtual corrections, thus leaving the large logarithm enhancement.

In order to obtain a more general formula, let us use the notation of $W_{RV\dots R}$ to indicate the hardest first gluon is real, the second hardest is virtual, and so on to

the softest gluon that is real. Thus, combine both virtual and real parts, one can obtain the results as

$$\begin{aligned} \frac{1}{\sigma_0} d\sigma_m &= \bar{\alpha}_s \frac{d\omega_1}{\omega_1} \frac{d\Omega_1}{4\pi} (W_R + W_V) \\ &+ \frac{\bar{\alpha}_s^2}{2!} \frac{d\omega_1}{\omega_1} \frac{d\Omega_1}{4\pi} \frac{d\omega_2}{\omega_2} \frac{d\Omega_2}{4\pi} (W_{RR} + W_{RV} + W_{VR} + W_{VV}) \\ &+ O(\bar{\alpha}_s^3). \end{aligned} \quad (3.1.17)$$

To better understand the structure of the above formula, we check it at the two-loop level, where the gluons can be either real or virtual. If both are real, we can obtain the expression

$$W_{RR} = P_{ab}^{12} = \begin{cases} P_{ab}^1 (P_{a1}^2 + P_{ab}^2) \\ P_{ab}^2 (P_{a1}^1 + P_{2b}^1) \end{cases}, \quad (3.1.18)$$

which holds for either $\omega_1 \gg \omega_2$ or $\omega_2 \gg \omega_1$. If the harder gluon is real and the softer gluon is virtual, then the real emission establishes the $(a1)$ and $(1b)$ dipoles, which both contribute a virtual contribution, thus we have

$$W_{RV} = -P_{ab}^1 (P_{a1}^2 + P_{1b}^2), \quad (3.1.19)$$

On the other hand, if the harder gluon is virtual, then we get the $-P_{ab}^1$ from the first emission, while the original (ab) dipole produces the real emission. Therefore, we have

$$W_{RV} = -P_{ab}^1 P_{ab}^2. \quad (3.1.20)$$

Finally, if both gluons are virtual, then the (ab) dipole produces both of them, then we have

$$W_{VV} = P_{ab}^1 P_{ab}^2. \quad (3.1.21)$$

Thus, we have two independent integrands, that we will deal with in the next section

$$P_{ab}^{12} = W_{RR} = -W_{RV}, \quad (3.1.22)$$

$$P_{ab}^1 P_{ab}^2 = W_{VV} = -W_{VR}. \quad (3.1.23)$$

For the 3-loop level, we can construct the integrands in the same way, and one could find 4 independent integrands, detailed discussions can be found in Ref. [60].

$$I_1 = P_{ab}^{123} = W_{RRR} = -W_{RRV}, \quad (3.1.24)$$

$$I_2 = P_{ab}^{12} (P_{a1}^3 + P_{b1}^3) = W_{RVV} = -W_{RVR}, \quad (3.1.25)$$

$$I_3 = P_{ab}^1 P_{ab}^{23} = -W_{VRR} = W_{VRV}, \quad (3.1.26)$$

$$I_4 = P_{ab}^1 P_{ab}^2 P_{ab}^3 = W_{VVV} = -W_{VVV}. \quad (3.1.27)$$

It is straightforward to check that in the above result, the sum of all contributions gives zero, as expected since there will be a complete cancellation in the inclusive cross-section.

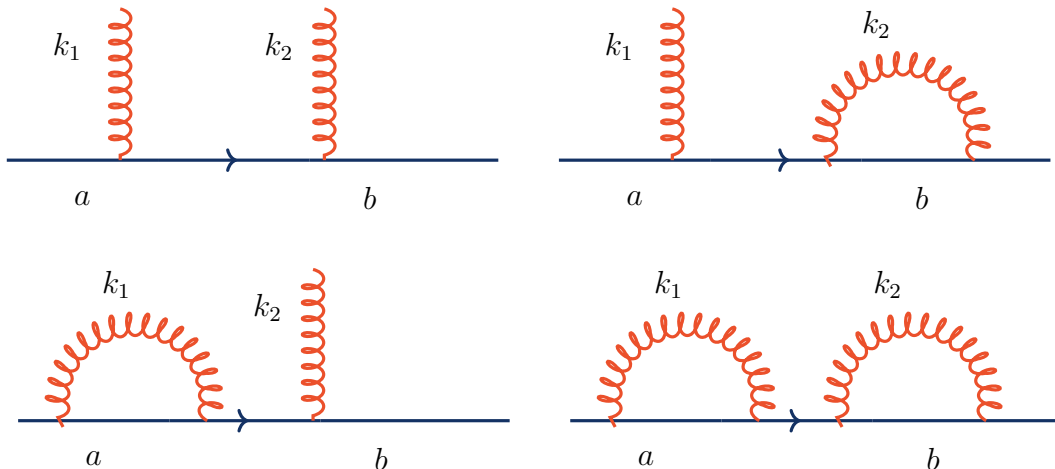


Figure 3.1. Feynman diagrams for the $O(\alpha_s)$ corrections

3.1.2 Non-global hemisphere mass integral

In the previous section, we have defined the real and virtual contributions to the matrix elements in the SEO approximation. In order to obtain the distribution, we need to perform the integration for these matrix elements against a measurement function, which is only sensitive to real emissions, since virtual gluons are never measured [60]. In this section, we will perform the fixed-order calculations up to 3 loops. For higher loops, we find it simpler to extract the result via BMS equation, which will be explained in the next section.

In this section, we will calculate the right-hemisphere mass defined as $\rho = \frac{M_R}{Q}$, we then have the cumulative cross-section as the integral of the matrix-element squared times a measurement function

$$S(\rho) = \int d\Phi_m |M_{ab}^{1\dots m}|^2 u(\{p_i\}), \quad (3.1.28)$$

where the measurement function for the hemisphere mass cumulative is

$$u(\{p_i\}) = \Theta\left(\rho Q - \sum_i 2(p_i \cdot n) \theta_R(p_i)\right). \quad (3.1.29)$$

In the frame where the jets are back to back along $n^\mu = (1, \vec{n})$ and $\bar{n}^\mu = (1, -\vec{n})$, the right hemisphere projector is defined by $\theta_R(p) \equiv \theta(\vec{p} \cdot \vec{n})$. Since only the hardest gluon contributes, we can treat the emissions independently and re-write the measurement function as

$$u(\{p_i\}) = \prod_i u(p_i), \quad (3.1.30)$$

where

$$u(p_1) = \Theta(\rho Q - 2p_1 \cdot n) \theta_R(p_1) + \theta_L(p_1), \quad (3.1.31)$$

and $\theta_L(p) = \theta(-\vec{p} \cdot \vec{n}) = 1 - \theta_R(p)$ is the left hemisphere projector. This will greatly simplify the calculation, and it is enough to capture the leading NGLs. For higher accuracy, the measurement function needs to be factorized into a product of terms in Laplace space, similar to the NLL calculation for the global part.

For one gluon emission, we can write the cross-section as

$$S^{(1)}(\rho) = \frac{\alpha_s}{\pi} \int W_R u(p_1) + \frac{\alpha_s}{\pi} \int W_V, \quad (3.1.32)$$

in order to write the equation in a more efficient way, we have dropped the phase space term, and rewrite the measurement function, Eq.(3.1.30) as

$$u(p_1) \equiv 1_R \theta_{1 < \rho} + 1_L, \quad (3.1.33)$$

here, 1_R means the gluon 1 goes to the right hemisphere and $\theta_{1 < \rho}$ means the contribution of gluon 1 is less than ρ . Therefore, using Eq.(3.1.16), we find the result

$$S^{(1)}(\rho) = \bar{\alpha}_s \int P_{ab}^1 (1_R \theta_{1 < \rho} + 1_L - 1) = -\bar{\alpha}_s \int P_{ab}^1 1_R \theta_{1 < \rho}, \quad (3.1.34)$$

which is the leading logarithm from the global part. For the two emissions case, we find

$$\begin{aligned} S^{(2)}(\rho) &= \bar{\alpha}_s^2 \int_{1>2} W_{RR} (1_R \theta_{1 < \rho} + 1_L) (2_R \theta_{2 < \rho} + 2_L) + \bar{\alpha}_s^2 \int_{1>2} W_{RV} (1_R \theta_{1 < \rho} + 1_L) \\ &+ \bar{\alpha}_s^2 \int_{1>2} W_{VR} (2_R \theta_{2 < \rho} + 2_L) + \bar{\alpha}_s^2 \int_{1>2} W_{VV}. \end{aligned} \quad (3.1.35)$$

In the above equation, we have assumed that gluon 1 is harder, thus $\theta_{\rho < 1} \theta_{\rho < 2} = \theta_{\rho < 2}$, we can then insert the two emission matrix element, Eq. (3.1.18)-(3.1.21), which gives the result

$$S^{(2)}(\rho) = \bar{\alpha}_s^2 \int_{1>2} 1_R 2_R \theta_{\rho < 1} \theta_{\rho < 2} P_{ab}^1 P_{ab}^2 - \bar{\alpha}_s^2 \int_{1>2} 1_L 2_R \theta_{\rho < 2} (P_{ab}^{12} - P_{ab}^1 P_{ab}^2), \quad (3.1.36)$$

the first term comes from the global part as both gluons are going right, this can also be double-checked by the calculation

$$\bar{\alpha}_s^2 \int 1_R 2_R \theta_{\rho < 1} \theta_{\rho < 2} P_{ab}^1 P_{ab}^2 = \frac{1}{2} [S^{(1)}(\rho)]^2, \quad (3.1.37)$$

which is the second-order expansion of $\exp[S^{(1)}(\rho)]$, as we expected. The factor $1/2$ comes from the symmetry factor, since there are two energy ordering for the independent emission.

The second term of Eq.(3.1.36) gives the leading non-global logarithm as

$$\begin{aligned}
S_{NG}^{(2)} &= -\bar{\alpha}_s^2 \int_{1>2} 1_L 2_R \theta_{\rho < 2} (P_{ab}^{12} - W_{ab}^1 W_{ab}^2) \\
&= -\bar{\alpha}_s^2 \int_0^Q \frac{d\omega_2}{\omega_2} \int_R \frac{d\Omega_2}{4\pi} \int_{\omega_2}^Q \frac{d\omega_1}{\omega_1} \int_L \frac{d\Omega_1}{4\pi} \Theta \left(\omega_2 - \frac{\rho Q}{2(n2)} \right) \\
&\times \left[\frac{(n\bar{n})}{(n1)(12)(2\bar{n})} + \frac{(n\bar{n})}{(n2)(21)(1\bar{n})} - \frac{(n\bar{n})}{(n1)(1\bar{n})} \frac{(n\bar{n})}{(n2)(2\bar{n})} \right] \\
&\simeq -\bar{\alpha}_s^2 \frac{\pi^2}{24} \log^2 \rho, \tag{3.1.38}
\end{aligned}$$

which is exactly the same result as Eq.(2.4.7) at large N_c limit. The above calculation can be simplified by replacing $\Theta \left(\omega_2 - \frac{\rho Q}{2(n2)} \right) \rightarrow \Theta(\omega_2 - \rho)$, because the leading non-global logarithm comes from out-of-jet soft emission, therefore the differences only contribute to sub-leading terms.

At order α_s^3 , using the same method outlined above, one finds the expression

$$\begin{aligned}
S^{(3)}(\rho) &= \bar{\alpha}_s^3 \int_{1>2>3} 1_R 2_R 3_R \theta_{\rho < 3} (-I_4) + \bar{\alpha}_s^3 \int_{1>2>3} 1_R 2_L 3_R \theta_{\rho < 3} (I_3 - I_4) \\
&+ \bar{\alpha}_s^3 \int_{1>2>3} 1_L 2_R 3_R \theta_{\rho < 3} (I_2 - I_4) \\
&+ \bar{\alpha}_s^3 \int_{1>2>3} 1_L 2_L 3_R \theta_{\rho < 3} (-I_1 + I_2 + I_3 - I_4). \tag{3.1.39}
\end{aligned}$$

In order to find the 3-loop NGLs, we have to subtract the global logarithms from Eq.(3.1.39), the result and discussion can be found in Ref. [60]. However, the calculation for 3 loops and beyond is simpler by using the BMS equation, which we will introduce in the next section.

3.2 Evolution equation: Banfi-Marchesini-Smye

In [59], Banfi, Marchesini and Smye (BMS) have proposed an evolution equation to resum the leading NGLs based on energy ordering, which is the basis of Monte Carlo simulation as we have briefly introduced in Sec. 2.5.1, where in order to derive the evolution equation each branching involves color singlet dipoles in the large N_c limit. For hemisphere jet mass, the BMS equation can be written as

$$\partial_L G_{ab}(L) = \int \frac{d\Omega_j}{4\pi} W_{ab}^j [\theta_L(j) G_{aj}(L) G_{jb}(L) - G_{ab}(L)], \tag{3.2.1}$$

the derivation is identical to the the out-of-jet energy given in [59], here W_{ab}^j is the dipole radiator factor

$$W_{ab}^j = \frac{(ab)}{(aj)(jb)}, \tag{3.2.2}$$

where we have defined $(ab) \equiv \frac{a \cdot b}{\omega_a \omega_b} = 1 - \cos \theta_{ab}$ and $\theta_L(j)$ restricts the integral to the left-hemisphere. Recall that in our configuration n^μ points to the right-hemisphere and \bar{n}^μ to the left, so

$$\cos \theta_n = -1, \cos \theta_{\bar{n}} = 1. \quad (3.2.3)$$

The solution of the BMS equation are a set of functions $G_{ab}(L)$ indexed by light-like directions a^μ and b^μ , which are equivalent to the solid angles Ω_a and Ω_b on the sphere. Moreover, these functions are evaluated at

$$L \equiv N_c \frac{\alpha_s}{\pi} \log \frac{1}{\rho}, \quad (3.2.4)$$

which give all the single (both global and non-global) logarithms of the color dipole in a^μ and b^μ directions. In particular, the hemisphere mass are given by $G_{n\bar{n}}(L)$. Furthermore, the $G_{ab}(L)$ function can be factorized into two pieces

$$G_{ab}(L) = g_{ab}(L) \exp \left[-L \int_R \frac{d\Omega_j}{4\pi} W_{ab}^j \right], \quad (3.2.5)$$

where the second term is the Sudakov form factor that accounts for global logarithms. The first term is the pure NGLs result which satisfies

$$\partial_L g_{ab}(L) = \int_L \frac{d\Omega_j}{4\pi} W_{ab}^j [U_{abj}(L) g_{aj}(L) g_{jb}(L) - g_{ab}(L)], \quad (3.2.6)$$

with

$$U_{abj}(L) = \exp \left[L \int_R \frac{d\Omega_1}{4\pi} (W_{ab}^1 - W_{aj}^1 - W_{jb}^1) \right]. \quad (3.2.7)$$

3.2.1 Perturbative expansion of the BMS equation

Now let us check the perturbative expansion of the BMS equation, and compare the integrands at 2 and 3 loops that have been derived in Sec. 3.1.2. Firstly, we write the perturbative expansion of the solution as

$$g_{ab}(L) = \sum_{n=0}^{\infty} g_{ab}^{(n)}, \quad (3.2.8)$$

with $g_{ab}^{(n)}$ proportional to L^n . We could perform the same expansion for U_{abj} , and set the first term for both of them as $g_{ab}^{(0)} = 1$ and $U_{abj}^{(0)} = 1$, due to all NGLs start at $O(\alpha_s^2)$

At order L , the expansion of function U_{abj} can be written as

$$U_{abj}^{(1)} = L \int_R \frac{d\Omega_2}{4\pi} (W_{ab}^2 - W_{aj}^2 - W_{jb}^2), \quad (3.2.9)$$

therefore one find the expansion of BMS equation at 2-loop level as

$$\partial_L g_{ab}^{(2)}(L) = L \int_L \frac{d\Omega_1}{4\pi} W_{ab}^1 \left[\int_R \frac{d\Omega_2}{4\pi} (W_{ab}^2 - W_{aj}^2 - W_{jb}^2) \right]. \quad (3.2.10)$$

Solving the above equation is pretty straightforward, since the integral has no L dependence, and one finds the result as

$$g_{ab}^{(2)}(L) = -\frac{1}{2} L^2 \int 1_L 2_R (P_{ab}^{12} - W_{ab}^1 W_{ab}^2), \quad (3.2.11)$$

where $\int 1_L 2_R = \int_L \frac{d\Omega_1}{4\pi} \int_R \frac{d\Omega_2}{4\pi}$, and the above result agrees with Eq.(3.1.38). For the perturbative expansion at 3-loop level, we need insert $U_{abj}^{(2)}$ and $g_{ab}^{(2)}$ back into the BMS equation, which gives

$$\begin{aligned} \partial_L g_{ab}^{(3)}(L) &= \frac{1}{2} L^2 \int 1_L 2_R 3_R W_{ab}^1 (W_{a1}^2 + W_{1b}^2 - W_{ab}^2) (W_{a1}^3 + W_{1b}^3 - W_{ab}^3) \\ &\quad - \frac{1}{2} L^2 \int 1_L 2_R 3_R W_{ab}^1 [(P_{a1}^{23} - W_{a1}^2 W_{a1}^3) + (P_{1b}^{23} - W_{1b}^2 W_{1b}^3) \\ &\quad - (P_{ab}^{23} - W_{ab}^2 W_{ab}^3)], \end{aligned} \quad (3.2.12)$$

which one can easily check if the above equation agrees with Eq.(3.1.39)

3.2.2 Calculation of U_{abj}

Before iterating to solve the BMS equation, it is useful to perform the calculation of U_{abj} in Eq.(3.2.7). Moreover, the explicit expression of U_{abj} would also help us unravel the symmetry of the BMS equation.

Note that in Eq.(3.2.6), the emission j is always in the left hemisphere, hence we could fix the direction in the right hemisphere to the hemisphere axis n . Thus, we only need U_{anj} and U_{abj} with both ab and j going left. Recall the dipole radiator from Eq.(3.2.2), which depends on the round bracket inner product

$$(ab) = 1 - \cos\theta_{ab} = 1 - \cos\theta_a \cos\theta_b - \cos(\phi_a - \phi_b) \sin\theta_a \sin\theta_b, \quad (3.2.13)$$

It is helpful to define the square bracket as one of the vectors that reflects the opposite hemisphere from the round bracket:

$$[ab] = (\bar{a}b) = 1 + \cos\theta_a \cos\theta_b - \cos(\phi_a - \phi_b) \sin\theta_a \sin\theta_b. \quad (3.2.14)$$

For both a and b are left, there are no collinear singularities in the angular integral and we can easily integrate the dipole radiator as

$$\int_R \frac{d\Omega_1}{4\pi} W_{ab}^1 = \frac{1}{2} \log \frac{[ab]}{2\cos\theta_a \cos\theta_b}. \quad (3.2.15)$$

Then insert all three integrals into Eq.(3.2.7), one could find the result

$$U_{abj}(L) = 2^{L/2} \cos^L \theta_j \left\{ \frac{[ab]}{[aj][jb]} \right\}^{L/2}. \quad (3.2.16)$$

Therefore, the BMS equation becomes

$$\begin{aligned} \partial_L g_{ab}(L) &= \frac{1}{4\pi} \int_0^1 d\cos\theta_j \int_0^{2\pi} d\phi_j \frac{(ab)}{(aj)(jb)} \\ &\times \left[2^{L/2} \cos^L \theta_j \left\{ \frac{[ab]}{[aj][jb]} \right\}^{L/2} g_{aj}(L) g_{jb}(L) - g_{ab}(L) \right]. \end{aligned} \quad (3.2.17)$$

When one of the directions is in the right hemisphere, the dipole radiator integral in Eq.(3.2.15) has a collinear divergence, but the U_{anj} is still finite and the result is

$$U_{anj}(L) = 2^{L/2} \cos^L \theta_j \left\{ \frac{(an)}{[aj](jn)} \right\}^{L/2}, \quad (3.2.18)$$

Therefore, one can re-write the BMS equation as

$$\begin{aligned} \partial_L g_{an}(L) &= \frac{1}{4\pi} \int_0^1 d\cos\theta_j \int_0^{2\pi} d\phi_j \frac{(an)}{(aj)(jn)} \\ &\times \left[2^{L/2} \cos^L \theta_j \left\{ \frac{(an)}{[aj](jn)} \right\}^{L/2} g_{aj}(L) g_{jn}(L) - g_{an}(L) \right]. \end{aligned} \quad (3.2.19)$$

3.2.3 Symmetries of the BMS equation

Before solving the BMS equation, let's first check the degrees of freedom of $g_{ab}(L)$ for different a and b , where the directions of a and b can be arbitrary angles (θ_a, ϕ_a) and (θ_b, ϕ_b) on the sphere. We note that $g_{ab}(L)$ can only depend on the azimuthal separation $\Delta\phi = \phi_a - \phi_b$, since there is an obvious cylindrical symmetry with respect to the hemisphere axis.

Unfortunately, the BMS equation is a non-linear integro-differential equation, which is too complicated to be solved analytically. However, it has been observed that the structure of BMS equation is formally similar to the Balitsky–Kovchegov (BK) equation, which describes the gluon saturation in high energy scattering [68, 69], and it is invariant under conformal transformation that forms the group $SL(2, \mathbb{C})$ [70]. Therefore, it is natural to look for a similar symmetry in BMS equation.

In order to unveil the symmetry of the BMS equation, it is useful to consider the change of variables by stereographic projection [71, 72]

$$z = \frac{\sin\theta}{1 + \cos\theta} e^{i\phi}. \quad (3.2.20)$$

The projection is shown in Fig. 3.2, with the stereographic transformation, the angle space (θ, ϕ) is mapped to the complex plane.

Now, we can re-write the BMS equation in terms of z . Firstly, the angle from the hemisphere axis is

$$\cos\theta = \frac{1 - |z|^2}{1 + |z|^2}, \quad (3.2.21)$$

and angular integral measures can be re-written as

$$d\Omega = d\cos\theta d\phi = \frac{4dzd\bar{z}}{(1 + |z|^2)^2}, \quad (3.2.22)$$

moreover, the round and square brackets, i.e. Eq.(3.2.13) and (3.2.14) become

$$(ij) = 2 \frac{|z_i - z_j|^2}{(1 + |z_i|^2)(1 + |z_j|^2)}, \quad (3.2.23)$$

$$[ij] = (ij) + 2 \left(\frac{1 - |z_i|^2}{1 + |z_i|^2} \right) \left(\frac{1 - |z_j|^2}{1 + |z_j|^2} \right), \quad (3.2.24)$$

thus, the measure times the radiator becomes

$$d\Omega_j W_{ab}^j = 2dzd\bar{z} \frac{|z_a - z_b|^2}{|z_a - z_j|^2 |z_j - z_b|^2}. \quad (3.2.25)$$

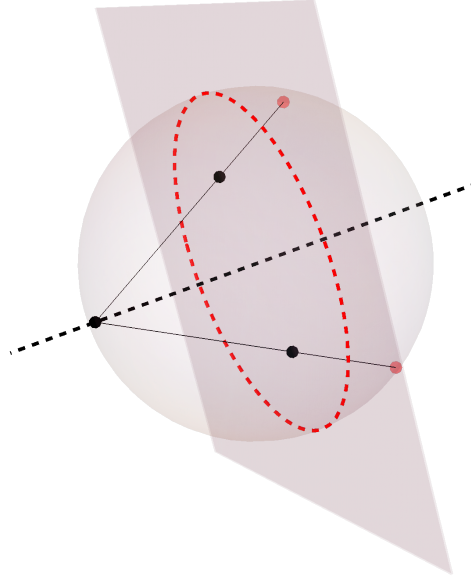


Figure 3.2. Stereographic projection of the jet directions, the angles (θ, ϕ) are measured respect to the cone axis.

Furthermore, as the angle and square brackets come from Lorentzian inner products, thus we could make use of the hyperbolic distance on the disk as

$$\langle ij \rangle = \frac{|z_i - z_j|^2}{(1 + |z_i|^2)(1 + |z_j|^2)} = \frac{(ij)}{2\cos\theta_i \cos\theta_j}. \quad (3.2.26)$$

Therefore, the brackets become

$$\langle ij \rangle = 2\cos\theta_i\cos\theta_j \langle ij \rangle, \quad [ij] = 2\cos\theta_i\cos\theta_j (1 + \langle ij \rangle). \quad (3.2.27)$$

With all the information above, plugging all of them into the BMS equation for the left-hemisphere, i.e. Eq.(3.2.17), we have

$$\begin{aligned} \partial_L g_{ab}(L) &= \frac{dzd\bar{z}}{2\pi} \frac{|z_a - z_b|^2}{|z_a - z_j|^2 |z_j - z_b|^2} \\ &\times \left\{ \left[\frac{1 + \langle ab \rangle}{(1 + \langle aj \rangle)(1 + \langle jb \rangle)} \right]^{L/2} g_{aj}(L) g_{jb}(L) - g_{ab}(L) \right\}. \end{aligned} \quad (3.2.28)$$

In this form, we can easily verify its symmetry, which is similar to BK equation. First, we note that the holomorphic half of the radiator times the measure

$$dz_j \frac{(z_a - z_b)}{(z_a - z_j)(z_j - z_b)}, \quad (3.2.29)$$

is invariant under (i) $z \rightarrow z + \lambda$, ($\lambda \in \mathbb{C}$); (ii) $z \rightarrow \lambda z$, ($\lambda \neq 0$) and (iii) $z \rightarrow -1/z$, which forms the group $\text{SL}(2, \mathbb{C})$

$$z \rightarrow z' = \frac{\alpha z + \beta}{\gamma z + \delta}, \quad \alpha\delta - \beta\gamma = 1. \quad (3.2.30)$$

The restriction of the integration region breaks this symmetry down to the subgroup $\text{SL}(2, \mathbb{R})$. Unlike in the context of the BK equation, where the symmetry is less useful because it is broken by the initial condition, the initial condition of the BMS holds the symmetry trivially as $g_{ab}(L=0) = 1$ for all a and b . Since both the equation and the initial condition are invariant under the transformation, the solution $g_{ab}(L)$ must also have this symmetry. Therefore, the solution of BMS equation only depends on the distance between a and b on the disk after the projection as

$$g_{ab}(L) = g(\langle ab \rangle, L) = g\left(\frac{1 - \cos\theta_{ab}}{2\cos\theta_i\cos\theta_j}, L\right), \quad (3.2.31)$$

this will simplify our calculation, as this reduces the three degrees of freedom of $g_{ab}(L)$ to one, i.e., $g(\theta_a, \theta_b, \Delta\phi, L) \rightarrow g(\langle ab \rangle, L)$.

3.3 Perturbative calculation of NGLs

With all the discussion and simplification in the last section, now we are ready to perform the calculation for the order-by-order result of NGLs via the perturbative expansion of BMS equation. Moreover, it is more convenient to perform the integrals over angles, since BMS equation is invariant under the stereographic projection. Thus, we can rewrite the 1-loop Sudakov factor in the exponent of Eq.(3.2.7) as

$$r_{ij} = \frac{1}{2} \log(1 + \langle ij \rangle) = \frac{1}{2} \log \frac{[ij]}{2\cos\theta_i\cos\theta_j}. \quad (3.3.1)$$

Then the BMS equation becomes

$$\partial_L g_{ab}(L) = \frac{1}{4\pi} \int_0^1 d\cos\theta_j \int_0^{2\pi} d\phi_j \frac{(ab)}{(aj)(jb)} \left[e^{L(r_{ab}-r_{aj}-r_{jb})} g_{aj}(L) g_{jb}(L) - g_{ab}(L) \right]. \quad (3.3.2)$$

Therefore, to obtain the formula to calculate the m-loop NGLs, one could expand the above equation recursively, here we only list the expression up to 4-loop:

$$\partial_L g_{ab}^{(2)}(L) = \frac{1}{4\pi} \int_0^1 d\cos\theta_j \int_0^{2\pi} d\phi_j \frac{(ab)}{(aj)(jb)} L (r_{ab} - r_{aj} - r_{jb}), \quad (3.3.3)$$

$$\begin{aligned} \partial_L g_{ab}^{(3)}(L) &= \frac{1}{4\pi} \int_0^1 d\cos\theta_j \int_0^{2\pi} d\phi_j \frac{(ab)}{(aj)(jb)} \left[\frac{L^2}{2} (r_{ab} - r_{aj} - r_{jb})^2 \right. \\ &\quad \left. + g_{aj}^{(2)}(L) + g_{jb}^{(2)}(L) - g_{ab}^{(2)}(L) \right] \end{aligned} \quad (3.3.4)$$

$$\begin{aligned} \partial_L g_{ab}^{(4)}(L) &= \frac{1}{4\pi} \int_0^1 d\cos\theta_j \int_0^{2\pi} d\phi_j \frac{(ab)}{(aj)(jb)} \left[\frac{L^3}{3!} (r_{ab} - r_{aj} - r_{jb})^3 \right. \\ &\quad \left. + L (r_{ab} - r_{aj} - r_{jb}) \left(g_{aj}^{(2)} + g_{jb}^{(2)} \right) + g_{aj}^{(3)}(L) + g_{jb}^{(3)}(L) - g_{ab}^{(3)}(L) \right], \end{aligned} \quad (3.3.5)$$

which are straightforward to solve, once the azimuthal angle integral and the polar angle integral are calculated, and the lower order NGLs are known. Detailed discussion for the calculation of azimuthal angle integrals and polar angle integrals can be found in Ref. [60].

Here, we collect the analytical results up to 3-loop, in order to check the numerical solutions that will be discussed later in this chapter. For opposite hemisphere NGLs, we have

$$\frac{1}{L^2} g_{an}^{(2)}(L) = -\frac{\pi^2}{24}, \quad (3.3.6)$$

$$\frac{1}{L^3} g_{an}^{(3)}(L) = \frac{\zeta(3)}{12}. \quad (3.3.7)$$

The results for both a and b in the left hemisphere are given by

$$\frac{1}{L^2} g_{ab}^{(2)}(L) = -\frac{1}{4} G(-1, -1; x) + \frac{1}{4} G(-1, 0; x), \quad (3.3.8)$$

$$\begin{aligned} \frac{1}{L^3} g_{ab}^{(3)}(L) &= \frac{\pi^2}{36} G(-1; x) - \frac{1}{4} G(-1, -1 - 1; x) + \frac{1}{4} G(-1, -10; x) \\ &\quad + \frac{1}{12} G(-1, 0, -1; x) - \frac{1}{12} G(-1, 0, 0; x), \end{aligned} \quad (3.3.9)$$

where we have defined $x = \langle ab \rangle$, and the function G is Goncharov polylogarithm (GPL), details about GPLs can be find in App. C.3.

Using the analytic results up to and including 4 loops, we could calculate the hemisphere NGLs to 5-loop. The result is

$$g_{n\bar{n}}(L) = 1 - \frac{\pi^2}{24} L^2 + \frac{\zeta(3)}{12} L^3 + \frac{\pi^4}{34560} L^4 + \left(\frac{17\zeta(5)}{480} - \frac{\pi^2\zeta(3)}{360} \right) L^5 + \dots, \quad (3.3.10)$$

where we recall that $L = \frac{\alpha_s}{\pi} N_c \log \frac{m_L}{m_R}$. And plots of $g_{n\bar{n}}(L)$ up to 5-loop and the ratio to Dasgupta-Salam fit are shown in Fig. 3.3, where Dasgupta-Salam fit was proposed in Ref. [6], which was obtained by fit to their Monte Carlo result:

$$g_{n\bar{n}}^{(DS)} = \exp \left[-\frac{\pi^2}{24} L^2 \frac{1 + 0.18L^2}{0.33L^{1.33}} \right]. \quad (3.3.11)$$

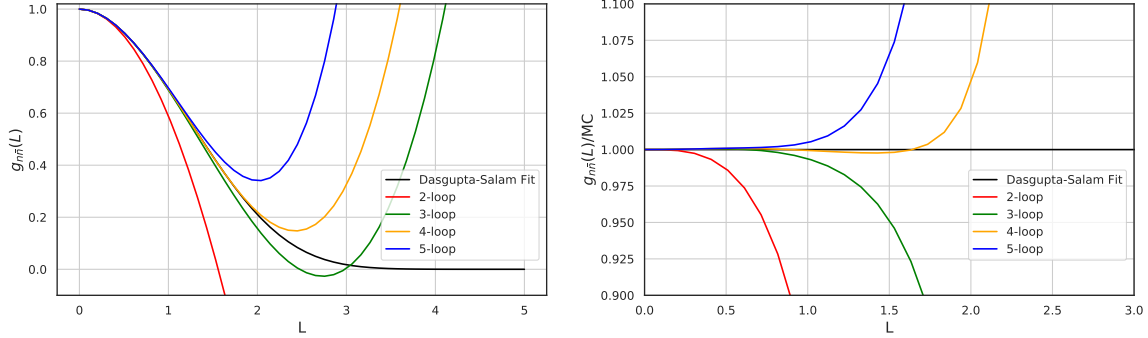


Figure 3.3. Comparisons of the fixed-order result up to 5-loop with the Dasgupta-Salam fit for the leading logarithmic resummation of the NGLs. The radius of convergence are shown in the right side

3.3.1 Partial resummed result

Following the reference [59, 60], we rewrite the BMS equation in the form

$$\partial_L g_{ab}(L) = \int_L \frac{d\Omega_j}{4\pi} W_{ab}^j g_{ab}(L) [U_{abj}(L) - 1] + \int_L \frac{d\Omega_j}{4\pi} W_{ab}^j U_{abj} [g_{aj}(L) g_{jb}(L) - g_{ab}(L)], \quad (3.3.12)$$

where the second term only contributes to NGLs start at 3-loop, and this term contains all sources of non-linear contributions. Thus, if we ignore it, the BMS equation reduces to a linear evolution equation, which is straightforward to solve. For the opposite-hemisphere case, i.e. $a = n$ and $b = \bar{n}$, we have

$$\begin{aligned} \partial_L g_{n\bar{n}}^{(2R)}(L) &= g_{n\bar{n}}^{(2R)}(L) \int_L \frac{d\Omega_j}{4\pi} W_{n\bar{n}}^j [U_{n\bar{n}j}(L) - 1] \\ &= -\frac{1}{2} (\gamma_E L + \log \Gamma(1+L)), \end{aligned} \quad (3.3.13)$$

in the second line, we have integrated with the property of the di-gamma function, the solution to this differential equation is

$$g_{n\bar{n}}^{(2R)}(L) = \exp^{-\frac{1}{2}(\gamma_E L + \log \Gamma(1+L))} = 1 - \frac{\pi^2}{24} L^2 + \frac{\zeta(3)}{6} L^3 + \dots, \quad (3.3.14)$$

the above result includes odd powers of its expansion, unlike the naive exponentiation of the 2-loop result, i.e. $g_{ab}(L) = \exp\left(-\frac{\pi^2}{24} L^2\right)$, but the partially resummed result is not particularly useful, since the 3-loop expansion is not correct as we explained before. Nevertheless, it does give us a few hints:

- This solution is similar to the solution of RGE for global logarithms [64], which is usually solved in Laplace space.
- The expansion of the partial resummed result contains half of the 3-loop leading NGL, unlike the naive expansion of the 2-loop result, which only includes odd powers of L in its expansion.
- The non-linear source term for BMS equation is separated, which can be linearized similar to the way that one recovers the Balitsky-Fadin-Kuraev-Lipatov (BFKL) equation from BK equation.

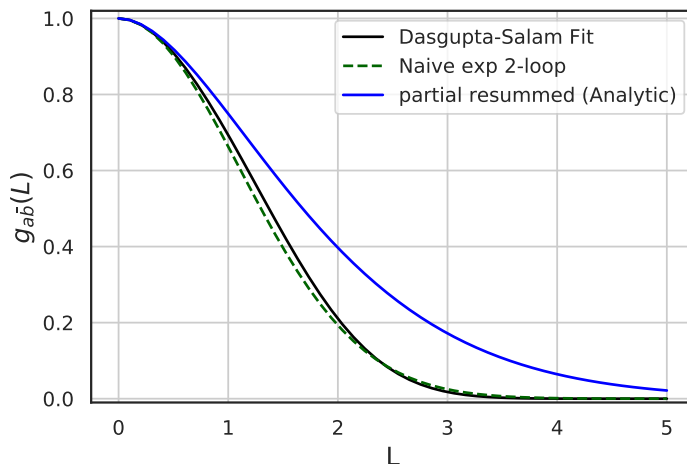


Figure 3.4. Comparison between the Dasgupta-Salam fit (black), naive exponentiation of the 2-loop result (dashed, green) and the partial resummed result (blue)

3.3.2 Dressed gluon approximation

Another alternative method to resum NGLs is the so-called dressed gluon approximation, which reorganize the degrees of freedom that contribute to NGLs into an expansion in identified soft jets, referred to as dressed gluons [61, 73]. The dressed gluon can be defined by an all-orders factorization theorem, and then resummed by renormalization group evolution, details can be found in Ref. [61]. In this section, we will focus on relating the dress gluon approximation with the various expansions proposed in the literature.

Thus instead of counting in the order of coupling, we can also perform the expansion in the number of resolved soft subjets as proposed by the dressed gluon approximation. Moreover, it is interesting to relate the dressed gluon approximation to the BMS equation, which we expand the non-global function g_{ab} by the soft object as

$$g_{ab}(L) = 1 + \tilde{g}_{ab}^{(1)}(L) + \tilde{g}_{ab}^{(2)}(L) + \dots \quad (3.3.15)$$

Insert this expansion back to the BMS equation, we find the expansion for function $\tilde{g}_{ab}^{(1)}(L)$ as

$$\partial_L \tilde{g}_{ab}^{(1)}(L) = \int_L \frac{d\Omega_j}{4\pi} W_{ab}^j [U_{abj} - 1], \quad (3.3.16)$$

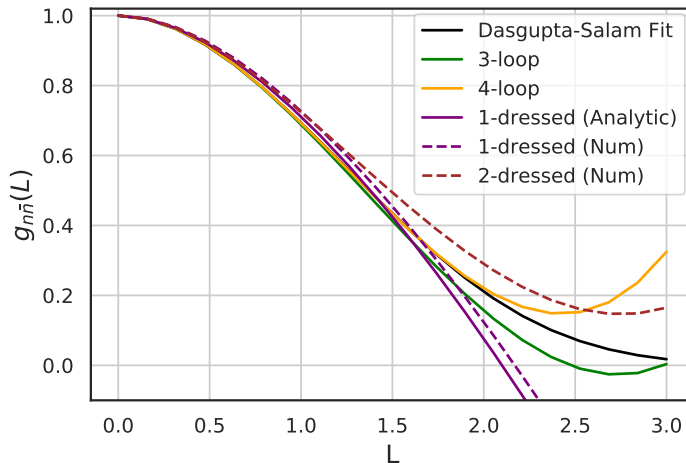


Figure 3.5. Comparison of the one- and two-dressed gluon approximation to the 3- and 4-loop fixed order results and Dasgupta-Salam fit

which is very similar to the 2-loop resummation formula, Eq.(3.3.13), but not itself exponentiated. The above equation is equivalent to the one-dressed gluon result. We can continue to perform the same method for the higher order dressed gluon expansion. The differential equation for $\tilde{g}_{ab}^{(2)}(L)$ is

$$\partial_L \tilde{g}_{ab}^{(2)}(L) = \int_L \frac{d\Omega_j}{4\pi} W_{ab}^j \left\{ U_{abj}(L) \left[g_{aj}^{(1)}(L) + g_{jb}^{(1)}(L) \right] - g_{ab}^{(1)}(L) \right\}. \quad (3.3.17)$$

Therefore, one could build up the full solution of BMS equation by continuing to include higher orders in this expansion. The numerical results for one- and two-dressed gluon are shown in Fig. 3.5, the better numerical results via neural network (NN) will be included in the next section, and then compare with the results from other approaches in the literature.

3.4 Solving differential equations with neural networks

In recent years, artificial intelligence (AI) and machine learning (ML) are developed rapidly, both within and outside academia. These modern techniques have also provided powerful tools for the study of high-energy physics. For example, the classification for discriminating the signal from the background processes based on event selection cuts [74], or the classification of complex objects such as jets, according to the radiation pattern imprints in the detector [75]. Other applications with neural networks include regress between data points [76] or identify outliers or anomalies [77].

In this section, we present a different way to use these powerful artificial neural network algorithms, namely find solutions to differential equations as an optimization task, which was proposed in Ref. [78]. This method can dramatically speed

up needed theory calculations. First, we will introduce this method with some ordinary differential equation examples. We then apply it to the calculation for the perturbative expansion of the BMS equation.

3.4.1 A brief introduction to neural networks

The artificial neural network is an algorithm designed to perform an optimization process that requires a loss function to calculate the model error. Thus, one could, in general, solve mathematical equations with the form $F(\vec{x}) = 0$ via the neural network, by defining and minimizing the loss function [79]. On the other hand, differential equations play an important role in all areas of theoretical physics. However, in practice they may not be directly solvable, i.e., do not have analytic solutions. Instead, solutions can be approximated using numerical methods. Standard numerical methods for solving differential equations include the Runge-Kutta method, linear multistep methods, finite-element methods [80].

As stated by the universal approximation theorem [81, 82]: an artificial neural network with a single hidden layer can approximate any arbitrarily complex function with enough neurons, which indicates the neural network could perform well in solving complicated mathematical expressions.

Now, we consider the feed-forward NN with n inputs, m outputs, and a single hidden layer with k units. Thus the output of this network can be written as

$$N_m(\vec{x}, \{w, \vec{b}\}) = \sum_{k,n} w_{mk}^f g(w_{mn}^h x_n + b_k^h) + b_m^f, \quad (3.4.1)$$

where g is the activation function, and h and f denote the hidden and final layer, respectively. We use the single neural network with m outputs to solve m coupled differential equation systems.

Then, the m coupled j^{th} order differential equations can be expressed as

$$F_m(\vec{x}, \phi_m(\vec{x}), \nabla \phi_m(\vec{x}), \dots, \phi_m^j(\vec{x})) = 0, \quad (3.4.2)$$

with this form, we could easily convert the problem of solving equations to an optimization procedure, where the approximate solution $\hat{\phi}_m(\vec{x})$ should minimize the square of the left-hand side of Eq.(3.4.2). Therefore, we could identify the solution as the network output, e.g. $\hat{\phi}_m(\vec{x}) \equiv N_m(\vec{x}, \{w, \vec{b}\})$.

Moreover, we include the boundary conditions as extra terms in the loss function. Thus, the domain can be discretized into a finite number of training points \vec{x}^i , and the approximate solutions $\hat{\phi}_m(\vec{x})$ could be obtained by finding the set of weights and biases $\{w, \vec{b}\}$, which the loss function is minimized. For i_{max} training examples, the loss function can be written as

$$L(\{w, \vec{b}\}) = \frac{1}{i_{\text{max}}} \sum_{i,m} F_m(\vec{x}^i, \hat{\phi}_m(\vec{x}^i), \dots, \nabla^j \hat{\phi}_m(\vec{x}^i))^2 + \sum_{BC} \left(\nabla^j \hat{\phi}_m(\vec{x}_b) - K(\vec{x}_b) \right)^2, \quad (3.4.3)$$

where the second term represents the squares of the boundary conditions at the boundary \vec{x}_b . Thus the task is then to minimize the loss function $L(\{w, \vec{b}\})$ in the neural network.

3.4.2 Ordinary differential equation examples

To show how well this novel approach can solve ordinary differential equation (ODE), first, we apply it to the first and second-order ODE, which the analytic solutions are known. The equations are

$$\frac{d\phi}{dx} + \left(x + \frac{1 + 3x^2}{1 + x + x^3} \right) \phi - x^3 - 2x - x^2 \frac{1 + 3x^2}{1 + x + x^3} = 0, \quad (3.4.4)$$

with the boundary condition $\phi(0) = 1$ in the domain $x \in [0, 2]$, and

$$\frac{d^2\phi}{dx^2} + \frac{1}{5} \frac{d\phi}{dx} + \phi + \frac{1}{5} e^{-\frac{x}{5}} \cos x = 0, \quad (3.4.5)$$

with boundary conditions $\phi(0) = 0$ and $\frac{d}{dx}\phi(0) = 0$ in the domain $x \in [0, 2]$.

For the neural network architecture, we chose a single hidden layer of 10 units with sigmoid activation functions. Then, we just need to pass the differential equations and boundary conditions to the loss function, as described in Eq.(3.4.3), and proceed with the optimization procedure. In Fig. 3.6, the results of the neural network output are shown, compared to the analytic solutions of Eq.(3.4.4) and Eq.(3.4.5), where the numerical difference between the numerical and analytic solutions are shown in the bottom panel.

Instead of solving the second-order ODE example directly. We reduce the second-order equation to two first order ODE simply by define $\psi = \frac{d\phi}{dx}$, and rewrite the loss function and optimize it with two neural network output, we get the same result as have shown in Fig. 3.6. In general, we could extend to solving coupled non-linear differential equations with no analytic solution, which is exactly the same task that we need to perform, in order to resum the leading NGLs via BMS equation, more details will be discussed at the end of this chapter.

3.4.3 Structure of BFKL equation

As we have pointed out in Sec. 3.3.1, one could extend the partial resummed equation with the corrections from the non-linear terms, where the linearization of the non-linear source term should have the same structure of BFKL equation. In this section, we will discuss the BFKL kernel's contribution to the BMS equation. The structure of BFKL like equation will also be introduced, following the discussion in Ref. [83].

To begin with, let us recall the second term of Eq.(3.3.12), which contains all the non-linear behaviour of BMS equation. We can linearize the BMS equation by rewrite $g_{ij} = 1 - x_{ij}$ and drop the non-linear terms, which should contain

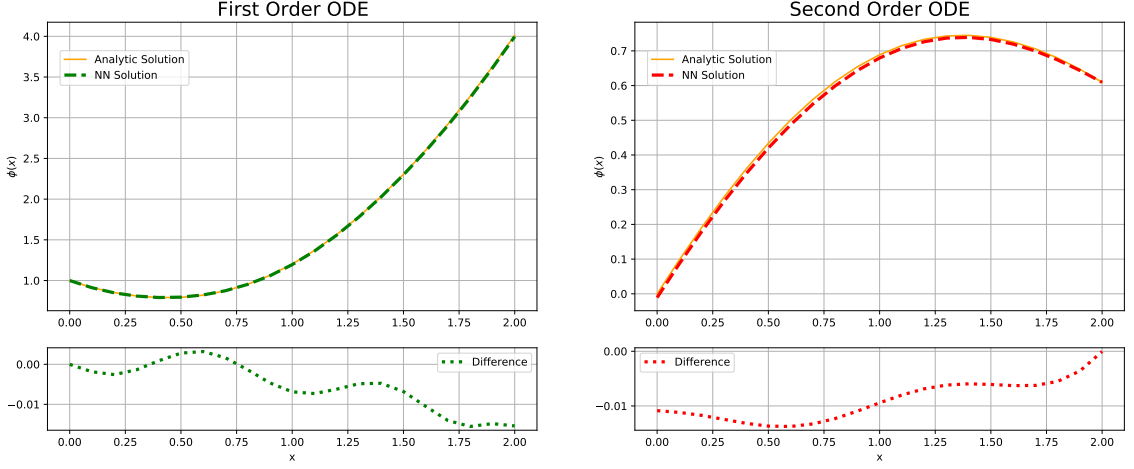


Figure 3.6. The solutions to the first and second-order of Eq.(3.4.5) and Eq.(3.4.5), and the bottom panel shows the numerical difference between the analytic solution and NN prediction

more information than the partially resummed approach. Thus, we can define the second term after linearization as

$$B(x_{ab}; J) = \int_J \frac{d\Omega_j}{4\pi} W_{ab}(j) (x_{aj} + x_{jb} - x_{ab}), \quad (3.4.6)$$

when $J = S^2$, i.e. integrate over the whole celestial sphere, then it is conformally related to the position space form of the kernel of the BFKL equation. In the bracket, the first two terms originate from emission out of aj and jb dipoles from the branching of the parent ab dipole, and the last term comes from the virtual corrections.

In Ref. [83], an evolution equation for heavy quark-antiquark pair multiplicity was discussed for resumming soft logarithms

$$\partial_\tau I(\rho_{ab}, \tau) = \int \frac{d\Omega_j}{2\pi} \frac{\rho_{ab}}{\rho_{aj}\rho_{jb}} [I(\rho_{aj}, \tau) + I(\rho_{jb}, \tau) - I(\rho_{ab}, \tau)], \quad (3.4.7)$$

with $\rho_{ab} = \frac{1}{2}(1 - \cos\theta_{ij})$, which have similar structure as Eq.(3.4.6). For simplicity, we replace $\rho_{ab} \rightarrow \rho$, $\rho_{aj} \rightarrow \rho_1$ and $\rho_{jb} \rightarrow \rho_2$. The dipole radiator factor can be written as

$$\frac{\rho}{\rho_1\rho_2} = \frac{1}{\rho_1} + \frac{1}{\rho_2} + \frac{\rho - \rho_1 - \rho_2}{\rho_1\rho_2}, \quad (3.4.8)$$

where the last term regulates the kernel for both $\rho_1 \rightarrow 0$ and $\rho_2 \rightarrow 0$, and the evolution equation becomes

$$\partial_\tau I(\rho, \tau) = \int \frac{d\Omega_j}{2\pi} \left\{ \frac{2}{\rho_2} \left[\frac{\rho}{\rho_1} I(\rho_1, \tau) - I(\rho, \tau) \right] - \frac{\rho - \rho_1 - \rho_2}{2\rho_1\rho_2} I(\rho_1, \tau) \right\}. \quad (3.4.9)$$

With the help of

$$\int \frac{d\Omega_j}{2\pi} \frac{2}{\rho_2} = \int_0^1 \frac{d\rho_1}{|\rho_1 - \rho|}, \quad \int \frac{d\Omega_j}{2\pi} \frac{\rho - \rho_1 - \rho_2}{\rho_1\rho_2} = - \int_0^1 \frac{d\rho_1}{\rho_1}, \quad (3.4.10)$$

one could write the evolution equation as

$$\partial_\tau I(\rho, \tau) = \int_0^1 \frac{d\rho_1}{|\rho_1 - \rho|} \left[\frac{\rho}{\rho_1} I(\rho_1, \tau) - I(\rho, \tau) \right] + \int_0^1 \frac{d\rho_1}{\rho_1} I(\rho, \tau), \quad (3.4.11)$$

and if one neglects the lower bound in the second integral, the equation is formally the same as the BFKL equation. This form is also desired for our purpose for exploiting the solution of BMS equation with the invariant distance $\langle ab \rangle$. We leave this study for future work.

3.4.4 Numerical results for NGLs

With all the discussions above, now we are ready to solve the BMS equation with the artificial neural network. The only thing left is the integration part of BMS equation, where the analytical solution doesn't exist, thus we need to solve it numerically. The numerical integration could, in general, be performed by the Autograd function in Pytorch. However, for simplicity, here we only solve it with the finite difference method (FDM).

To start with, let us solve the fixed-order expansion with the FDM, where the fixed order expansion up to 4-loop can be written as

$$\partial g_{ab}^{(2)}(L) = \int_L \frac{d\Omega_j}{4\pi} W_{ab}^j U_{abj}^{(1)}(L), \quad (3.4.12)$$

$$\begin{aligned} \partial g_{ab}^{(3)}(L) &= \int_L \frac{d\Omega_j}{4\pi} W_{ab}^j U_{abj}^{(2)}(L) \\ &+ \int_L \frac{d\Omega_j}{4\pi} W_{ab}^j \left[g_{aj}^{(2)}(L) + g_{jb}^{(2)}(L) - g_{ab}^{(2)}(L) \right], \end{aligned} \quad (3.4.13)$$

$$\begin{aligned} \partial g_{ab}^{(4)}(L) &= \int_L \frac{d\Omega_j}{4\pi} W_{ab}^j U_{abj}^{(3)}(L) + \int_L \frac{d\Omega_j}{4\pi} W_{ab}^j U_{abj}^{(1)}(L) g_{ab}^{(2)}(L) \\ &+ \int_L \frac{d\Omega_j}{4\pi} W_{ab}^j U_{abj}^{(1)}(L) \left[g_{aj}^{(2)}(L) + g_{jb}^{(2)}(L) - g_{ab}^{(2)}(L) \right] \\ &+ \int_L \frac{d\Omega_j}{4\pi} W_{ab}^j \left[g_{aj}^{(3)}(L) + g_{jb}^{(3)}(L) - g_{ab}^{(3)}(L) \right], \end{aligned} \quad (3.4.14)$$

where in each order, the first term comes from the expansion of the partial re-summed formula, and the second term is linearized from Eq.(3.3.12). In practice, when solving the above equations numerically, one registers the values of the solution for all discretized points in the plane (\vec{x}_a, \vec{x}_b) at each step of iteration. However, as noted in Sec. 3.2.3, the solution of BMS equation, i.e. $g_{ab}(L)$, only depends on the invariant distance $\langle ab \rangle$. Thus, this symmetry reduces the four degrees of freedom (Ω_a, Ω_b) to one, which means the simple solution of $g_{\vec{n}b}$ tells the value of g for an arbitrary direction of a and b . Therefore, we only need to discretize the angle into n_θ and n_ϕ bins and solve the equation by summing the integrand with step size $\Delta L = L/n_L$.

For fixed-order expansion beyond 4-loop, non-linear behavior will start to contribute. The full numerical solution is still under development, but with the help of

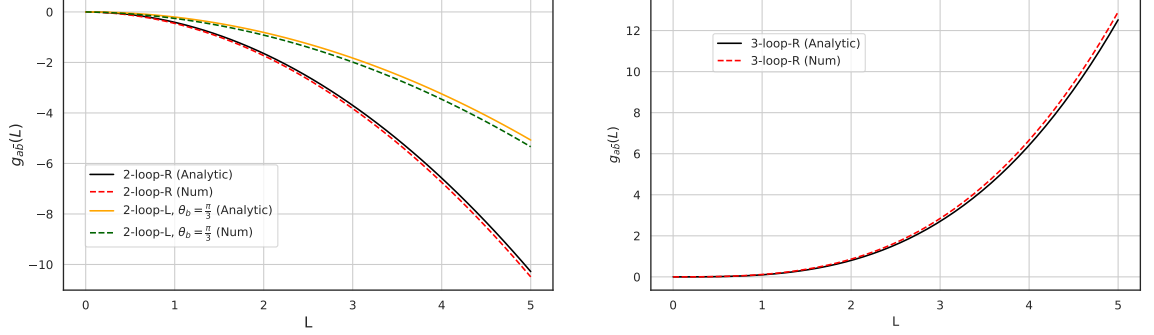


Figure 3.7. Numerical solutions to the 2- and 3-loop expansion of BMS equation, and compare with the analytical solutions in Eq. (3.3.6)-(3.3.9)

the analytical solution in Ref. [60], we could get the numerical result with arbitrary a and b up to 7-loop level, where the iteration formula can be written as

$$\begin{aligned} \partial g_{ab}^{(i+1)}(L) = & \int_L \frac{d\Omega_j}{4\pi} W_{ab}^j U_{abj}^{(i)}(L) + \sum_{k=1}^{k<i} \int_L \frac{d\Omega_j}{4\pi} W_{ab}^j U_{abj}^{(k)}(L) g_{ab}^{(i-k)}(L) \\ & + \sum_{k=1}^{k<i} \int_L \frac{d\Omega_j}{4\pi} W_{ab}^j U_{abj}^{(k-1)}(L) \left[g_{aj}^{(i-k+1)}(L) + \right. \\ & \left. + g_{jb}^{(i-k+1)}(L) - g_{ab}^{(i-k+1)}(L) + \sum_{l=1}^{l<i-k-1} g_{aj}^{(i-k-l)} g_{jb}^{(l+1)} \right]. \end{aligned} \quad (3.4.15)$$

It is also interesting to improve the partial resummed result with the corrections from the non-linear term in Eq. (3.3.12), which is similar to the matching of resummation to fixed-order result. There are different matching schemes proposed in the literature, two of the widely used schemes are R -matching and the $\log(R)$ -matching [84,85], where the $\log(R)$ -matching scheme is believed to be theoretically the most stable [85], results for the $\log(R)$ -matching are shown in Fig. 3.8, where the radius of convergence is improved with higher loop matching.

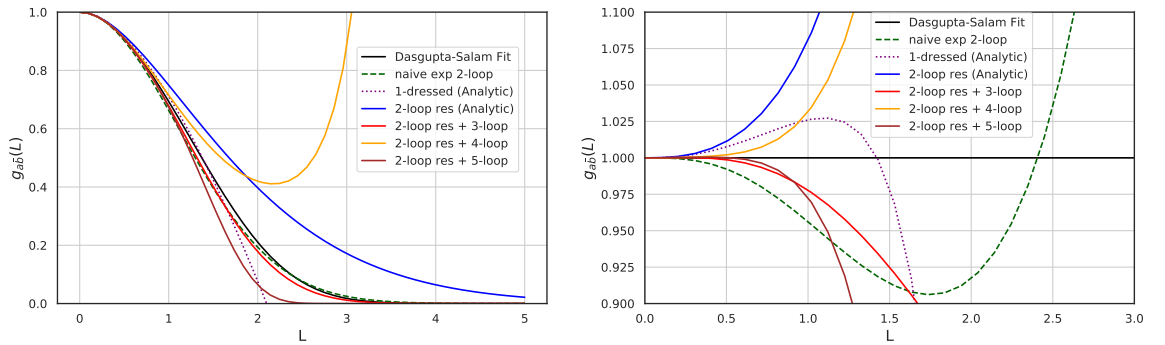


Figure 3.8. Comparisons of the matched result with the Dasgupta-Salam fit, naive exponentiation of the 2-loop result and the dressed gluon approach, with the ratio to the MC fit shown in the right side

Now we could come back to the neural network approach, since we have just double-checked the numerical calculation for the integration part with the FDM. Thus we only need to insert the numerical solution of the integration back to Pytorch. Here, we apply it to the dressed-gluon calculation, the results are shown in Fig. 3.9, which the accuracy has improved compared to Fig. 3.5. We could also apply this method to the fixed-order calculation with the iteration of the differential equation, similar to the one we derived in Eq.(3.4.15).

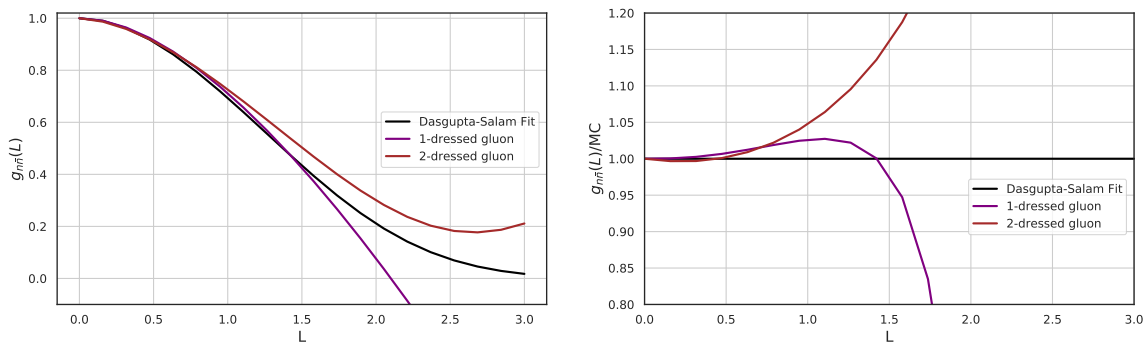


Figure 3.9. Neural network approach for one- and two-dressed gluon calculation, with the ratio to the MC fit shown in the right side

3.4.5 Plan for next steps

As a first step to finish this project, we would like to solve the fixed-order expansion of BMS equation up to 8-loops and comparing results with exiting literature [73]. Since our method is essentially a combination of linearized BMS equation and the analytic results up to 4-loop order, thus we want to determine the impact of the non-linear term in BMS equation by exploring the difference with the fixed-order expansion of the linearized BMS equation. Then, we could perform the full numerical calculation for the fixed-order expansion of BMS equation.

Furthermore, we could also apply the neural network method to perform the numerical resummation of the leading NGLs, i.e. solve the full BMS equation numerically, and again this could be achieved by fully discretize the BMS equation, which transforms the task of solving a non-linear integro-differential equation, to n coupled differential equations.

The plan for the future study include exploring the relation between BMS and BK equation (include the corresponding linearized version) and describing the evolution of next-to-leading NGLs at finite N_c . More details will be explained in Sec. 5.2.

4 Probing color Flow with Jet Substructure

Contents

4.1	Seeing in color: jet superstructure	87
4.1.1	color flow	88
4.1.2	Jet pull and its projections	89
4.2	Curiosities: Sudakov safety	92
4.2.1	IRC-unsafe observables	92
4.2.2	Application: ratio of angularities	92
4.2.3	Safe companion of the pull angle	94
4.3	Theory predictions for the pull angle	95
4.3.1	Fixed-order calculation	96
4.3.2	Resummed results	99
4.3.3	Pull angle distribution	102
4.4	Safe projections of jet pull	105
4.4.1	Analog from a_T distribution	106
4.4.2	Global logarithms at NLL accuracy	107
4.4.3	Non-global logarithms	109
4.4.4	Resummed results	111
4.4.5	Towards phenomenology	113
4.5	Azimuthal asymmetry	118
4.5.1	Definition of the asymmetries	119

Understanding color flow in hard scattering processes plays an important role in high-energy physics. For instance, it can provide a powerful handle to distinguish the hadronic decay products of color singlets in the final state. This is particularly important in the $H \rightarrow b\bar{b}$ case. A powerful observable that was designed to probe color flow is jet pull, which was originally proposed in Ref. [86]. In this chapter, we present predictions from first-principle QCD for the jet pull and its derivative quantities.

4.1 Seeing in color: jet superstructure

Determining the color representation of a jet is highly non-trivial because the color quantum numbers that are carried by quarks and gluons are not directly

observable in experiments. The color representation must be inferred through its effect on kinematic distributions. A powerful observable that is sensitive to the color representation is called jet pull, which was originally proposed in Ref. [86].

In this chapter, we present the theoretical predictions of jet pull for measure QCD radiation pattern in the signal events, i.e. color-singlet decaying in two jets. The pull angle observable is particularly sensitive to color flow. However, unlike the most theoretically studied observables in high energy physics, the pull angle lacks the property of IRC safety, and so its distribution cannot be calculated in fixed-order perturbation theory.

4.1.1 color flow

As we have derived the Feynman rule for QCD in App. B.1, the underlying theory of QCD appears to be very similar to that of QED, The QED interaction is mediated by a massless photon corresponding to the single generator of the $U(1)$ local gauge symmetry, while QCD is mediated by eight massless gluons corresponding to the adjoint representation of $SU(3)$ local gauge symmetry. The single charge of QED is replaced by three color charges, r , g and b . Moreover, only particles that have non-zero color charge couple to gluons. In general, we could extend the symmetry of QCD to $SU(N_c)$.

In this section, we introduce the color flow by the Feynman rule for color flow based on color decomposition, which is widely used for the calculation of multiparton amplitudes. Amplitudes involving multiple quarks and gluons are difficult to calculate even at the tree level. One technique that has been developed to calculate these amplitudes efficiently is the systematic organization of the $SU(N)$ color algebra. To be specific, let us consider the amplitude of n gluons with colors a_1, \dots, a_n . At tree level, the amplitude can be decomposed as [87]

$$M(n_g) = \sum_{perm(2, \dots, n)} Tr(\lambda^{a_1} \dots \lambda^{a_n}) A(1, \dots, n), \quad (4.1.1)$$

where λ^a is the fundamental representation of $SU(N)$, and the sum is over the $(n-1)!$ permutations of $(2, \dots, n)$, and A is called the partial amplitude, depending on the four momenta and the polarization vectors of the n gluons.

Here, we treat the $SU(N)$ gluon field as $N \times N$ matrix $(A_\mu)_j^i$ with $i, j = 1, \dots, n$, instead of one-index field A_μ^a with $a = 1, \dots, N^2 - 1$. The n -gluon amplitude can be decomposed as [88]

$$M(n_g) = \sum_{perm(2, \dots, n)} \delta_{j_2}^{i_1} \dots \delta_{j_1}^{i_n} A(1, \dots, n), \quad (4.1.2)$$

where the upper indices transform under the fundamental representation, and the lower indices under the anti-fundamental representation. Moreover, the $SU(N)$ symmetry implies that color is conserved at the interaction vertices, similar to the electric charge is conserved at the QED vertex. Thus, the interaction vertex can be

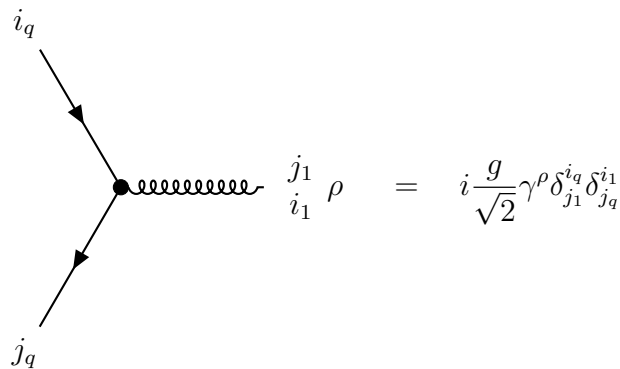


Figure 4.1. Color-flow Feynman rules for quark-gluon vertex

represented by the color-flow Feynman rule, for example, the quark-gluon vertex color-flow Feynman is shown in Fig. 4.1.

Now for a more physical picture, let us consider the main decay mode of an on-shell Higgs at the LHC, i.e. Higgs decay to bottom quarks ($H \rightarrow b\bar{b}$). Since the Higgs boson is a color singlet, the color factor in the matrix element at leading order has the form of $\delta_{j_q}^{i_q}$. The color string or dipole is shown in the left side of Fig. 4.2. This signature suffers from the huge QCD background $g \rightarrow b\bar{b}$, and there are two possible color connections, in both cases the outgoing quark connects the beam, as shown on the right side of Fig. 4.2. The color string picture treats gluons as bifundamentals, which is correct in the large N_c limit, and the sub-leading color corrections should contribute to $1/N_c^2$ 10% effect. The sub-leading color correlations will briefly be introduced in the next chapter.

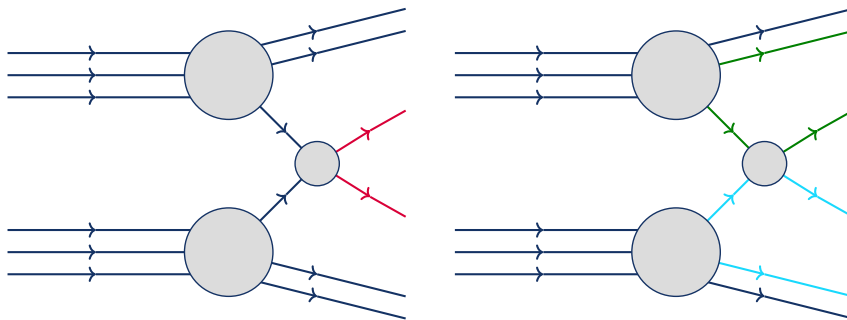


Figure 4.2. Possible color connections for signal ($p\bar{p} \rightarrow H \rightarrow b\bar{b}$) and for background ($p\bar{p} \rightarrow g \rightarrow b\bar{b}$)

4.1.2 Jet pull and its projections

Since the color flow is physical, it may be possible to extract the color connections from the jet substructure, and this would help temper the background for the color singlet process. Therefore, mapping the jet substructure for the color connections of the events can help us discriminate short-distance physics.

To extract the color connections, we must use information from the distribution of the observable hadrons. We can test this idea using a parton shower simulation [89–92]. The radiation pattern for events with $b\bar{b}$ in the final state, where quarks are color-connected to each other (signal) versus the final state quark color-connected to the beam (background) are shown in Fig. 4.3. More details about the simulation can be found in Ref. [86].

The parton shower simulation indicates that the radiation on each end of a color dipole is being pulled towards the other end of the dipole. Thus one could construct a jet shape for dijet events, shown in Fig. 4.4.

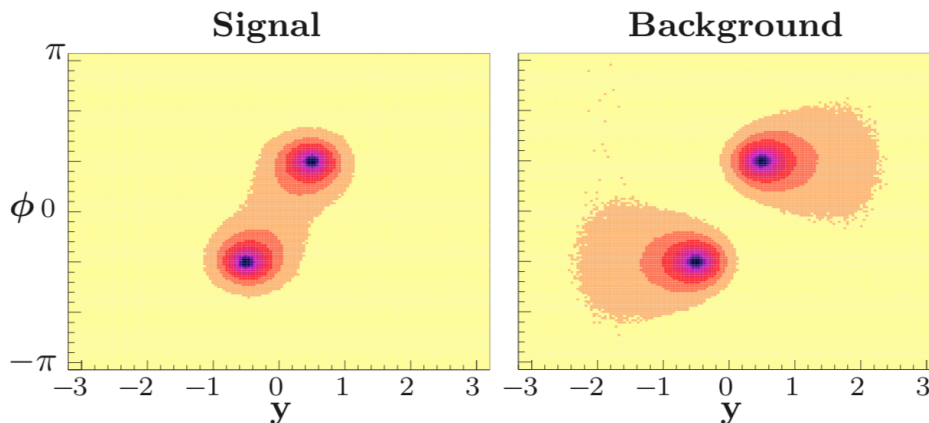


Figure 4.3. The radiation pattern from the parton shower simulation, for the b and \bar{b} color-connected to each other (left) and the b and \bar{b} color-connected to the beam (right), plot taken from [Gallicchio, Schwartz, 1001.5027]

Pull is a two-dimensional vector that points in the direction of dominant energy flow about a jet of interest that is particularly useful for determining if two jets form a color-singlet dipole, i.e. whether they originate from the decay of resonance that carries no color, such as an electro-weak boson. In a color-singlet dipole, emissions lie between the ends of the dipole; therefore the pull vector would point along the line that connects the momentum vectors of the jets.

The original expression of the pull vector \vec{t} from [86] was defined in the plane of rapidity y and azimuthal angle ϕ . The expression for the pull vector is

$$\vec{t} = \sum_{i \in J} \frac{p_{\perp i} |\vec{r}_i|^2}{p_{\perp J}} \hat{r}_i, \quad (4.1.3)$$

where p_i is the transverse momentum of the i^{th} particle in the jet J of interest. The vector \vec{r}_i is the relative rapidity and azimuthal angle of the particle from the jet axis:

$$\vec{r}_i = (y_i - y_J, \phi_i - \phi_J). \quad (4.1.4)$$

As a weighted sum of particle locations, the pull vector points from the jet axis in the direction of dominant energy flow. In this form, the pull vector is expressed in

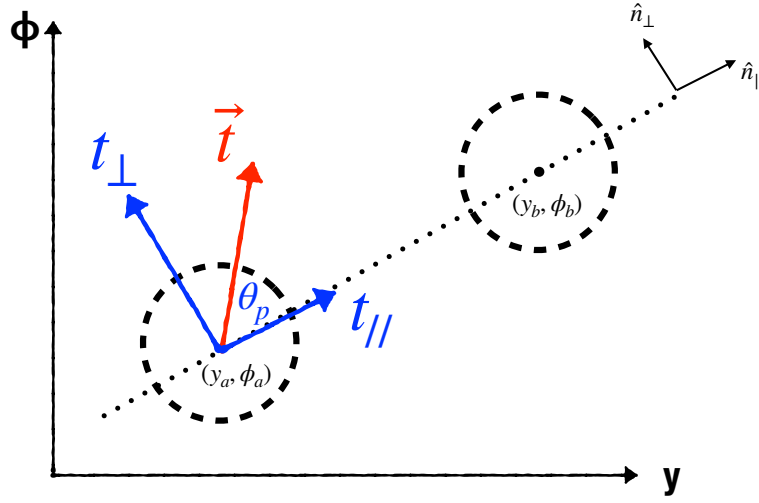


Figure 4.4. Pull vector of jet a and its projections in the rapidity (y) and azimuth (ϕ) plan, which are defined with respect the jet b.

coordinates natural at a hadron collider and has been used for the measurements at DØ and ATLAS, and for searches at CMS [93–97].

Moreover, we find it useful to introduce two unit vectors

$$\begin{aligned}\hat{n}_{\parallel} &= \frac{1}{\sqrt{\Delta y^2 + \Delta \phi^2}}(\Delta y, \Delta \phi) = (\cos \beta, \sin \beta), \\ \hat{n}_{\perp} &= \frac{1}{\sqrt{\Delta y^2 + \Delta \phi^2}}(-\Delta \phi, \Delta y) = (-\sin \beta, \cos \beta),\end{aligned}\quad (4.1.5)$$

where $\Delta y = y_b - y_a$ and $\Delta \phi = \phi_b - \phi_a$, as depicted in Fig. 4.4. The angle β has been introduced for future convenience. We now introduce two projections of the pull vector in the two directions identified by the unit vectors above:

$$t_{\parallel} = |\vec{t} \cdot \hat{n}_{\parallel}| \quad \text{and} \quad t_{\perp} = |\vec{t} \cdot \hat{n}_{\perp}|. \quad (4.1.6)$$

We will come back to the role of the absolute value in the expressions above in Section 4.4. Furthermore, we note that the magnitude of the pull vector can be expressed as

$$t = |\vec{t}| = \left| \frac{1}{p_{ta}} \sum_{i \in J} p_{ti} |\vec{r}_i|^2 \hat{r}_i \right| = \sqrt{t_{\parallel}^2 + t_{\perp}^2}, \quad (4.1.7)$$

while the pull angle can be written as

$$\theta_p = \cos^{-1} \frac{\vec{t} \cdot \hat{n}_{\parallel}}{t}. \quad (4.1.8)$$

It is easy to check that the pull magnitude t and the two projections t_{\parallel} and t_{\perp} are IRC safe observables. However, this property is lost when considering the pull angle, essentially because θ_p does not vanish in the presence of a single soft emission because the ratio t_{\parallel}/t is undetermined.

4.2 Curiosities: Sudakov safety

To date, IRC safety has been a key guiding principle for constructing observables, for which the virtual and real diagrams consistently combine according to the KLN theorem, thus yielding finite physical cross-sections order-by-order in perturbation theory. However, there are interesting observables in collider physics that are not IRC safe, which means they can not be defined at any fixed order in α_s , yet have a finite cross-section when the all-orders effects are included.

In this section, we present an explicit method to calculate the cross-section for IRC unsafe observables with the help of all-order resummation, then apply this method to the ratio of two angularities with different angular exponents, as an example.

4.2.1 IRC-unsafe observables

To begin with, consider an IRC unsafe observable u and its safe companion observable s , where the safe companion is chosen so that it regulates all singularities of u . This means, despite the probability of measuring u ,

$$p(u) = \frac{1}{\sigma} \frac{d\sigma}{du}, \quad (4.2.1)$$

is ill-defined at any order of the perturbative expansion, the conditional probability of measuring u given s , $p(u|s)$ is finite at all orders for $s \neq 0$. Moreover, because s is IRC safe, $p(s)$ is well-defined in any fixed-order and further can be calculated in resummed perturbation theory. This allows us to define the joint probability distribution

$$p(s, u) = p(s) p(u|s), \quad (4.2.2)$$

which is also finite at all perturbative orders. We then define

$$p(u) = \int ds p(s) p(u|s), \quad (4.2.3)$$

and if $p(s)$ regulates all singularities of $p(u|s)$, which ensure the above integral is finite, then we say u is Sudakov safe [37]. The perturbative Sudakov form factor exponentially suppresses the singular region of phase space.

4.2.2 Application: ratio of angularities

The first example of Sudakov safe observable discussed in the literature is the ratio of angularities [98], where the jet angularities are defined as

$$e_\alpha = \frac{1}{E_J} \sum_{i \in J} E_i \theta_i^\alpha. \quad (4.2.4)$$

Angularities are IRC safe for $\alpha > 0$, and the angle θ_i is measured with respect to an appropriately chosen jet axis. Moreover, the angularities represent a broad

class of IRC safe observables that are linear in the energy of each particle and weighted by positive powers of angles between them, these include thrust and jet mass.

Now, we consider the ratio observable formed by two different angularities measured on the same jet:

$$r_{\alpha,\beta} = \frac{e_\alpha}{e_\beta}, \quad (4.2.5)$$

and we choose the angular exponents $\alpha > \beta$, therefore $r_{\alpha,\beta} \in [0, 1]$. Moreover, the ratio of two IRC safe observables are not generically IRC safe, as both e_α and e_β go to zero in the region where radiation is soft or/and collinear with respect to the jet axis, but the ratio $r_{\alpha,\beta}$ can be arbitrary.

While the ratio $r_{\alpha,\beta}$ is not IRC safe, it is Sudakov safe. Therefore we could apply the joint probability method. For simplicity, in this section, we only compute the LL resummed cross-section of the ratio $r_{\alpha,\beta}$ by marginalizing the resummed double differential distribution of angularities:

$$\frac{d\sigma}{dr_{\alpha,\beta}} = \int de_\alpha de_\beta \frac{d^2\sigma}{de_\alpha de_\beta} \delta\left(r_{\alpha,\beta} - \frac{e_\alpha}{e_\beta}\right), \quad (4.2.6)$$

the Sudakov form factor in the double differential distribution provides exponential suppression of the singular region of phase space. We could also generalize this to a class of ratio observables $r = a/b$, therefore we can rewrite the above equation as

$$p(r) = \int da db p(a, b) \delta\left(r - \frac{a}{b}\right), \quad (4.2.7)$$

where a and b are IRC safe but r is not, as r is ill defined for $b = 0$ at every perturbative order. Integrating over a , one could find the result

$$p(r) = \int db p(b) p(r|b), \quad (4.2.8)$$

where we have used the definition of conditional probability, and r is Sudakov safe because of the all-orders Sudakov form factor from the safe companion $p(b)$.

In order to emphasize some features of the IRC unsafe observable, we perform the LL resummation in the strongly-ordered limit. In this limit, there are multiple emissions, but the value of the observable is determined by the leading emissions. Moreover, because the double differential cross-section is IRC safe, one can easily determine the LL distribution from the Lund diagram, as we have introduced in Sec. 2.1.3

$$\Delta(e_\alpha, e_\beta) = e^{-\frac{\alpha_s}{\pi} C_F \left(\frac{1}{\beta} \log^2 e_\beta + \frac{1}{\alpha - \beta} \log^2 \frac{e_\alpha}{e_\beta} \right)}, \quad (4.2.9)$$

where the Sudakov form factor at LL is directly obtained by calculating the forbidden region in the phase space. Thus, we get resummed double differential cross

section by differentiating with respect to e_α and e_β

$$\begin{aligned} \frac{d^2\sigma^{LL}}{de_\alpha de_\beta} &= \frac{\partial}{\partial e_\alpha} \frac{\partial}{\partial e_\beta} \Delta(e_\alpha, e_\beta) \\ &= \left(\frac{2\alpha_s}{\pi} \frac{C_F}{\alpha - \beta} \frac{1}{e_\alpha e_\beta} + \frac{4\alpha_s^2}{\pi^2} \frac{C_F^2}{\beta(\alpha - \beta)^2} \frac{1}{e_\alpha e_\beta} \log \frac{e_\beta}{e_\alpha} \log \frac{e_\beta^\alpha}{e_\alpha^\beta} \right) \Delta(e_\alpha, e_\beta). \end{aligned} \quad (4.2.10)$$

We also note that the Sudakov factor suppresses the singular region of the phase space at $e_\alpha \rightarrow 0$, $e_\beta \rightarrow 0$. Finally, we can obtain the differential cross section for the ratio observable $r_{\alpha,\beta}$ by inserting the above result back to Eq. (4.2.6), and for clarity, we have dropped the subscripts as $r_{\alpha,\beta} \rightarrow r$

$$\begin{aligned} \frac{d\sigma^{LL}}{dr} &= \frac{\sqrt{\alpha_s C_F \beta}}{\alpha - \beta} \frac{1}{r} \left(1 - 2 \frac{\alpha_s}{\pi} \frac{C_F}{\alpha - \beta} \log^2 r \right) \left(\operatorname{erf} \left[\frac{\sqrt{\alpha_s C_F \beta}}{\sqrt{\pi}(\alpha - \beta)} \log r \right] + 1 \right) e^{-\frac{\alpha_s}{\pi} \frac{C_F}{\alpha - \beta} \log^2 r} \\ &\quad - 2 \frac{\alpha_s}{\pi} \frac{C_F}{\alpha - \beta} \frac{\log r}{r} e^{-\frac{\alpha_s}{\pi} C_F \frac{\alpha}{(\alpha - \beta)^2} \log^2 r}, \end{aligned} \quad (4.2.11)$$

in the above equation, we have used the error function defined as:

$$\operatorname{erf}(x) = \frac{2}{\sqrt{\pi}} \int_0^x dt e^{-t^2}. \quad (4.2.12)$$

Moreover, expanding the above LL resummed result, we find

$$\frac{d\sigma^{LL}}{dr} = \sqrt{\alpha_s C_F} \frac{\sqrt{\beta}}{\alpha - \beta} \frac{1}{r} + O(\alpha_s), \quad (4.2.13)$$

which starts at $O(\sqrt{\alpha_s})$, as the ratio observables do not have a valid fixed-order expansion. Generically, this conclusion could extend to IRC unsafe observables, and more examples will be discussed later in this chapter.

4.2.3 Safe companion of the pull angle

We now come back to the jet pull \vec{t} , which is a two-dimensional vector defined by the magnitude t and angle ϕ_p . The angle measured with respect to the line connecting the momentum vectors of the two jets, ϕ_p is the pull angle observable. The pull vector magnitude t is itself IRC safe, and so can be calculated to any fixed-order. While the pull angle ϕ_p is not IRC safe, the problematic region of phase space is localized to $t = 0$, where the complete cross-section vanishes anyway. This motivates the calculation of the distribution of the pull angle $p(\phi_p)$ by the marginalization of a joint probability distribution of t and ϕ_p :

$$p(\phi_p) = \int dt p(t, \phi_p), \quad (4.2.14)$$

This only exists if the joint distribution is integrable, which is not true when calculated at fixed-order. Following our previous discussion, we can make progress by re-expressing the joint distribution in terms of a conditional probability:

$$p(\phi_p) = \int dt p(t, \phi_p) = \int dt p(t) p(\phi_p|t), \quad (4.2.15)$$

where $p(\phi_p|t)$ is the distribution of ϕ_p conditioned on the value of t . $p(\phi_p|t)$ is finite for $t \neq 0$, so can be calculated to any fixed-order, while $p(t)$ is finite at any fixed-order calculation and can be resummed to all-orders. Thus, to render the integral finite with the Sudakov form factor, we resum t and calculate the joint probability to fixed-order (fo):

$$p(\phi_p) \simeq \int dt p_{\text{resum}}(t) p_{\text{fo}}(\phi_p|t). \quad (4.2.16)$$

While this relationship is no longer an exact equality, it nevertheless exists, it is formally accurate to a fixed-order with $t \ll 1$, and as we discussed earlier, the pull magnitude t is called as the safe companion of the pull angle ϕ_p .

Now, we can calculate these two distributions, $p_{\text{resum}}(t)$ to all orders, and the other one $p_{\text{fo}}(\phi_p|t)$ at fixed-order. Firstly, let us start with the conditional distribution defined by

$$p_{\text{fo}}(\phi_p|t) = \frac{p_{\text{fo}}(t, \phi_p)}{p_{\text{fo}}(t)}, \quad (4.2.17)$$

where everything is calculated to the same order in α_s . Further, the fixed-order distribution of the pull magnitude is just a marginalization of the joint distribution

$$p_{\text{fo}}(t) = \int_0^{2\pi} d\phi_p p_{\text{fo}}(t, \phi_p), \quad (4.2.18)$$

so we just need to calculate the joint distribution. We will calculate $p_{\text{fo}}(t, \phi_p)$ to leading-order in α_s , in the soft and collinear limits; that is, to leading order for $t \ll 1$. The soft and collinear limits can be separated from one another with dimensional regularization and therefore can be calculated separately, more details about the calculation will be given in the next section.

4.3 Theory predictions for the pull angle

In this section, we present the analytic predictions from first-principles QCD for the pull vector. We focus on the calculation of the pull vector for color-singlet dipoles, as this is the case that has been studied experimentally in detail. Furthermore, the most useful feature of pull vector is the pull angle, which is the azimuthal angle about one of the jets in a pair with respect to the line connecting the jets. Both DØ and ATLAS experiments have measured the pull angle in the boosted, hadronic decays of W bosons from top quark decay [99–101].

For the calculations in this section, we use a modified version of the pull vector, which is identical to Eq.(4.1.3) for central jets in the collinear limit. The definition we use is

$$\vec{t}_{\text{modified}} = \sum_{i \in J} \frac{E_i \sin^2 \theta_i}{E_J} (\cos \phi_i, \sin \phi_i). \quad (4.3.1)$$

Here, E_i is the energy of particle i , θ_i is its angle from the jet axis, and ϕ_i is the azimuthal angle about the jet axis. The angle ϕ_i is measured with respect to a fiducial jet direction. This form is much more amenable to analytic calculations, and because the jet radii that we consider are typically relatively small ($R \simeq 0.4$), the collinear limit is a good approximation anyway. To correct for the difference between the original definition which is used in the experiment and this modified definition, we could match our resummed calculations to fixed-order results which would account for the difference. In what follows, we will refer to this version of the pull vector as \vec{t} , for brevity.

4.3.1 Fixed-order calculation

In this section, we calculate the pull vector distribution for emissions off of a color-connected dipole in the soft limit. This involves the calculation of the soft emission matrix element:

$$S_{n_1 n_2}(t, \phi_p) = -\mathbf{T}_1 \cdot \mathbf{T}_2 g^2 \mu^{2\epsilon} \int [d^d k]_+ \frac{2n_1 \cdot n_2}{k^+(k \cdot n_2)} \Theta \left(\tan^2 \frac{R}{2} - \frac{k^+}{k^-} \right) \times \delta \left(t - \frac{k^+ k^-}{E_J k^0} \right) \delta(\phi_p - \phi). \quad (4.3.2)$$

The light-like vectors n_1 and n_2 specify the direction of the ends of the dipole and $n_1 \cdot n_2 = 1 - \cos \theta_{12}$. We have centered a jet with radius R about the n_1 axis. Here, $[d^d k]_+$ is the phase space for an on-shell, positive energy particle in $d = 4 - 2\epsilon$ dimensions with momentum k :

$$\int [d^d k]_+ = \frac{1}{2^{4-2\epsilon} \pi^{5/2-\epsilon} \Gamma(1/2 - \epsilon)} \int_0^\infty \frac{dk^+}{(k^+)^{\epsilon}} \int_0^\infty \frac{dk^-}{(k^-)^{\epsilon}} \int_0^\pi d\phi \sin^{-2\epsilon} \phi, \quad (4.3.3)$$

here, k^+ and k^- are momentum components measured with respect to the n_1 axis, with $k^+ = k^0(1 - \cos \theta_{1k})$ and $k^- = k^0(1 + \cos \theta_{1k})$, where θ_{1k} is the angle between axis 1 and momentum k . k^0 is the energy of the particle. Finally, the angle ϕ is the azimuthal angle of the particle about the n_1 axis; that is, it is the pull angle, with $\phi = 0$ set by the line between axes n_1 and n_2 .

To evaluate the soft function, we can expand the dot product $k \cdot n_2$ in terms of n_1 :

$$\begin{aligned} k \cdot n_2 &= \frac{n_1 \cdot n_2}{2} k^- + \frac{\bar{n}_1 \cdot n_2}{2} k^+ - (n_1 \cdot n_2)^{1/2} (\bar{n}_1 \cdot n_2)^{1/2} (k^+ k^-)^{1/2} \cos \phi \\ &= \frac{1 - \cos \theta_{12}}{2} k^- + \frac{1 + \cos \theta_{12}}{2} k^+ - \sin \theta_{12} (k^+ k^-)^{1/2} \cos \phi. \end{aligned} \quad (4.3.4)$$

Then, all but one phase space integral can be done with the δ -functions. With an appropriate change of variables, the integral that remains can be written as

$$S_{n_1 n_2}(t, \phi_p) = -\mathbf{T}_1 \cdot \mathbf{T}_2 \frac{g^2}{4^{1-2\epsilon} \pi^{5/2-\epsilon} \Gamma(1/2-\epsilon)} \frac{1}{t^{1+2\epsilon}} \left(\frac{\mu^2 \tan^2 \frac{R}{2}}{E_J^2 \sin^2 \phi_p} \right)^\epsilon \int_0^1 du u^{-1+\epsilon} \\ \times \left(1 + u \tan^2 \frac{R}{2} \right)^{-2\epsilon} \left(1 + u \frac{\bar{n}_1 \cdot n_2}{n_1 \cdot n_2} \tan^2 \frac{R}{2} - 2u^{1/2} \left(\frac{\bar{n}_1 \cdot n_2}{n_1 \cdot n_2} \right)^{1/2} \tan \frac{R}{2} \cos \phi_p \right)^{-1}. \quad (4.3.5)$$

Note that

$$\frac{\bar{n}_1 \cdot n_2}{n_1 \cdot n_2} = \cot^2 \frac{\theta_{12}}{2}. \quad (4.3.6)$$

This integral can be performed in a series in ϵ using the $+$ -function expansion

$$u^{-1+\epsilon} = \frac{1}{\epsilon} \delta(u) + \left(\frac{1}{u} \right)_+ + \epsilon \left(\frac{\log u}{u} \right)_+ + \dots \quad (4.3.7)$$

Expanding to $1/\epsilon$ order (which is necessary for NLL resummation), we have

$$S_{n_1 n_2}(t, \phi_p) = -\mathbf{T}_1 \cdot \mathbf{T}_2 \frac{g^2}{4^{1-2\epsilon} \pi^{5/2-\epsilon} \Gamma(1/2-\epsilon)} \frac{1}{t^{1+2\epsilon}} \left(\frac{\mu^2 \tan^2 \frac{R}{2}}{E_J^2 \sin^2 \phi_p} \right)^\epsilon \quad (4.3.8) \\ \times \left[\frac{1}{\epsilon} + \int_0^1 du \left(\frac{1}{u} \right)_+ \left(1 + u \cot^2 \frac{\theta_{12}}{2} \tan^2 \frac{R}{2} - 2u^{1/2} \cot \frac{\theta_{12}}{2} \tan \frac{R}{2} \cos \phi_p \right)^{-1} \right].$$

After integrate over u , one can find the result as

$$S_{n_1 n_2}(t, \phi_p) = -\mathbf{T}_1 \cdot \mathbf{T}_2 \frac{g^2}{4^{1-2\epsilon} \pi^{5/2-\epsilon} \Gamma(1/2-\epsilon)} \frac{1}{t^{1+2\epsilon}} \left(\frac{\mu^2 \tan^2 \frac{R}{2}}{E_J^2 \sin^2 \phi_p} \right)^\epsilon \left[\frac{1}{\epsilon} \quad (4.3.9) \right. \\ \left. + 2 \cot \phi_p \tan^{-1} \frac{\frac{\tan \frac{R}{2}}{\tan \frac{\theta_{12}}{2}} \sin \phi_p}{1 - \frac{\tan \frac{R}{2}}{\tan \frac{\theta_{12}}{2}} \cos \phi_p} - \log \left(1 + \frac{\tan^2 \frac{R}{2}}{\tan^2 \frac{\theta_{12}}{2}} - 2 \frac{\tan \frac{R}{2}}{\tan \frac{\theta_{12}}{2}} \cos \phi_p \right) \right].$$

This can be expanded to find anomalous dimensions as the coefficients of the $1/\epsilon$ terms. Here, we will just show the leading result for $t > 0$ that is non-singular in ϵ . This corresponds to the lowest-order term in the fixed-order expansion in the soft limit. We find

$$\frac{d^2 \sigma^{\text{soft}}}{dt d\phi_p} = -\frac{\alpha_s}{\pi^2} \mathbf{T}_1 \cdot \mathbf{T}_2 \left[\frac{2}{t} \log \frac{\mu \tan \frac{R}{2}}{t E_J \sin \phi_p} \quad (4.3.10) \right. \\ \left. + \frac{1}{t} \left(2 \cot \phi_p \tan^{-1} \frac{\frac{\tan \frac{R}{2}}{\tan \frac{\theta_{12}}{2}} \sin \phi_p}{1 - \frac{\tan \frac{R}{2}}{\tan \frac{\theta_{12}}{2}} \cos \phi_p} - \log \left(1 + \frac{\tan^2 \frac{R}{2}}{\tan^2 \frac{\theta_{12}}{2}} - 2 \frac{\tan \frac{R}{2}}{\tan \frac{\theta_{12}}{2}} \cos \phi_p \right) \right) \right].$$

In this expansion, we do the $\overline{\text{MS}}$ subtraction and set the Euler-Mascheroni constant γ_E to 0. Integrating over ϕ , we find the soft contribution to the differential cross-section of the magnitude of pull, t :

$$\frac{d\sigma^{\text{soft}}}{dt} = -\frac{\alpha_s}{\pi} \mathbf{T}_1 \cdot \mathbf{T}_2 \left[\frac{2}{t} \log \frac{2\mu \tan \frac{R}{2}}{tE_J} - \log \left(1 - \frac{\tan^2 \frac{R}{2}}{\tan^2 \frac{\theta_{12}}{2}} \right) \right]. \quad (4.3.11)$$

The collinear contribution to the joint distribution can be calculated similarly. In this case, the collinear splitting function for a quark in dimensional regularization is:

$$\begin{aligned} J_q(t, \phi_p) &= \frac{\alpha_s C_F}{2\pi} \frac{(4\pi)^\epsilon}{\pi^{1/2} \Gamma(1/2 - \epsilon)} \left(\frac{\mu^2}{E_J^2} \right)^\epsilon \int_0^1 dz \int_0^\infty d\theta^2 \int_0^\pi d\phi \sin^{-2\epsilon} \phi \quad (4.3.12) \\ &\times (\theta^2)^{-1-\epsilon} z^{-2\epsilon} (1-z)^{-2\epsilon} \left(\frac{1 + (1-z)^2}{z} - \epsilon z \right) \delta(t - z(1-z)|1 - 2z|\theta^2) \delta(\phi_p - \phi) \\ &= \frac{\alpha_s C_F}{2\pi} \frac{(4\pi)^\epsilon}{\pi^{1/2} \Gamma(1/2 - \epsilon)} \frac{1}{t^{1+\epsilon}} \left(\frac{\mu^2}{E_J^2 \sin^2 \phi_p} \right)^\epsilon \\ &\times \int_0^1 dz z^{-1-\epsilon} (1-z)^{-\epsilon} |1 - 2z|^\epsilon (1 + (1-z)^2 - \epsilon z^2). \end{aligned}$$

The remaining integral can be done by expand in ϵ using the $+$ -function expansion. We find

$$\int_0^1 dz z^{-1-\epsilon} (1-z)^{-\epsilon} |1 - 2z|^\epsilon (1 + (1-z)^2 - \epsilon z^2) = -\frac{2}{\epsilon} - \frac{3}{2}. \quad (4.3.13)$$

Keeping only those terms that are independent of ϵ , we find

$$J_q(t, \phi_p) \simeq \frac{\alpha_s}{2\pi^2} C_F \left[\frac{2}{t} \log \frac{4tE_J^2 \sin^2 \phi_p}{\mu^2} - \frac{3}{2} \frac{1}{t} \right]. \quad (4.3.14)$$

To avoid double-counting in the soft and collinear limit when combined with the soft emission, we need to subtract from this its limit when $z \rightarrow 0$. In this case, we have

$$\begin{aligned} J_q^{(0)}(t, \phi_p) &= \frac{\alpha_s C_F}{\pi} \frac{(4\pi)^\epsilon}{\pi^{1/2} \Gamma(1/2 - \epsilon)} \left(\frac{\mu^2}{E_J^2} \right)^\epsilon \int_0^\infty dz \int_0^\infty d\theta^2 \int_0^\pi d\phi \sin^{-2\epsilon} \phi \\ &\times (\theta^2)^{-1-\epsilon} z^{-1-\epsilon} \delta(t - z\theta^2) \delta(\phi_p - \phi) \quad (4.3.15) \\ &= 0, \end{aligned}$$

as the integral over z is scaleless.

The cross section in the hard collinear limit is then the difference of these contributions:

$$\frac{d^2\sigma^{\text{coll}}}{dt d\phi_p} = \frac{\alpha_s}{2\pi^2} C_F \left[\frac{2}{t} \log \frac{4tE_J^2 \sin^2 \phi_p}{\mu^2} - \frac{3}{2} \frac{1}{t} \right]. \quad (4.3.16)$$

By integrating over ϕ_p , we find the collinear contribution to the cross section of the magnitude of pull, t :

$$\frac{d\sigma^{\text{coll}}}{dt} = \frac{\alpha_s C_F}{\pi t} \left[\log \frac{tE_J^2}{\mu^2} - \frac{3}{4} \right]. \quad (4.3.17)$$

Combining these soft and collinear results produces a lowest-order distribution that is independent of renormalization scale μ , we find

$$\begin{aligned} \frac{d^2\sigma^{\text{soft}}}{dt d\phi_p} + \frac{d^2\sigma^{\text{coll}}}{dt d\phi_p} = & \frac{\alpha_s C_F}{\pi^2 t} \left[\log \frac{4 \tan^2 \frac{R}{2}}{t} - \frac{3}{4} \right. \\ & \left. + 2 \cot \phi_p \tan^{-1} \frac{\frac{\tan \frac{R}{2}}{\tan \frac{\theta_{12}}{2}} \sin \phi_p}{1 - \frac{\tan \frac{R}{2}}{\tan \frac{\theta_{12}}{2}} \cos \phi_p} - \log \left(1 + \frac{\tan^2 \frac{R}{2}}{\tan^2 \frac{\theta_{12}}{2}} - 2 \frac{\tan \frac{R}{2}}{\tan \frac{\theta_{12}}{2}} \cos \phi_p \right) \right]. \end{aligned} \quad (4.3.18)$$

To determine the distribution of the magnitude of pull, we can integrate over $\phi \in [0, \pi]$. The integral of the explicit logarithm is 0, while the integral over the arctangent term can be done with contours. One finds

$$\frac{d\sigma}{dt} = \frac{\alpha_s C_F}{\pi t} \left[\log \frac{1}{t} - \frac{3}{4} - \log \left(\frac{1 - \frac{\tan^2 \frac{R}{2}}{\tan^2 \frac{\theta_{12}}{2}}}{4 \tan^2 \frac{R}{2}} \right) \right]. \quad (4.3.19)$$

4.3.2 Resummed results

Now, we calculate the resummed distribution of the pull magnitude. Because experimental analyses typically consider a W boson decaying into subjects with a small radius, we decide to perform the all-order calculation in the collinear limit, although determining the full-R dependence is a straightforward extension. We note that in this limit our definition of pull and the original one coincide.

The pull vector \vec{t} is an additive observable in that the contribution to the pull vector from additional soft emissions simply adds. The pull vector is recoil-free in the sense that soft emissions do not affect the direction of the jet axis to leading power in the pull magnitude $t \ll 1$. With these observations, to next-to-leading logarithmic accuracy (NLL) in the collinear limit, the double differential cross-section for the pull vector can be directly calculated from an infinite sum of jets with any number of emissions of energy fraction $\{z_i\}$ and emission angles $\{\theta_i\}$:

$$\begin{aligned} \frac{1}{\sigma} \frac{d^2\sigma}{d\vec{t}} = & \exp \left[- \int_0^{R^2} \frac{d\theta^2}{\theta^2} \int_0^1 dz \int_0^{2\pi} \frac{d\phi}{2\pi} \frac{\alpha_s}{2\pi} P_{qg \leftarrow q}(z) \right] \\ & \times \left[\sum_{n=0}^{\infty} \frac{1}{n!} \prod_{i=1}^n \int_0^{R^2} \frac{d\theta_i^2}{\theta_i^2} \int_0^1 dz_i \int_0^{2\pi} \frac{d\phi_i}{2\pi} \frac{\alpha_s}{2\pi} P_{qg \leftarrow q}(z_i) \right. \\ & \left. \times \delta \left(t_x - \sum_{i=1}^n z_i \theta_i^2 \cos \phi_i \right) \delta \left(t_y - \sum_{i=1}^n z_i \theta_i^2 \sin \phi_i \right) \right], \end{aligned} \quad (4.3.20)$$

where the momentum conservation of collinear emissions has been suppressed, and this expression ignores non-global logarithms and powers of the jet radius R .

The structure of the resummed results is akin to the well-known transverse-momentum resummation, as we have introduced in Sec. 2.2. Therefore, instead of repeating the material that we have already discussed before, we will use this section to illustrate how to perform the all-order resummation with the RGE approach.

Now, recall the RGE approach introduced in Sec 2.5.2, to NLL accuracy in conjugate b space, we have derived the general solution of the renormalization group equation in Eq.(2.5.31). The overall coefficient of the exponent differs for the soft and jet functions:

$$\begin{aligned}\Gamma_S &= -\Gamma_0, \\ \Gamma_J &= 2\Gamma_0.\end{aligned}\tag{4.3.21}$$

The coefficient of the non-cusp anomalous dimension, γ_0 , is defined from the expansion in α_s

$$\gamma = \sum_{n=0}^{\infty} \gamma^{(n)} \left(\frac{\alpha_s}{4\pi} \right)^{n+1},\tag{4.3.22}$$

which we need to extract from the fixed order calculation. From App. D.3, the coefficients of the non-cusp anomalous dimension for the jet and soft functions are

$$\begin{aligned}\gamma_S^{(0)} &= 4C_F \left[-\log \left(1 - \frac{\tan^2 \frac{R}{2}}{\tan^2 \frac{\theta_{12}}{2}} \right) - 2\gamma_E + 2i(\pi - \phi_b) \right], \\ \gamma_J^{(0)} &= 4C_F \left[\frac{3}{2} + 2\gamma_E - 2i(\pi - \phi_b) \right],\end{aligned}\tag{4.3.23}$$

and the canonical scales of the jet and soft functions in \vec{b} space are

$$\mu_S = \frac{E_J}{b \tan \frac{R}{2}},\tag{4.3.24}$$

$$\mu_J = \sqrt{\frac{2}{b}} E_J.\tag{4.3.25}$$

Note that when the components of \vec{t} are small ($|\vec{t}| \ll 1$), then either the momentum of the particles in the jet are very specific, or emissions are soft or collinear. If \vec{t} is small but the momentum of particles in the jet are not soft or collinear, then this configuration is non-singular and can be determined by matching to the fixed order result. Therefore, with \vec{t} small, the dominant contributions are from soft or collinear emissions. Soft and collinear emissions that contribute to the pull have different virtuality and pull is additive, so we can write the cross-section for measuring the pull vector in the factorized form:

$$\frac{d\sigma}{d\vec{t}} = H(Q^2) \int d^2t_s d^2t_c J(\vec{t}_c) S(\vec{t}_s) \delta^{(2)}(\vec{t} - \vec{t}_c - \vec{t}_s),\tag{4.3.26}$$

where $H(Q^2)$ is a hard function, $J(\vec{t}_c)$ is the jet function that describes collinear emissions, and $S(\vec{t}_s)$ is a soft function that describes coherent emissions from dipoles in the event. Moreover, we can simplify the convolution by Fourier transformation. Then, the cross-section for \vec{t} becomes

$$\begin{aligned} \frac{d\sigma}{d\vec{t}} &= \frac{1}{4\pi^2} H(Q^2) \int d^2t_s d^2t_c d^2b J(\vec{t}_c) S(\vec{t}_s) e^{i\vec{b}\cdot(\vec{t}-\vec{t}_c-\vec{t}_s)} \\ &= \frac{1}{4\pi^2} H(Q^2) \int d^2b J(\vec{b}) S(\vec{b}) e^{i\vec{b}\cdot\vec{t}}. \end{aligned} \quad (4.3.27)$$

The $J(\vec{b})$ is the Fourier transform of the jet function $J(\vec{t})$ (and similarly for the soft function), which can be obtained by insert the non-cusp anomalous dimension to the general solution of RGE, i.e. Eq.(2.5.31).

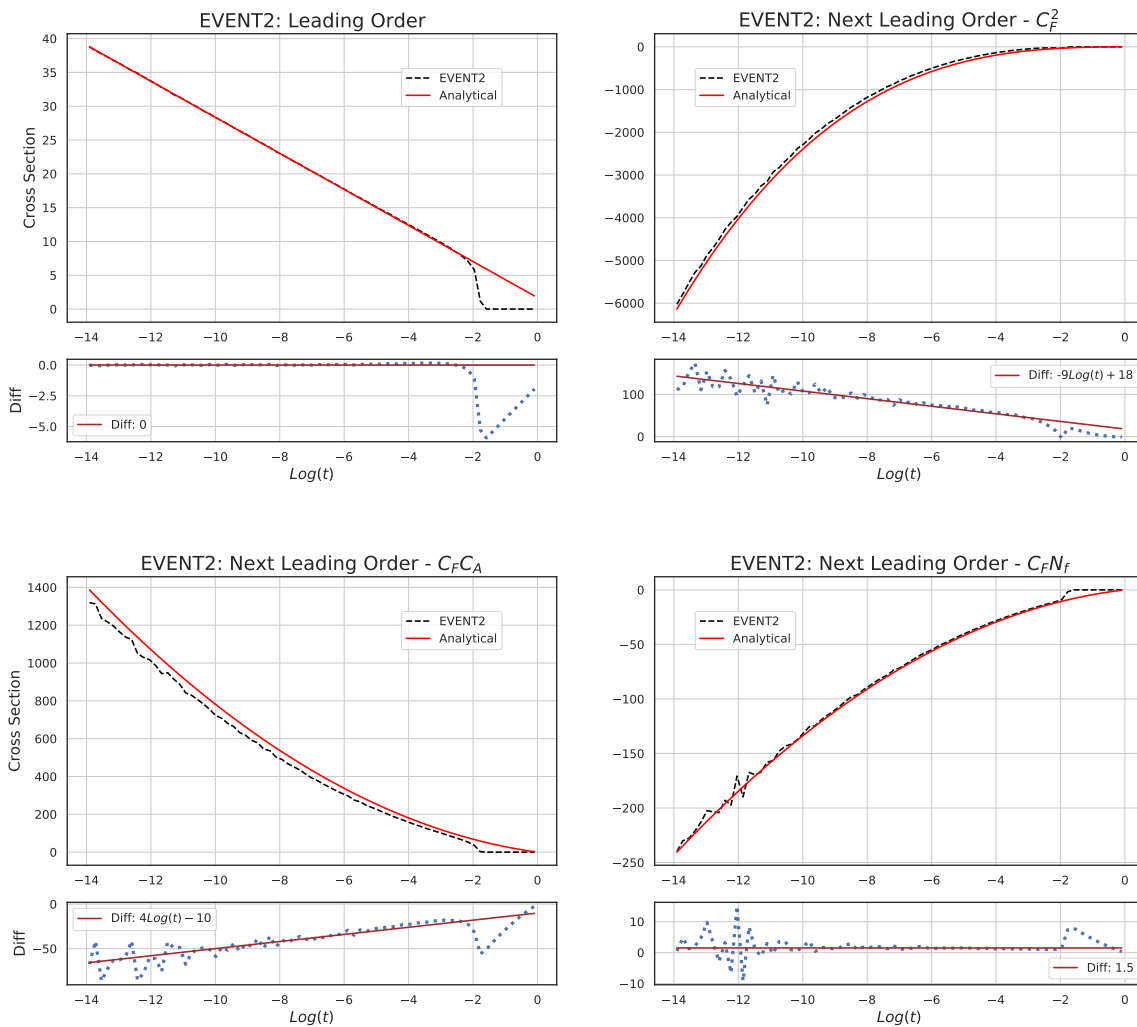


Figure 4.5. Double check the resummed calculation by compare the expansion of the resummed result and EVENT2 at both LO and NLO

So, in order to prove the equivalence between the traditional approach and RGE

approach, we define the resummed exponent in conjugate space from

$$J(\vec{b})S(\vec{b}) \equiv e^{-R(\vec{b})}. \quad (4.3.28)$$

Then we can compute the resummed exponent from both approaches, and we find exactly the same result at NLL accuracy as

$$-R(\vec{b}) = Lf_1(\lambda) + f_{2c}(\lambda) + f_{2s}(\lambda), \quad (4.3.29)$$

with

$$f_1(\lambda) = -\frac{C_i}{2\pi\beta_0\lambda} [(1-2\lambda)\log(1-2\lambda) - 2(1-\lambda)\log(1-\lambda)] \quad (4.3.30)$$

$$f_{2c}(\lambda) = -\frac{C_i B_i}{\pi\beta_0} \log(1-\lambda) - \frac{C_i \Gamma_1}{4\pi^2 \beta_0^2} [2\log(1-\lambda) - \log(1-2\lambda)] \quad (4.3.31)$$

$$- \frac{C_i \beta_1}{2\pi\beta_0^3} \left[\log(1-2\lambda) - 2\log(1-\lambda) + \frac{1}{2}\log^2(1-2\lambda) - \log^2(1-\lambda) \right]$$

$$f_{2s}(\lambda) = -\frac{C_F}{2\pi\beta_0} \log(1-2\lambda) \log \frac{1 - \frac{\tan^2 \frac{R}{2}}{\tan^2 \frac{\theta_{12}}{2}}}{2\tan^2 \frac{R}{2}}, \quad (4.3.32)$$

where the collinear section is identical to the one of the jet mass radiator calculated in the small R limit. To determine the distribution for the magnitude of the pull vector $p_{\text{resum}}(t)$, we simply integrate over the pull angle ϕ_p and the b -space azimuthal angle to find:

$$p_{\text{resum}}(t) = \frac{1}{\sigma} \frac{d\sigma}{dt} = t \int_0^\infty db b J_0(bt) e^{-R(b)}. \quad (4.3.33)$$

This expression can be explicitly expanded and evaluated to NLL with the two-loop running coupling, but we leave it implicit here.

The above resummed calculation can be double checked by subtract the expansion of resummed result from EVENT2, which is a Monte Carlo code for next-to-leading order corrections to two and three jet event observables in e^+e^- , results are shown in Fig. 4.5, which according to the C_F^2 channel the difference is $\sim \alpha_s^2 \log t$, which is beyond NLL accuracy, and the difference at $C_F C_A$ channel comes from the contribution of NGLs, this can be easily checked by adding the fixed-order result to $C_F C_A$ channel. Details about the fixed-order calculation for NGLs will be performed in the next section.

4.3.3 Pull angle distribution

There are two more things we include in our theoretical prediction of the pull angle. First, in the calculation of the fixed-order conditional distribution $p_{\text{fo}}(t, \phi_p)$, there is explicit dependence on the angle between the two ends of the color singlet dipole, θ_{12} . Our expression for $p_{\text{fo}}(t, \phi_p)$, then, needs to be convolved against the

distribution of this angle. For isotropic color-singlet decay, this distribution can be determined by boosting the rest frame decay to the lab frame. In the rest frame, if the four-vectors of the decay products are

$$p_1 = \left(\frac{m}{2}, 0, 0, \frac{m}{2} \right), \quad p_2 = \left(\frac{m}{2}, 0, 0, -\frac{m}{2} \right), \quad (4.3.34)$$

then, in the boosted frame the energies of the decay products are

$$E_1 \rightarrow \frac{\gamma m}{2}(1 + \beta \cos \theta), \quad E_2 \rightarrow \frac{\gamma m}{2}(1 - \beta \cos \theta). \quad (4.3.35)$$

Note that the energy of the decaying particle in the boosted frame, $E = \gamma m$, and therefore the velocity of the boost is

$$\beta = \sqrt{1 - \frac{m^2}{E^2}}. \quad (4.3.36)$$

The angle θ is the boost angle. The angle between the decay products can be found by demanding that they reproduce the heavy particle's invariant mass:

$$m^2 = 2E_1 E_2 (1 - \cos \theta_{12}) \quad \implies \quad \cos \theta_{12} = 1 - \frac{2m^2}{E^2} \frac{1}{1 - \beta^2 \cos^2 \theta}. \quad (4.3.37)$$

The distribution of the angle between the decay products is then

$$p(\cos \theta_{12}) = \frac{1}{\sqrt{\gamma^4 - \gamma^2}} \frac{1}{\sqrt{1 - \frac{2}{\gamma^2} - \cos \theta_{12}}} \frac{1}{(1 - \cos \theta_{12})^{3/2}} \\ \times \Theta \left(1 - \frac{2}{\gamma^2} - \cos \theta_{12} \right), \quad (4.3.38)$$

where γ is the boost factor. For comparison with data, we need to integrate over all possible subject angles accepted by the experimental cuts. From ATLAS's analysis, most of the top quarks will be produced at or near rest, and so the W boson's boost factor is approximately

$$\gamma = \frac{m_t^2 + m_W^2}{2m_t m_W} \simeq 1.3. \quad (4.3.39)$$

ATLAS also requires that the jets on which the pull angle is calculated to have a minimum transverse momentum of $p_{\perp, \min} = 25$ GeV, so assuming a purely transverse decay, the maximum angle between the jets is

$$\cos \theta_{12} \gtrsim 1 - \frac{m_W^2}{2p_{\perp, \min}(\gamma m_W - p_{\perp, \min})} \simeq -0.62. \quad (4.3.40)$$

We use these parameters to form our complete theory prediction.

The last component of our theoretical prediction is the inclusion of non-perturbative corrections from hadronization. Due to the additivity of the pull vector, hadronization corrections can be included to leading power by convolution of the perturbative

distribution with a model shape function [102–106]. This shape function encodes the kinematic distribution of non-perturbative emissions on which the pull vector is measured and is peaked around energies comparable to the QCD scale, Λ_{QCD} . Thus, we parametrize the non-perturbative distribution of the pull vector as:

$$p_{\text{np}}(t, \phi_p) \propto \tanh\left(\frac{1}{a\phi_p(2\pi - \phi_p)}\right) \delta\left(t - \frac{\Omega}{E_J}\right), \quad (4.3.41)$$

where the constant of proportionality is defined by normalization. Here, $\Omega \simeq \Lambda_{\text{QCD}}$, and the functional dependence of the pull angle ϕ_p has a free parameter a for which $a \rightarrow 0$ yields a flat distribution in ϕ_p and $a \rightarrow \infty$ is a δ -function at $\phi_p = 0$. This form of non-perturbative distribution is motivated by noting that in the center-of-mass frame of the color-singlet decay, at the lowest order emissions are uniform in azimuth about the decay axis. When boosted to the lab frame, this naturally clusters emissions at small values of ϕ_p . We find that varying the parameter $a \in [0, \frac{1}{4}]$ is sufficient in order to estimate the dependence on the precise shape of non-perturbative corrections.

With all of these pieces in place, we can finally complete the theoretical prediction of the pull angle distribution. Step-by-step, the perturbative joint distribution $p_{\text{pert}}(t, \phi_p)$ of the pull magnitude and angle is

$$\begin{aligned} p_{\text{pert}}(t, \phi_p) &= \int_{-0.62}^{-0.18} d \cos \theta_{12} p_{\text{resum}}(t) p_{\text{fo}}(\phi_p | t) p(\cos \theta_{12}), \end{aligned} \quad (4.3.42)$$

where the integration bounds follow from the earlier discussion of the boost of the W boson in the lab frame. Non-perturbative corrections can be included by convolution carefully vectorially summing the components of the pull vector:

$$\begin{aligned} p(t, \phi_p) &= \int_0^\infty dt' \int_0^{2\pi} d\phi' \int_0^\infty dt'' \int_0^{2\pi} d\phi'' p_{\text{perp}}(t', \phi') p_{\text{np}}(t'', \phi'') \\ &\quad \times \delta\left(\phi_p - \cos^{-1} \frac{t' \cos \phi' + t'' \cos \phi''}{t}\right) \\ &\quad \times \delta\left(t - \sqrt{t'^2 + t''^2 + 2t't'' \cos(\phi' - \phi'')}\right). \end{aligned} \quad (4.3.43)$$

Finally, integrating over the pull magnitude yields the pull angle distribution:

$$p(\phi_p) = \int_0^\infty dt p(t, \phi_p). \quad (4.3.44)$$

Our theoretical prediction is plotted in Fig. 4.6. On the left-hand side, we show the pull distribution as computed in perturbative QCD and with hadronization corrections as described above. At small ϕ_p , the lower edge of the band corresponds to $a = 0$, while the upper one to $a = \frac{1}{4}$. For comparison, we also show

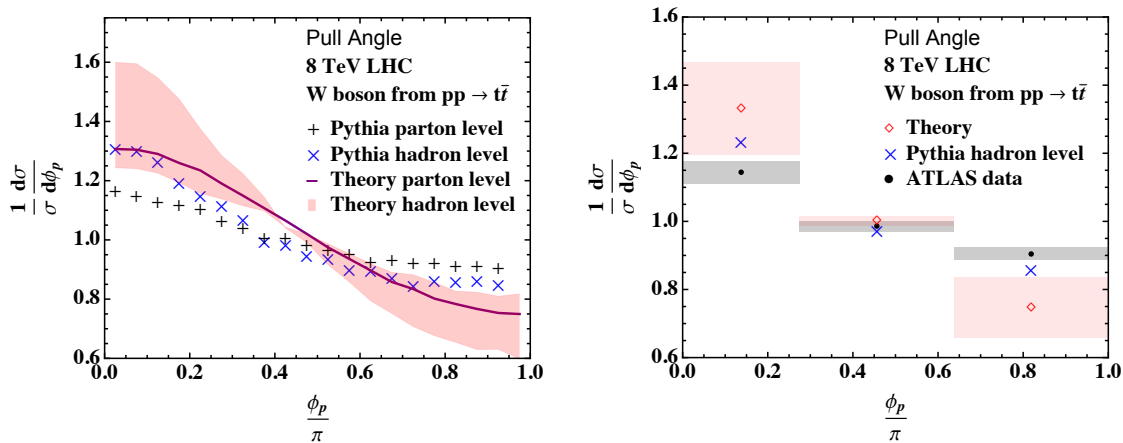


Figure 4.6. In the left plot we show the distribution of the pull angle in various approximations. Monte Carlo simulations from Pythia are shown at parton level (black +) and hadron level (blue \times). Our theory prediction is also shown at parton level (purple line) and with varying hadronization corrections (light-red band). In the right plot we compare our hadron-level result (red \diamond) to the ATLAS data (black \bullet), as well as to the Monte Carlo simulation (blue \times).

simulated data both at parton level and hadron level. To produce the simulated events, we follow the experimental analysis of [100], where the pull angle is measured on all particles from the two jets from hadronic W decay in semi-leptonic $t\bar{t}$ events. Therefore we generate semi-leptonic $pp \rightarrow t\bar{t}$ events at the 8 TeV LHC with MadGraph v2.6.4 [107] and then showered in Pythia v8.240 [89]. FastJet v3.3.2 [48] was used to impose phase space restrictions from the ATLAS analysis, find jets, and calculate the pull angle.

Finally, on the right-hand side of Fig. 4.6, we compare theory and Monte Carlo predictions at hadron-level to data collected by the ATLAS experiment of [100], which are available from HEPData [108]. As the central value of our hadron-level theoretical prediction, we consider the midpoint of the $0 < a < \frac{1}{4}$ band. We note that both theoretical calculation and simulation predict a distribution of the pull angle that is slightly more peaked at small values than data, which was also observed in ATLAS’s analysis.

4.4 Safe projections of jet pull

Despite the fact that we managed to obtain a first-principle description for pull angle, the calculation still suffered from large theoretical uncertainties due to pull angle being Sudakov safe instead of IRC safe, where the theoretical understanding of Sudakov safe observables is still in its infancy, it is not clear how theoretical accuracy can be achieved beyond the first order. Furthermore, while IRC safety ensures the presence of a kinematical region where non-perturbative effects are genuine power corrections, no such guarantee exists for Sudakov-safe observables and consequently, non-perturbative physics can contribute to the observable as an order-one effect.

In this section we overcome these difficulties by defining suitable projections of jet pull, which are similar to the projections of transverse momentum as the structure of the resummed results of pull is akin to the transverse-momentum resummation. These safe projections share many of the desirable features of the pull angle, but at the same time are IRC safe, which enables us to perform perturbative calculations at a well-defined, and in principle improvable, accuracy.

Moreover, we concentrate on measuring pull on one of the two jets originating from the hadronic, i.e. $b\bar{b}$, decay of a Higgs boson, while taking the other jet as reference. More specifically, we focus on the inclusive production of the Higgs together with a Z boson, which pull can provide a valuable handle in distinguishing the above production of a Higgs boson from the dominant QCD background (specifically $g \rightarrow b\bar{b}$), as suggested in the original article. Furthermore, this measurement can be also be performed in the boosted regime, where the decay products are reconstructed into a single two-pronged jet. In this case, jet pull can be measured on one of the subjects.

4.4.1 Analog from a_T distribution

Our first aim in what follows is to obtain all-order predictions for the above safe observables at NLL accuracy. In the previous section, we have already performed a resummed calculation for the pull magnitude t , which then played the role of the IRC safe companion observable in the Sudakov safe calculation for pull angle. However, in that calculation, we have resorted to the collinear limit. Here, we want to relax this approximation and also consider contributions from soft emissions at wide-angle, expressed as a power series in the jet radius R .

Before performing the resummed calculation for the safe projection, we also want to explore the relation between the difference between the a_T and q_T distribution at leading order in $O(\alpha_s)$. As we are expecting the same relation between the safe projection t_{\parallel} and pull magnitude t , so that we could use this relation to double-check our calculation. Moreover, because pull and its projections are jet shape, which the initial state radiation only contributes to the soft wide-angle start at the NLL accuracy. Thus for the comparison for a_T and q_T , we also only consider the final state radiation. The LO result for a_T is already collected in Eq.(2.2.29), while the leading order result for q_T can be obtained simply from the expansion of the modified LL result as

$$\Sigma^{(1)}(q_T) = \alpha_s C_F \left(\log^2 \frac{M}{q_T} - \frac{3}{2} \log \frac{M}{q_T} \right). \quad (4.4.1)$$

We note that the logarithms found for a_T are the same as those for the q_T variable with the replacement $2a_T \rightarrow q_T$. In other words, as far as the logarithmic dependence is concerned, we obtain the same result for the cross-section of a_T and $q_T/2$. The only other effect is a constant term generated from the azimuthal

angle-dependent term $|\sin\phi|$. Thus the relation is

$$\Sigma^{(1)}(a_T) - \Sigma^{(1)}\left(\frac{q_T}{2}\right) = -C_F \frac{\alpha_s \pi^2}{2\pi \cdot 3}. \quad (4.4.2)$$

The calculation for t_{\parallel} and t is straightforward, therefore instead of repeating the above steps, we only include the comparison for the leading order result of pull magnitude t , safe projection t_{\parallel} and, jet mass ρ from EVENT2, shown in Fig. 4.7.

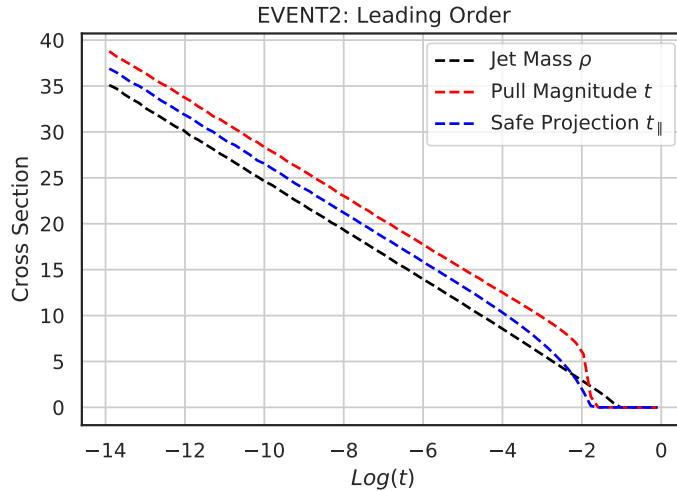


Figure 4.7. Comparison between the leading order result of pull magnitude, safe projection and the jet mass from EVENT2

4.4.2 Global logarithms at NLL accuracy

Similar to the NLL resummation formalism for pull vector derived in the previous section, the all-order expression can be easily arrived at by noting that the pull vector is additive and recoil-free at leading power, essentially because of the quadratic dependence on $|\vec{r}_i|$ of Eq. (4.1.3). Despite the fact that we have in mind to measure jet pull on the hadronic decay products of a Higgs boson, we note that in the collinear limit the resummed cross-section is universal and does not depend on the event surrounding the jet we are measuring. Thus, the resummed expression for the pull magnitude can be directly calculated from an infinite sum of emissions of energy fraction z_i and (small) emission angles $\theta_i \ll R$

$$\begin{aligned} \frac{1}{\sigma} \frac{d\sigma}{dt} = & \exp \left[- \int_0^{R^2} \frac{d\theta^2}{\theta^2} \int_0^1 dz \int_0^{2\pi} \frac{d\phi}{2\pi} \frac{\alpha_s(z\theta p_{ta})}{2\pi} P_{gq}(z) \right] \\ & \times \left[\sum_{n=0}^{\infty} \frac{1}{n!} \prod_{i=1}^n \int_0^{R^2} \frac{d\theta_i^2}{\theta_i^2} \int_0^1 dz_i \int_0^{2\pi} \frac{d\phi_i}{2\pi} \frac{\alpha_s(z_i \theta_i p_{ta})}{2\pi} P_{gq}(z_i) \right. \\ & \left. \times \delta \left(t - \sqrt{\left(\sum_{i=1}^n z_i \theta_i^2 \cos \phi_i \right)^2 + \left(\sum_{i=1}^n z_i \theta_i^2 \sin \phi_i \right)^2} \right) \right], \quad (4.4.3) \end{aligned}$$

where R is the radius of the jet we are measuring. For definiteness, we are going to define jets using the anti- k_t algorithm [53]. The function $P_{gq} = C_F \frac{1+(1-z)^2}{z}$ represents the collinear splitting probability of a quark into a quark and a gluon and appears in the resummation formula because at NLL the parton originating a jet in $H \rightarrow b\bar{b}$ decay is always a quark. A more refined calculation, namely NLL', would also account for the relative $\mathcal{O}(\alpha_s)$ probability of measuring pull on a gluon-initiated jet and would therefore also feature the splitting probabilities P_{gg} and P_{qg} . As already noted in Ref. [109], the structure of the resummed results is akin to the well-known transverse-momentum resummation, e.g. [110, 111], and consequently, the sum over the emissions can be performed explicitly in the conjugate space of Fourier-Hankel moments:

$$\frac{1}{\sigma} \frac{d\sigma}{dt} = \int_0^\infty db (bt) J_0(bt) e^{-2C_F \mathcal{R}_c(b)}, \quad (4.4.4)$$

where $J_0(x)$ is the Bessel function and $\mathcal{R}_c(b)$ is the collinear radiator, which, at this accuracy, depends exclusively on the magnitude of the Fourier conjugate vector $b = |\vec{b}|$:

$$\mathcal{R}_c(b) = \int_0^{R^2} \frac{d\theta^2}{\theta^2} \int_0^1 dz \frac{\alpha_s(z\theta p_{ta})}{2\pi} \frac{P_{gq}(z)}{2C_F} \Theta(z\theta^2 - \bar{b}^{-1}), \quad (4.4.5)$$

with $\bar{b} = b \frac{e^{\gamma_E}}{2}$. Explicit expressions for the NLL radiator will be reported in Section 4.4.4.

The projections of the pull vector we are interested in can be found by following the same steps. We have

$$\begin{aligned} \frac{1}{\sigma} \frac{d\sigma}{dt_\perp} = \exp & \left[- \int_0^{R^2} \frac{d\theta^2}{\theta^2} \int_0^1 dz \int_0^{2\pi} \frac{d\phi}{2\pi} \frac{\alpha_s(z\theta p_{ta})}{2\pi} P_{gq}(z) \right] \\ & \times \left[\sum_{n=0}^\infty \frac{1}{n!} \prod_{i=1}^n \int_0^{R^2} \frac{d\theta_i^2}{\theta_i^2} \int_0^1 dz_i \int_0^{2\pi} \frac{d\phi_i}{2\pi} \frac{\alpha_s(z_i \theta_i p_{ta})}{2\pi} P_{gq}(z_i) \right. \\ & \left. \times \delta \left(t_\perp - \left| \sum_{i=0}^n (-z_i \theta_i^2 \cos \phi_i \sin \beta + z_i \theta_i^2 \sin \phi_i \cos \beta) \right| \right) \right], \end{aligned} \quad (4.4.6)$$

where the δ function comes from the definition of the observable t_\perp in Eq. (4.1.6). Note that in this case, such constraint involves a one-dimensional sum, while the analogous term in the pull magnitude distribution, Eq. (4.4.3), involved a vector sum. This situation presents strong similarities with the resummation of equivalent variables in the context of transverse-momentum resummation, such as a_T and ϕ^* [44, 47]. Thus, as in that case, the all-order sum can be performed in a conjugated Fourier space. We obtain

$$\frac{1}{\sigma} \frac{d\sigma}{dt_\perp} = \frac{2}{\pi} \int_0^\infty db \cos(bt_\perp) e^{-2C_F \mathcal{R}_c(b)}, \quad (4.4.7)$$

where the radiator in b space is the same as the one obtained for the pull magnitude. Finally, we find that, at this accuracy, the t_{\parallel} and t_{\perp} distributions share an identical collinear structure:

$$\frac{1}{\sigma} \frac{d\sigma}{dt_{\parallel}} = \frac{2}{\pi} \int_0^{\infty} db \cos(bt_{\parallel}) e^{-2C_F \mathcal{R}_c(b)}. \quad (4.4.8)$$

In order to achieve the full NLL accuracy, the soft emissions at wide-angle must be included, from general considerations we expect them to be suppressed in the small jet radius limit. However, unlike collinear radiation discussed above, the explicit form of soft contributions depends on the underlying hard processes we are considering. Physically, this comes about because soft gluons can attach to any hard parton, resulting in a potentially complicated pattern of color correlations. In our current study, the situation is not too complicated because we are focusing on measuring pull on jets originating from a color-singlet, while the color structure is much richer when considering jets originating from higher-dimensional color representations [112]. In particular, the hard process we are considering at Born level is

$$q\bar{q} \rightarrow H(\rightarrow b\bar{b}) Z(\rightarrow l^+l^-). \quad (4.4.9)$$

The soft contribution to the NLL radiator can be written as the sum over dipoles that can emit a soft gluon. In our case we only have two dipoles: the one formed by the initial-state partons and the one made up by the two bottom quarks, which we consider massless, therefore we have

$$\mathcal{R}_s = -2\mathbf{T}_1 \cdot \mathbf{T}_2 \mathcal{R}_{12} - 2\mathbf{T}_a \cdot \mathbf{T}_b \tilde{\mathcal{R}}_{ab}, \quad (4.4.10)$$

where 1,2 refers to the initial state and a,b to the final state. \mathbf{T}_i are the color insertion operators, and the tilde on the second contribution indicates that we have subtracted the collinear contribution already included in \mathcal{R}_c . Because we are considering final-state jets produced by the decay of a singlet state, the color algebra is trivial:

$$\begin{aligned} \mathbf{T}_1 + \mathbf{T}_2 = 0 &\Rightarrow \mathbf{T}_1 \cdot \mathbf{T}_2 = -\frac{1}{2} (\mathbf{T}_1^2 + \mathbf{T}_2^2) = -C_F, \\ \mathbf{T}_a + \mathbf{T}_b = 0 &\Rightarrow \mathbf{T}_a \cdot \mathbf{T}_b = -\frac{1}{2} (\mathbf{T}_a^2 + \mathbf{T}_b^2) = -C_F \end{aligned} \quad (4.4.11)$$

The detailed calculation for the soft contribution to the NLL radiator, i.e. \mathcal{R}_{12} and $\tilde{\mathcal{R}}_{ab}$ will be performed at App. D.4. And the explicit expressions for the full NLL radiator will be reported in Sec. 4.4.4.

4.4.3 Non-global logarithms

As we discussed earlier, the jet pull is a non-global observable, therefore for the full NLL accuracy predictions, non-global logarithms must be included. We focus

on the final-state dipole ab and we consider the double differential distribution in the pull magnitude and pull angle at $\mathcal{O}(\alpha_s^2)$. In order to calculate the leading non-global logarithmic contribution to the pull vector, it is suffice to consider correlated soft gluon emission from the dipole in which the two soft gluons have parametrically separated energies $k_h \gg k_s$, in the phase-space region where the harder gluon lies outside the measured jet, while the second one is inside. The matrix element for this non-global contribution can then be expressed as

$$\begin{aligned}
\frac{d^2\sigma^{\text{NG}}}{dt d\phi_p} &= \frac{\alpha_s^2 C_F C_A}{16\pi^4} \int_0^1 \frac{dk_{\perp h}}{k_{\perp h}} \int_{-\infty}^{\infty} dy_h \int_{-\pi}^{\pi} d\phi_h \int_0^1 \frac{dk_{\perp s}}{k_{\perp s}} \int_{-\infty}^{\infty} dy_s \int_{-\pi}^{\pi} d\phi_s \\
&\times \frac{2p_a \cdot p_b}{(p_a \cdot k_h)(p_b \cdot k_h)} \frac{(p_a \cdot k_h)(p_b \cdot k_s) + (p_a \cdot k_s)(p_b \cdot k_h) - (p_a \cdot p_b)(k_h \cdot k_s)}{(p_a \cdot k_s)(p_b \cdot k_s)(k_h \cdot k_s)} \\
&\times \Theta(R^2 - (y_s - y_a)^2 - (\phi_s - \phi_a)^2) \Theta((y_h - y_a)^2 + (\phi_h - \phi_a)^2 - R^2) \\
&\times \Theta(k_{\perp h} \cosh y_h - k_{\perp s} \cosh y_s) \delta(t - k_{\perp s} ((y_s - y_a)^2 + (\phi_s - \phi_a)^2)) \\
&\times \delta\left(\theta_p - \cos^{-1} \frac{(y_s - y_a) \cos \beta + (\phi_s - \phi_a) \sin \beta}{\sqrt{(y_s - y_a)^2 + (\phi_s - \phi_a)^2}}\right). \tag{4.4.12}
\end{aligned}$$

Note that in the expression, the dependence on the perp magnitudes has been pulled out of all the matrix elements and made explicit. The integral over $k_{\perp s}$ and $k_{\perp h}$ can be easily performed. Furthermore, for compactness, we can shift the y and ϕ coordinates to be measured with respect to the location of jet a , i.e. without loss of generality we can set $y_a = \phi_a = 0$ in Eq. (4.4.12).

From this point, we will start approximating the integrals that remain. First, we only work to find the leading NGLs for $t \ll 1$. Then, we consider the phase-space constraints that remain and we notice that, in the small jet radius limit, we have the following scaling $y_h \sim y_s \sim R \ll 1$. Therefore, in the explicit logarithm of the integrals, we can simply remove the hyperbolic cosine factors, as their contribution will be purely beyond leading NGL. Correspondingly, because $R \ll 1$, we can push the bounds of integration on ϕ_s, ϕ_h safely to infinity. The integrals then become

$$\begin{aligned}
\frac{d^2\sigma^{\text{NG}}}{dt d\phi_p} &= \frac{\alpha_s^2 C_F C_A}{16\pi^4} \frac{1}{t} \int_{-\infty}^{\infty} dy_h \int_{-\infty}^{\infty} d\phi_h \int_{-\infty}^{\infty} dy_s \int_{-\infty}^{\infty} d\phi_s \frac{2p_a \cdot p_b}{(p_a \cdot k_h)(p_b \cdot k_h)} \\
&\times \frac{(p_a \cdot k_h)(p_b \cdot k_s) + (p_a \cdot k_s)(p_b \cdot k_h) - (p_a \cdot p_b)(k_h \cdot k_s)}{(p_a \cdot k_s)(p_b \cdot k_s)(k_h \cdot k_s)} \log \frac{y_s^2 + \phi_s^2}{t} \\
&\times \Theta(y_s^2 + \phi_s^2 - t) \Theta(R^2 - y_s^2 - \phi_s^2) \Theta(y_h^2 + \phi_h^2 - R^2) \\
&\times \delta\left(\theta_p - \cos^{-1} \frac{y_s \cos \beta + \phi_s \sin \beta}{\sqrt{y_s^2 + \phi_s^2}}\right). \tag{4.4.13}
\end{aligned}$$

Similar to the one-gluon dipoles previously discussed, the integrals are more easily performed in polar coordinates, see Eq. (D.4.2):

$$\begin{aligned}
y_i &= r_i \cos \gamma_i, \\
\phi_i &= r_i \sin \gamma_i. \tag{4.4.14}
\end{aligned}$$

Then, the integrals become

$$\begin{aligned} \frac{d^2\sigma^{\text{NG}}}{dt d\phi_p} &= \frac{\alpha_s^2 C_F C_A}{16\pi^4} \frac{1}{t} \int_0^\infty dr_h r_h \int_0^{2\pi} d\gamma_h \int_0^\infty dr_s r_s \int_0^{2\pi} d\gamma_s \frac{2p_a \cdot p_b}{(p_a \cdot k_h)(p_b \cdot k_h)} \\ &\times \frac{(p_a \cdot k_h)(p_b \cdot k_s) + (p_a \cdot k_s)(p_b \cdot k_h) - (p_a \cdot p_b)(k_h \cdot k_s)}{(p_a \cdot k_s)(p_b \cdot k_s)(k_h \cdot k_s)} \\ &\times \log \frac{r_s^2}{t} \Theta(r_s^2 - t) \Theta(R - r_s) \Theta(r_h - R) \delta(\theta_p - \gamma_s + \beta). \end{aligned} \quad (4.4.15)$$

Now, we need to express the soft matrix element in these coordinates. Additionally, we work in the small jet radius limit, $R \ll 1$, and note that the dominant contribution to the NGLs comes from the region of phase space in which $r_s \lesssim r_h \sim R$. We will thus expand the matrix element to first order in the $R \ll 1$ limit with this identified scaling. We find

$$\begin{aligned} \frac{d^2\sigma^{\text{NG}}}{dt d\phi_p} &= \left(\frac{\alpha_s}{2\pi}\right)^2 C_F C_A \frac{\pi}{3} \frac{\log \frac{R^2}{t}}{t} \left(1 + \frac{24(1 - \log 2)}{\pi^2} R \right. \\ &\times \left. \frac{\sin \Delta\phi \sin(\theta_p + \beta) + \sinh \Delta y \cos(\theta_p + \beta)}{\cosh \Delta y - \cos \Delta\phi} + \mathcal{O}(R^2) \right). \end{aligned} \quad (4.4.16)$$

The first term in this expansion is the familiar expression for the narrow jet mass NGL matrix element. Note that this differs by a factor of 2π from the familiar expression for the jet mass NGLs; this factor is recovered when θ_p is integrated over. Furthermore, if we integrate over the full range for θ_p , then the contribution which is linear in R vanishes, leading to

$$\frac{d\sigma^{\text{NG}}}{dt} = \left(\frac{\alpha_s}{2\pi}\right)^2 C_F C_A \frac{2\pi^2}{3} \frac{\log \frac{R^2}{t}}{t} + \mathcal{O}(R^2). \quad (4.4.17)$$

It is easy to verify that at NLL accuracy the same expression as Eq. (4.4.17) holds for the projections t_{\parallel} and t_{\perp} .

4.4.4 Resummed results

We are now in a position to collect all the results derived so far and obtain an NLL resummed prediction for the safe projections of the pull vector we are considering. In this section, we investigate the structure of NGLs that affect the different projections of the pull vector. The all-order differential distribution can be written as:

$$\frac{1}{\sigma} \frac{d\sigma}{dv} = \int_0^\infty db \mathcal{F}_v(bv) e^{-C_F \mathcal{R}(b)} \mathcal{S}^{\text{NG}}(b), \quad (4.4.18)$$

with

$$\mathcal{F}_v(x) = \begin{cases} x J_0(x), & \text{if } v = t, \\ \frac{2}{\pi} \cos(x), & \text{if } v = t_{\parallel}, t_{\perp}. \end{cases} \quad (4.4.19)$$

The resummed exponent \mathcal{R} can be written in terms of leading (second line) and next-to-leading (third to sixth lines) contributions:

$$\begin{aligned}
\mathcal{R} &= 2\mathcal{R}_c + 2\tilde{\mathcal{R}}_{ab} + 2\mathcal{R}_{12} \\
&= \frac{(1-2\lambda)\log(1-2\lambda) - 2(1-\lambda)\log(1-\lambda)}{2\pi\alpha_s\beta_0^2} \\
&\quad + \frac{B_q}{\pi\beta_0}\log(1-\lambda) + \frac{K}{4\pi^2\beta_0^2}[2\log(1-\lambda) - \log(1-2\lambda)] \\
&\quad + \frac{\beta_1}{2\pi\beta_0^3}\left[\log(1-2\lambda) - 2\log(1-\lambda) + \frac{1}{2}\log^2(1-2\lambda) - \log^2(1-\lambda)\right] \\
&\quad + \frac{1}{\pi\beta_0}\log\frac{p_{ta}R}{\mu_R}[\log(1-2\lambda) - 2\log(1-\lambda)] \\
&\quad - \frac{R^2}{8\pi\beta_0}\left[4 + \frac{\cosh\Delta y + \cos\Delta\phi}{\cosh\Delta y - \cos\Delta\phi}\right]\log(1-2\lambda) + \mathcal{O}(R^4), \tag{4.4.20}
\end{aligned}$$

with $\lambda = \alpha_s\beta_0\log(\bar{b}R^2)^1$ and $\alpha_s = \alpha_s(\mu_R)$, where μ_R is the renormalization scale, which we can vary around the hard scale p_{ta} in order to assess missing higher-order corrections. In the above results the β function coefficients β_0 and β_1 are defined as

$$\beta_0 = \frac{11C_A - 2n_f}{12\pi}, \quad \beta_1 = \frac{17C_A^2 - 5C_An_f - 3C_Fn_f}{24\pi^2}, \tag{4.4.21}$$

and

$$B_q = \frac{3}{4}, \quad K = C_A\left(\frac{67}{18} - \frac{\pi^2}{6}\right) - \frac{5}{9}n_f. \tag{4.4.22}$$

Finally, as already mentioned, in the small- R limit, the non-global contribution can be taken equal to the hemisphere case. The resummation of NGLs can be performed in the large- N_c limit exploiting a dipole cascade picture. We make use of the following parametrization [6]:

$$\mathcal{S}^{\text{NG}} = \exp\left[-C_FC_A\frac{\pi^2}{3}\frac{1+(a\tau)^2}{1+(b\tau)^c}\tau^2\right], \tag{4.4.23}$$

with $\tau = -\frac{1}{4\pi\beta_0}\log(1-2\lambda)$, with $a = 0.85C_A$, $b = 0.86C_A$, and $c = 1.33$.

Finally, we note that the above results are valid for jets defined with the anti- k_t algorithm, which acts as a perfect cone in the soft limit [53]. Had we use a different clustering measure, such as Cambridge/Aachen [51, 52] or the k_t -algorithm [49, 50], nontrivial clustering logarithms would have modified both the global and non-global contributions to the resummed exponent [113–115].

¹Strictly speaking, jet radius dependence in the argument of the logarithms only appears in this order in the soft-collinear contributions. However, we find that including it in the whole radiator leads to better numerical stability. The difference between these choices is beyond NLL accuracy.

4.4.5 Towards phenomenology

As discussed above, for all the theoretical ingredients that go into an NLL calculation for the jet pull projections. We now turn our attention towards some preliminary phenomenological studies. After discussing a simple model of non-perturbative corrections due to the hadronization process, we move to compare our resummed results to the one obtained by a general-purpose Monte Carlo event generator. While doing so, we also discuss the numerical impact of the various contributions that we have computed thus far.

Because the pull vector is both an additive observable and recoil-free, corrections due to non-perturbative physics and hadronization can be modelled by a shape function [102–106]. This shape function is then convolved with the perturbative distribution to produce a non-perturbative distribution. The shape function depends on a dimensionful relative transverse-momentum scale ϵ , and it has most of its support around $\epsilon = \Lambda_{\text{QCD}}$, the QCD scale. The shape function for the pull vector also has non-trivial azimuthal angle dependence, because non-perturbative emissions will be emitted in a preferential direction according to the dipole configuration.

In this section, we will construct a shape function for the pull vector, assuming that it exclusively has support at $\epsilon = \Lambda_{\text{QCD}}$. Further, we will assume that the dominant non-perturbative emission lies exactly at the boundary of the jet on which we measure the pull vector, and its azimuthal distribution about the jet axis is uniform. We will see that a non-uniform distribution of the pull vector is generated by a preferential emission of higher-energy non-perturbative emissions at small values of the pull angle.

To construct the shape function with these restrictions, we first note that the scale ϵ for emission from a dipole with ends defined by the light-like directions p_a and p_b is

$$\epsilon = \Lambda_{\text{QCD}} = \sqrt{(k \cdot p_a)(k \cdot p_b)}, \quad (4.4.24)$$

where k is the four-momentum of the non-perturbative emission. The pull vector depends on the momentum transverse to the beam axis, k_t , and its value is constrained by the non-perturbative scale. Expressing the momentum k as

$$k = k_t(\cosh y, \cos \phi, \sin \phi, \sinh y), \quad (4.4.25)$$

we can express k_t as

$$k_t = \frac{\Lambda_{\text{QCD}}}{(\cosh(y - y_a) - \cos(\phi - \phi_a))^{1/2} (\cosh(y - y_b) - \cos(\phi - \phi_b))^{1/2}}. \quad (4.4.26)$$

Now, we expand this expression to second order in the jet radius R , fixing the angle between the non-perturbative emission and the jet axis n_a to be R :

$$R^2 = (y - y_a)^2 + (\phi - \phi_a)^2. \quad (4.4.27)$$

We find

$$k_t = \frac{2\Lambda_{\text{QCD}}}{R} \frac{\sqrt{p_{ta}p_{tb}}}{m_H} + 2\Lambda_{\text{QCD}} \frac{(p_{ta}p_{tb})^{3/2}}{m_H^3} [\cos(\varphi + \beta) \sinh \Delta y + \sin(\varphi + \beta) \sin \Delta\phi] + \mathcal{O}(R). \quad (4.4.28)$$

The relative rapidity Δy , azimuth $\Delta\phi$, and angle β were defined in the beginning of this section. The azimuthal angle φ defines the angle about the jet axis p_a with respect to p_b . Finally, we have introduced the transverse momentum of the ends of the dipole p_{ta} and p_{tb} and note that they are constrained by the Higgs mass:

$$m_H^2 = 2p_{ta}p_{tb}(\cosh \Delta y - \cos \Delta\phi). \quad (4.4.29)$$

With this construction, the shape function for the non-perturbative k_t and azimuthal angle φ is

$$F(k_t, \varphi) = \frac{1}{2\pi} \delta \left(k_t - \frac{2\Lambda_{\text{QCD}}}{R} \frac{\sqrt{p_{ta}p_{tb}}}{m_H} - 2\Lambda_{\text{QCD}} \frac{(p_{ta}p_{tb})^{3/2}}{m_H^3} [\cos(\varphi + \beta) \sinh \Delta y + \sin(\varphi + \beta) \sin \Delta\phi] \right). \quad (4.4.30)$$

Given the perturbative pull vector distribution $\frac{1}{\sigma} \frac{d^2\sigma^{\text{pert}}}{d\vec{t}^2}$, we now want to find the non-perturbative pull vector distribution $\frac{1}{\sigma} \frac{d^2\sigma^{\text{np}}}{d\vec{t}^2}$ through convolution with the shape function. The contribution to pull from the non-perturbative emissions that we identified in the rest frame of the Higgs boson will be

$$\vec{t}_{\text{np}}(k_t, \varphi) = \frac{k_t R^2}{p_{ta}} (\cos \varphi, \sin \varphi). \quad (4.4.31)$$

It then follows that the non-perturbative distribution of the pull vector is

$$\begin{aligned} \frac{d^2\sigma^{\text{np}}}{d\vec{t}^2} &= \int_0^\infty dk_t \int_0^{2\pi} d\varphi F(k_t, \varphi) \frac{d^2\sigma^{\text{pert}}}{d\vec{t}^2} (\vec{t} - \vec{t}_{\text{np}}(k_t, \varphi)) \\ &= \int_0^{2\pi} \frac{d\varphi}{2\pi} \frac{d^2\sigma^{\text{pert}}}{d\vec{t}^2} (\vec{t} - \vec{t}_{\text{np}}(k_t, \varphi)), \end{aligned} \quad (4.4.32)$$

where we leave the dependence on the non-perturbative transverse momentum k_t implicit.

To understand the behavior of the leading non-perturbative corrections, we expand the above expression in powers of Λ_{QCD} . Furthermore, we note that because of the particular choice of the reference frame we have used in this section, $\varphi = 0$

corresponds to the line joining the two jet centers. Thus, we obtain

$$\begin{aligned} \frac{d^2\sigma^{\text{np}}}{dt_{\parallel}dt_{\perp}} &= \frac{d^2\sigma^{\text{pert}}}{dt_{\parallel}dt_{\perp}} - \int_0^{2\pi} \frac{d\varphi}{2\pi} \vec{t}_{\text{np}}(k_t, \varphi) \cdot \nabla \left(\frac{d^2\sigma^{\text{pert}}}{dt_{\parallel}dt_{\perp}} \right) + \mathcal{O}\left(\frac{\Lambda_{\text{QCD}}^2}{m_H^2}\right) \\ &= \left[1 - \frac{\Lambda_{\text{QCD}}R^2\sqrt{p_{ta}p_{tb}^3}}{m_H^3\sqrt{\Delta y^2 + \Delta\phi^2}} \left((\Delta y \sinh \Delta y + \Delta\phi \sin \Delta\phi) \frac{\partial}{\partial t_{\parallel}} \right. \right. \\ &\quad \left. \left. + (\Delta y \sin \Delta\phi - \Delta\phi \sinh \Delta y) \frac{\partial}{\partial t_{\perp}} \right) \right] \frac{d^2\sigma^{\text{pert}}}{dt_{\parallel}dt_{\perp}}. \end{aligned} \quad (4.4.33)$$

Because of the derivative dependence in this non-perturbative correction, its effect can be included to the lowest order in both Λ_{QCD} and α_s with a shift of the appropriate argument of the perturbative cross-section. For the cross-sections of t_{\parallel} and t_{\perp} individually, we have

$$\frac{d\sigma^{\text{np}}}{dt_{\parallel}} = \frac{d\sigma^{\text{pert}}}{dt_{\parallel}} \left(t_{\parallel} - \frac{\Lambda_{\text{QCD}}R^2\sqrt{p_{ta}p_{tb}^3}}{m_H^3\sqrt{\Delta y^2 + \Delta\phi^2}} (\Delta y \sinh \Delta y + \Delta\phi \sin \Delta\phi) \right) + \mathcal{O}(\Lambda_{\text{QCD}}^2, \alpha_s), \quad (4.4.34)$$

$$\frac{d\sigma^{\text{np}}}{dt_{\perp}} = \frac{d\sigma^{\text{pert}}}{dt_{\perp}} \left(t_{\perp} - \frac{\Lambda_{\text{QCD}}R^2\sqrt{p_{ta}p_{tb}^3}}{m_H^3\sqrt{\Delta y^2 + \Delta\phi^2}} (\Delta y \sin \Delta\phi - \Delta\phi \sinh \Delta y) \right) + \mathcal{O}(\Lambda_{\text{QCD}}^2, \alpha_s). \quad (4.4.35)$$

The leading non-perturbative correction to the magnitude of the pull vector t can be found by exploiting its relationship to t_{\parallel} and t_{\perp} :

$$t = \sqrt{t_{\parallel}^2 + t_{\perp}^2}. \quad (4.4.36)$$

Then, we have that the pull magnitude distribution becomes

$$\frac{d\sigma^{\text{np}}}{dt} = \frac{d\sigma^{\text{pert}}}{dt} \left(t - \frac{\Lambda_{\text{QCD}}R^2\sqrt{p_{ta}p_{tb}^3}}{m_H^3} \sqrt{\sinh^2 \Delta y + \sin^2 \Delta\phi} \right) + \mathcal{O}(\Lambda_{\text{QCD}}^2, \alpha_s). \quad (4.4.37)$$

We are now ready to perform some phenomenological studies of our results. We start by assessing the numerical impact of the different contributions that are included in our resummed results, namely collinear emissions, final-state radiation (FSR), i.e. the $\mathcal{O}(R^2)$ contribution arising from the final-state dipole, initial-state radiation (ISR), and non-global logarithms. The results are shown in Fig. 4.8, on the left for the pull magnitude distribution and on the right for the t_{\parallel} distribution (at NLL this is the same as t_{\perp}). The plots are for a representative phase-space point: $\Delta y = 1$, $\Delta\phi = \frac{\pi}{6}$ and $p_{ta} = p_{tb} = \frac{m_H}{\sqrt{2(\cosh \Delta y - \cos \Delta\phi)}} \simeq 110$ GeV, which corresponds to a symmetric decay of the Higgs boson. We note that the collinear approximation describes the two distributions well, down to the values of the observables $\sim 10^{-3}$. Below that, in the Sudakov region, the impact of soft-emissions

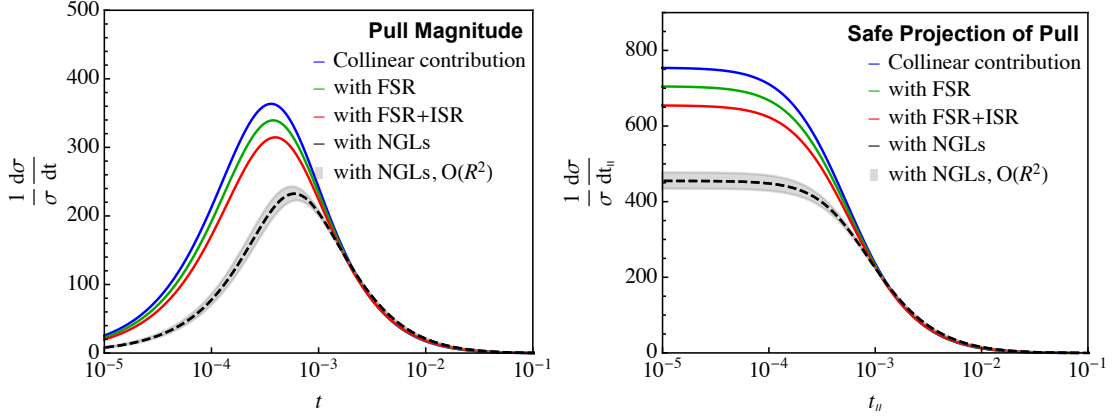


Figure 4.8. Impact of the different contributions to all-order next-to-leading logarithmic resummation of the pull magnitude (left) and the safe projection t_{\parallel} (right). Soft gluon contributions at wide-angle are included as an expansion in the jet radius R through $\mathcal{O}(R^2)$, while the non-global logarithmic contribution is accounted for at $\mathcal{O}(R^0)$. At this accuracy, the distribution of the orthogonal projection t_{\perp} is identical to t_{\parallel} .

at large angle becomes sizeable. However, we note that finite R corrections, which characterize FSR and ISR are not very large, due to the smallness of the jet radius parameter $R = 0.4$, employed in this study. Perhaps surprising is the relatively large contribution due to non-global logarithms. This last contribution is shown with an uncertainty band that aims to probe the impact of $\mathcal{O}(R^2)$ corrections to the non-global contribution, which is not included here. The band is constructed by rescaling the $\mathcal{O}(R^0)$ coefficient by the factor $(1 + aR^2)$ and by varying $-1 \leq a \leq 1$. We note that this uncertainty is not large, due to the relatively small value of the jet radius employed here.

By comparing the two distributions, t , and t_{\parallel} , we note that the former exhibits a Sudakov peak, while the latter appears to develop a plateau for $t_{\parallel} < 10^{-4}$. This behavior is completely analogous to what is found when looking at Q_T and a_T/ϕ^* distributions [44]. Small values of t or t_{\parallel} can be obtained by soft/collinear emissions or by kinematical cancellations and the behavior of t_{\parallel} signals the fact that kinematical cancellation is the dominant mechanism and prevents the formation of the Sudakov peak, as opposed to what happens with t . This behavior can be explained by performing a simple calculation at the double logarithmic accuracy:

$$\begin{aligned} \frac{d\sigma}{dt_{\parallel}} &= \frac{1}{\pi} \int_0^{\infty} db \cos(bt_{\parallel}) e^{-\frac{\alpha_s C_F}{2\pi} \log^2 b} = \frac{1}{\pi} \int_0^{\infty} db e^{-\frac{\alpha_s C_F}{2\pi} \log^2 b} [1 + \mathcal{O}(t_{\parallel}^2)] \\ &= \sqrt{\frac{2}{\alpha_s C_F}} e^{\frac{\pi}{2\alpha_s C_F}} + \mathcal{O}(t_{\parallel}^2) \end{aligned} \quad (4.4.38)$$

which indicates the differential cross section goes to a constant at small t_{\parallel} .

Next, in Fig. 4.9 we show our final NLL predictions for t (left) and t_{\parallel} (right), with an estimate of the perturbative uncertainty, which we obtain by varying the renormalization scale in the range $\frac{p_t}{2} \leq \mu_R \leq 2p_t$. Furthermore, we also show the NLL calculation supplemented by our estimate of non-perturbative contri-

butions due to the hadronization process, i.e. Eqs. (4.4.34) and (4.4.37), using $\Lambda_{\text{QCD}} = 1 \text{ GeV}$. We note that because of the R^2 coefficient, the size of non-perturbative corrections is rather small. We expect our simple implementation of non-perturbative corrections to fail in the peak (plateau) region, where one should retain more information about the shape function. Therefore, we only plot our NLL curves with non-perturbative corrections down to $t \sim 2 \cdot 10^{-3}$ and $t_{\parallel} \sim 10^{-3}$, respectively.

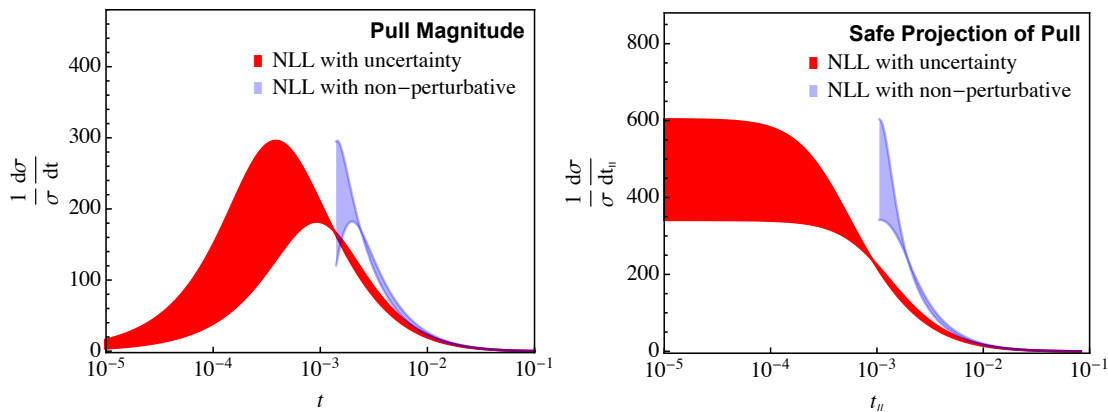


Figure 4.9. Plots of the NLL predictions for t (left) and t_{\parallel} (right), together with an estimate of the theoretical uncertainties, obtained by varying the renormalisation scale. The plots also show how the curve is modified once the shift due to non-perturbative corrections is applied.

In Fig. 4.10, we compare our results to those obtained with a general-purpose Monte Carlo event generator. We generate a single event $pp \rightarrow HZ$ at $\sqrt{s} = 13 \text{ TeV}$, with the Higgs decaying in $b\bar{b}$ and Z leptonically, using MadGraph v2.6.6 [107] and we then shower this event many times in Pythia v8.240 [89]. FastJet v3.3.2 [48] is used to find jets and calculate the pull variables. The Monte Carlo results for t and t_{\parallel} are then compared to our NLL predictions, supplemented by the non-perturbative corrections. We find decent agreement between the Monte Carlo and our NLL prediction for t and t_{\parallel} , supplemented by non-perturbative corrections. We note that the NLL and Monte Carlo predictions depart at the tail of the distributions. This effect is more noticeable for the pull magnitude and it signals the fact that the resummation alone is not enough to describe the distribution at large t and matching to fixed-order is needed.

Finally, we expect additional non-perturbative contributions from the Underlying Event due to multiple parton-parton interactions and pileup, due to multiple proton-proton interactions per bunch crossing. We have not included these effects in our studies, but we anticipate that their scaling with the jet radius will be the same as FSR, which we did calculate in this paper, albeit with a different, non-perturbative, coefficient.

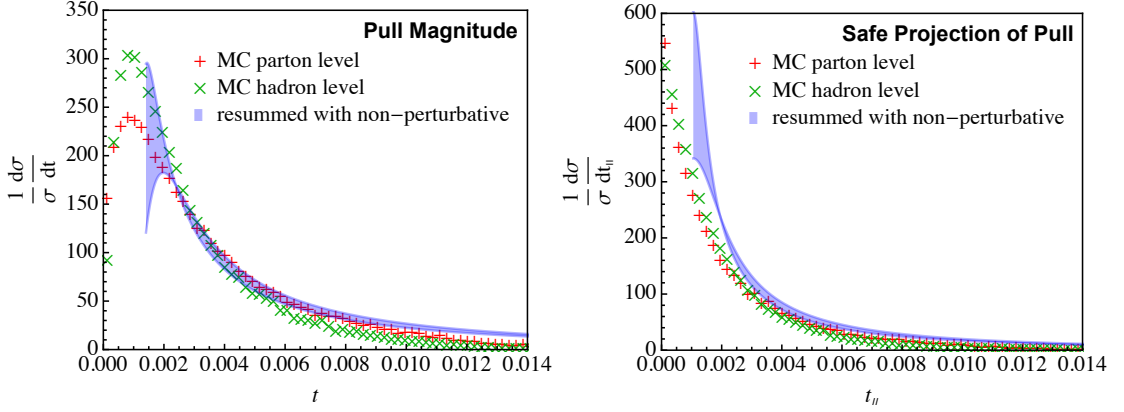


Figure 4.10. Comparison of the distributions computed at NLL and supplemented with non-perturbative corrections, to a numerical simulation obtain with the event generator Pythia v8.240.

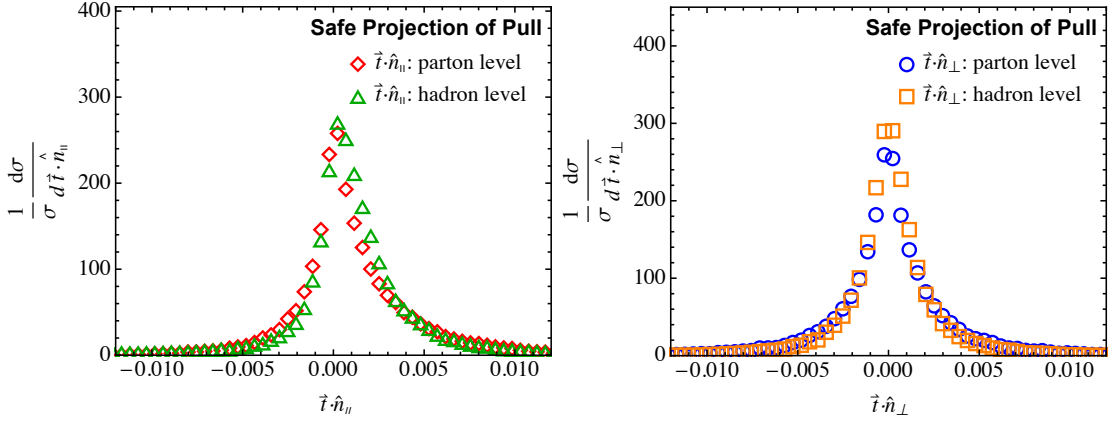


Figure 4.11. Monte-Carlo simulations of the $\vec{t} \cdot \hat{n}_{\parallel}$ and $\vec{t} \cdot \hat{n}_{\perp}$ distributions, left and right respectively, measured on $H \rightarrow b\bar{b}$ events generated with Pythia v8.240. The plots show results at both parton and hadron level.

4.5 Azimuthal asymmetry

The projections of the pull vector we have discussed in the previous section exhibit nice theoretical properties. In particular, the IRC safety ensures perturbative calculability, while non-perturbative contributions can be treated as (power) corrections. Moreover, the definitions of the projections resulted in observables that share many similarities in their all-order behavior with variables that are among the most-studied in particle physics, such as the transverse momentum of a vector boson and its projections. However, the presence of an absolute value in Eq.(4.1.6) leads to a loss of information. For instance, an emission in the rapidity-azimuth region between the two jets and an emission outside could potentially contribute to the same value of t_{\perp} or t_{\parallel} .

4.5.1 Definition of the asymmetries

In Fig. 4.11 we perform a Monte-Carlo study of these distributions for the color singlet decay $H \rightarrow b\bar{b}$, using again the event generator Pythia v8.240, with the same kinematical settings of the previous section. For each distribution, we show both parton-level and hadron-level results. We would expect the $\vec{t} \cdot \hat{n}_\perp$ to be roughly symmetric about zero, while the distribution of $\vec{t} \cdot \hat{n}_\parallel$ should be skewed in the direction of the color-connected leg of the dipole, here the positive direction. The plots show that this is indeed the case. In order to emphasize these features even more, we can build the

$$\mathcal{A}_\parallel = \frac{t_\parallel}{\sigma} \frac{d\sigma}{dt_\parallel} \Big|_{\vec{t} \cdot \hat{n}_\parallel > 0} - \frac{t_\parallel}{\sigma} \frac{d\sigma}{dt_\parallel} \Big|_{\vec{t} \cdot \hat{n}_\parallel < 0}, \quad (4.5.1)$$

$$\mathcal{A}_\perp = \frac{t_\perp}{\sigma} \frac{d\sigma}{dt_\perp} \Big|_{\vec{t} \cdot \hat{n}_\perp > 0} - \frac{t_\perp}{\sigma} \frac{d\sigma}{dt_\perp} \Big|_{\vec{t} \cdot \hat{n}_\perp < 0} \quad (4.5.2)$$

We expect \mathcal{A}_\parallel to be more marked than \mathcal{A}_\perp and this is indeed what is found in the simulations, as shown in Fig. 4.12.

We note that the above asymmetries are still IRC safe and therefore can be calculated in perturbation theory. Indeed, we could argue that \mathcal{A}_\parallel is essentially the IRC safe version of the pull angle distribution. The definitions of the asymmetries in Eq. (4.5.1) make explicit references to the sign of the scalar product which is used to project the pull vector. This constraint essentially introduces a new boundary in phase-space which renders the all-order structure of these observables richer. While we expect that this resummation can still be achieved, in this work we limit ourselves to analytically evaluate the asymmetries at fixed-order. The lowest-order contribution to the asymmetries originates from wide-angle soft emissions. In particular, we find that the contribution denoted by \mathcal{A} in Eq. (D.4.9) does not vanish when we integrated separately over the $\vec{t} \cdot \hat{n}_i > 0$ and $\vec{t} \cdot \hat{n}_i < 0$ regions. We find

$$\mathcal{A}_\parallel = \frac{\alpha_s C_F}{\pi} \left[\frac{4R \cos \beta \sinh \Delta y + \sin \beta \sin \Delta \phi}{\pi \cos \Delta \phi - \cosh \Delta y} + \mathcal{O}(R^3) \right] + \mathcal{O}(\alpha_s^2), \quad (4.5.3)$$

$$\mathcal{A}_\perp = \frac{\alpha_s C_F}{\pi} \left[\frac{4R \cos \beta \sin \Delta \phi - \sin \beta \sinh \Delta y}{\pi \cos \Delta \phi - \cosh \Delta y} + \mathcal{O}(R^3) \right] + \mathcal{O}(\alpha_s^2). \quad (4.5.4)$$

Interestingly, the asymmetries are sensitive to odd powers of the jet radius, in the small- R expansion. This comes about because of the restrictions on the angular integrations imposed by the $\vec{t} \cdot \hat{n}_i > 0$ and $\vec{t} \cdot \hat{n}_i < 0$ constraints. We also point out that these asymmetries essentially depend on soft radiation, while collinear contributions cancel out. Soft radiation exhibit strong sensitivity to the pattern of color correlations and therefore these observables can provide a valuable testing ground for Monte Carlo parton showers that attempt to go beyond the large- N_c limit, e.g. [116, 117].

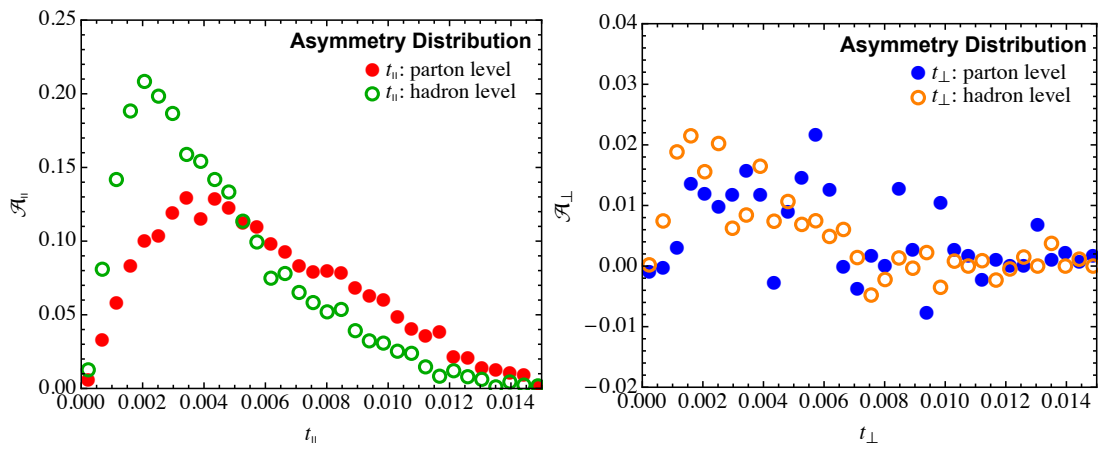


Figure 4.12. Monte-Carlo simulations of the \mathcal{A}_{\parallel} and \mathcal{A}_{\perp} distributions, left and right respectively, measured on $H \rightarrow b\bar{b}$ events generated with Pythia v8.240. The plots show results at both parton and hadron level.

5 Conclusion and Outlook

In this thesis, we have presented detailed studies for two important types of observables that go beyond the traditional borders of pQCD, i.e. non-global and IRC unsafe observables. In particular, in this thesis, we focused on developing all-order resummation techniques in perturbative QCD, which extend to regions where the fixed-order calculation is not sufficient.

With the aim to explain the lack of tools within the traditional techniques, we start with an overview of the first-principle calculations. First of all, we have presented a general discussion for the infrared singularities in QCD, in order to understand the singularities in perturbative QCD and derive the factorization properties.

In Chapter 2, we discussed different approaches to resummation, where the enhanced logarithms are accounted for to all orders, either using the RGE evolution of each kinematically enhanced subprocess that enters the factorization theorem, or directly identifying factorization and exponentiation properties of QCD matrix elements. In this thesis, we have mostly followed the second approach, and as an example, the resummation formalism for threshold and transverse momentum was derived at NLL accuracy. We then moved to the discussion about the calculation of jet properties, i.e. jet substructure, for which non-global logarithms arise due to radiation in the limited phase-space region. Non-global observables are more subtle to treat to all orders because they receive contributions from correlated soft emission.

In Chapter 3, we have explored the structure of non-global logarithms, with an emphasis on the hemisphere jet mass distribution in e^+e^- collisions. The leading NGLs can be computed using the strong energy-ordering approximation, for which the matrix elements are simplified. Moreover, this approximation also led to the BMS equation that resums the leading contributions in the large N_c limit. While the BMS equation cannot be solved analytically, we have explored an iterative approach to the full solution. Moreover, we have built a differential equation solver with both the traditional numerical method and the novel approach with artificial neural networks. This NN approach can dramatically speed up needed theory calculations.

During most of my doctorate, I have devoted myself to probing the color flow with jet substructure, where a powerful observable that is able to probe color flow is jet pull. I have focused on the calculation of the pull vector for color-singlet dipoles, i.e. the signal process. The most useful feature of the pull vector for studying color dipoles is the pull angle, which has been measured by both DØ and ATLAS experiments. However, unlike the most theoretically studied observables for jet physics, the pull angle lacks the property of IRC safety, thus cannot be calculated in fixed-order perturbation theory. In Chapter 4, we have presented the analytical predictions for pull angle with the help of Sudakov safety. In this context, distribution is rendered finite by including all-orders resummation. We have also introduced infra-red and collinear safety projections of jet pull and performed their resummation.

The theoretical understanding of these observables led us to introduce novel azimuthal asymmetry distributions that measure the radiation pattern by looking at the difference between the jet pull vector pointing towards and away from the other jet of interest. In particular, the asymmetry distribution \mathcal{A}_{\parallel} can be considered the IRC version of the pull angle distribution. As expected, these asymmetries essentially depend on soft radiation. Due to their sensitivity to wide-angle soft radiation, these asymmetries could play an important role in assessing sub-leading color correlations.

The definition of asymmetries essentially introduces a new boundary in phase-space which renders the all-order structure of these observables richer. As we mentioned above, the pull asymmetry is sensitive to wide-angle soft radiation, where the leading non-trivial contribution starts from NLL accuracy, thus the NGLs need to be resummed to provide accurate predictions.

Regarding the future research projects, although we could, in general, perform the iterative approach to resum the NGLs, an interesting challenge is the inclusion of finite N_c effects, which is highly nontrivial even at the leading logarithmic level. Therefore, a novel approach for the resummation with full color is important, applying this method to study the effect of color correlations in observables like the pull asymmetry would be the first step in this work. Below, we outline our plans for future work, which could be split into two separate paths.

5.1 Soft Radiation Beyond Leading color

The asymmetric behavior we have observed is related to the nontrivial dependence of the radiation pattern as a function of the azimuth. Since collinear radiation gives symmetric contributions, this effect is driven by soft radiation. Thus, we could define the asymmetry cross-section as

$$\frac{d^2\sigma^{asym}}{d\vec{t}} \equiv \frac{d^2\sigma}{d\vec{t}} - \left\langle \frac{d^2\sigma}{d\vec{t}} \right\rangle_{av.} = \frac{d^2\sigma}{d\vec{t}} - \frac{1}{2\pi} \frac{d\sigma}{tdt} \quad (5.1.1)$$

where we have subtracted the azimuthal angle averaged terms, and this distribution should be equivalent as a two-dimensional version of \mathcal{A}_{\parallel} and \mathcal{A}_{\perp} , as introduced in Sec. 4.5.1, the density plot for the fixed-order calculation is shown in Fig. 5.1.

Currently, the global part of pull asymmetry has been resummed up to NLL accuracy, for higher logarithm accuracy the two-loop soft function is needed, similar to the calculation of hemisphere soft function [63], we leave this study for future work. Moreover, because of the new boundary, the NGLs must be resummed. This could be performed by re-derive and solve the BMS equation for the asymmetry. However, the BMS equation only includes leading color accuracy. For the evolution equation with the sub-leading color effects, the full solution is still under development.

Therefore, we would like to develop a novel approach for the resummation with sub-leading color, unlike the leading color approximation, which one can view each event as a collection of independent color dipoles. However, including the sub-leading color corrections is highly nontrivial, since one needs to keep track of the rapidly growing number of color configurations from higher-dimensional color representations. A better understanding of color flow in higher-dimensional color representation could also help the experimental measurement of Higgs and probe new physics.

For the next project, the ultimate goal is to perform the resummation of non-global observables with the full color and implement it into a numerical code that can be used for phenomenology, which the Sherpa resummation plugin [118] offers a natural framework. In particular, we would like to apply this method to study pull asymmetry. Furthermore, to obtain a reliable description in the whole range, matching the resummed result with the fixed-order result is needed, this could be obtained from a program like SoftSERVE [119] or Comix [120] included in Sherpa. The matched prediction (NNLL+NLO) can be compared to state-of-the-art Monte Carlo event generators such as Sherpa, which achieves high-theoretical accuracy exploiting multi-jet merging at NLO.

As a first step, we want to check if the pull asymmetry is sensitive to soft radiation, this can be done by a Monte-Carlo study of the asymmetry distributions for $e^+e^- \rightarrow$ three jets events at parton level, where the pull is measured on pairs of jets. Moreover, It will be interesting to investigate the sub-leading color effect with the recently introduced numerical resummation at sub-leading color in Ref. [121].

Furthermore, the jet pull is additive and recoil-free at leading power, because of the quadratic dependence on Eq. (4.1.3). Therefore, It would be interesting to study observables with a generalized $|\vec{r}_i|^\alpha$ dependence, and employing different recombination schemes in the jet algorithm, such as winner-take-all [122], in order to maintain the recoil-free property. And in soft-collinear limit, the generalized pull magnitude is equivalent to angularities, defined in Eq. (4.2.4).

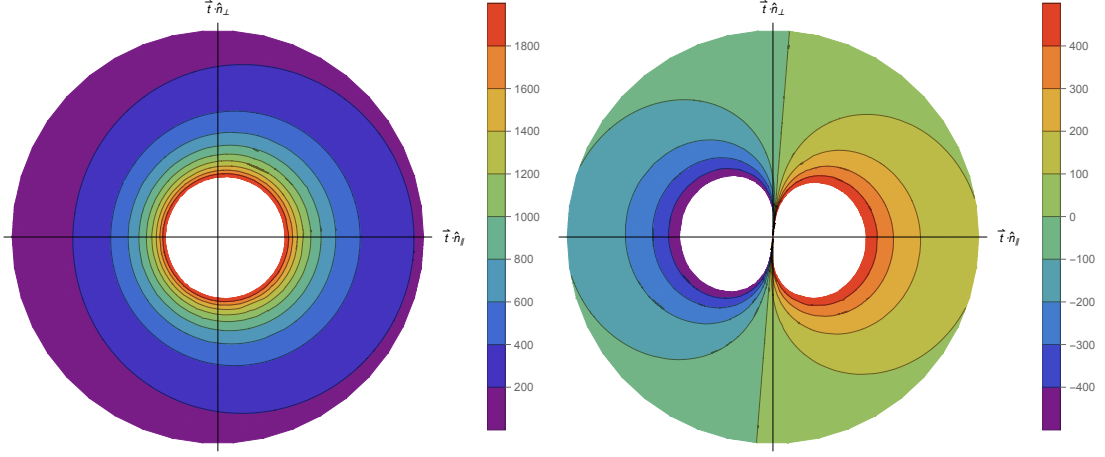


Figure 5.1. Joint distribution of $\vec{t} \cdot \hat{n}_{\parallel}$ and $\vec{t} \cdot \hat{n}_{\perp}$ and the joint asymmetry distribution, left and right respectively

5.2 Solver of RG-evolution framework

Besides the parton shower approach, we are also interested to continue developing the neural network method to include the finite N_c effects to non-global observables. On the other hand, the general resummation process can be described as introducing non-local correlation operators and exploits their RG evolution. In particular, the factorization theorem, i.e., the convolution of the soft and jet functions, can be simplified into a product form in Laplace space as

$$\sigma = H \cdot J \cdot \bar{J} \cdot S. \quad (5.2.1)$$

Computations based on this structure have been used to resum large logarithm enhancements for many observables. More generally, the logarithms of global, infrared, and collinear safe observables can be resummed by solving the RG-evolution equation

$$\frac{\partial}{\partial \log \mu} F = \gamma F, \quad (5.2.2)$$

where F represents part of the factorized cross-section in Laplace space. Thus we would like to extend our neural network method to a general solver for the RG-evolution framework, and then apply it to develop a general method for resummation. For example, we could extract the anomalous dimensions with the Integration by Parts (IBP) based differential equations [123].

Moreover, the neural network method could apply to a handful of integro-differential evolution equations. For example, the integro-differential equation of DGLAP type can be written as

$$u \frac{d}{du} G(x, u) = \frac{\alpha(u)}{2\pi} \int_x^1 \frac{dy}{y} G(y, u) P\left(\frac{x}{y}\right), \quad (5.2.3)$$

where the function $P(x)$ is the splitting function. The standard method is to take Mellin N-moment to both side

$$u \frac{d}{du} \int_0^1 dx x^{N-1} G(x, u) = \frac{\alpha(u)}{2\pi} \gamma(N, \alpha(u)) M[G(y, u), y](N), \quad (5.2.4)$$

where the anomalous dimension $\gamma(N, \alpha(u))$ is defined by $\int_0^1 dx x^{N-1} P(x)$, and $M[G(x, u), x](N)$ is the Mellin moment of $G(x, u)$, and the full solution can be obtained by the inverse Mellin transformation. On the other hand, with the help of neural network, we could solve it directly by convert it to n coupled first-order differential equations.

Given the formal similarity between BMS and BK equation, therefore, besides applying the tricks that we have learned from BK equation and its linearization (BFKL equation) to solve the BMS equation, exploring the BMS-BK duality is also interesting. Moreover, the BK equation has a finite N_c generalization, which is called as Jalilian-Marian, Iancu, McLerran, Weigert, Leonidov and Kovner (JIMWLK) equation [124, 125], this could give us some hints for derive the evolution equation for NGLs at finite N_c [126].

Furthermore, in Ref. [127, 128] the relation between BFKL and DGLAP equation were explored. Moreover, in $N = 4$ supersymmetric Yang-Mills theory, due to the vanishing β function, the structure of the BFKL and DGLAP equations is simplified, and the anomalous dimensions of DGLAP splitting functions at small x limit can be obtained from the BFKL equation [129]. Therefore, applying our neural network method to exploring new approach for duality relations between sets of QCD evolution equations is also interesting.

As a first example, we can apply our method to a toy model of unintegrated gluon distribution in the small x limit with fixed-coupling constant, which we leave only leading term in the splitting function as

$$P_{gg}(z, \alpha) = 2z, \quad (5.2.5)$$

in this case, the anomalous dimension is $\gamma(N, \alpha) = \frac{2}{N+1}$, and we can obtain the analytical result as a Bessel function by inverse Mellin transformation as [130, 131]

$$G(x, u) = x I_0 \left(\sqrt{\frac{\alpha}{\pi} \log \log \frac{1}{x}} \right). \quad (5.2.6)$$

Recently the BK equation, have been calculated beyond leading order with collinear improvement [132]. thus, it is possible to extend the method, which we have developed so far, to apply to BMS/BK equation with full NLO accuracy.

A Basics of QFT

We collect here some well known results in QFT that are used throughout the thesis

A.1 S-matrix and LSZ reduction formula

In quantum theory, the scattering matrix (S-matrix) describe the scattering process which can be viewed as a transition from an initial state $|i\rangle$ to a final state $|f\rangle$. More formally, we could define the S-matrix as a scattering operator S connecting the particle states in Hilbert space as $\langle i|S|f\rangle$. Moreover the probability of scattering is given by $|\langle i|S|f\rangle|^2$. Furthermore, the trivial part, i.e. process with no scattering occurs, can be separated by rewriting the S-matrix as

$$S = \mathbf{1} + iT \tag{A.1.1}$$

LSZ theorem

To obtain the S-matrix elements, i.e. scattering amplitudes, one must calculate the corresponding vertex function and multiply it by the field renormalization constants $Z_i^{1/2}$ for each external line i , this process is called as Lehmann- Symanzik-Zimmermann (LSZ) reduction formula, details of its derivation can be found in Ref. [13]. It connects the S-matrix to the time-ordered correlation functions, i.e., vacuum expectation values of time-ordered products of field operators, of the interacting quantum theory. For scalar particle, the LSZ reduction can be written as

$$\begin{aligned} \langle f|i\rangle &= i^{n+n'} \int d^4x_1 e^{ik_1x_1} (-\partial_1^2 + m^2) \cdots d^4x_{1'} e^{ik_{1'}x_{1'}} (-\partial_{1'}^2 + m^2) \cdots \\ &\times \langle 0|T\phi(x_1) \cdots \phi(x_{1'}) \cdots |0\rangle. \end{aligned} \tag{A.1.2}$$

Ward identities in QED

The scattering amplitude M for a process that includes an external photon with four-momentum k_μ as

$$M = \epsilon^\mu M_\mu \tag{A.1.3}$$

Then the Ward identity reads: $k^\mu M_\mu = 0$. In order to derive this identity, we begin by recalling the LSZ formula for the massive vectorial particle in the initial or final state

$$\langle f|i\rangle = i\epsilon^\mu \int d^4x_1 e^{-ik\cdot x} (-\partial^2) \cdots \langle 0|TA_\mu(x) \cdots |0\rangle, \quad (\text{A.1.4})$$

and the classical equation of motion for A^μ in spinor electrodynamics is

$$-Z_3 \partial^2 A_\mu = Z_1 j_\mu, \quad (\text{A.1.5})$$

where j_μ is the electromagnetic current, therefore we have

$$\langle f|i\rangle = i\epsilon^\mu Z_3^{-1} Z_1 \int d^4x_1 e^{-ik\cdot x} \cdots [\langle 0|Tj_\mu(x) \cdots |0\rangle + \text{contact terms}], \quad (\text{A.1.6})$$

where the contact terms arise due to the classical equation of motion hold inside quantum correlation functions only up to contact terms, which doesn't generate singularities in the k^2 s. So they do not contribute to the S-matrix.

Now let us try replacing ϵ^μ with k^μ , where we can write the factor of ik^μ as $-\partial^\mu$ acting on the e^{-ikx} , and then we can integrate by parts to get $-\partial^\mu$ acting on the correlation function. Then, we have $\partial^\mu \langle 0|Tj_\mu(x) \cdots |0\rangle$ on the right-hand side. Thus, we have the result

$$\partial^\mu \langle 0|Tj_\mu(x) \cdots |0\rangle = \text{contact terms}, \quad (\text{A.1.7})$$

where in the above equation, we have used the Noether current as the exact symmetry obeys $\partial^\mu j_\mu = 0$. This is the Ward (or Ward–Yakahashi) identity. And again, the contact terms do not have the right singularities to contribute to $\langle f|i\rangle$. Therefore, $\langle f|i\rangle$ vanishes if we replace an external photon's polarization vector ϵ_μ with its four-momentum k_μ .

A.2 Recursion relation for the phase space

The two-body phase space integral is the basis of computing the higher body phase space formula. We start by calculating it in the rest frame for the two-body system, as $P = p_1 + p_2 = (\sqrt{s}, 0, 0, 0)$. Thus, we have

$$\begin{aligned} d\Phi_2 &= \frac{d^3p_1}{(2\pi)^3 2E_1} \frac{d^3p_2}{(2\pi)^3 2E_2} (2\pi)^4 \delta^{(4)}(P - p_1 - p_2) \\ &= \frac{d^3p_1}{(2\pi)^3 2E_1} \frac{d^3p_2}{(2\pi)^3 2E_2} (2\pi)^4 \delta^{(3)}(p_1 - p_2) \delta(\sqrt{s} - E_1 - E_2) \\ &= \frac{p^2 dp d\cos\theta d\phi}{(2\pi)^3 2\sqrt{m_1^2 + p^2} 2\sqrt{m_2^2 + p^2}} \frac{1}{2\sqrt{m_2^2 + p^2}} (2\pi) \delta(\sqrt{s} - \sqrt{m_1^2 + p^2} - \sqrt{m_2^2 + p^2}). \end{aligned} \quad (\text{A.2.1})$$

We can solve the delta function as

$$\delta(\sqrt{s} - \sqrt{m_1^2 + p^2} - \sqrt{m_2^2 + p^2}) = \frac{\delta(p - \sqrt{s}\bar{\beta}/2)}{p/E_1 + p/E_2}, \quad (\text{A.2.2})$$

with

$$\bar{\beta} = \sqrt{1 - \frac{2(m_1 + m_2)^2}{s} + \frac{(m_1 - m_2)^2}{s}}. \quad (\text{A.2.3})$$

Therefore, we can write the phase space integral as

$$\begin{aligned} d\Phi_2 &= \frac{d\cos\theta d\phi}{(2\pi)^3} \frac{p^2}{2E_1 2E_2} \frac{2\pi}{p/E_1 + p/E_2} \Big|_{p=\sqrt{s\bar{\beta}/2}, E_i=\sqrt{m_i^2+p^2}} \\ &= \frac{d\cos\theta d\phi}{(2\pi)^2} \frac{p}{4(E_1 + E_2)} \Big|_{p=\sqrt{s\bar{\beta}/2}, E_i=\sqrt{m_i^2+p^2}} \\ &= \frac{\bar{\beta}}{8\pi} \frac{d\cos\theta}{2} \frac{d\phi}{2\pi}, \end{aligned} \quad (\text{A.2.4})$$

It is worth point out that, for the special case, when two masses are equal $m_1 = m_2 = m$. Then we have

$$\bar{\beta} = \sqrt{1 - \frac{m^2}{E^2}}, \quad (\text{A.2.5})$$

which is nothing but $\beta = v/c$.

Three-Body Phase Space

It is useful to decompose multi-body phase space integral into a product of two-body phase space integrals. As an example, we could decompose a three-body phase space into a product of two two-body phase space integrals, we exploit the following identity

$$\begin{aligned} 1 &= \frac{ds_{23}}{2\pi} 2\pi \delta(s_{23} - k_{23}^2) \cdot \frac{d^4 k_{23}}{(2\pi)^4} (2\pi)^4 \delta^{(4)}(k_{23} - k_2 - k_3) \\ &= \frac{ds_{23}}{2\pi} \frac{d^3 k_{23}}{(2\pi)^3} (2\pi)^4 \delta^{(4)}(k_{23} - k_2 - k_3), \end{aligned} \quad (\text{A.2.6})$$

where s_{23} is the mass square of the particle whose four-momentum is k_{23}^μ . Then we have

$$\begin{aligned} d\Phi_3 &= \prod_{i=1}^3 \frac{d^3 k_i}{(2\pi)^3 2E_i} (2\pi)^4 \delta^{(4)}(q - k_1 - k_2 - k_3) \\ &= \prod_{i=1}^3 \frac{d^3 k_i}{(2\pi)^3 2E_i} (2\pi)^4 \delta^{(4)}(q - k_1 - k_2 - k_3) \cdot \frac{ds_{23}}{2\pi} \frac{d^3 k_{23}}{(2\pi)^3} (2\pi)^4 \delta^{(4)}(k_{23} - k_2 - k_3) \\ &= \frac{ds_{23}}{2\pi} d\Phi_2(k_1, k_{23}) d\Phi_2(k_2, k_3), \end{aligned} \quad (\text{A.2.7})$$

where the 2-body phase space is

$$d\Phi_2(k_2, k_3) = \frac{\bar{\beta}_{23}(\frac{m_2^2}{s_{23}}, \frac{m_3^2}{s_{23}})}{8\pi} \frac{d\cos\theta_{23}}{2} \frac{d\phi_{23}}{2\pi}, \quad (\text{A.2.8})$$

$$d\Phi_2(k_1, k_{23}) = \frac{\bar{\beta}_1(\frac{m_1^2}{s}, \frac{s_{23}}{s})}{8\pi} \frac{d\cos\theta_1}{2} \frac{d\phi_1}{2\pi}. \quad (\text{A.2.9})$$

Recursion Relation for the Phase Space

The above result can be extended to n-body kinematics, the result read as

$$d\Phi_n(P; p_1, \dots, p_n) = \frac{dm_{n-1,n}^2}{2\pi} d\Phi_{n-1}(P; p_1, \dots, p_{n-1,n}) d\Phi_2(p_{n-1,n}; p_{n-1}, p_n). \quad (\text{A.2.10})$$

A.3 Techniques for loop calculations

In this appendix we collect a few tools that is useful for evaluating multi-loop calculations.

Feynman Parametrization

Feynman Parametrization is a technique to rewrite the denominators so that one could evaluate the integral more easily. The idea is to introduce auxiliary parameters to make the denominator simpler, for example:

$$\frac{1}{AB} = \int_0^1 dx \frac{1}{(xA + (1-x)B)^2}. \quad (\text{A.3.1})$$

This can also generalized to N denominators as

$$\frac{1}{A_1 \cdots A_n} = (n-1)! \int_0^1 dx_1 \cdots \int_0^1 dx_n \frac{\delta(1 - \sum_i^n x_i)}{[\sum_i^n x_i A_i]^n}, \quad (\text{A.3.2})$$

Useful Integrals

Here, we also collect some useful Integrals over loop momenta that performed in d dimensions:

$$\int \frac{d^d k}{(2\pi)^d} \frac{(-k^2)^r}{[-k^2 + C - i\epsilon]^m} = \frac{i(4\pi)^\epsilon}{16\pi^2} [C - i\epsilon]^{2+r-m-\epsilon} \frac{\Gamma(r+d/2)}{\Gamma(d/2)} \frac{\Gamma(m-r-2+\epsilon)}{\Gamma(m)}. \quad (\text{A.3.3})$$

Loop Integral

$$\begin{aligned} \int \frac{d^d k}{(2\pi)^d} \frac{1}{[k^2 - \Delta]^3} &= -i \frac{\Gamma(1+\epsilon)}{2(4\pi)^{d/2}} \Delta^{-1-\epsilon}, \\ \int \frac{d^d k}{(2\pi)^d} \frac{k^2}{[k^2 - \Delta]^3} &= i \frac{d}{4} \frac{\Gamma(1+\epsilon)}{\epsilon} \frac{\Delta^{-1-\epsilon}}{(4\pi)^{d/2}}. \end{aligned} \quad (\text{A.3.4})$$

A.4 The large N limit

For classes of gauge theories, whose gauge group can be written as $N \times N$ square matrices, for example, the $SU(N)$ or $SO(N)$ group. In QCD, the large

N approximation is widely used, i.e. approximating QCD with $N \rightarrow \infty$. In this approximation, one can view each event as a collection of independent color dipoles.

In this section, we review the basic idea of the large N limit by deriving the double-line counting rule for large N QCD [133]. We start by considering extending QCD to N colors and N_f flavors. Thus the quark fields are represented by the N -dimensional vectors, and the gauge fields are represented by $N \times N$ traceless matrices t^a , $A_\mu = t^a A_\mu^a$, with index in the adjoint representation of $SU(N)$, and the covariant derivative is

$$D_\mu = \partial_\mu + i \frac{g}{\sqrt{N}} A_\mu. \quad (\text{A.4.1})$$

The gauge coupling constant is replaced by $g \rightarrow \frac{g}{\sqrt{N}}$, which is necessary to keep the theory non-trivial at the large N limit.

One way to understand the scaling of the coupling constant is from the β function

$$\mu \frac{d}{d\mu} \alpha_s(\mu) = -\beta_0 \frac{\alpha_s^2}{2\pi} + O(\alpha_s^3), \quad (\text{A.4.2})$$

with

$$\beta_0 = \frac{11}{3}N - \frac{2}{3}N_f. \quad (\text{A.4.3})$$

Thus, replacing g by g/\sqrt{N} gives

$$\mu \frac{d}{d\mu} \alpha_s(\mu) = - \left(\frac{11}{3} - \frac{2}{3} \frac{N_f}{N} \right) \frac{\alpha_s^2}{2\pi} + O(\alpha_s^3), \quad (\text{A.4.4})$$

now the β function has a well-defined limit as $N \rightarrow \infty$.

For the N counting rules for QCD, one needs to count the powers of N in the Feynman diagram. The quark propagator is

$$\langle \psi^a(x) \bar{\psi}^b(x) \rangle = \delta^{ab} S(x-y), \quad (\text{A.4.5})$$

which is represented diagrammatically by a single line, and the color at the beginning and the end of the line is the same, due to δ^{ab} . The gluon propagator can be written as

$$\langle A_{\mu b}^a(x) A_{\mu b}^c(y) \rangle = D_{\mu\nu}(x-y) \left(\frac{1}{2} \delta_d^a \delta_b^c - \frac{1}{2N} \delta_b^a \delta_d^c \right), \quad (\text{A.4.6})$$

where $A_{\mu b}^a(x) = A_\mu^A (T^A)_b^a$, with a and b are indices in the N and \bar{N} representations. The gluon propagator can then be represented using 't Hooft's double line notation, shown in Fig. A.1

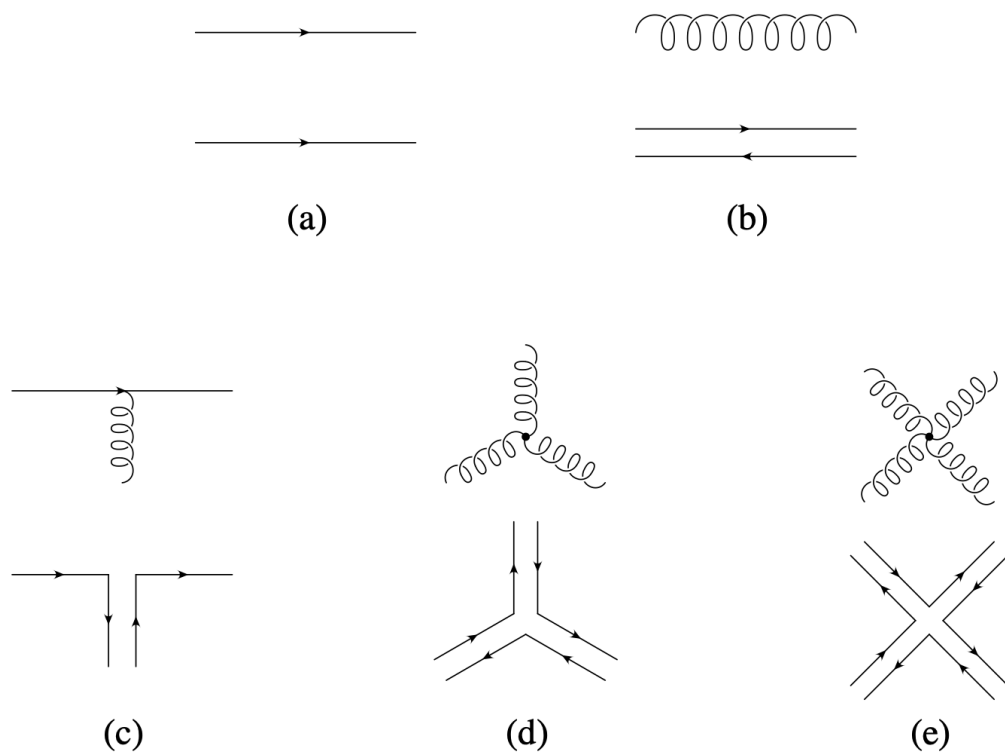


Figure A.1. 't Hooft's double line notation diagrams, figure taken from [A. Manohar, hep-ph/9802419]

B Basics of QCD

B.1 Lagrangian and Feynman rules of QCD

In this section, we summarize the Feynman rules for vertices and propagators in QCD. To begin with, one needs to gauge fix the gauge part of the Lagrangian in order to derive the Feynman rules, for example, the gluon propagator can be extracted using the Faddeev-Popov procedure. For any non-abelian gauge theory, a problem arises which has to be done precisely for the gauge invariance, and it becomes convenient to introduce Faddeev-Popov ghosts explicitly, and possibly to encode the gauge symmetry in a BRST formulation.

With all the ingredients mentioned above, the full Lagrangian becomes:

$$\mathcal{L} = \mathcal{L}_{QCD} + \mathcal{L}_{gauge-fixing} + \mathcal{L}_{ghost}, \quad (\text{B.1.1})$$

for simplicity we choose the Lorenz gauge, then the gauge fixing and Faddeev-Popov-ghost terms are defined as

$$\mathcal{L}_{gauge-fixing} = -\frac{1}{2\lambda} (t_a \partial^\mu A_\mu^a)^2, \quad (\text{B.1.2})$$

$$\mathcal{L}_{ghost} = \bar{\eta}^a \partial^\mu (\delta^{ab} \partial_\mu - g_s f^{abc} A_\mu^c) \eta^b, \quad (\text{B.1.3})$$

where λ is a arbitrary gauge parameter, η is a complex scalar field in the adjoint representation of SUN_c group and the parentheses in Eq.(B.1.3) can be viewed as a covariant derivative. The gluon propagator in the Lorenz gauge is given by

$$\Delta_{\mu\nu}^{ab}(p) = \frac{i\delta^{ab}}{p^2} \left(-g_{\mu\nu} + (1 - \lambda) \frac{p_\mu p_\nu}{p^2} \right), \quad (\text{B.1.4})$$

for $\lambda = 1$, the expression of Eq.(B.1.4) is simplified, this gauge is called Feynman Gauge. Now, we are ready to present the QCD Feynman rules, and for simplicity, we write them in Feynman Gauge. Feynman Rules are summarized below:

Quark propagator:

$$\begin{array}{c} \longrightarrow \\ p \end{array} = \frac{i}{\not{p} - m + i\epsilon} \quad (\text{B.1.5})$$

Gluon propagator:

$$\begin{array}{c} \mu, a \\ \text{~~~~~} \\ \nu, b \\ p \end{array} = \frac{-ig^{\mu\nu}\delta^{ab}}{p^2 + i\epsilon} \quad (\text{B.1.6})$$

Ghost propagator:

$$\begin{array}{c} a \\ \text{-----} \\ p \\ \text{-----} \\ b \end{array} = \frac{i\delta^{ab}}{p^2 + i\epsilon} \quad (\text{B.1.7})$$

Quark-gluon vertex:

$$\begin{array}{c} \nearrow \\ \bullet \\ \searrow \\ \text{~~~~~} \\ \rho \end{array} = -ig_s t^a \gamma^\rho \quad (\text{B.1.8})$$

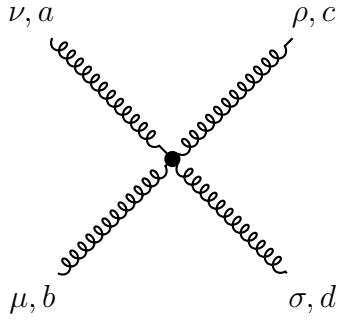
Ghost-gluon vertex:

$$\begin{array}{c} \mu, a, p_1 \\ \text{-----} \\ \bullet \\ \text{~~~~~} \\ \rho, c, k \\ \text{-----} \\ \nu, b, p_2 \end{array} = g_s f^{abc} k^\rho \quad (\text{B.1.9})$$

3-gluon vertex:

$$\begin{array}{c} \nu, b, p_2 \\ \text{~~~~~} \\ \bullet \\ \text{~~~~~} \\ \rho, c, k \\ \text{~~~~~} \\ \mu, a, p_1 \end{array} = -g_s f^{abc} [g^{\mu\nu}(p_1 - p_2)^\rho + g^{\nu\rho}(p_2 - k)^\mu + g^{\rho\mu}(k - p_1)^\nu] \quad (\text{B.1.10})$$

4-gluon vertex:



$$= -ig_s^2 [f^{ead} f^{ebc} (g^{\mu\nu} g^{\sigma\rho} - g^{\mu\rho} g^{\nu\sigma}) + f^{eac} f^{ebd} (g^{\mu\nu} g^{\sigma\rho} - g^{\mu\sigma} g^{\nu\rho}) + f^{eab} f^{ecd} (g^{\mu\sigma} g^{\nu\rho} - g^{\mu\rho} g^{\nu\sigma})] \quad (\text{B.1.11})$$

B.2 Running coupling

Coefficients of Beta function

The coefficients of the beta function, Eq.(1.1.3) up to four-loop in $\overline{\text{MS}}$ scheme are given by [134–136]

$$\beta_0 = \frac{11}{3}C_A - \frac{4}{3}T_F n_f, \quad (\text{B.2.1})$$

$$\beta_1 = \frac{34}{3}C_A^2 - \left(\frac{20}{3}C_A + 4C_F\right)T_F n_f, \quad (\text{B.2.2})$$

$$\beta_2 = \frac{2857}{54}C_A^3 + 2\left(C_F^2 - \frac{205}{18}C_F C_A - \frac{1415}{54}C_A^2\right)T_F n_f + 4\left(\frac{11}{9}C_F + \frac{79}{54}C_A\right)T_F^2 n_f^2, \quad (\text{B.2.3})$$

$$\beta_3 = 4826.16 \quad (N_C = 3, n_f = 5). \quad (\text{B.2.4})$$

Accuracy up to N³LL accuracy

Now let us proceed to evaluate Eq.(1.1.2) explicitly at finite orders of accuracy up to N³LL accuracy

$$\begin{aligned} \log \frac{\mu}{\mu_F} &= -\frac{2\pi}{\beta_0} \int_{\alpha_s(\mu_F)}^{\alpha_s(\mu)} \frac{d\alpha}{\alpha^2} \frac{1}{1 + \frac{\alpha}{4\pi} \frac{\beta_1}{\beta_0} + \left(\frac{\alpha}{4\pi}\right)^2 \frac{\beta_2}{\beta_0} + \left(\frac{\alpha}{4\pi}\right)^3 \frac{\beta_3}{\beta_0}} \quad (\text{B.2.5}) \\ &= -\frac{2\pi}{\beta_0} \int_{\alpha_s(\mu_F)}^{\alpha_s(\mu)} \frac{d\alpha}{\alpha^2} \left[1 - \frac{\alpha}{4\pi} \frac{\beta_1}{\beta_0} + \left(\frac{\alpha}{4\pi}\right)^2 \left(\frac{\beta_1^2}{\beta_0^2} - \frac{\beta_2}{\beta_0}\right) \right. \\ &\quad \left. - \left(\frac{\alpha}{4\pi}\right)^3 \left(\frac{\beta_1^3}{\beta_0^3} - \frac{2\beta_1\beta_2}{\beta_0^2} + \frac{\beta_3}{\beta_0}\right) \right], \end{aligned}$$

where we will use color codes to track terms of LL, NLL NNLL and N³LL accuracy. The running coupling must itself have a perturbative expansion in $\alpha_s(\mu_F)$, at LL, we have

$$\frac{1}{\alpha_s(\mu)} - \frac{1}{\alpha_s(\mu_F)} = \frac{X-1}{\alpha_s(\mu_F)} = \frac{\beta_0}{2\pi} \log \frac{\mu}{\mu_F}. \quad (\text{B.2.6})$$

Thus, at higher accuracy up to N³LL we have the expansion

$$\frac{\alpha_s(\mu_R)}{\alpha_s(\mu)} = X + \frac{\alpha_s(\mu_R)}{4\pi} X_1 + \left(\frac{\alpha_s(\mu_R)}{4\pi}\right)^2 X_2 + \left(\frac{\alpha_s(\mu_R)}{4\pi}\right)^3 X_3 + \dots \quad (\text{B.2.7})$$

which plugged back into Eq.(B.2.5), we could obtain the coefficients of the running coupling:

$$X_1 = \frac{\beta_1}{\beta_0} \log X, \quad (\text{B.2.8})$$

$$X_2 = \frac{\beta_2}{\beta_0} \left(1 - \frac{1}{X}\right) + \frac{\beta_1^2}{\beta_0^2} \left(\frac{\log X}{X} + \frac{1}{X} - 1\right), \quad (\text{B.2.9})$$

$$\begin{aligned} X_3 &= \frac{1}{X^2} \left[\frac{\beta_3}{2\beta_0} (X^2 - 1) + \frac{\beta_1\beta_2}{\beta_0^2} (X + \log X - X^2) \right. \\ &\quad \left. = \frac{\beta_1^3}{2\beta_0^3} (((1 - X)^2 - \log^2 X)) \right]. \end{aligned} \quad (\text{B.2.10})$$

B.3 NLO real corrections for the cross-section $e^+e^- \rightarrow$

In this section, we collect the materials for calculating the next-to-leading order (NLO) real correction for the electromagnetic vertex, shown in Fig. 1.4b. The matrix element of the real contribution is proportional to

$$\sum_{Spin} |M_3|^2 \sim \frac{s_{12}}{s_{23}} + \frac{s_{23}}{s_{13}} + \frac{2s_{12}s_{123}}{s_{13}s_{23}}, \quad (\text{B.3.1})$$

where $s_{ij} = (p_i + p_j)^2$, $s_{ijk} = (p_i + p_j + p_k)^2$, we have labeled the index of the final state quark and anti-quark as 1 and 2, whereas the gluon was labeled as 3. And the sum in the front indicates the sum over the spin of final state particle and the average over the initial once. Therefore, amplitude is singular in the limits of $s_{13} \rightarrow 0$ and $s_{23} \rightarrow 0$.

We can further simplify the above equation by rewriting it in terms of energy fractions, i.e., $x_i = 2k_i \cdot Q/Q^2$, where Q is the center-of-mass energy, defined by $Q = k_1 + k_2 + k_3$. Thus the matrix element becomes

$$\sum_{Spin} |M_3|^2 \sim \frac{x_1^2 + x_2^2}{(1-x_1)(1-x_2)} = \frac{1 + (1-x_3)^2}{x_3} \left(\frac{1}{1-x_1} + \frac{1}{1-x_2} \right) - 2, \quad (\text{B.3.2})$$

where the term contain the soft singularity and correspond to the splitting kernel $p_{g \leftarrow q}(x) = \frac{1+(1-x)^2}{x}$, which describes the probability of collinear splitting as introduced in Sec. 1.3. Therefore the first two term of Eq. B.3.2 indicate two possible collinear behavior.

Now, we could evaluate the phase-space integral with the dimensional regularization, and the singularities appear in terms of the ϵ pole as

$$\sigma_{q\bar{q}}^{(1)} = \sigma_0 \frac{C_F}{\Gamma(1-\epsilon)} \left(\frac{4\pi\mu^2}{s} \right)^\epsilon \left(-\frac{2}{\epsilon^2} - \frac{3}{\epsilon} - 8 + O(\epsilon) \right) \quad (\text{B.3.3})$$

B.4 Quark self-energy diagram

In this section, we calculate the quark self-energy diagram $-i\Sigma(q)$, shown in the last two diagrams in Fig. 1.4a. For massless quarks, it is given in the Feynman gauge as

$$-i\Sigma(q) = -2C_F\mu^{2\epsilon}g_s^2(1-\epsilon) \int \frac{d^d g}{(2\pi)^d} \frac{\not{g} + \not{q}}{(g^2 + 2q \cdot g)}, \quad (\text{B.4.1})$$

where q is the external, on-shell momentum. The above integral can be re-written using the results shown in App. A.3:

$$\begin{aligned} \int \frac{d^d g}{(2\pi)^d} \frac{\not{g} + \not{q}}{(g^2 + 2q \cdot g)} &= \int \frac{d^d g}{(2\pi)^d} \int_0^1 d\alpha \frac{\not{g} + \not{q}}{[\alpha(g^2 + 2q \cdot g) + (1-\alpha)g^2]^2} \\ &= \int_0^1 d\alpha (1-\alpha) \not{q} \int \frac{d^d k}{(2\pi)^d} \frac{1}{k^4} \\ &= \frac{i\not{q}}{2} \frac{\Omega_d}{(2\pi)^d} \int_0^\infty d\tilde{k}_E \tilde{k}_E^{d-5}. \end{aligned} \quad (\text{B.4.2})$$

Here, we have re-written the denominator by using the Feynman parameter, and the integration variable was changed to $k = g + \alpha q$. Moreover, the term that proportional to \not{k} was discarded since it is antisymmetric thus must vanish upon integration. And finally, the k -integral was rotated to Euclidean space.

The above result reveals that it has an infrared divergence due to the contributions as $\tilde{k}_E \rightarrow 0$ as $d \leq 4$, and an ultraviolet divergence due to the contributions as $\tilde{k}_E \rightarrow \infty$ for $d \geq 4$. Therefore, this integral vanishes as

$$\int_0^\infty d\tilde{k}_E \tilde{k}_E^{d-5} = \int_0^\Lambda d\tilde{k}_E \tilde{k}_E^{d-5} + \int_\Lambda^\infty d\tilde{k}_E \tilde{k}_E^{d-5} = \frac{\Lambda^{-2\epsilon}}{-2\epsilon} - \frac{\Lambda^{-2\epsilon'}}{-2\epsilon'}, \quad (\text{B.4.3})$$

where we have split the integral with an arbitrary energy scale Λ . Therefore, the infrared and ultraviolet divergence cancel with each other, thus the self-energy diagrams don't contribute, as guaranteed by the LSZ reduction theorem.

B.5 PDF renormalization

In this section, we summarize the basic process for the PDF renormalization. To begin with, we define the bare partonic cross-section $d\sigma$

$$d\sigma_{ij}(s) = \int dz_1 dz_2 \Gamma_{ik}(z_1) d\bar{\sigma}_{kl}(z_1 z_2 s) \Gamma_{lj}(z_2). \quad (\text{B.5.1})$$

Where $d\bar{\sigma}$ is the renormalized(finite) partonic cross section and Γ_{ik} is the transition functions. Next, for calculation of the the renormalized hadronic cross section. Define the renormalized(finite) PDF \bar{f} :

$$\begin{aligned}\bar{f}(\eta) &= \int_0^1 \int_0^1 dx dz f(x) \Gamma(z) \delta(\eta - xz) \\ &= \int_\eta^1 \frac{dz}{z} f\left(\frac{\eta}{z}\right) \Gamma(z) \equiv f(\eta) \otimes \Gamma(\eta).\end{aligned}\tag{B.5.2}$$

Now for the infrared safe hadronic cross section

$$d\sigma_{AB}^H(s) = \int d\eta_1 d\eta_2 \bar{f}_{kA}(\eta_1) d\bar{\sigma}_{kl}(\eta_1 \eta_2 s) \bar{f}_{lB}(\eta_2),\tag{B.5.3}$$

where $\eta_1, \eta_2 \in [0, 1]$ is defined by $\eta_1 = x_1 z_1$ and $\eta_2 = x_2 z_2$. Then connection of renormalized and non-renormalized hadronic cross section is:

$$\begin{aligned}d\sigma_{AB}^H(s) &= \int dx_1 dx_2 dz_1 dz_2 f_{iA}(x_1) \Gamma_{ik}(z_1) d\bar{\sigma}_{kl}(z_1 z_2 s) \Gamma_{jl}(z_2) f_{jB}(x_2) \\ &= \int dx_1 dx_2 f_{iA}(x_1) d\sigma_{ij}(s) f_{jB}(x_2),\end{aligned}\tag{B.5.4}$$

which is the hadronic cross-section defined by the hard scattering cross-section with the PDF, and only contains unrenormalized things.

C Transforms and Special Functions

In this appendix, we collect useful results for Laplace/Mellin transformations and special functions that have used throughout the thesis

C.1 Laplace and Mellin transforms

Laplace transforms

The Laplace transform of a function $f(t)$ is defined by

$$\tilde{f}(s) = \int_0^{\infty} dt e^{-st} f(t). \quad (\text{C.1.1})$$

Then the inverse is defined as:

$$f(t) = \frac{1}{2\pi i} \int_{c-i\infty}^{c+i\infty} ds e^{st} \tilde{f}(s), \quad (\text{C.1.2})$$

which can be proofed as

$$\begin{aligned} \frac{1}{2\pi i} \int_{c-i\infty}^{c+i\infty} ds e^{st} \tilde{f}(s) &= \int_0^{\infty} dt' f(t') \frac{1}{2\pi i} \int_{c-i\infty}^{c+i\infty} ds e^{s(t-t')} \\ &= \begin{cases} g(t) & t \geq 0 \\ 0 & t < 0 \end{cases}. \end{aligned} \quad (\text{C.1.3})$$

Mellin transform

The Mellin transform is a special case of Laplace transform, when the function $f(x)$ is defined in the range $0 < x < 1$, we can take the Laplace transform by setting $x = e^{-t}$. Thus we have

$$\tilde{f}(N) \equiv \mathcal{M}[f] = \int_0^1 dx x^{N-1} f(x), \quad (\text{C.1.4})$$

which is called Mellin transform, and according to Eq.(C.1.2), the inverse transform can be written as

$$f(x) = \frac{1}{2\pi i} \int_{N_0-i\infty}^{N_0+i\infty} dN x^{-N} \tilde{f}(N). \quad (\text{C.1.5})$$

C.2 Fourier transform

The n-dimensional Fourier transform is defined as

$$\tilde{f}(\vec{b}) \equiv \mathcal{F}[f] = \frac{1}{(2\pi)^{n/2}} \int d^n x e^{-i\vec{b}\cdot\vec{x}} f(\vec{x}), \quad (\text{C.2.1})$$

and the inverse Fourier transform is given by

$$f(\vec{x}) = \frac{1}{(2\pi)^{n/2}} \int d^n x e^{i\vec{b}\cdot\vec{x}} \tilde{f}(\vec{b}). \quad (\text{C.2.2})$$

For the transformation that focus on the radius, i.e.

$$f(x_1, \dots, x_n) = f(r), \quad (\text{C.2.3})$$

then the Fourier transform can be simplified as

$$\tilde{f}(b) = \frac{1}{(2\pi)^{n/2}} \int d^n x e^{-i\vec{b}\cdot\vec{x}} f(r) = b^{1-n/2} \int_0^\infty dr r^{n/2} f(r) J_{n/2-1}(br), \quad (\text{C.2.4})$$

where the function J is the Bessel function. For the case with $n = 2$, it is called the Hankel transform:

$$f(b) = \int_0^\infty dr r J_0(br) f(r). \quad (\text{C.2.5})$$

C.3 Special functions

Euler Gamma function

The Euler Gamma function is defined as

$$\Gamma(z) = \int_0^\infty dt e^{-t} t^{z-1}, \quad (\text{C.3.1})$$

which it is easy to verify that $\Gamma(z)$ satisfy the recursion relation

$$\Gamma(z+1) = z\Gamma(z), \quad (\text{C.3.2})$$

by integrating by parts:

$$\begin{aligned} \Gamma(z+1) &= -e^{-t} t^z \Big|_0^\infty + z \int_0^\infty dt e^{-t} t^{z-1} \\ &= z\Gamma(z). \end{aligned} \quad (\text{C.3.3})$$

For $z = n$ is integer, the above equation is factorial, thus we have

$$\Gamma(n+1) = n!. \quad (\text{C.3.4})$$

Moreover, for Gamma function computed in all half-integers can be obtained using subsequently the recursion relation of Eq.(C.3.2), for example:

$$\Gamma\left(\frac{1}{2}\right) = \sqrt{\pi}. \quad (\text{C.3.5})$$

Poly-gamma functions

The logarithmic derivative of the Gamma function is usually called Di-gamma function:

$$\psi(z) = \frac{d}{dz} \log \Gamma(z). \quad (\text{C.3.6})$$

And we can obtain the recursion relation by using Eq.(C.3.2)

$$\psi(z+1) = \psi(z) + \frac{1}{z}, \quad (\text{C.3.7})$$

for positive integer n , we can obtain

$$\psi(n+1) = \psi(1) + 1 + \frac{1}{2} + \cdots + \frac{1}{n}, \quad (\text{C.3.8})$$

where the first term $-\psi(1)$ is called as the Euler-Mascheroni constant

$$\gamma_E = -\psi(1) = 0.577216 \cdots \quad (\text{C.3.9})$$

For higher-order derivatives, i.e. the Poly-gamma functions, are defined as

$$\psi_n(z) = \frac{d^{n+1}}{dz^{n+1}} \log \Gamma(z), \quad (\text{C.3.10})$$

thus, the Di-gamma function is the lowest order Poly-gamma ψ_0 . Similarly, we can obtain the recursion relation

$$\psi_n(z+1) = \psi_n(z) + (-1)^n n! \frac{1}{z^{n+1}}. \quad (\text{C.3.11})$$

Goncharov polylogarithm

In this section, we summarize the definition and properties of Goncharov polylogarithm (GPL) that we have used in Sec. 3.3, more details about GPLs can be found in Ref. [137]. Firstly, recall the definition of the classical polylogarithms:

$$Li_n(x) = \sum_{k=1}^{\infty} \frac{x^k}{k^n}, \quad |z| < 1, \quad (\text{C.3.12})$$

and it can also be defined iteratively as

$$Li_n(x) = \int_0^x \frac{dt}{t} Li_{n-1}(t), \quad (\text{C.3.13})$$

with $Li_1(x) = -\log(1-x)$. These polylogarithms can be written in terms of GPLs as

$$Li_n\left(\frac{x}{a}\right) = -G(\underbrace{0, \dots, 0}_{n-1}, a; x), \quad (\text{C.3.14})$$

where the GPLs are defined by

$$G(b_1, \dots, b_n; x) = \int_0^x \frac{dt}{t - b_1} (b_2, \dots, b_n; x), \quad (\text{C.3.15})$$

with $G(; x) = 1$, where $b_1, \dots, b_n, x \in \mathbb{C}$.

Here, we also summarize two equalities for index $\{a, \dots, a\}$ and $\{0, \dots, 0\}$:

$$G(\underbrace{0, \dots, 0}_n; x) = \frac{1}{n!} \log^n x, \quad (\text{C.3.16})$$

$$G(\underbrace{a, \dots, a}_n; x) = \frac{1}{n!} \log^n \left(1 - \frac{x}{a}\right). \quad (\text{C.3.17})$$

Plus distribution

Here, we discuss some properties of the plus distribution function $[f(x)]_+$ defined by

$$\int_0^1 [f(x)]_+ g(x) dx \equiv \int_0^1 f(x) [g(x) - g(1)] dx, \quad (\text{C.3.18})$$

where the function f typically is non-integrable at the point $x = 1$. For $x < 1$, they can be thought as itself. i.e.

$$[f(x)]_+ = f(x) \text{ for } x < 1. \quad (\text{C.3.19})$$

Moreover, the plus distribution function defined in Eq.(C.3.18) regularizes functions diverge at $x \rightarrow 1$. Thus the integral with the test function $g(x)$ is finite. In particular, we could use it to regularize the pole at $x = 1$ as

$$\lim_{\epsilon \rightarrow 0} \frac{1}{(1-x)^{1+2\epsilon}} = -\frac{1}{2\epsilon} \delta(1-x) + \frac{1}{(1-x)_+} + O(\epsilon). \quad (\text{C.3.20})$$

One can easily prove the following identities

$$[f(x)]_+ g(x) = [f(x)]_+ g(1) + f(x) (g(x) - g(1)), \quad (\text{C.3.21})$$

$$[f(x) g(x)]_+ = [f(x)]_+ g(x) - \left(\int_0^1 [f(y)]_+ g(y) dy \right) \delta(1-x). \quad (\text{C.3.22})$$

D Analytical Expressions

D.1 One-Loop Feynman Integrals

In this appendix, we summarize some detailed calculations for the strategy of regions discussed in Sec. 1.2.4. To begin with, again we consider the simplest example, namely one-loop vertex corrections in QCD, as discussed in Sec. 1.1.4, which the vertex correction requires the evaluation of the following Feynman integral

$$I = i\mu^{4-d} \int d^d k \frac{1}{(k^2 + i\epsilon) [(k+l)^2 + i\epsilon] [(k+p)^2 + i\epsilon]}, \quad (\text{D.1.1})$$

where $d = 4 - 2\epsilon$ is the dimensional regulator. In the following, we will show the contribution of each of the non-vanishing regions as discussed in Sec. 1.2.4. To begin with, we evaluate when the integration momentum is considered hard, thus one can rewrite and expand the propagator denominators as

$$\begin{aligned} (k+l)^2 &= \underbrace{k^2}_{O(1)} + 2(\underbrace{k_+ \cdot l_-}_{O(\lambda^2)} + \underbrace{k_- \cdot l_+}_{O(1)} + \underbrace{k_\perp \cdot l_\perp}_{O(\lambda)}) + \underbrace{l^2}_{O(\lambda^2)} \\ &= k^2 + 2k_- \cdot l_+ + O(\lambda), \end{aligned} \quad (\text{D.1.2})$$

and similarly

$$(k+p)^2 = k^2 + 2k_+ \cdot p_- + O(\lambda). \quad (\text{D.1.3})$$

Thus the contribution of the hard region to the integral I is given by

$$I_h = i\pi^{-d/2} \mu^{4-d} \int d^d k \frac{1}{(k^2 + i\epsilon) (k^2 + 2k_- \cdot l_+ + i\epsilon) (k^2 + 2k_+ \cdot p_- + i\epsilon)}. \quad (\text{D.1.4})$$

Using the same results, we can obtain the integrals for the soft and collinear region as

$$I_c = i\pi^{-d/2} \mu^{4-d} \int d^d k \frac{1}{(k^2 + i\epsilon) (k^2 + 2k_- \cdot l_+ + i\epsilon) ((k+p)^2 + i\epsilon)}, \quad (\text{D.1.5})$$

$$I_s = i\pi^{-d/2} \mu^{4-d} \int d^d k \frac{1}{(k^2 + i\epsilon) (2k_- \cdot l_+ + l^2 + i\epsilon) (2k_+ \cdot p_- + p^2 + i\epsilon)}. \quad (\text{D.1.6})$$

More about the discussion and result for each component of the integration can be found in [26].

D.2 Multiple soft emission in QED

We can generalize the emission of a single gluon to multiple emissions from the same quark line

$$dW_n \simeq \frac{1}{n!} \prod_{i=1}^n dW_1(q_i), \quad (\text{D.2.1})$$

where the $1/n!$ is the symmetry factor for identical emissions.

The emission of multiple soft photons to all orders can be described by introducing a generating functional:

$$\Phi^{real}[u(q)] \equiv 1 + \sum_{n=1}^{\infty} \int dW_n(q_1, \dots, q_n) u(q_1) \times \dots \times u(q_n), \quad (\text{D.2.2})$$

where we introduced the weight function u for each emission, which acts as phase-space constraint, which we have introduced in Sec. 1.5. Insert Eq.(2.5.2) to Eq.(D.2.1), we obtain the corrections due to real emission

$$\begin{aligned} \Phi^{real}[u(q)] &= 1 + \sum_{n=1}^{\infty} \frac{1}{n!} [dW_1(q) u(q)] \\ &= \exp \left[\int dW_1 u(q) \right]. \end{aligned} \quad (\text{D.2.3})$$

To find the total correction, we also need to consider the virtual contribution. On Sec. 1.5, we have found that the total soft emission has a vanishing effect. Thus, we can exploit this result by imposing:

$$\Phi[u(q)]|_{u=1} = 1. \quad (\text{D.2.4})$$

This is referred to as the unitarity condition, which allows us to correctly normalize Φ by

$$\begin{aligned} \Phi[u(q)] &= \frac{\Phi^{real}[u(q)]}{\Phi^{real}[u(q)=1]} \\ &= \exp \{dW_1[u(q) - 1] \Theta(Q - w) \Theta(w\theta - Q_0)\}. \end{aligned} \quad (\text{D.2.5})$$

D.3 Extracting the non-cusp anomalous dimension for pull calculation

From Eq. (4.3.9), we can determine the anomalous dimension of the soft function from the expansion in ϵ . In the $\overline{\text{MS}}$ scheme, the expansion of the angular coefficient is

$$\frac{g^2}{4^{1-2\epsilon} \pi^{5/2-\epsilon} \Gamma(1/2-\epsilon)} = \frac{4\pi\alpha_s}{4^{1-2\epsilon} \pi^{5/2-\epsilon} \Gamma(1/2-\epsilon)} = \frac{\alpha_s}{\pi^2} \left(1 - \epsilon^2 \frac{\pi^2}{4} + \dots \right). \quad (\text{D.3.1})$$

The $+$ -function expansion of the pull magnitude is

$$t^{-1-2\epsilon} = -\frac{1}{2\epsilon}\delta(t) + \left(\frac{1}{t}\right)_+ - 2\epsilon\left(\frac{\log t}{t}\right)_+ + \dots \quad (\text{D.3.2})$$

Then, the expansion of Eq. 4.3.9 is:

$$\begin{aligned} S_{n_1 n_2}(t, \phi_p) &= \frac{1}{\pi}\delta(t) + \frac{\alpha_s C_F}{\pi^2} \left[-\frac{1}{2\epsilon^2}\delta(t) + \frac{1}{2\epsilon}\delta(t)f(\phi_p) + \frac{1}{\epsilon}\left(\frac{1}{t}\right)_+ \right. \\ &\quad - \frac{1}{2\epsilon}\delta(t)\log\frac{\mu^2 \tan^2 \frac{R}{2}}{E_J^2 \sin^2 \phi_p} - \frac{1}{4}\delta(t)\log^2\frac{\mu^2 \tan^2 \frac{R}{2}}{E_J^2 \sin^2 \phi_p} - \frac{1}{2}\delta(t)f(\phi_p)\log\frac{\mu^2 \tan^2 \frac{R}{2}}{E_J^2 \sin^2 \phi_p} \\ &\quad \left. + \left(\frac{1}{t}\right)_+ \log\frac{\mu^2 \tan^2 \frac{R}{2}}{E_J^2 \sin^2 \phi_p} + \left(\frac{1}{t}\right)_+ f(\phi_p) - 2\left(\frac{\log t}{t}\right)_+ + \delta(t)\frac{\pi^2}{8} \right]. \end{aligned} \quad (\text{D.3.3})$$

Here, $f(\phi_p)$ is shorthand for the long expression with logarithms and arctangents for ϕ_p .

From this expression, we would like to rewrite in from (t, ϕ_p) to (t_x, t_y) . This will enable us to directly transform into b -space in which the cross section can simply be expressed by a product, rather than convolution, of functions. After resummation, we can transform back to real space and integrate over t to determine the distribution of ϕ_p . Because of the δ -function structure of this function, it's first easiest to Fourier transform directly. Note that

$$S_{n_1 n_2}(b, \phi_b) = \int_0^\infty dt \int_0^\pi d\phi_p S_{n_1 n_2}(t, \phi_p) e^{-itb \cos(\phi_p - \phi_b)}, \quad (\text{D.3.4})$$

where b is the magnitude in b -space and ϕ_b is its azimuthal angle.

Now, from the expansion of the soft function, much of these integrals can be done explicitly. We will only worry about the terms that correspond to $1/\epsilon$ poles, as those determine the anomalous dimensions at NLL accuracy, and are all that is needed for NLL resummation. First, if the t dependence is a δ -function, for an arbitrary function $g(\phi_p)$ of the pull angle, we find

$$\int_0^\infty dt \int_0^\pi d\phi_p \delta(t) g(\phi_p) e^{-itb \cos(\phi_p - \phi_b)} = \int_0^\pi d\phi_p g(\phi_p). \quad (\text{D.3.5})$$

Then, we need to integrate over the azimuthal angle ϕ_p . Doing the integral over the logarithm term, we have

$$\int_0^\pi d\phi_p \log\frac{\mu^2 \tan^2 \frac{R}{2}}{E_J^2 \sin^2 \phi_p} = \pi \log\frac{4\mu^2 \tan^2 \frac{R}{2}}{E_J^2}. \quad (\text{D.3.6})$$

Integrating over the $f(\phi_p)$ term, we find

$$\int_0^\pi d\phi_p f(\phi_p) = -\pi \log\left(1 - \frac{\tan^2 \frac{R}{2}}{\tan^2 \frac{\theta_{12}}{2}}\right). \quad (\text{D.3.7})$$

When the t -dependence is in the $+$ -function, we have

$$\begin{aligned} \int_0^\infty dt \int_0^\pi d\phi_p \left(\frac{1}{t}\right)_+ e^{-itb \cos(\phi_p - \phi_b)} \\ = - \int_0^\pi d\phi_p \left[\log \cos(\phi_p - \phi_b) + \log b + \gamma_E + i\frac{\pi}{2} \right]. \end{aligned} \quad (\text{D.3.8})$$

Then, integrating over ϕ_p , we find

$$\int_0^\infty dt \int_0^\pi d\phi_p \left(\frac{1}{t}\right)_+ e^{-itb \cos(\phi_p - \phi_b)} = -\pi \left(\gamma_E + i(\pi - \phi_b) + \log \frac{b}{2} \right). \quad (\text{D.3.9})$$

Combining these results, it follows that the b -space anomalous dimension of the soft function is:

$$\gamma_S = \frac{\alpha_s C_F}{\pi} \left[\log \frac{E_J^2}{\mu^2 b^2 \tan^2 \frac{R}{2}} - \log \left(1 - \frac{\tan^2 \frac{R}{2}}{\tan^2 \frac{\theta_{12}}{2}} \right) - 2\gamma_E - 2i(\pi - \phi_b) \right]. \quad (\text{D.3.10})$$

We can do the same thing for the jet function. Expanding Eq. 4.3.12

$$\begin{aligned} J_q(t, \phi_p) &= \frac{\alpha_s C_F}{2\pi} \frac{(4\pi)^\epsilon}{\pi^{1/2} \Gamma(1/2 - \epsilon)} \frac{1}{t^{1+\epsilon}} \left(\frac{\mu^2}{E_J^2 \sin^2 \phi_p} \right)^\epsilon \left(-\frac{2}{\epsilon} - \frac{3}{2} \right) \\ &= \frac{\alpha_s C_F}{\pi^2} \left(\frac{1}{\epsilon^2} \delta(t) + \frac{1}{\epsilon} \delta(t) \log \frac{\mu^2}{4E_J^2 \sin^2 \phi_p} + \frac{1}{\epsilon} \frac{3}{4} \delta(t) - \frac{1}{\epsilon} \left(\frac{1}{t} \right)_+ \right). \end{aligned} \quad (\text{D.3.11})$$

The anomalous dimension of the jet function is therefore

$$\gamma_J = 2 \frac{\alpha_s C_F}{\pi} \left[\log \frac{b\mu^2}{2E_J^2} + \frac{3}{4} + \gamma_E + i(\pi - \phi_b) \right]. \quad (\text{D.3.12})$$

The sum of the anomalous dimensions of the jet and soft functions are:

$$\gamma_J + \gamma_S = \frac{\alpha_s C_F}{\pi} \left[\log \frac{\mu^2}{4E_J^2 \tan^2 \frac{R}{2}} + \frac{3}{2} - \log \left(1 - \frac{\tan^2 \frac{R}{2}}{\tan^2 \frac{\theta_{12}}{2}} \right) \right]. \quad (\text{D.3.13})$$

This is independent of the value of \vec{b} , as it must be. The remaining logarithms are canceled by the anomalous dimension of the hard function and the out-of-jet soft function.

D.4 Soft emissions at wide angle

We start by considering the contribution from the initial-state dipole. Indicating with p_1 and p_2 the momenta of the incoming quarks and with k the momentum of the soft gluon, we have

$$\mathcal{R}_{12} = \int dk_t k_t dy \frac{d\phi}{2\pi} \frac{\alpha_s(k_t)}{2\pi} \frac{p_1 \cdot p_2}{p_1 \cdot k p_2 \cdot k} \Theta_{\text{jet}} \Theta_{\text{pull}}, \quad (\text{D.4.1})$$

where Θ_{jet} enforces the gluon to be recombined with one of the final-state partons (say parton a) to form the jet we are interested in, and Θ_{pull} enforces the gluon contribution to the observable of choice to be above a certain value.

The above integrals can be easily evaluated by introducing polar coordinates in the rapidity-azimuth plane:

$$\begin{aligned} y - y_a &= r \cos \alpha, \\ \phi - \phi_a &= r \sin \alpha. \end{aligned} \quad (\text{D.4.2})$$

With this choice of variables, the observables become

$$\begin{aligned} t &= |\vec{t}| = zr^2, \\ t_{\parallel} &= |\vec{t} \cdot \hat{n}_{\parallel}| = zr^2 |\cos(\alpha - \beta)|, \\ t_{\perp} &= |\vec{t} \cdot \hat{n}_{\perp}| = zr^2 |\sin(\alpha - \beta)|, \end{aligned} \quad (\text{D.4.3})$$

with $z = \frac{k_t}{p_{ta}}$. The angle β was introduced in Eq. (4.1.5). Note that $\alpha - \beta$ is just the pull angle.

Thus, for the pull magnitude, we obtain

$$\mathcal{R}_{12} = \int_0^1 \frac{dz}{z} \frac{\alpha_s(zp_{ta})}{\pi} \int_0^R dr r \int_0^{2\pi} \frac{d\alpha}{2\pi} \Theta(zr^2 > t) = R^2 \int_t^1 \frac{dz}{z} \frac{\alpha_s(zp_{ta})}{2\pi} + \dots \quad (\text{D.4.4})$$

where the dots indicate subleading contributions. To NLL, the same expression also holds for t_{\parallel} and t_{\perp} :

$$\begin{aligned} \mathcal{R}_{12} &= \int_0^1 \frac{dz}{z} \frac{\alpha_s(zp_{ta})}{\pi} \int_0^R dr r \int_0^{2\pi} \frac{d\alpha}{2\pi} \Theta(zr^2 |\cos(\alpha - \beta)| > t_{\parallel}) \\ &= R^2 \int_{t_{\parallel}}^1 \frac{dz}{z} \frac{\alpha_s(zp_{ta})}{2\pi} + \dots \end{aligned} \quad (\text{D.4.5})$$

$$\begin{aligned} \mathcal{R}_{12} &= \int_0^1 \frac{dz}{z} \frac{\alpha_s(zp_{ta})}{\pi} \int_0^R dr r \int_0^{2\pi} \frac{d\alpha}{2\pi} \Theta(zr^2 |\sin(\alpha - \beta)| > t_{\perp}) \\ &= R^2 \int_{t_{\perp}}^1 \frac{dz}{z} \frac{\alpha_s(zp_{ta})}{2\pi} + \dots \end{aligned} \quad (\text{D.4.6})$$

where again the dots indicate subleading contributions.

Thus far we have calculated the soft wide-angle contribution directly in momentum space. This is in principle sufficient at NLL accuracy that we are working on. Nevertheless, in order to smoothly combine the soft contribution to the collinear one previously computed, we find it convenient to perform the whole resummation in moment (b) space. Therefore to NLL we can write the soft contribution from the initial-state dipole as

$$\mathcal{R}_{12} = R^2 \int_{1/\bar{b}}^1 \frac{dz}{z} \frac{\alpha_s(zp_{ta})}{2\pi}. \quad (\text{D.4.7})$$

Next, we consider soft-wide angle emissions off the final-state ab dipole. As in the previous case, we find it convenient to express the phase-space integrals in polar coordinates. We have

$$\begin{aligned}\mathcal{R}_{ab} &= \int dk_t k_t dy \frac{d\phi}{2\pi} \frac{\alpha_s(\kappa_{ab})}{2\pi} \frac{p_a \cdot p_b}{p_a \cdot k p_b \cdot k} \Theta_{\text{jet}} \Theta_{\text{pull}} \\ &= \int_0^1 \frac{dz}{z} \int_0^R dr \int_0^{2\pi} \frac{d\alpha}{2\pi} \frac{\alpha_s(\kappa_{ab})}{2\pi} \left[\frac{2}{r} + \mathcal{A}(\alpha, \beta) + \mathcal{B}(\alpha, \beta)r + \dots \right] \Theta_{\text{pull}},\end{aligned}\tag{D.4.8}$$

where the argument of the running coupling $\kappa_{ab}^2 = \frac{2 p_a \cdot k p_b \cdot k}{p_a \cdot p_b}$ is the transverse momentum of the gluon with respect to the dipole, in the dipole rest frame. We calculate this contribution as a power expansion in the jet radius R , which corresponds to expanding the integrand in powers of r . The first contribution within the square brackets is the soft and collinear piece, which we have already accounted for in \mathcal{R}_c . Therefore, we consider

$$\tilde{\mathcal{R}}_{ab} = \int_0^1 \frac{dz}{z} \int_0^R dr \int_0^{2\pi} \frac{d\alpha}{2\pi} \frac{\alpha_s(\kappa_{ab})}{2\pi} [\mathcal{A}(\alpha, \beta) + \mathcal{B}(\alpha, \beta)r + \dots] \Theta_{\text{pull}}.\tag{D.4.9}$$

The first term above, namely \mathcal{A} gives no contribution when we integrate over all possible angles. It would give rise to an $\mathcal{O}(R)$ correction if we impose further angular restrictions. We will come back to this observation in Section 4.5. The \mathcal{B} term gives rise to a contribution which is identical in all cases. Therefore, at NLL we have

$$\tilde{\mathcal{R}}_{ab} = \frac{R^2}{4} \frac{\cosh \Delta y + \cos \Delta \phi}{\cosh \Delta y - \cos \Delta \phi} \int_{1/\bar{b}}^1 \frac{dz}{z} \frac{\alpha_s(z p_{ta})}{2\pi} + \mathcal{O}(R^4).\tag{D.4.10}$$

List of Abbreviations

$\overline{\text{MS}}$ Minimal Subtraction

N^3LL next-to-next-to-next-to-leading logarithm

1PI 1-particle-irreducible

BFKL Balitsky-Fadin-Kuraev-Lipatov

BK Balitsky–Kovchegov

BMS Banfi, Marchesini and Smye

CMW Catani-Marchesini-Webber

DGLAP Dokshitzer-Gribov-Lipatov-Altarelli - Parisi

DIS deep inelastic scattering

DLLA double leading logarithmic approximation

EFT effective field theory

FDM finite difference method

GPL Goncharov polylogarithm

IR infrared

IRC infrared and collinear

JIMWLK Jalilian-Marian, Iancu, McLerran, Weigert, Leonidov and Kovner

KLN Kinoshita-Lee-Nauenberg

LHC Large Hadron Collider

LL leading logarithm

LO leading order

LSZ Lehmann- Symanzik-Zimmermann

MC Monte-Carlo

MPI multiple parton interactions

N³LO next-to-next-to-next-to-leading order

NGLs non-global logarithms

NLL next-to-leading logarithm

NLO next-to-leading order

NN neural network

NNLL next-to-next-to-leading logarithm

NNLO next-to-next-to-leading order

NP non-perturbative

ODE ordinary differential equation

PDF parton distribution function

pQCD Perturbative Quantum Chromodynamics

QCD Quantum Chromodynamics

QED Quantum Electrodynamics

QFT quantum field theory

RG renormalisation-group

RGE renormalization group evolution

RR double real

RV real-virtual

S-matrix scattering matrix

SCET Soft-Collinear Effective Theory

SEO strong energy ordering

SM Standard Model

UV ultraviolet

VV double virtual

List of Figures

1	The geometric series for the exact propagator.	3
2	Cancellation between the real production and virtual loop contribution for gluon 2	5
3	QCD color rules for quark–gluon vertices. Black lines denote Feynman-diagram style vertices, colored lines show QCD color connection lines.	6
4	Outline of the thesis: The color denotes the different sections of the thesis. The ovals describe the needed theoretical tools, and the dashed arrowhead lines correspond to the path related to future projects	7
1.1	Deep inelastic scattering in the parton model.	12
1.2	One-loop vertex corrections	15
1.3	Branching of incoming and outgoing gluons	16
1.4	Feynman diagrams for the $O(\alpha_s)$ corrections in $e^+e^- \rightarrow$ hadrons . .	19
1.5	Gluon emission from an external fermion line.	21
1.6	Double emission of a gluon from a fermion line	22
1.7	General form of diagrams with collinear singularities in QED	24
1.8	Vertex for photon splitting into electron-positron pair	27
1.9	Vertices contribute to parton evolution in QCD.	28
1.10	Emission of n gluons from a quark line, strongly ordered	29
1.11	Real corrections for the Drell-Yan process	30
1.12	Recursion relation for 3-body phase space	31
1.13	Plot of truncated power series expansion and its Padé approximants [1/1]	35
2.1	Lund diagram: emissions of soft/collinear gluons are uniformly distributed	40
2.2	Illustration of jets in Hadron-Hadron Collisions	49
2.3	Lund diagram for the jet mass distribution	52
2.4	Correlated emission of two soft gluons	54
2.5	Scale separation and of the calculational procedure in renormalization group improved perturbation theory	62
3.1	Feynman diagrams for the $O(\alpha_s)$ corrections	68
3.2	Stereographic projection of the jet directions, the angles (θ, ϕ) are measured respect to the cone axis.	74

3.3	Comparisons of the fixed-order result up to 5-loop with the Dasgupta-Salam fit for the leading logarithmic resummation of the NGLs. The radius of convergence are shown in the right side	77
3.4	Comparison between the Dasgupta-Salam fit(black), naive exponentiation of the 2-loop result (dashed, green) and the partial resummed result (blue)	78
3.5	Comparison of the one- and two-dressed gluon approximation to the 3- and 4-loop fixed order results and Dasgupta-Salam fit	79
3.6	The solutions to the first and second-order of Eq.(3.4.5) and Eq.(3.4.5), and the bottom panel shows the numerical difference between the analytic solution and NN prediction	82
3.7	Numerical solutions to the 2- and 3-loop expansion of BMS equation, and compare with the analytical solutions in Eq. (3.3.6)-(3.3.9)	84
3.8	Comparisons of the matched result with the Dasgupta-Salam fit, naive exponentiation of the 2-loop result and the dressed gluon approach, with the ratio to the MC fit shown in the right side	84
3.9	Neural network approach for one- and two-dressed gluon calculation, with the ratio to the MC fit shown in the right side	85
4.1	Color-flow Feynman rules for quark-gluon vertex	89
4.2	Possible color connections for signal ($p\bar{p} \rightarrow H \rightarrow b\bar{b}$) and for background ($p\bar{p} \rightarrow g \rightarrow b\bar{b}$)	89
4.3	The radiation pattern from the parton shower simulation, for the b and \bar{b} color-connected to each other (left) and the b and \bar{b} color-connected to the beam (right), plot taken from [Gallicchio, Schwartz, 1001.5027]	90
4.4	Pull vector of jet a and its projections in the rapidity (y) and azimuth (ϕ) plan, which are defined with respect the jet b.	91
4.5	Double check the resummed calculation by compare the expansion of the resummed result and EVENT2 at both LO and NLO	101
4.6	In the left plot we show the distribution of the pull angle in various approximations. Monte Carlo simulations from Pythia are shown at parton level (black +) and hadron level (blue \times). Our theory prediction is also shown at parton level (purple line) and with varying hadronization corrections (light-red band). In the right plot we compare our hadron-level result (red \diamond) to the ATLAS data (black \bullet), as well as to the Monte Carlo simulation (blue \times).	105
4.7	Comparison between the leading order result of pull magnitude, safe projection and the jet mass from EVENT2	107
4.8	Impact of the different contributions to all-order next-to-leading logarithmic resummation of the pull magnitude (left) and the safe projection t_{\parallel} (right). Soft gluon contributions at wide-angle are included as an expansion in the jet radius R through $\mathcal{O}(R^2)$, while the non-global logarithmic contribution is accounted for at $\mathcal{O}(R^0)$. At this accuracy, the distribution of the orthogonal projection t_{\perp} is identical to t_{\parallel}	116

4.9	Plots of the NLL predictions for t (left) and t_{\parallel} (right), together with an estimate of the theoretical uncertainties, obtained by varying the renormalisation scale. The plots also show how the curve is modified once the shift due to non-perturbative corrections is applied.	117
4.10	Comparison of the distributions computed at NLL and supplemented with non-perturbative corrections, to a numerical simulation obtain with the event generator Pythia v8.240.	118
4.11	Monte-Carlo simulations of the $\vec{t} \cdot \hat{n}_{\parallel}$ and $\vec{t} \cdot \hat{n}_{\perp}$ distributions, left and right respectively, measured on $H \rightarrow b\bar{b}$ events generated with Pythia v8.240. The plots show results at both parton and hadron level.	118
4.12	Monte-Carlo simulations of the \mathcal{A}_{\parallel} and \mathcal{A}_{\perp} distributions, left and right respectively, measured on $H \rightarrow b\bar{b}$ events generated with Pythia v8.240. The plots show results at both parton and hadron level.	120
5.1	Joint distribution of $\vec{t} \cdot \hat{n}_{\parallel}$ and $\vec{t} \cdot \hat{n}_{\perp}$ and the joint asymmetry distribution, left and right respectively	124
A.1	't Hooft's double line notation diagrams, figure taken from [A. Manohar, hep-ph/9802419]	132

Acknowledgments

First and foremost, I would like to express my profound gratitude to my supervisor Dr. Simone Marzani for his patient guidance, continuous support and his encouragement throughout last five years; all of which were indispensably conducive to the fruition of this thesis.

I also want to thank Dr. Andrew Larkoski, for all the help and useful discussions. I extend my thanks to Dr. Michael Spannowsky for collaborating and inviting me to IPPP durham during Nov. 2019, where a part of the research for this thesis was conducted.

Among the other people I want to thank Dr. Steffen Schumann and Dr. Andrea Banfi for accepting as external reference and going through all these pages.

I am also thankful to my family, my parents as well as my friends, for having given me the opportunity to be who I am and for all the love they have shown me up to now.

References

- [1] T. Kinoshita, “Mass singularities of Feynman amplitudes,” *J. Math. Phys.*, vol. 3, pp. 650–677, 1962. [4](#)
- [2] T. Lee and M. Nauenberg, “Degenerate Systems and Mass Singularities,” *Phys. Rev.*, vol. 133, pp. B1549–B1562, 1964. [4](#)
- [3] C. Anastasiou, C. Duhr, F. Dulat, F. Herzog, and B. Mistlberger, “Higgs Boson Gluon-Fusion Production in QCD at Three Loops,” *Phys. Rev. Lett.*, vol. 114, p. 212001, 2015. [4](#)
- [4] R. Abbate, M. Fickinger, A. H. Hoang, V. Mateu, and I. W. Stewart, “Thrust at N^3 LL with Power Corrections and a Precision Global Fit for $\alpha_s(m_Z)$,” *Phys. Rev. D*, vol. 83, p. 074021, 2011. [5](#)
- [5] G. Bell, A. Hornig, C. Lee, and J. Talbert, “ e^+e^- angularity distributions at NNLL’ accuracy,” *JHEP*, vol. 01, p. 147, 2019. [5](#)
- [6] M. Dasgupta and G. Salam, “Resummation of nonglobal QCD observables,” *Phys. Lett. B*, vol. 512, pp. 323–330, 2001. [5](#), [53](#), [56](#), [64](#), [77](#), [112](#)
- [7] R. Appleby and G. Salam, “Theory and phenomenology of nonglobal logarithms,” in *38th Rencontres de Moriond on QCD and High-Energy Hadronic Interactions*, 5 2003. [5](#)
- [8] Y. L. Dokshitzer, V. A. Khoze, A. H. Mueller, and S. Troian, *Basics of perturbative QCD*. 1991. [9](#), [57](#)
- [9] R. Ellis, W. Stirling, and B. Webber, *QCD and collider physics*, vol. 8. Cambridge University Press, 2 2011. [9](#), [33](#)
- [10] J. Collins, *Foundations of perturbative QCD*, vol. 32. Cambridge University Press, 11 2013. [9](#)
- [11] J. Campbell, J. Huston, and F. Krauss, *The Black Book of Quantum Chromodynamics: A Primer for the LHC Era*. Oxford University Press, 12 2017. [9](#)
- [12] G. F. Sterman, “Partons, factorization and resummation, TASI 95,” in *Theoretical Advanced Study Institute in Elementary Particle Physics (TASI 95): QCD and Beyond*, pp. 327–408, 6 1995. [9](#)

- [13] M. D. Schwartz, *Quantum Field Theory and the Standard Model*. Cambridge University Press, 3 2014. [9](#), [127](#)
- [14] R. P. Feynman and J. M. Cline, “Feynman Lectures on the Strong Interactions,” 6 2020. [9](#)
- [15] D. Gross and F. Wilczek, “Asymptotically Free Gauge Theories - I,” *Phys. Rev. D*, vol. 8, pp. 3633–3652, 1973. [10](#)
- [16] P. Baikov, K. Chetyrkin, and J. Kühn, “Five-Loop Running of the QCD coupling constant,” *Phys. Rev. Lett.*, vol. 118, no. 8, p. 082002, 2017. [11](#)
- [17] R. P. Feynman, “Very high-energy collisions of hadrons,” *Phys. Rev. Lett.*, vol. 23, pp. 1415–1417, 1969. [11](#), [14](#)
- [18] J. C. Collins and D. E. Soper, “Large Order Expansion in Perturbation Theory,” *Annals Phys.*, vol. 112, pp. 209–234, 1978. [12](#)
- [19] M. Mariño, *Instantons and Large N: An Introduction to Non-Perturbative Methods in Quantum Field Theory*. Cambridge University Press, 9 2015. [13](#)
- [20] J. C. Collins and D. E. Soper, “The Theorems of Perturbative QCD,” *Ann. Rev. Nucl. Part. Sci.*, vol. 37, pp. 383–409, 1987. [13](#)
- [21] J. C. Collins, D. E. Soper, and G. F. Sterman, *Factorization of Hard Processes in QCD*, vol. 5, pp. 1–91. 1989. [13](#)
- [22] J. Bjorken and E. A. Paschos, “Inelastic Electron Proton and gamma Proton Scattering, and the Structure of the Nucleon,” *Phys. Rev.*, vol. 185, pp. 1975–1982, 1969. [14](#)
- [23] L. Landau, “On analytic properties of vertex parts in quantum field theory,” *Nucl. Phys.*, vol. 13, no. 1, pp. 181–192, 1960. [17](#)
- [24] J. D. Bjorken, *Experimental tests of Quantum electrodynamics and spectral representations of Green’s functions in perturbation theory*. PhD thesis, Stanford U., 1959. [17](#)
- [25] M. Beneke and V. A. Smirnov, “Asymptotic expansion of Feynman integrals near threshold,” *Nucl. Phys. B*, vol. 522, pp. 321–344, 1998. [20](#)
- [26] T. Becher, A. Broggio, and A. Ferroglia, *Introduction to Soft-Collinear Effective Theory*, vol. 896. Springer, 2015. [21](#), [143](#)
- [27] E. Laenen, L. Magnea, G. Stavenga, and C. D. White, “Next-to-Eikonal Corrections to Soft Gluon Radiation: A Diagrammatic Approach,” *JHEP*, vol. 01, p. 141, 2011. [23](#)
- [28] C. F. von Weizsacker, “Radiation emitted in collisions of very fast electrons,” *Z. Phys.*, vol. 88, pp. 612–625, 1934. [25](#)
- [29] E. J. Williams, “Correlation of certain collision problems with radiation the-

- ory,” *Kong. Dan. Vid. Sel. Mat. Fys. Med.*, vol. 13N4, no. 4, pp. 1–50, 1935. [25](#)
- [30] M. E. Peskin and D. V. Schroeder, *An Introduction to quantum field theory*. Reading, USA: Addison-Wesley, 1995. [27](#)
- [31] V. N. Gribov and L. N. Lipatov, “Deep inelastic e p scattering in perturbation theory,” *Sov. J. Nucl. Phys.*, vol. 15, pp. 438–450, 1972. [28](#)
- [32] V. N. Gribov and L. N. Lipatov, “e+ e- pair annihilation and deep inelastic e p scattering in perturbation theory,” *Sov. J. Nucl. Phys.*, vol. 15, pp. 675–684, 1972. [28](#)
- [33] Y. L. Dokshitzer, “Calculation of the Structure Functions for Deep Inelastic Scattering and e+ e- Annihilation by Perturbation Theory in Quantum Chromodynamics.,” *Sov. Phys. JETP*, vol. 46, pp. 641–653, 1977. [28](#)
- [34] G. Altarelli and G. Parisi, “Asymptotic Freedom in Parton Language,” *Nucl. Phys. B*, vol. 126, pp. 298–318, 1977. [28](#)
- [35] G. F. Sterman and S. Weinberg, “Jets from Quantum Chromodynamics,” *Phys. Rev. Lett.*, vol. 39, p. 1436, 1977. [33](#)
- [36] G. Luisoni and S. Marzani, “QCD resummation for hadronic final states,” *J. Phys. G*, vol. 42, no. 10, p. 103101, 2015. [33](#), [57](#), [59](#)
- [37] A. J. Larkoski, S. Marzani, and J. Thaler, “Sudakov Safety in Perturbative QCD,” *Phys. Rev. D*, vol. 91, no. 11, p. 111501, 2015. [33](#), [92](#)
- [38] E. Borel., “Mémoire sur les séries divergen,” *Ann. Sci. Ec. Norm. Super. 16*, no. 9, 1899. [34](#)
- [39] E. Leroy. *Ann. Fac. Sci. Toulouse 2*, no. 317, 1900. [35](#)
- [40] B. Andersson, G. Gustafson, L. Lonnblad, and U. Petterson, “Coherence Effects in Deep Inelastic Scattering,” *Z. Phys. C*, vol. 43, p. 625, 1989. [40](#)
- [41] V. Sudakov, “Vertex parts at very high-energies in quantum electrodynamics,” *Sov. Phys. JETP*, vol. 3, pp. 65–71, 1956. [41](#)
- [42] S. Catani, D. de Florian, M. Grazzini, and P. Nason, “Soft gluon resummation for Higgs boson production at hadron colliders,” *JHEP*, vol. 07, p. 028, 2003. [44](#)
- [43] G. Bozzi, S. Catani, D. de Florian, and M. Grazzini, “Transverse-momentum resummation and the spectrum of the Higgs boson at the LHC,” *Nucl. Phys. B*, vol. 737, pp. 73–120, 2006. [45](#)
- [44] A. Banfi, M. Dasgupta, and S. Marzani, “QCD predictions for new variables to study dilepton transverse momenta at hadron colliders,” *Phys. Lett. B*, vol. 701, pp. 75–81, 2011. [45](#), [108](#), [116](#)

- [45] A. Banfi, M. Dasgupta, S. Marzani, and L. Tomlinson, “Probing the low transverse momentum domain of Z production with novel variables,” *JHEP*, vol. 01, p. 044, 2012. [45](#)
- [46] M. Vesterinen and T. Wyatt, “A Novel Technique for Studying the Z Boson Transverse Momentum Distribution at Hadron Colliders,” *Nucl. Instrum. Meth. A*, vol. 602, pp. 432–437, 2009. [45](#)
- [47] A. Banfi, M. Dasgupta, and R. M. Duran Delgado, “The $a(T)$ distribution of the Z boson at hadron colliders,” *JHEP*, vol. 12, p. 022, 2009. [45](#), [108](#)
- [48] M. Cacciari, G. P. Salam, and G. Soyez, “FastJet User Manual,” *Eur. Phys. J. C*, vol. 72, p. 1896, 2012. [49](#), [105](#), [117](#)
- [49] S. D. Ellis and D. E. Soper, “Successive combination jet algorithm for hadron collisions,” *Phys. Rev. D*, vol. 48, pp. 3160–3166, 1993. [49](#), [112](#)
- [50] S. Catani, Y. L. Dokshitzer, M. Seymour, and B. Webber, “Longitudinally invariant K_t clustering algorithms for hadron hadron collisions,” *Nucl. Phys. B*, vol. 406, pp. 187–224, 1993. [49](#), [112](#)
- [51] Y. L. Dokshitzer, G. Leder, S. Moretti, and B. Webber, “Better jet clustering algorithms,” *JHEP*, vol. 08, p. 001, 1997. [49](#), [112](#)
- [52] M. Wobisch and T. Wengler, “Hadronization corrections to jet cross-sections in deep inelastic scattering,” in *Workshop on Monte Carlo Generators for HERA Physics (Plenary Starting Meeting)*, pp. 270–279, 4 1998. [49](#), [112](#)
- [53] M. Cacciari, G. P. Salam, and G. Soyez, “The anti- k_t jet clustering algorithm,” *JHEP*, vol. 04, p. 063, 2008. [49](#), [108](#), [112](#)
- [54] M. Seymour, “Jet shapes in hadron collisions: Higher orders, resummation and hadronization,” *Nucl. Phys. B*, vol. 513, pp. 269–300, 1998. [50](#)
- [55] S. Catani, B. Webber, and G. Marchesini, “QCD coherent branching and semiinclusive processes at large x,” *Nucl. Phys. B*, vol. 349, pp. 635–654, 1991. [53](#)
- [56] D. Yennie, S. C. Frautschi, and H. Suura, “The infrared divergence phenomena and high-energy processes,” *Annals Phys.*, vol. 13, pp. 379–452, 1961. [58](#)
- [57] R. A. Brandt, F. Neri, and M.-a. Sato, “Renormalization of Loop Functions for All Loops,” *Phys. Rev. D*, vol. 24, p. 879, 1981. [60](#)
- [58] G. P. Korchemsky and G. Marchesini, “Structure function for large x and renormalization of Wilson loop,” *Nucl. Phys. B*, vol. 406, pp. 225–258, 1993. [60](#)
- [59] A. Banfi, G. Marchesini, and G. Smye, “Away from jet energy flow,” *JHEP*, vol. 08, p. 006, 2002. [64](#), [70](#), [77](#)

- [60] M. D. Schwartz and H. X. Zhu, “Nonglobal logarithms at three loops, four loops, five loops, and beyond,” *Phys. Rev. D*, vol. 90, no. 6, p. 065004, 2014. [64](#), [65](#), [67](#), [68](#), [70](#), [76](#), [77](#), [84](#)
- [61] A. J. Larkoski, I. Moulton, and D. Neill, “Non-Global Logarithms, Factorization, and the Soft Substructure of Jets,” *JHEP*, vol. 09, p. 143, 2015. [64](#), [78](#)
- [62] M. Balsiger, T. Becher, and D. Y. Shao, “NLL’ resummation of jet mass,” *JHEP*, vol. 04, p. 020, 2019. [64](#)
- [63] R. Kelley, M. D. Schwartz, R. M. Schabinger, and H. X. Zhu, “The two-loop hemisphere soft function,” *Phys. Rev. D*, vol. 84, p. 045022, 2011. [64](#), [123](#)
- [64] T. Becher and M. D. Schwartz, “A precise determination of α_s from LEP thrust data using effective field theory,” *JHEP*, vol. 07, p. 034, 2008. [64](#), [78](#)
- [65] Y.-T. Chien and M. D. Schwartz, “Resummation of heavy jet mass and comparison to LEP data,” *JHEP*, vol. 08, p. 058, 2010. [64](#)
- [66] A. Bassetto, M. Ciafaloni, and G. Marchesini, “Jet Structure and Infrared Sensitive Quantities in Perturbative QCD,” *Phys. Rept.*, vol. 100, pp. 201–272, 1983. [65](#)
- [67] G. Marchesini and B. R. Webber, “Simulation of QCD Jets Including Soft Gluon Interference,” *Nucl. Phys. B*, vol. 238, pp. 1–29, 1984. [66](#)
- [68] I. Balitsky, “Operator expansion for high-energy scattering,” *Nucl. Phys. B*, vol. 463, pp. 99–160, 1996. [73](#)
- [69] Y. V. Kovchegov, “Small x $F(2)$ structure function of a nucleus including multiple pomeron exchanges,” *Phys. Rev. D*, vol. 60, p. 034008, 1999. [73](#)
- [70] K. J. Golec-Biernat and A. Stasto, “On solutions of the Balitsky-Kovchegov equation with impact parameter,” *Nucl. Phys. B*, vol. 668, pp. 345–363, 2003. [73](#)
- [71] Y. Hatta and T. Ueda, “Jet energy flow at the LHC,” *Phys. Rev. D*, vol. 80, p. 074018, 2009. [73](#)
- [72] E. Avsar, Y. Hatta, and T. Matsuo, “Soft gluons away from jets: Distribution and correlation,” *JHEP*, vol. 06, p. 011, 2009. [73](#)
- [73] A. J. Larkoski, I. Moulton, and D. Neill, “The Analytic Structure of Non-Global Logarithms: Convergence of the Dressed Gluon Expansion,” *JHEP*, vol. 11, p. 089, 2016. [78](#), [85](#)
- [74] H. M. McGlone, *Neural Network Analysis in Higgs Search using $t\bar{t}H$, $H \rightarrow b\bar{b}$ and TAG Database Development for ATLAS*. PhD thesis, Glasgow U., 2009. [79](#)
- [75] P. T. Komiske, E. M. Metodiev, and M. D. Schwartz, “Deep learning in

- color: towards automated quark/gluon jet discrimination,” *JHEP*, vol. 01, p. 110, 2017. [79](#)
- [76] R. T. D’Agnolo and A. Wulzer, “Learning New Physics from a Machine,” *Phys. Rev. D*, vol. 99, no. 1, p. 015014, 2019. [79](#)
- [77] J. H. Collins, K. Howe, and B. Nachman, “Extending the search for new resonances with machine learning,” *Phys. Rev. D*, vol. 99, no. 1, p. 014038, 2019. [79](#)
- [78] M. L. Piscopo, M. Spannowsky, and P. Waite, “Solving differential equations with neural networks: Applications to the calculation of cosmological phase transitions,” *Phys. Rev. D*, vol. 100, no. 1, p. 016002, 2019. [79](#)
- [79] H. Lee and I. S. Kang, “Neural algorithm for solving differential equations,” *Journal of Computational Physics*, vol. 91, no. 1, pp. 110–131, 1990. [80](#)
- [80] G. K. Gupta, R. Sacks-Davis, and P. E. Tescher, “A review of recent developments in solving odes,” *ACM Comput. Surv.*, vol. 17, p. 5–47, Mar. 1985. [80](#)
- [81] K. Hornik, M. Stinchcombe, and H. White, “Multilayer feedforward networks are universal approximators,” *Neural Networks*, vol. 2, no. 5, pp. 359 – 366, 1989. [80](#)
- [82] K. Hornik, “Approximation capabilities of multilayer feedforward networks,” *Neural Networks*, vol. 4, no. 2, pp. 251 – 257, 1991. [80](#)
- [83] G. Marchesini and E. Onofri, “Exact solution of BFKL equation in jet-physics,” *JHEP*, vol. 07, p. 031, 2004. [81](#), [82](#)
- [84] R. W. Jones, M. Ford, G. P. Salam, H. Stenzel, and D. Wicke, “Theoretical uncertainties on alpha(s) from event shape variables in e+ e- annihilations,” *JHEP*, vol. 12, p. 007, 2003. [84](#)
- [85] S. Catani, L. Trentadue, G. Turnock, and B. Webber, “Resummation of large logarithms in e+ e- event shape distributions,” *Nucl. Phys. B*, vol. 407, pp. 3–42, 1993. [84](#)
- [86] J. Gallicchio and M. D. Schwartz, “Seeing in Color: Jet Superstructure,” *Phys. Rev. Lett.*, vol. 105, p. 022001, 2010. [87](#), [88](#), [90](#)
- [87] M. L. Mangano, S. J. Parke, and Z. Xu, “Duality and Multi - Gluon Scattering,” *Nucl. Phys. B*, vol. 298, pp. 653–672, 1988. [88](#)
- [88] F. Maltoni, K. Paul, T. Stelzer, and S. Willenbrock, “Color Flow Decomposition of QCD Amplitudes,” *Phys. Rev. D*, vol. 67, p. 014026, 2003. [88](#)
- [89] T. Sjostrand, S. Ask, J. R. Christiansen, R. Corke, N. Desai, P. Ilten, S. Mrenna, S. Prestel, C. O. Rasmussen, and P. Z. Skands, “An Introduction to PYTHIA 8.2,” *Comput. Phys. Commun.*, vol. 191, pp. 159–177, 2015. [90](#), [105](#), [117](#)

- [90] T. Gleisberg, S. Hoeche, F. Krauss, M. Schonherr, S. Schumann, F. Siegert, and J. Winter, “Event generation with SHERPA 1.1,” *JHEP*, vol. 02, p. 007, 2009. [90](#)
- [91] G. Corcella, I. G. Knowles, G. Marchesini, S. Moretti, K. Odagiri, P. Richardson, M. H. Seymour, and B. R. Webber, “HERWIG 6: An Event generator for hadron emission reactions with interfering gluons (including supersymmetric processes),” *JHEP*, vol. 01, p. 010, 2001. [90](#)
- [92] P. Z. Skands and S. Weinzierl, “Some remarks on dipole showers and the DGLAP equation,” *Phys. Rev. D*, vol. 79, p. 074021, 2009. [90](#)
- [93] S. Chatrchyan *et al.*, “Observation of a new boson at a mass of 125 GeV with the CMS experiment at the LHC,” *Phys. Lett.*, vol. B716, pp. 30–61, 2012. [91](#)
- [94] S. Chatrchyan *et al.*, “Search for the standard model Higgs boson produced in association with a W or a Z boson and decaying to bottom quarks,” *Phys. Rev.*, vol. D89, no. 1, p. 012003, 2014. [91](#)
- [95] S. Chatrchyan *et al.*, “Search for invisible decays of Higgs bosons in the vector boson fusion and associated ZH production modes,” *Eur. Phys. J.*, vol. C74, p. 2980, 2014. [91](#)
- [96] V. Khachatryan *et al.*, “Measurement of electroweak production of two jets in association with a Z boson in proton-proton collisions at $\sqrt{s} = 8$ TeV,” *Eur. Phys. J.*, vol. C75, no. 2, p. 66, 2015. [91](#)
- [97] V. Khachatryan *et al.*, “Search for dark matter in proton-proton collisions at 8 TeV with missing transverse momentum and vector boson tagged jets,” *JHEP*, vol. 12, p. 083, 2016. [Erratum: JHEP08,035(2017)]. [91](#)
- [98] A. J. Larkoski and J. Thaler, “Unsafe but Calculable: Ratios of Angularities in Perturbative QCD,” *JHEP*, vol. 09, p. 137, 2013. [92](#)
- [99] V. M. Abazov *et al.*, “Measurement of Color Flow in $t\bar{t}$ Events from $p\bar{p}$ Collisions at $\sqrt{s} = 1.96$ TeV,” *Phys. Rev. D*, vol. 83, p. 092002, 2011. [95](#)
- [100] G. Aad *et al.*, “Measurement of colour flow with the jet pull angle in $t\bar{t}$ events using the ATLAS detector at $\sqrt{s} = 8$ TeV,” *Phys. Lett. B*, vol. 750, pp. 475–493, 2015. [95](#), [105](#)
- [101] M. Aaboud *et al.*, “Measurement of colour flow using jet-pull observables in $t\bar{t}$ events with the ATLAS experiment at $\sqrt{s} = 13$ TeV,” *Eur. Phys. J. C*, vol. 78, no. 10, p. 847, 2018. [95](#)
- [102] G. P. Korchemsky and G. F. Sterman, “Power corrections to event shapes and factorization,” *Nucl.Phys.*, vol. B555, pp. 335–351, 1999. [104](#), [113](#)
- [103] G. Korchemsky and S. Tafat, “On power corrections to the event shape distributions in QCD,” *JHEP*, vol. 0010, p. 010, 2000. [104](#), [113](#)

- [104] S. Bosch, B. Lange, M. Neubert, and G. Paz, “Factorization and shape function effects in inclusive B meson decays,” *Nucl.Phys.*, vol. B699, pp. 335–386, 2004. [104](#), [113](#)
- [105] A. H. Hoang and I. W. Stewart, “Designing gapped soft functions for jet production,” *Phys.Lett.*, vol. B660, pp. 483–493, 2008. [104](#), [113](#)
- [106] Z. Ligeti, I. W. Stewart, and F. J. Tackmann, “Treating the b quark distribution function with reliable uncertainties,” *Phys.Rev.*, vol. D78, p. 114014, 2008. [104](#), [113](#)
- [107] J. Alwall, R. Frederix, S. Frixione, V. Hirschi, F. Maltoni, *et al.*, “The automated computation of tree-level and next-to-leading order differential cross sections, and their matching to parton shower simulations,” *JHEP*, vol. 1407, p. 079, 2014. [105](#), [117](#)
- [108] “Measurement of colour flow with the jet pull angle in $t\bar{t}$ events using the ATLAS detector at $\sqrt{s} = 8$ TeV.” <https://doi.org/10.17182/hepdata.71235>, 2015. [105](#)
- [109] A. J. Larkoski, S. Marzani, and C. Wu, “Theory Predictions for the Pull Angle,” *Phys. Rev.*, vol. D99, no. 9, p. 091502, 2019. [108](#)
- [110] G. Parisi and R. Petronzio, “Small Transverse Momentum Distributions in Hard Processes,” *Nucl. Phys.*, vol. B154, pp. 427–440, 1979. [108](#)
- [111] J. C. Collins, D. E. Soper, and G. F. Sterman, “Transverse Momentum Distribution in Drell-Yan Pair and W and Z Boson Production,” *Nucl. Phys.*, vol. B250, pp. 199–224, 1985. [108](#)
- [112] Y. Bao and A. J. Larkoski, “Calculating Pull for Non-Singlet Jets,” 2019. [109](#)
- [113] A. Banfi and M. Dasgupta, “Problems in resumming interjet energy flows with k_t clustering,” *Phys. Lett. B*, vol. 628, pp. 49–56, 2005. [112](#)
- [114] Y. Delenda, R. Appleby, M. Dasgupta, and A. Banfi, “On QCD resummation with $k(t)$ clustering,” *JHEP*, vol. 12, p. 044, 2006. [112](#)
- [115] A. Banfi, M. Dasgupta, K. Khelifa-Kerfa, and S. Marzani, “Non-global logarithms and jet algorithms in high-pT jet shapes,” *JHEP*, vol. 08, p. 064, 2010. [112](#)
- [116] Z. Nagy and D. E. Soper, “Parton showers with more exact color evolution,” *Phys. Rev.*, vol. D99, no. 5, p. 054009, 2019. [119](#)
- [117] J. R. Forshaw, J. Holguin, and S. Plätzer, “Parton branching at amplitude level,” *JHEP*, vol. 08, p. 145, 2019. [119](#)
- [118] E. Gerwick, S. Hoeche, S. Marzani, and S. Schumann, “Soft evolution of multi-jet final states,” *JHEP*, vol. 02, p. 106, 2015. [123](#)

- [119] G. Bell, R. Rahn, and J. Talbert, “Generic dijet soft functions at two-loop order: correlated emissions,” *JHEP*, vol. 07, p. 101, 2019. [123](#)
- [120] T. Gleisberg and S. Hoeche, “Comix, a new matrix element generator,” *JHEP*, vol. 12, p. 039, 2008. [123](#)
- [121] S. Höche and D. Reichelt, “Numerical resummation at sub-leading color in the strongly ordered soft gluon limit,” 1 2020. [123](#)
- [122] A. J. Larkoski, D. Neill, and J. Thaler, “Jet Shapes with the Broadening Axis,” *JHEP*, vol. 04, p. 017, 2014. [123](#)
- [123] A. V. Kotikov, “Differential equations and Feynman integrals,” in *Antidifferentiation and the Calculation of Feynman Amplitudes*, 2 2021. [124](#)
- [124] J. Jalilian-Marian, A. Kovner, L. D. McLerran, and H. Weigert, “The Intrinsic glue distribution at very small x ,” *Phys. Rev. D*, vol. 55, pp. 5414–5428, 1997. [125](#)
- [125] J. Jalilian-Marian, A. Kovner, A. Leonidov, and H. Weigert, “The Wilson renormalization group for low x physics: Towards the high density regime,” *Phys. Rev. D*, vol. 59, p. 014014, 1998. [125](#)
- [126] H. Weigert, “Nonglobal jet evolution at finite $N(c)$,” *Nucl. Phys. B*, vol. 685, pp. 321–350, 2004. [125](#)
- [127] R. D. Ball and S. Forte, “The Small x behavior of Altarelli-Parisi splitting functions,” *Phys. Lett. B*, vol. 465, pp. 271–281, 1999. [125](#)
- [128] R. D. Ball and S. Forte, “All order running coupling BFKL evolution from GLAP (and vice-versa),” *Nucl. Phys. B*, vol. 742, pp. 158–175, 2006. [125](#)
- [129] A. V. Kotikov and L. N. Lipatov, “DGLAP and BFKL equations in the $N = 4$ supersymmetric gauge theory,” *Nucl. Phys. B*, vol. 661, pp. 19–61, 2003. [Erratum: *Nucl.Phys.B* 685, 405–407 (2004)]. [125](#)
- [130] G. Alvarez and I. Kondrashuk, “Analytical solution to DGLAP integro-differential equation via complex maps in domains of contour integrals,” *J. Phys. Comm.*, vol. 4, no. 7, p. 075004, 2020. [125](#)
- [131] J. Blumlein, “On the $k(T)$ dependent gluon density of the proton,” in *3rd Workshop on Deep Inelastic Scattering and QCD (DIS 95)*, pp. 265–268, 4 1995. [125](#)
- [132] B. Ducloué, E. Iancu, A. Mueller, G. Soyez, and D. Triantafyllopoulos, “Non-linear evolution in QCD at high-energy beyond leading order,” *JHEP*, vol. 04, p. 081, 2019. [125](#)
- [133] A. V. Manohar, “Large N QCD,” in *Les Houches Summer School in Theoretical Physics, Session 68: Probing the Standard Model of Particle Interactions*, pp. 1091–1169, 2 1998. [131](#)

-
- [134] O. Tarasov, A. Vladimirov, and A. Zharkov, “The Gell-Mann-Low Function of QCD in the Three Loop Approximation,” *Phys. Lett. B*, vol. 93, pp. 429–432, 1980. [135](#)
- [135] S. Larin and J. Vermaseren, “The Three loop QCD Beta function and anomalous dimensions,” *Phys. Lett. B*, vol. 303, pp. 334–336, 1993. [135](#)
- [136] T. van Ritbergen, J. Vermaseren, and S. Larin, “The Four loop beta function in quantum chromodynamics,” *Phys. Lett. B*, vol. 400, pp. 379–384, 1997. [135](#)
- [137] A. Goncharov, “Multiple polylogarithms and mixed tate motives,” *arXiv: Algebraic Geometry*, 2001. [141](#)